TRENDS AND SOURCES OF ATMOSPHERIC AEROSOLS INFERRED FROM SURFACE OBSERVATIONS, SATELLITE REMOTE SENSING AND CHEMICAL TRANSPORT MODELING

by

Chi Li

Submitted in partial fulfilment of the requirements
for the degree of Doctor of Philosophy

at

Dalhousie University
Halifax, Nova Scotia
November 2018

Table of Contents

List of Tables

List of Figures

Abstract

Improving the understanding of sources and processes driving the variation of atmospheric aerosols is critical for quantifying their air quality and climate implications and for formulating regulatory policies. This thesis presents four projects that exploit multiple observation data and modeling tools to quantify and interpret aerosol trends and sources.

Global visibility records are filtered and processed to assess historical trends in atmospheric haze. Spatially coherent trends in the screened inverse visibility (1/Vis) are consistent with trends in collocated aerosol measurements over the US and Europe. Trend transitions of 1/Vis in the eastern US, Europe and eastern Asia are significantly associated ($r \sim 0.7$-0.9) with the variation of sulfur dioxide emissions, reflecting historical socioeconomic events and environmental regulation activities.

The 1/Vis dataset over the eastern US reveals significant changes in the dominant aerosol seasonality from winter maxima to summer maxima over 1946-1975. By interpreting seasonal contrasts in 1/Vis trends with a historical emission inventory of aerosol sources, we attribute these changes to increasing sulfate and decreasing primary carbonaceous aerosols. Summer 1/Vis increases faster over the southeastern US than over the northeast during 1956-1975, suggesting concurrent increase in secondary organic aerosols.

A simulation with the GEOS-Chem chemical transport model downscaled with satellite-derived $PM_{2.5}$ identifies a significant increase (0.28 $\mu g\ m^{-3}yr^{-1}$, $p < 0.05$) in global population-weighted $PM_{2.5}$ concentration over 1989-2013, driven by increasing organic aerosols (0.10 $\mu g\ m^{-3}yr^{-1}$), nitrate (0.05 $\mu g\ m^{-3}yr^{-1}$), sulfate (0.04 $\mu g\ m^{-3}yr^{-1}$) and ammonium (0.03 $\mu g\ m^{-3}yr^{-1}$). These four components predominantly drive trends in population-weighted mean $PM_{2.5}$ over populous regions of South Asia (0.94 $\mu g\ m^{-3}yr^{-1}$), East Asia (0.66 $\mu g\ m^{-3}yr^{-1}$), Western Europe (-0.47 $\mu g\ m^{-3}yr^{-1}$) and North America (-0.32 $\mu g\ m^{-3}yr^{-1}$). Trends in area-weighted mean and population-weighted mean $PM_{2.5}$ composition differ significantly.

Two inversion methods are tested for ammonia emission estimates using the GEOS-Chem model and its adjoint at coarse ($2^\circ \times 2.5^\circ$) and fine ($0.25^\circ \times 0.3125^\circ$) resolutions. Comparing to four-dimensional variational assimilation, the iterative finite difference mass balance approach requires fewer iterations to yield smaller errors in the top-down inventories at coarse resolution, while consistently shows larger errors at fine resolution.

List of Abbreviations and Symbols Used

Symbol	Unit	Description
1/Vis	Mm^{-1}	Inverse visibility
4D-Var		Four-dimensional variational assimilation
AERONET		Aerosol Robotic Network
AOD		Aerosol optical depth
APEI		Air Pollutant Emissions Inventory
AVHRR		Advanced Very High Resolution Radiometer
b_{abs}	Mm^{-1}	Absorption coefficients
BC		Black carbon
b_{ext}	Mm^{-1}	Extinction coefficients
BRAVO		Big Bend Regional Aerosol and Visibility Observational Study
BSOA		Secondary organic aerosols from biogenic carbon
b_{sp}	Mm^{-1}	Scattering coefficients
BVOC		Biogenic volatile organic compounds
C		Contrast of radiation intensity of the background and the object
CAC		Criteria Air Contaminants
CCN		Cloud condensation nuclei
C_{crit}		Critical radiation intensity contrast discernible by human eye
CEDS		Community Emission Data System
CI		Confidence interval
CrIS		Cross-track Infrared Sounder
CSN		Chemical Speciation Network
CTM		Chemical transport model
DOFS		Degrees of freedom for signal
EANET		Acid Deposition Monitoring Network in East Asia
EC		Elemental carbon
EDGAR		Emissions Database for Global Atmospheric Research
EMEP		European Monitoring and Evaluation Programme
GBD		Global Burden of Disease Study
GCHP		GEOS-Chem with the high performance option
GCM		General circulation model
GEIA		Global Emissions InitiAtive
GEOS		Goddard Earth Observing System
GFED		Global Fire Emissions Database

GMAO		Global Modeling and Assimilation Office
GSOD		Global summary of the day
H_2SO_4		Sulfuric acid
HEMCO		Harvard-NASA Emissions Component
HNO_3		Nitric acid
I	$W\ m^{-2}sr^{-1}$	Radiation intensity
IBMB		Iterative basic mass balance method
IFDMB		Iterative finite difference mass balance method
IMPROVE		Interagency Monitoring of PROtected Visual Environments program
IPCC		Intergovernmental panel on climate change
ISD		Integrated Surface Database
MEGAN		Model of Emissions of Gases and Aerosols from Nature
MERRA		Modern-Era Retrospective analysis for Research and Applications
MISR		Multi-angle Imaging SpectroRadiometer
MK		Mann-Kendall trend detection
MODIS		Moderate Resolution Imaging Spectroradiometer
N_2O_5		Dinitrogen pentoxide
NAPS		National Air Pollution Surveillance program
NCEI		National Centers for Environmental Information
NCEP		National Center for Environmental Prediction
NEI		National Emission Inventory
NH_3		Ammonia
NH_4NO_3		Ammonium nitrate
NME		Normalized mean error
NO_2		Nitrogen dioxide
NOAA		National Oceanic and Atmospheric Administration
NO_x		Nitrogen oxides
OA		Organic aerosols
OC		Organic carbon
OM/OC		Ratio between organic aerosol and organic carbon mass
OMI		Ozone Monitoring Instrument
p		p-value in statistical significance tests
PM		Atmospheric aerosols, or particulate matter
$PM_{2.5}$	$\mu g\ m^{-3}$	Aerosol particles with an aerodynamic diameter below 2.5 μm
POA		Primary organic aerosols
PWM		population-weighted mean
r		Pearson correlation coefficient

RETRO		REanalysis of the TROpospheric chemical composition
RH	%	relative humidity
SeaWiFS		Sea-viewing Wide Field-of-view Sensor
SEDAC		Socioeconomic Data and Applications Center
SI		Supporting Information
SIA		Secondary inorganic aerosols
Sim_{ds}		downscaled simulation
SO_2		Sulfur dioxide
SOA		Secondary organic aerosols
SSA		Single scattering albedo
SSR	W m^{-2}	Surface solar radiation
$Trend_{sat}$		Satellite-based PM2.5 trends
US		United States of America
US EPA		United States Environmental Protection Agency
UVAI		Ultraviolet aerosol index
Vis	km	Visibility
VOC		Volatile organic compounds
W10	m/s	10-m horizontal wind speed
WHO		World Health Organization
WMO		World Meteorological Organization
α		Ångström exponent
β		Sensitivity of changes in concentrations to emission changes
σ_{abs}	m^2	Absorption cross section
σ_{sp}	m^2	Scattering cross section
Ω	molecules cm^{-2}	Column density

Acknowledgements

Every chapter of this thesis contains the invaluable outcome of the insightful brainstorming, discussion and comments from my advisor, Dr. Randall Martin. I would like to firstly convey my appreciation to your knowledge, encouragement and guidance on my research, which have significantly consolidated my ability to work independently and in collaborations. Thanks also to your financial support, as well as to these awarded by the Killam Trusts Foundation, the Atlantic Computational Excellence Network and the Government of Nova Scotia.

A lot of people made my journey at Dalhousie University a memorable academic and life experience. Thanks to my committee members, Dr. Rachel Chang and Dr. Glen Lesins. The dozens of hours of discussion with you on this project is truly helpful and greatly appreciated. I am lucky to meet the members of the Atmospheric Composition Analysis Group who are excellent scientists and friends. The scientific discussion and technical help from Brian Boys, Matt Cooper, Betty Croft, Melanie Hammer, Colin Lee, Max Manning, Jun Meng, Sajeev Philip, Sacha Ruzzante, Aaron van Donkelaar, Crystal Weagle and Junwei Xu are fruitful and critical to this thesis. Thanks to Balagopal Pillai and Ross Dickson for always being responsive of technical questions, and to the Physics Office for their assistance on every process and paperwork of this PhD program.

I am also privileged to have received crucial contributions and comments from many external collaborators. These people include the co-authors of Chapter 4: Michael Brauer, Monica Crippa, Eloise Marais, Adam Reff, David Ridley, Madeleine Strum and Qiang Zhang. I am also grateful to the contributions to Chapter 5 from Daven Henze, Jennifer Kaiser, Mark Shephard and Lin Zhang. Besides, this work benefits greatly from personal communications with Yang Feng, Jing Li, Kaicun Wang, Xiaolan Wang, Jia Xing, Xuesong Zhang and the GEOS-Chem support team. Also, special thanks to the ten anonymous reviewers for their constructive comments that greatly improved the quality of Chapters 2-4. Lastly, this work could not be realized without the data maintainers of various dataset used that are publicly available.

I must express my sincere thanks to my family and friends. Thank you to my mother Yanhong Qi and my father Yunxiang Li, for your unconditional support and encouragement during the past years. To my kindly grandfather Shengjin Qi, I would never have accomplished this much without being inspired and shaped by your uprightness, clemency and perseverance.

To everyone who helped or is helping me find my unique self, thank you and best wishes.

Chapter 1. Introduction

1.1 Aerosols

Atmospheric aerosols, or particulate matter (PM), are liquid or solid particles suspended in the Earth's atmosphere. Aerosols consist of thousands of chemical species from various sources (Section 1.2), span a wide range of sizes with implications on their ability to affect radiation (Section 1.3), experience aging processes in the atmosphere such as condensation, coagulation and internal mixing (Fuzzi et al., 2015; Khalizov et al., 2009; Trivitayanurak et al., 2008), could be transported distantly (Prospero and Lamb, 2003; Ridley et al., 2012; Xu et al., 2017), and are removed from the atmosphere within ~1 week (Croft et al., 2014; Kristiansen et al., 2016; Ramanathan et al., 2001).

Aerosols play a critical role in atmospheric radiation and climate change. According to IPCC (2013), the effective radiative forcing of aerosols (−0.9 Wm^{-2}) indicates an overall cooling effect that could potentially counteract a significant portion of warming from greenhouse gases (2.83 Wm^{-2}). Meanwhile the high uncertainty (i.e. 5 to 95% confidence interval, –1.9 to –0.1 Wm^{-2}) of aerosol radiative forcing contributes to the greatest portion of uncertainties in the total anthropogenic forcing (1.1 to 3.3 Wm^{-2}). Aerosol radiative forcing is exerted to the atmosphere via (directly) the aerosol-radiation interaction (Bellouin et al., 2005) and (indirectly) the aerosol-cloud interaction (Rosenfeld et al., 2014; Stevens and Feingold, 2009). Confidence in the current understanding of the latter is still low (IPCC, 2013), while accurate estimation of the former requires global knowledge of the 3-D distribution of aerosol size, shape, chemical composition and mixing state (Myhre et al., 2017).

Aerosols also have various environmental implications, such as contributing to soil acidification (Zhang et al., 2012a), altering vegetation growth by strengthening diffuse radiation (Mercado et al., 2009), degrading visibility (Wang et al., 2009), and impairing human health (Fuzzi et al., 2015; Wang et al., 2009). Fine aerosols, usually referred to as aerosol particles with an aerodynamic diameter below 2.5 μm ($PM_{2.5}$), attract particular research interests for their ability to penetrate into human lungs and significant association

with respiratory and cardiovascular diseases (Dockery et al., 1993; Dominici et al., 2006; Lim et al., 2012). The global burden of diseases (GBD) project estimates that exposure to ambient and indoor $PM_{2.5}$ contribute to 4.1 million and 2.6 million premature deaths in 2016, ranking the 6th and 8th among all health risk factors, respectively (Gakidou et al., 2017). Besides the integrated exposure-response function, these estimates of $PM_{2.5}$ health effects are sensitive to the accuracy and resolution (Li et al., 2016c; Punger and West, 2013) of $PM_{2.5}$ concentration.

Anthropogenic perturbation to climate change and air quality are inherently connected (Fiore et al., 2012). Advancing the understanding of global aerosol distribution and variation is fundamental for characterizing their climate and health effects, and for guiding mitigation strategies. The following sections review sources and processes that drive the variability of atmospheric aerosols (Section 1.2), aerosol optical properties that determine their radiative effects (Section 1.3), and existing observation data and modeling tools (Section 1.4). Goals and outlines of this research are provided in Section 1.5.

1.2 Aerosol Chemical Composition

Chemical composition of aerosols largely determine their size and microphysical properties, and are insightful to identify sources and processes (Hand et al., 2012a; Kahn and Gaitley, 2015; Snider et al., 2016). Aerosols are mainly composed of sea salts (mostly sodium chloride), secondary inorganic aerosols (including sulfuric acid, ammonium sulfate and ammonium nitrate), black carbon (BC), mineral species (mostly desert dust), as well as thousands of organic aerosol (OA) species (Fuzzi et al., 2015; Pöschl, 2005; Philip et al., 2014b; Snider et al., 2016; Zhang et al., 2007). These chemical components are either directly emitted as primary particles, or formed via secondary processes (e.g. nucleation and photochemistry) from gaseous precursors.

1.2.1 Sea Salt and Dust

Constituting the two main coarse and natural aerosol components, sea salt and mineral dust aerosols are both primary, and are dominant in aerosol mass over remote ocean and desert regions. Sea salt emissions from sea spray and dust emission from soil or crustal

erosion are both associated with surface wind speed (Ginoux et al., 2001; Jaeglé et al., 2011). Sea salt emission is also sensitive to sea water temperature, salinity and composition (Grythe et al., 2014), and dust emission also depends on surface vegetation cover and soil moisture (Kim et al., 2017; Prospero and Lamb, 2003; Ridley et al., 2014). Besides natural dust, anthropogenic sources of dust due to land use practices (Paul et al., 2012; Webb and Pierre, 2016) and fugitive/industrial processes (Philip et al., 2017) also make a significant contribution to total dust and aerosol mass over semi-arid and urban regions.

1.2.2 Secondary Inorganic Aerosols

Secondary inorganic aerosols (SIA) represent most of water soluble ions in fine aerosols, constituting 20%-60% of total $PM_{2.5}$ (Hand et al., 2012a; Zhang et al., 2007; Zhang et al., 2012b). The formation of SIA begins with the photochemical oxidation of primary gases, i.e. sulfur dioxide (SO_2) and nitrogen oxides (NO_x), to sulfuric acid (H_2SO_4) and nitric acid (HNO_3) (Heald et al., 2012; Kim et al., 2015; Walker et al., 2012). H_2SO_4 is mostly in the condensed phase in ambient conditions due to its low vapor pressure, meanwhile ambient HNO_3 is in gas phase. Another important SIA precursor is ammonia (NH_3). NH_3 would preferentially neutralize H_2SO_4, then the extra NH_3 could form ammonium nitrate (NH_4NO_3) with HNO_3 (Holt et al., 2015; Pinder et al., 2008a). NH_4NO_3 is semivolatile, thus nitrate particle yields under thermodynamic equilibrium depend on temperature and humidity (Heald et al., 2012; Li et al., 2018a; Wang et al., 2013). With excessive NH_3 (high NH_3 and low H_2SO_4) nitrate is HNO_3 sensitive, otherwise nitrate formation is limited by NH_3 (Holt et al., 2015). H_2SO_4 and NH_3 are also critical for new particle formation (Kirkby et al., 2011), another pathway to form secondary aerosols.

SO_2 and NO_x have both anthropogenic (e.g. fossil fuel combustion) and natural (e.g. volcanic eruption for SO_2 and lightning for NO_x) origins (Fisher et al., 2011; Murray et al., 2012; Xing et al., 2013). Over marine regions, a significant SO_2 source is conversion from biogenic dimethyl sulfide (Kettle et al., 1999). Coal combustion in power generation facilities contribute to over 50% of SO_2 emissions globally and over North America, Europe and South Asia (Li et al., 2017b; Lu et al., 2011; Smith et al., 2011b; Vestreng et al., 2007; Xing et al., 2013), while over China coal use in industry is the largest emitter of SO_2 (Li et al., 2017b; Lu et al., 2011; Ma et al., 2017). The industry sector also contributes

to the greatest proportion of NO_x emission over China (Li et al., 2017b; Ma et al., 2017), while over developed regions transportation is generally the dominant source sector for NO_x (Crippa et al., 2016; Xing et al., 2013). Apart from biomass burning and other natural sources, NH_3 is dominantly emitted by agricultural sources (Paulot et al., 2014; Zhang et al., 2018b) and is hard to regulate.

1.2.3 Primary Carbonaceous Aerosols

Primary organic aerosols (POA) and BC are emitted directly from incomplete fossil fuel or biomass burning processes, and are dominant aerosol species over boreal and tropical biomass burning regions (Martin et al., 2010b; Tiitta et al., 2014; Warneke et al., 2009). Global anthropogenic emissions of organic carbon (OC) and BC are dominantly from the use of solid fuels (i.e. coal and wood) for residential heating and cooking in developing countries (Bond et al., 2007; Lu et al., 2011; Wang et al., 2014b), which also contributes dominantly to global premature mortality due to household air pollution (Forouzanfar et al., 2016; Gakidou et al., 2017). Meanwhile the importance of vehicle emissions for OC and BC is more pronounced over developed countries, where the use of solid fuels has historically been substantially reduced (Bond et al., 2007; Hoesly et al., 2018; Ridley et al., 2018; Wang et al., 2014b).

1.2.4 Secondary Organic Aerosols

Formation of secondary organic aerosols (SOA) originates from volatile organic compounds (VOC) which get oxidized and then the oxidation products could partition to the condensed phase (Hoyle et al., 2011). With thousands of species and their unique formation pathways and characteristics, SOA is poorly constrained and represent a major research challenge in atmospheric science (Tsigaridis et al., 2014).

VOC has both anthropogenic and biogenic sources, the latter accounting for more than 80% of the total emission (Guenther et al., 2012). Isoprene and monoterpenes are the dominant emitted species, together contributing to 80% of biogenic VOC (BVOC) emissions (Sindelarova et al., 2014). Although BVOC emission depends little on anthropogenic influence, SOA formation from BVOC may be enhanced substantially by anthropogenic emissions. Observed significant changes in SOA yields under more polluted

environment (Shilling et al., 2013; Xu et al., 2015a; Xu et al., 2016) could be attributable to (1) more existing POA that facilitate reversible portioning to particle phase (Carlton et al., 2010), (2) high SO_2/sulfate that enhance reactive uptake of isoprene SOA (Budisulistiorini et al., 2015; Marais et al., 2016), (3) complicated role of NO_x on BVOC oxidation (Ng et al., 2007; Zhang et al., 2018a), and (4) changes in aerosol water that could mediate SOA yields (Nguyen et al., 2015; Pye et al., 2017), etc.

1.3 Aerosol Optical Properties

The aerosol direct radiative forcing depends on the 3-D distribution of aerosol optical properties, i.e. the abilities of aerosols to scatter or absorb radiation, as well as surface reflectivity (Myhre et al., 2017). The core optical property is aerosol extinction (b_{ext}), i.e. the sum of the aerosol scattering (b_{sp}) and absorption (b_{abs}) coefficients. Other important aerosol optical parameters for radiative forcing could be derived from b_{ext}, b_{sp} and b_{abs}, e.g. aerosol optical depth that is the columnar integration of b_{ext}, single scattering albedo (SSA = b_{sp}/b_{ext}) that represents the relative strength of scattering and absorption, phase function that describes the angular distribution of b_{sp}, and Ångström exponent (α) that indicates the spectral dependence of b_{ext}, b_{sp} or b_{abs} (Dubovik et al., 2002; Dubovik et al., 2006; O'Neill et al., 2003). b_{sp} and b_{abs} are determined by aerosol concentration, as well as its scattering (σ_{sp}) and absorption (σ_{abs}) cross section (Pitchford et al., 2007). σ_{sp} and σ_{abs} are wavelength-dependent, and vary with different chemical composition, hygroscopicity, sizes, shapes, and mixing state. These properties also affect aerosols' ability to activate as cloud condensation nuclei (CCN) and their indirect radiative forcing.

Aerosol chemical composition determines its hygroscopicity and complex refractive index, the latter indicating relative ability to scatter and absorb radiation (Dubovik et al., 2002; Li et al., 2013). SIA and sea salt are nearly purely scattering and strongly hygroscopic, while BC, dust and some of OA (also called brown carbon) are major absorbing particles and are less hygroscopic (Hammer et al., 2016; Martin et al., 2003b). Aerosol size largely determines the spectral range of radiation that aerosols are sensitive to. Fine particles are most efficient in scattering solar radiation while coarse particles (e.g. dust) could also significantly alter longwave radiation (Drury et al., 2010; Ridley et al., 2016). Particle

shape deviating from spherical assumption would significantly modify the optical properties especially for coarse aerosols (Dubovik et al., 2006; Li et al., 2014a; Meng et al., 2010). Finally, different aerosol mixing states can further alter particle size, hygroscopicity and refractive index, and hence optical properties (Bond et al., 2006; Khalizov et al., 2009; Lack and Cappa, 2010; Lesins et al., 2002).

1.4 Observation and Modeling

With large diversity of different properties and a relatively short lifetime relying on meteorology (Fuzzi et al., 2015; Kristiansen et al., 2016; Pöschl, 2005), aerosols exhibit strong spatiotemporal variability. For example, annual mean surface concentration of total $PM_{2.5}$ and composition vary by 2 orders of magnitude among different regions (van Donkelaar et al., 2016; Weagle et al., 2018). Additional observations of aerosols and their precursors are crucially needed to better understand aerosol sources, processes and properties. It is also important to represent existing knowledge of aerosols sources and processes in models to interpret and complement observations for evaluating their climate and health effects, and to infer possible changes under future scenarios.

1.4.1 In Situ Measurements

In situ observational aerosol data sets are essential for characterizing aerosol composition and properties, as well as constraining model representations. Integrated field experiments that track the 4-D evolution of aerosol composition and precursors are especially valuable for characterizing multi-scale aerosol sources and processes (e.g. Jacob et al., 2010; Kulmala et al., 2011; Logan et al., 2010; Martin et al., 2010a). Long-term routine measurements of surface aerosol mass concentration, composition and deposition (e.g. Dabek-Zlotorzynska et al., 2011; Hand et al., 2012a; Snider et al., 2016; Tørseth et al., 2012; Vet et al., 2014; Zhang et al., 2012b) provide information on spatial distribution, trends and seasonal variations.

Besides direct measurements, observational information of aerosol optical properties is also valuable. Surface b_{sp} and b_{abs} measurements are available for the recent two decades over North America and Europe (Collaud Coen et al., 2013; Hand et al., 2014a). AOD,

SSA and other columnar aerosol optical parameters have been continuously retrieved by sunphotometers of the global Aerosol Robotic Network (AERONET) (Dubovik et al., 2002; Li et al., 2014b), and also by other regional networks (e.g. Che et al., 2015; Mitchell et al., 2017). The higher the aerosol concentration, the stronger the aerosol scattering that attenuates direct radiation and intensifies diffuse radiation, and consequently the lower the visibility (Li et al., 2016a). Therefore, worldwide horizontal visibility observations that span several decades could be used as a proxy to estimate long-term changes in aerosol loading (Founda et al., 2016; Husar et al., 2000; Wang et al., 2009).

1.4.2 Satellite Remote Sensing

Remote sensing is a widely used technique of inferring abundance of atmospheric composition based on their interaction with radiation as measured by optical sensing instruments. Satellite remote sensing is the only observational information of aerosols (e.g. AOD, SSA and b_{ext} profile) and important precursors (e.g. SO_2, NO_2, and NH_3) at the global scale and with nearly continuous sampling (e.g. Jethva et al., 2014; Kaufman et al., 2002; Levelt et al., 2018; Levy et al., 2015; Van Damme et al., 2014), which complements in situ measurements over broad areas not covered by ground-based data. Satellite data facilitate global estimates of long-term surface air quality such as $PM_{2.5}$ and nitrogen dioxide (NO_2) (Geddes et al., 2016; van Donkelaar et al., 2016), and are valuable in constraining radiative forcing (Bellouin et al., 2005; Johannes et al., 2008; Yu et al., 2006) and emission inventories (Lamsal et al., 2011; McLinden et al., 2016; Xu et al., 2013; Zhu et al., 2013). Meanwhile satellite retrievals are expected to suffer from measurement noise, calibration accuracy, cloud/snow/bright scenes, vertical sensitivities, and assumptions on surface states, *a priori* profile, and optical properties, etc. (e.g. Li et al., 2009; Rodgers, 2000; Young et al., 2013). Therefore, extensive evaluation and error quantification are usually necessary before these applications (Ridley et al., 2016; Shi et al., 2011; van Donkelaar et al., 2016).

1.4.3 Chemical Transport Modeling

Improved understanding of atmospheric composition and their processes from observations could be generalized into updated mathematical representations in

atmospheric models. Model simulations could also serve to interpret ambient observations to infer sources or processes, and to investigate possible changes under assumed scenarios. With varying focus on thermodynamics, chemistry or climate, different atmospheric models exist from molecular level to synoptic scale (e.g. Bey et al., 2001; Fountoukis and Nenes, 2007; Zhang et al., 2010). Chemical transport models (CTM), such as the GEOS-Chem model used in this thesis, simulate the spatial variation and temporal evolution of atmospheric chemistry based on inputs of emission and meteorology data. Comparing to models targeting dynamics and climate change such as general circulation models (GCM), CTMs are designed to focus on investigating the processes of emission, advection, chemistry and deposition, while generally ignoring feedbacks on meteorology.

One specific application of CTMs is the inverse modeling for emission inventories. Based on observed concentrations of atmospheric composition, an inversion algorithm could be applied with CTM to optimize the emissions (i.e. $\mathbf{x}$) that best reproduce observations (i.e. $\mathbf{y}$), accounting for errors in both observations and the model. Such inversion could be done by a full calculation and optimization inversion of the sensitivities from emissions to observations (i.e. $\frac{\partial \mathbf{y}}{\partial \mathbf{x}}$, where $\mathbf{x}$ and $\mathbf{y}$ are both vectors), such as GEOS-Chem adjoint-based four-dimensional variational (4D-Var) assimilation (Jacob et al., 2016; Paulot et al., 2014; Zhu et al., 2013). Alternatively, the inversion could be simplified by assuming a localized and linear relationship (Lamsal et al., 2011; Martin et al., 2003a).

1.5 Goals and Outlines of this Work

Substantial changes in aerosols have occurred over recent decades as is evident in observations, as this thesis will discuss in more detail. These changes relate with changes in aerosol sources. This thesis compiles multiple in situ observations and satellite data and use a chemical transport model to better understand global and regional aerosol trends and sources.

Few observations reported information about historical aerosol changes before 1990s. In Chapter 2, we infer trends in atmospheric haze as represented by inverse visibility (1/Vis) over more than 3000 ground stations worldwide. We discuss the processes and necessities of data quality control of this aerosol proxy, and present trends from late 1920s over the US, and from early 1970s over Europe and East Asia. We highlight the strong association

of observed 1/Vis trends with historical SO_2 emissions. This work was published in *Atmos. Chem. Phys.* in 2016.

Aerosol seasonal variation reflects the dominance of chemical composition. Based on the developed 1/Vis dataset in Chapter 3, we discover and report, for the first time, significant changes in the dominant aerosol seasonality over the eastern US, from winter maxima to summer maxima over 1946-1975. We attribute this historical change to increasing dominance of sulfate and SOA and decreasing aerosol fraction of POA and BC, based on seasonal contrasts in 1/Vis trends and historical anthropogenic emissions. This work was published in *Environmental Science and Technology Letters* in 2018.

Compared to changes in total aerosol loading such as $PM_{2.5}$, changes in aerosol chemical composition are more insightful on changes in specific sources. In Chapter 4, we collect time-varying emission inventories and conduct a 25-year global GEOS-Chem simulation. Downscaled with satellite-derived $PM_{2.5}$, this simulation reports regional diversities in dominant aerosol species that drive trends in the health-relevant population-weighted $PM_{2.5}$ concentration, and highlights the dominant contribution of OA to the increase in population-weighted $PM_{2.5}$ globally and over the most populous regions of South and East Asia. This work was published in *Environmental Science and Technology* in 2017.

Uncertainties in "bottom-up" ammonia (NH_3) emission estimates are a significant source of simulation errors of ammonia and aerosols in chemical transport models. Emerging satellite remote sensing observations of NH_3 abundance are promising to infer "top-down" emission constraints. Various inverse modeling methods exist, while their applicability has not been evaluated for NH_3 emissions. In Chapter 5, we use the GEOS-Chem model and its adjoint to simulate NH_3 column densities observed by satellite instruments with known emissions and apply two "top-down" inversion methods from these pseudo observations. The goals of this work were to evaluate their applicability at coarse and fine resolutions, contrast their difference in performances, and interpret its implications for realistic emission inversions.

Chapter 2. Evaluation and Application of Multi-decadal Visibility Data for Trend Analysis of Atmospheric Haze

2.1 Abstract

There are few multi-decadal observations of atmospheric aerosols worldwide. This study applies global hourly visibility (Vis) observations at more than 3000 stations to investigate historical trends in atmospheric haze over 1945-1996 for the US, and over 1973-2013 for Europe and eastern Asia. A comprehensive data screening and processing framework is developed and applied to minimize uncertainties and construct monthly statistics of inverse visibility (1/Vis). This data processing includes removal of relatively clean cases with high uncertainty, and change point detection to identify and separate methodological discontinuities such as the introduction of instrumentation. Although the relation between 1/Vis and atmospheric extinction coefficient (b_{ext}) varies across different stations, spatially coherent trends of the screened 1/Vis data exhibit consistency with the temporal evolution of collocated aerosol measurements, including the b_{ext} trend of -2.4% yr^{-1} (95% CI: -3.7, -1.1% yr^{-1}) vs. 1/Vis trend of -1.6% yr^{-1} (95% CI: -2.4, -0.8% yr^{-1}) over the US for 1989-1996, and the fine aerosol mass ($PM_{2.5}$) trend of -5.8% yr^{-1} (95% CI: -7.8, -4.2% yr^{-1}) vs. 1/Vis trend of -3.4% yr^{-1} (95% CI: -4.4, -2.4% yr^{-1}) over Europe for 2006-2013. Regional 1/Vis and Emissions Database for Global Atmospheric Research (EDGAR) sulfur dioxide (SO_2) emissions are significantly correlated over the eastern US for 1970-1995 ($r = 0.73$), over Europe for 1973-2008 ($r \sim 0.9$) and over China for 1973-2008 ($r \sim 0.9$). Consistent "reversal points" from increasing to decreasing in SO_2 emission data are also captured by the regional 1/Vis time series (e.g. late 70s for the eastern US, early 1980s

for western Europe, late 1980s for eastern Europe, and mid 2000s for China). The consistency of 1/Vis trends with other in situ measurements and emission data demonstrates promise in applying these quality assured 1/Vis data for historical air quality studies.

2.2 Introduction

Atmospheric aerosols have broad implications for air quality and climate change. The Global Burden of Disease (GBD) assessment attributed ambient exposure to aerosol particles with an aerodynamic diameter below 2.5 μm ($PM_{2.5}$) as the sixth largest overall risk factor for premature mortality with 3.2 million premature deaths per year (Lim et al., 2012). Aerosols are also considered to be the most uncertain component for global radiative forcing (IPCC, 2013). Aerosols are formed from a variety of emission sources and chemical processes with a short tropospheric lifetime against different removal mechanisms, yielding a highly variable spatiotemporal distribution that is not well understood (Fuzzi et al., 2015). Information on long-term aerosol temporal evolution is crucially needed across a range of disciplines. Historical $PM_{2.5}$ exposure and its trends are needed to understand changes in Global Burden of Disease (Brauer et al., 2012), and to guide mitigation actions (Apte et al., 2015; Wong et al., 2004). Observations are needed to evaluate historical emission inventories that are crucial to accurately represent the changes in aerosol sources and its consequent feedbacks on climate (Lu et al., 2011; Smith et al., 2011b; Xu et al., 2013). Aerosol trend analysis is also fundamental to assessing radiative forcing, evaluating model processes, and projecting future changes (Chin et al., 2014; Leibensperger et al., 2012; Li et al., 2014b). Various studies have been carried out to investigate aerosol trends using in situ measurements (Collaud Coen et al., 2013; Hand et al., 2012b; Murphy et al., 2011), satellite/ground remote sensing (Hsu et al., 2012; Li et al., 2014b; Zhang and Reid, 2010), and analysis of measurements with models (Boys et al., 2014; Chin et al., 2014; Pozzer et al., 2015; Turnock et al., 2015). However, these studies are mostly limited to the recent 2 decades, since few satellite or in situ aerosol observations exist over land prior to the 1990s. Long-term observations of aerosols at the global scale are needed to place

current knowledge of their spatial distribution and temporal evolution in a historical context for all these applications.

Visibility observations offer an alternative information source for the investigation of historical aerosol trends. Horizontal visibility (Vis) from worldwide meteorological stations and airports is mainly determined by the optical extinction (b_{ext}) of the atmospheric boundary layer, and has been recognized as a proxy of the atmospheric aerosol burden/loading (Husar et al., 2000). Historical Vis data from more than 3000 stations have been applied to characterize decadal trends in global aerosol optical depth (AOD) from 1973 to 2007 (Wang et al., 2009). Regional trend studies of Vis were also conducted for populated areas e.g. the US (Husar et al., 1981; Schichtel et al., 2001), Europe (Vautard et al., 2009) and China (Che et al., 2007; Chen and Wang, 2015; Lin et al., 2014; Wu et al., 2012; Wu et al., 2014), and the inferred trends were usually attributed to changes in anthropogenic emission. Another study employing Vis over desert regions (Mahowald et al., 2007) found an association of Vis with meteorology factors such as drought index (based on precipitation and temperature) and surface wind speeds. Trends in Vis data interpreted with other data sets also supported studies of several aerosol related climate trends such as the western Pacific subtropical high (Qu et al., 2013) and precipitation (Rosenfeld et al., 2007; Stjern et al., 2011).

Despite the abundance of the above-mentioned studies, the interpretation of Vis data and their trends might be limited by insufficient data processing or poor data quality. Multi-decadal Vis data might contain possible variation or even reversal in haze trends as expected from historical emission and surface solar radiation (SSR) data (Lu et al., 2010) (Stern, 2006; Streets et al., 2006; Wild et al., 2005). It is of particular interest how these changes would associate with the trends of air quality, and would be captured by the Vis data. Detailed variation in global Vis trends are rarely reported in these previous studies. On the other hand, Vis data are inherently uncertain because most Vis are recorded through human observations with variable protocols. For example, an increase in inverse visibility (1/Vis) has been reported over the US during 1993-2010 (Wang et al., 2012) that is opposite in sign with the significant decline (>10% decade^{-1}) of observed $PM_{2.5}$, sulfate and b_{ext} (US EPA, 2012; Attwood et al., 2014; Hand et al., 2012b; Hand et al., 2014a), and raises questions about the quality of Vis observations.

This study revisits the Vis observations to characterize historical trends of atmospheric haze by asserting two major efforts: a more comprehensive data quality assurance processing and a more detailed trend analysis for separate periods. This analysis provides multi-decadal information about air quality evolution and its connections to emission trends over major industrialized regions. To facilitate interpretation, the theoretical relationship between Vis and atmospheric extinction is reviewed in the following section. Section 2.4 describes the data and processing methods, followed by an evaluation of the screened monthly 1/Vis and its trends using in situ measurements in Section 2.5. Section 2.6 provides an extensive discussion of the resultant spatial distribution and temporal variation of the derived 1/Vis trends for three highly populated regions (i.e. the US, Europe and eastern Asia), and comparative analysis of these trends with sulfur dioxide (SO_2) emission data. Section 2.7 summarizes this work and its implications.

2.3 Relationship between Vis and b_{ext}

Visibility is a measure of the transparency of the atmosphere, and is defined as the greatest distance at which a black object can be recognized against the horizon sky (WMO, 2008). The visibility of a particular object (i.e. visibility marker) is determined by the contrast *C* between the radiation intensity *I* of the background *b* and of the object *o* reaching an observer at distance *x* from the object:

$$C(x) = \frac{I_b(x) - I_0(x)}{I_b(x)} \tag{2-1}$$

Under assumptions of a plane-parallel atmosphere and homogeneous background intensity (i.e. constant sky brightness), *C* exhibits an exponential decay based on Beer's law,

$$C(x) = C_0 \exp(-b_{ext} x) \tag{2-2}$$

where b_{ext} is the extinction of the atmosphere (including extinction of aerosols and molecules). Since Vis represents the furthest distance corresponding to a minimum critical contrast C_{crit} below which the observer cannot discern the object, we have

$$C_{crit} = C_0 \exp(-b_{ext} Vis) \quad (2\text{-}3)$$

Rearranging to solve for b_{ext} yields

$$b_{ext} = \frac{K}{Vis} \quad (2\text{-}4)$$

where $K = -ln\frac{C_{crit}}{C_0}$. This is the Koschmieder equation (Griffing, 1980), representing a linear relationship between 1/Vis and b_{ext}. The slope K of this relationship is mainly determined by two factors: the inherent contrast at the object's position C_0 and the critical contrast of the observer's eye C_{crit}. This equation is only valid for a plane-parallel and homogeneous atmosphere. For situations with high gradients of b_{ext} (e.g. smoke plumes), this could readily break down. Even for ideal conditions, this relationship could vary due to the variation of C_0 (change of markers or observing conditions) and/or C_{crit} (change of observer or protocol). It is sometimes assumed that the object is perfectly black ($C_0 = 1$) so that K is only determined by C_{crit}. Nevertheless, K still varies from 1.5 to 3.9 (e.g. Husar and Wilson, 1993; Schichtel et al., 2001; Wang et al., 2009) because of different C_{crit} values or different observing conditions. Below we similarly find that even where 1/Vis is highly correlated with b_{ext} data, K still varies significantly for different stations.

2.4 Data and Processing

2.4.1 Visibility Data

We begin with raw Vis data from synoptic observations over 1929-2013 in the Integrated Surface Database (ISD, https://catalog.data.gov/dataset/integrated-surface-global-hourly-data) archived at the NOAA's National Centers for Environmental Information (NCEI). ISD data are generated through merging hundreds of data sources (Smith et al., 2011a). The data from different networks have different report frequencies (e.g. hourly, 3-hourly, 6-hourly, etc.). We reject the daily averaged data called "global summary of the day" (GSOD) since an arithmetic mean could bias the daily and monthly statistics because of threshold and discreteness issues, as discussed in Section 2.4.1.2. Each processing step is described below.

2.4.1.1 Conventional screening

We begin with "conventional screening" using algorithms adapted from prior studies. We eliminate effects on Vis of weather conditions such as fog, precipitation, low cloud and high relative humidity (RH > 90%, estimated from temperature and dew point) following the description in Husar et al. (2000). A sensitivity test that limited conditions to RH < 80% reduced data density but yielded similar trend results without changing the main findings in this study. Potential human errors are reduced by statistical checks of daily spikes and non-repeating values following Lin et al. (2014). Duplicate stations with different names are combined, and stations lacking geolocation information are removed following Willett et al. (2013). After this screening step, 21,703 stations remain from the 30,895 original ISD sites.

2.4.1.2 Threshold filtering

We develop a filter to address spatial and temporal variation in the threshold of reported Vis. The "threshold" is the maximum reported Vis at a station that often depends on the furthest employed Vis marker. Vis above this threshold is not resolved. Thus the threshold acts as an artificial detection limit. The ability of Vis data to capture the variation of b_{ext} is weak when the air is clean and/or the adopted threshold Vis at the station is low. We identify the 99th percentile of reported Vis in each year as the threshold for each station, and reject months with ≤ 50% of the data below the threshold. This approach differs from eliminating stations with low thresholds (e.g. Husar et al., 2000). Observations could still be meaningful at heavily polluted stations even if the threshold is low, while for clean stations with high thresholds most of the reported Vis could remain unresolved. To further ensure data representativeness and variability, data are removed for any month with less than 4 different days of data or with nearly identical percentile values (i.e. the ratio of 50th and 25th percentile Vis is less than 1.07 or the ratio of the 25th to 10th percentile Vis is less than 1.1) following Husar et al. (2000). This data screening step further reduces the number of qualified station to 10,446.

We describe the monthly Vis level with nonparametric statistics rather than arithmetic mean for a few reasons. First, an arithmetic mean would have biased monthly statistics due to the variable fraction (50-100% after the threshold filtering) of Vis reported under the

threshold in 1 month. Second, Vis is recorded as discrete values with coarse and uneven increments, and is not normally distributed (Schichtel et al., 2001). The protocol of reporting Vis varies across stations, depending on local regulations and available Vis markers. Both issues would affect the GSOD data or the monthly mean 1/Vis so we work with the raw data. We follow the convention to adopt the 75th percentile 1/Vis as the monthly representation of haziness (Husar et al., 2000; Qu et al., 2013). Other statistics, such as 50th and 90th percentile 1/Vis lead to similar trends and do not alter the conclusion of this study. However, the 50th percentile is closer to and more vulnerable to the detection limit, while the 90th percentile tends to be more susceptible to extreme events. Husar et al. (1987) assessed the effects of different choices of statistics. Below we commonly refer to the 75th percentile as "monthly 1/Vis" unless stated otherwise.

2.4.1.3 Completeness check

Completeness criteria are applied for further screening. A year of data is removed if less than 6 months in this year is available to guarantee annual representativeness. Short-term time series covering less than 7 years are also removed since they offer little information on trends. A total of 6,466 stations comply with these standards and remain in the data archive.

2.4.1.4 Change point detection

Sudden discontinuities in characteristics of the derived monthly time series of 1/Vis are frequently found even after the comprehensive filtering. Any change of the Vis marker (i.e. change of C_0) or observing standard (i.e. change of C_{crit}) could alter the relationship (K) between b_{ext} and 1/Vis, introducing inconsistency in the time series unrelated to actual b_{ext} change. For example, instrumentation (e.g. telephotometers, transmissometers and scatterometers) has replaced human observers at many sites in the US (Kessner et al., 2013) and to a lesser extent in Europe (Vautard et al., 2009), but there is a lack of documentation recording when and at which stations this switch occurred. Such artificial changes could seriously bias the inferred trends if not addressed. Various methods have been proposed to detect abrupt "change points" (Costa and Soares, 2009; Reeves et al., 2007). For example, the RHtest software package developed for multiple change point detection is based on

penalized maximal t and F test (Wang et al., 2007; Wang, 2008b) embedded in a recursive testing algorithm (Wang, 2008a). We adopt the FindU function in the RHtest (version 4, available at http://etccdi.pacificclimate.org/) software to detect "type-1" change points (without reference time series). We manually examine all reported change points for possible false detections. By visually inspecting each remaining station from Section 2.4.1.3, we retain only obvious structural discontinuities in the time series of 50th or 75th monthly percentiles from the candidate change points provided by the RHtest results.

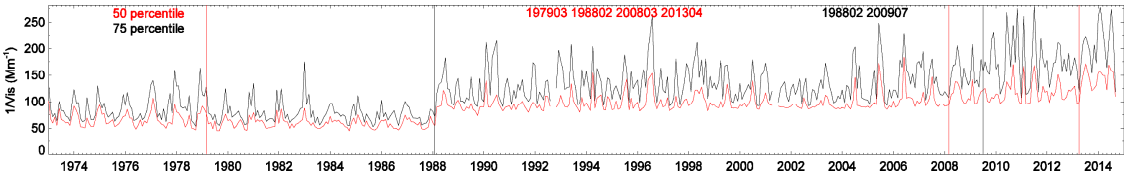

Figure 2-1. An example of change point detection and determination based on the time series of 50th (red) and 75th (black) percentiles of monthly 1/Vis. Automatically detected change points are represented by vertical lines. Text in the inset lists the dates of automatically detected points. In this example, five significant change points are identified, in which February 1988 is determined as the separation point for further analysis, while other reported breaks are considered to be false detections.

Figure 2-1 shows an example of change point detection based on the time series of 50th and 75th percentiles of monthly 1/Vis at one ISD station. The change points are reported in three different types (95% confidence): significant change, possibly significant (undetermined) change and insignificant change. In this example, although four significant changes for the 50th percentiles 1/Vis and two significant change points for the 75th percentiles 1/Vis are reported, only one candidate (February, 1988) indicated by both time series is considered to be an obvious discontinuity and chosen as the actual change point.

The candidate change points provided by RHtest allow greater efficiency than pure manual detection, which is prohibitive for thousands of stations. Any gap of more than 4 years in a time series is also considered to be a change point. Such a large gap could obscure protocol changes and introduce uncertainties in the derived trends without separation. We analyze separately the 1/Vis time series before and after the determined change points. Finally, we eliminate any year of data with annual 1/Vis (average of monthly 1/Vis) less than 40 Mm^{-1} to address the poor data variation and representativeness of clean environments, as will be discussed in Section 2.5.1.

We acknowledge that, although guided by RHtest results and a synthetic analysis based on the time series of 50th and 75th percentiles, this is still a subjective method. A small fraction of determined change points could be extreme events, while a few undetected change points missed by this subjective judgement might remain in the analysis. Several time series with irregular temporal variation are also removed during the visual examination. In summary, only 1/Vis time series considered to be consistent and continuous are analyzed here.

A total of 3,930 stations (5,320 time series) remain after this processing step, in which 856 sites (22%) are diagnosed as containing change points and thus separated. This small fraction of structural discontinuities generally has minor impacts on the large-scale trend features and regional trends in Section 2.6 according to our sensitivity test using data without separation. But the separated data reduce spatial incoherency in the derived trend maps, and are more reliable for studies over small areas or independent stations, as shown in Figure 2-1.

The threshold filtering (Section 2.4.1.2) and change point detection (Section 2.4.1.4) are designed to ensure basic representativeness and continuity of the derived monthly 1/Vis time series, and are the main differences of this processing from prior investigations.

2.4.1.5 Distribution of stations

Figure 2-2 (top) shows the ISD stations and the number of years with available data for 1929-2013 before and after data processing. Most of the remaining stations are located in the US (753), Europe (1625) and eastern Asia (791). More than 6000 removed stations have less than 7 years of data as indicated in the left panel. Many other removed stations have small population density or harsh observing environment (e.g. islands and polar regions), which might correspond to poor observing conditions or maintenance.

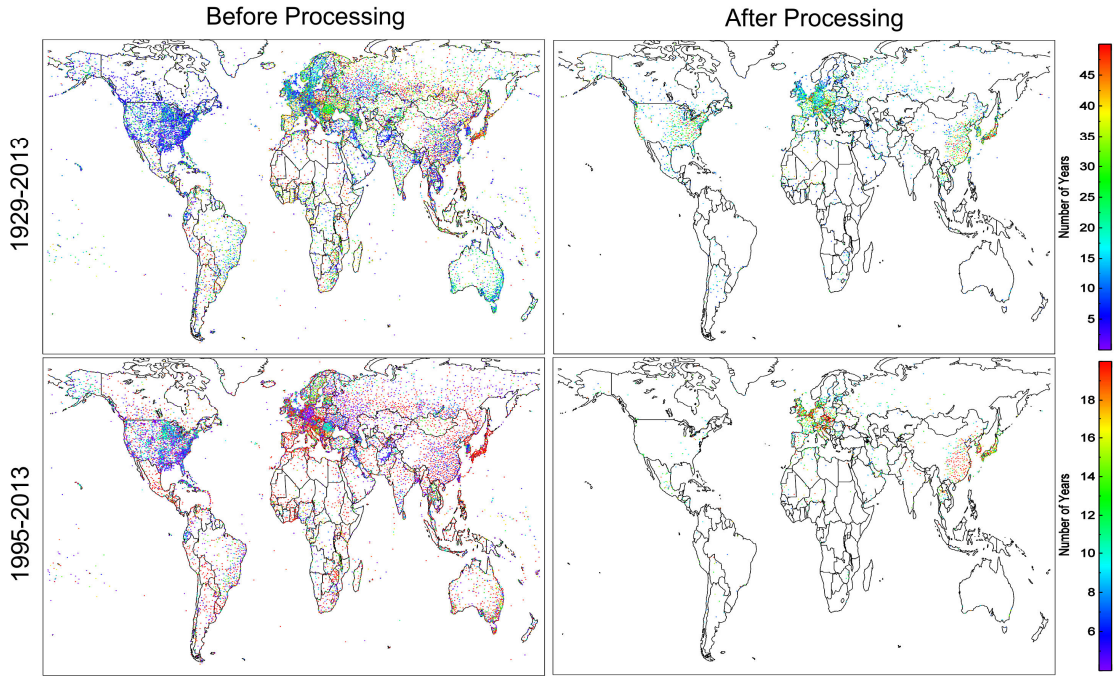

Figure 2-2. Distribution of Integrated Surface Database (ISD) stations before (left) and after (right) data screening. Colors indicate the number of years with available visibility data for (upper) 1929-2013 and (lower) 1995-2013.

Figure 2-2 (bottom) shows that most US stations are screened after the mid 1990s. This is because more than 90% of the ISD stations gradually switched to employ a low Vis threshold of 10 miles (~16 km) after the mid 1990s (Figure 2-S1), probably due to the introduction of unified instrumentation (Kessner et al., 2013). A maximum Vis of 16 km may be sufficient for airport navigation and weather reports, but this threshold Vis under clear sky conditions represents a moderate pollution level, and clean cases are not resolved. Thus most of the US stations with such low thresholds are rejected during the threshold screening. In contrast, screened stations remain densely distributed with long-term data over Europe and eastern Asia after the mid 1990s because the adopted thresholds are generally higher and more consistent (Figure 2-S1).

2.4.2 Complementary In Situ Data

We adopt complementary data to evaluate and interpret the constructed monthly 1/Vis time series and trends. The measured and calculated aerosol optical data from the Interagency Monitoring of PROtected Visual Environments (IMPROVE) program (http://vista.cira.colostate.edu/improve/Data/data.htm) are employed to evaluate the

screened 1/Vis data and its trends after 1988. IMPROVE applies empirical mass extinction and RH growth factors to measured mass of aerosol components to calculate and report ambient b_{ext} in a 3-4 day frequency (Pitchford et al., 2007), and for several stations concurrent measurements of aerosol scattering coefficient (b_{sp}) are also made at hourly frequency using nephelometers. We generate monthly mean total b_{ext} (including aerosol extinction and site-specific Rayleigh scattering) and b_{sp} from data with RH < 90% and status flags as "V0" (valid). Any month with less than 4 available days for averaging is abandoned. Pitchford et al. (2007) demonstrated that the estimated b_{ext} is consistent with measured b_{sp}. We also find high correlation (r = 0.90, N = 3439) between monthly b_{ext} and b_{sp} across IMPROVE stations (Figure 2-S2).

The measurement of b_{ext} or b_{sp} is sparse outside the US. Therefore we obtain long-term measurements of fine particulate matter mass ($PM_{2.5}$) from the European Monitoring and Evaluation Programme (EMEP, http://ebas.nilu.no) for comparison over Europe (Tørseth et al., 2012). Forty-five stations of data collected by filter-based ambient samplers are used. Similarly, these daily $PM_{2.5}$ data are averaged monthly provided at least four valid measurements are available.

2.4.3 SO_2 Emission Data

We apply bottom-up total anthropogenic SO_2 emission inventories to interpret historical 1/Vis trends. This approach exploits the close relation of sulfate aerosol concentration with SO_2 emission due to the short time scale of SO_2 oxidation (Chin et al., 1996; Chin et al., 2014; Daum et al., 1984; Hand et al., 2012b), the major $PM_{2.5}$ contribution from sulfate aerosols over land for most populated areas (Chin et al., 2014), and the dominance of sulfate for light extinction due to its hygroscopicity (Hand et al., 2014a). We employ three different SO_2 emission data sets, including country-level data for 1850-2005 (Smith et al., 2011b; Smith et al., 2011c), gridded data from EDGAR (Emissions Database for Global Atmospheric Research) version 4.2 (Olivier et al., 1994) at 0.1 degree resolution for 1970-2008 (http://edgar.jrc.ec.europa.eu/), and data from Lu et al. (2011) at 0.5 degree resolution for 1996-2010 over China. The data from Smith et al. (2011b) are referred to as "Smith emissions" below. The data from Lu et al. (2011) are referred to as "Lu emissions".

2.4.4 Trend Analysis

In this study, we separately calculate trends for several periods of 8-10 years to allow possible trend reversal, and to include stations with short-term data. The choice of study periods is mainly based on the historical SO_2 emission data. Figure 2-S3 shows the Smith emission data for several representative countries. SO_2 emission trends in the US changed direction at ~1944, ~1954, and again at ~1973. Also, for most eastern European countries, there is a sharp reduction of SO_2 emission starting from ~1989 after the breakdown of the communist system, while the 1997 Asian financial crisis affected the SO_2 emission trend in Korea. It is of particular interest to examine how Vis is affected by these emission changes. Data for most ISD stations outside the US start from the year 1973, and representative coverage of Vis stations over the US starts from the year 1945, although the earliest records after screening start from 1929. Based on these transition points of SO_2 trends and Vis data availability, eight periods (1945-1953, 1954-1963,1964-1972, 1973-1980, 1981-1988, 1989-1996, 1997-2005, 2006-2013) are chosen to be analyzed in detail over the US, while the latter five periods are studied for Europe and eastern Asia. We also briefly examine two short periods before 1945 (1929-1934 and 1935-1944) over the US where stations are less spatially representative (not included in regional quantitative analysis) but still show prominent trend information in 1/Vis.

We assess the linear trend and its significance (p value, two-tail test) in the deseasonalized monthly anomalies using Sen's slope (Sen, 1968) and the Mann-Kendall (MK) test (Kendall, 1975; Mann, 1945). All monthly data are deseasonalized by removing multi-year monthly means of each period before trend estimation. Pre-whitening is introduced to reduce the effect of lag-1 autocorrelation (Yue et al., 2002), and 95% confidence interval (CI) of the slope is calculated (Li et al., 2014b). This nonparametric trend estimation method is insensitive to missing values and outliers in the time series, and does not require a normal distribution, thus it has been widely adopted to study aerosol trends in previous studies (Collaud Coen et al., 2013; Papadimas et al., 2008). Least square trends (Weatherhead et al., 1998) are also calculated, and are found to be consistent with the MK-Sen trends. For all the 8027 calculated slopes in 1/Vis, 88% are unanimously diagnosed as significant (90% confidence, $p < 0.1$) or insignificant by both methods. For the significant trends 76% of their differences are within 20%. Relative trends are

calculated by normalizing the absolute MK-Sen slopes to the multi-year mean of monthly 1/Vis in the corresponding period to facilitate the comparison and interpretation with other in situ data.

Short-term trends of 8-10 years are expected to be less statistically robust and more sensitive to extremes. For each period, a time series is required to contain at least half of the total months and two-thirds of the total years (e.g. at least 60 monthly data in at least 7 years for a 10 year period) for the calculated trend to be representative. This step only reduces the number of stations at which trends are reported, but does not further screen the data.

The meaning and observing methods of daytime and nighttime data differ. According to WMO (2008), Vis at night, as determined using illuminated objects, also depends on the light source intensity, the adaptation of the observer's eyes to darkness and the observer's illuminance threshold. We compare the relative trends calculated using daytime and nighttime data to the combined trends adopted in this paper, over all remaining sites and the eight periods. The 5183 daytime trends have a correlation of 0.85 with the combined trends, in which 84% of the differences between significant trends ($p < 0.1$) are within 50%. For the comparison between 4109 nighttime and combined trends, the correlation is 0.80 and 78% of the differences between significant trends are within 50%. Therefore, after representing the data as a monthly resolution and normalizing the changes in 1/Vis to relative trends, the daytime and nighttime data show generally consistent trends in haze level compared to the combined data, and do not meaningfully alter our results and conclusions.

We calculate composite trends based on monthly 1/Vis averaged from an ensemble of stations (e.g. for the time series of collocated stations in Section 2.5 or defined regions in Section 2.6). To ensure temporal representativeness, a station is considered in the average only if two-thirds of the total months of data are available for the study period. Qualified stations are gridded to 1 degree resolution before averaging to avoid biased averaging towards more densely distributed areas. To ensure spatial representativeness, only monthly data derived from at least 75% of the total grids (i.e. number of unique grids covered by all the monthly data) for each study period are used in the composite trend estimation. This

strategy reduces sampling difference within each period; however the composite 1/Vis for different periods might be averaged from a different distribution of stations. We expect the uncertainty from spatially variant *K* and data quality to be random, and to be reduced by spatial averaging and by normalizing the slopes into relative trends. Over these regions, we also calculate several time series and trends for longer merged periods with consistent station coverage and similar trends, to assess the consistency of the short-term trends.

2.5 Evaluation against In Situ Data

2.5.1 Comparison with IMPROVE b_{ext} and EMEP $PM_{2.5}$

We compare the monthly IMPROVE b_{ext} data with the quality controlled monthly 1/Vis from Section 2.4.1. Collocations are considered between IMPROVE and ISD time series over 1988-2013 within the distance of less than 1 degree and altitude difference of less than 500 m. One IMPROVE station could pair with more than one ISD station and vice versa. A total of 59 collocations (each with at least 20 paired monthly values) are made. We expect a maximum correlation of 0.9 given the relation between measured b_{sp} and calculated b_{ext} (Figure 2-S2). Similarly, we create collocations between ISD 1/Vis and EMEP $PM_{2.5}$ on a monthly basis, and expect a weaker correlation due to variation of aerosol water and mass extinction efficiency.

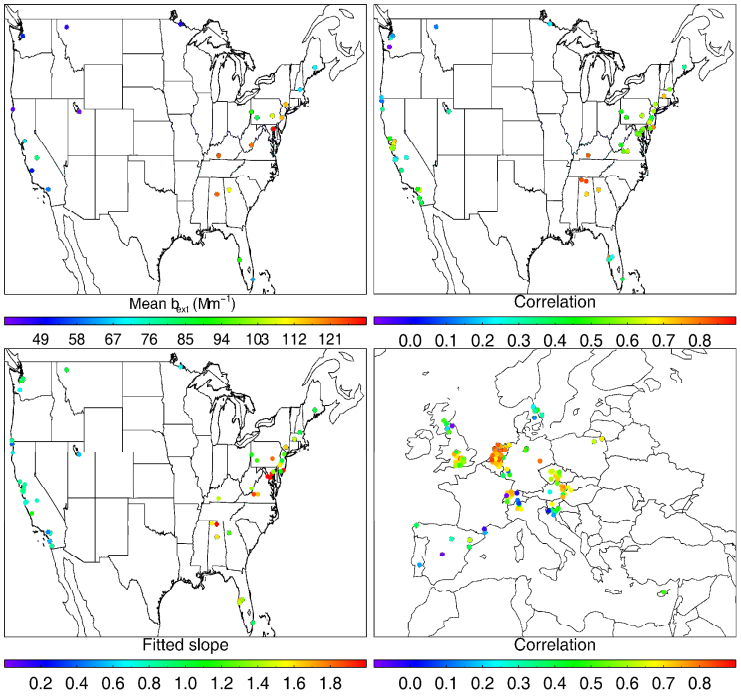

Figure 2-3. Spatial distribution of (top left) average of the collocated b_{ext} of IMPROVE stations, (top right) Pearson correlation coefficients between collocated pairs of monthly ISD 1/Vis and IMPROVE b_{ext}, (bottom left) slope of monthly b_{ext} against monthly 1/Vis after linear fitting through the origin point using the reduced major-axis linear regression (Ayers, 2001) and (bottom right) Pearson correlation coefficients between collocated pairs of monthly ISD 1/Vis and EMEP $PM_{2.5}$.

Figure 2-3 shows the comparison results between collocated 1/Vis and b_{ext} over the US. This evaluation highlights the following major findings.

1) The mean b_{ext} level of collocated IMPROVE stations after 1990 is below 50 Mm^{-1} for the western US, and below 120 Mm^{-1} for the eastern US (top left). As discussed in Section 2.4.1, the low threshold Vis of ~16 km (equivalent to b_{ext} ~100 – 240 Mm^{-1} depending on K) recently adopted by most US stations fails to resolve actual b_{ext} variation under this relatively clean environment. Thus many stations are rejected by the threshold filtering.

2) As shown in the top right panel, correlation coefficients of monthly values vary from ~0 to 0.85. About half of the collocations (29 out of 59) have $r < 0.5$, while 10 collocated ISD stations have $r > 0.7$. The overall moderate correlation is not unexpected, as is similarly found in previous studies (Mahowald et al., 2007; Wang et al., 2012). Correlations are expected to differ from station to station, due to the inherent difference in

observing conditions, protocols, and residual uncertainties. This preliminary evaluation suggests that Vis data at individual stations can be unreliable, and in the following discussion we focus on interpreting regionally coherent observations.

3) Correlations generally exceed 0.5 in the eastern US, where the mean b_{ext} is higher due to higher aerosol concentration (Hand et al., 2012a; van Donkelaar et al., 2015) and to a larger fraction of hygroscopic sulfate aerosols (Hand et al., 2012a). The correlation increases significantly with the mean b_{ext}, indicating the tendency for better 1/Vis representativeness in more polluted regions. As previously discussed, at lower b_{ext} more reported Vis are close to the threshold Vis, thus the true 1/Vis tends to be less well resolved. Also, because the Vis data are reported in discrete values, clean stations with a narrow dynamic range of b_{ext} have few reportable Vis to capture the continuous b_{ext} variation. Moreover, the increment of adjacent reportable Vis is relatively coarse in cleaner conditions (WMO, 2008), and atmospheric homogeneity might break down for longer distances. All these factors weaken the ability of Vis to capture b_{ext} variation in clean environments. Wang et al. (2012) found low correlation of 1/Vis with PM_{10} over the US and Canada, and similarly attributed this to low aerosol concentrations and higher Vis uncertainty over North America. Thus we apply the 40 Mm^{-1} threshold of annual 1/Vis to further filter the data as introduced in Section 2.4.1.4. Without this screening, seven of eight stations with mean 1/Vis < 40 Mm^{-1} were found to exhibit low correlations ($r < 0.25$) with collocated b_{ext}. Different thresholds from 10 to 70 Mm^{-1} were tested, and thresholds above 40 Mm^{-1} ceased to improve the consistency with the few sites reporting b_{ext}.

4) The slope of fitted linear relationship (bottom left) between 1/Vis and b_{ext} varies from ~0.8 to ~2 even over the eastern US where correlations are higher. This supports the expectation that this slope (K) would differ spatially with observing conditions (Griffing, 1980; Husar et al., 2000; Schichtel et al., 2001), as discussed in Section 2.3. Thus in the later analysis we focus on the relative trend of 1/Vis which is independent of K.

Figure 2-3 (bottom right) also shows the correlation between monthly 1/Vis and $PM_{2.5}$ over Europe. Although the relation of 1/Vis with $PM_{2.5}$ is expected to be more uncertain than with b_{ext}, we find more stations with high correlation ($r > 0.5$) over Europe (93 out of 129, 72%) than over the US (51%). Wang et al. (2012) similarly found higher correlation

of 1/Vis with PM_{10} over Europe and China than over the US and Canada. The higher thresholds and higher concentration of fine aerosol over Europe (van Donkelaar et al., 2015) allow 1/Vis to better resolve $PM_{2.5}$ variation there. These findings suggest more reliability of Vis observations at areas with both higher aerosol loading and sufficiently high thresholds to resolve b_{ext} variation, e.g. the three populated regions investigated in this study.

2.5.2 Trend Evaluation

Figure 2-4 shows the spatial distribution of relative trends in 1/Vis, in IMPROVE estimated b_{ext} and in measured b_{sp} over the US for 1989-2013. Overall, the trend maps of 1/Vis, b_{ext} and b_{sp} show a dominant trend of decreasing haziness over the continental US after 1988, which reflects reduction of aerosol sources (Hand et al., 2014a; Leibensperger et al., 2012). The overall decrease across the US is consistent with recent trend studies employing IMPROVE b_{ext} (Hand et al., 2014a) and b_{sp} (Collaud Coen et al., 2013) data, and is determined by the reduction of both aerosol mass and hygroscopicity (Attwood et al., 2014). For the last two periods (1997-2013), the number of available ISD stations for trend analysis is dramatically reduced by their detection limit and improved air quality. Although the remaining sparse ISD stations still show overall consistency in trends with nearby b_{ext} and b_{sp}, they cannot provide spatially coherent and aggregated trend information. We thus suggest that the ISD Vis data over the US are not appropriate for studying haze trends after the mid 1990s, and limit our analysis to data before 1996 for this region. Over 1989-1996, the 1/Vis trends still reproduce the b_{ext} trends, with decreasing tendencies in the eastern and western US. For this period, 15 ISD stations and 9 IMPROVE stations with significant trends are collocated and labeled. Thus the apparent discrepancy in sign of trends in 1/Vis (Wang et al., 2012) with trends in other aerosol measurements (US EPA, 2012; Attwood et al., 2014; Hand et al., 2012b; Hand et al., 2014a) is resolved by more comprehensive data processing and screening.

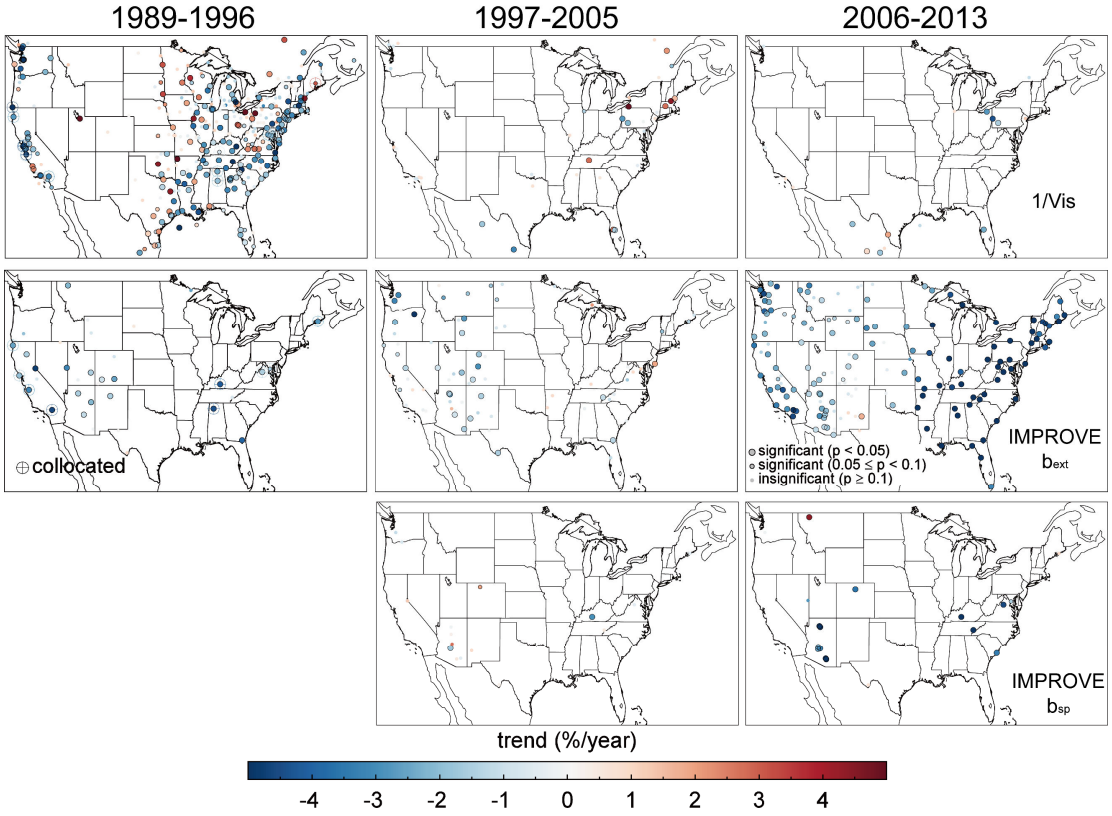

Figure 2-4. Spatial distribution of relative trends in 1/Vis (top row), IMPROVE b_{ext} (middle row), and IMPROVE b_{sp} (bottom row) over the US for 1989-2013. Larger colored points with black outline indicate trends with at least 95% significance, smaller colored points with black outline represent trends with 90%-95% significance, and colored points without outline indicate insignificant trends. Stations with cross and circle symbols are collocated between the ISD and IMPROVE networks over 1989-1996 for composite time series analysis in Figure 2-6.

Figure 2-5 shows the spatial distribution of relative trends in 1/Vis and $PM_{2.5}$ over Europe for 2006-2013. There is a tendency of greater reductions in 1/Vis over western Europe than over eastern Europe as examined further in Section 2.6.2. The dominant decreasing trends of $PM_{2.5}$ are adequately captured by the 1/Vis trends, especially at the 19 ISD and 10 EMEP collocated sites with significant trends, as discussed further below.

Figure 2-6 (top) shows the composite time series of the collocated 1/Vis and b_{ext} stations over the US for 1989-1996. The seasonal variation of the averaged b_{ext} is well reproduced by that of collocated 1/Vis, with a correlation of 0.77 between these two time series. Both composite 1/Vis and b_{ext} show a peak in summer months, due mostly to increased aerosol concentration in warm months because of increased photochemical activity and biogenic emission (Chen et al., 2012; Hand et al., 2012a). The trend of

collocated 1/Vis (-1.6% yr^{-1}; 95% CI: -2.4, -0.8% yr^{-1}) is within the confidence intervals of the decrease of b_{ext} (-2.4% yr^{-1}; 95% CI: -3.7, -1.1% yr^{-1}). The slight underestimation may reflect the weak sensitivity of discrete 1/Vis data to the continuous decrease of b_{ext} in clean environments due to the threshold and discreteness issues.

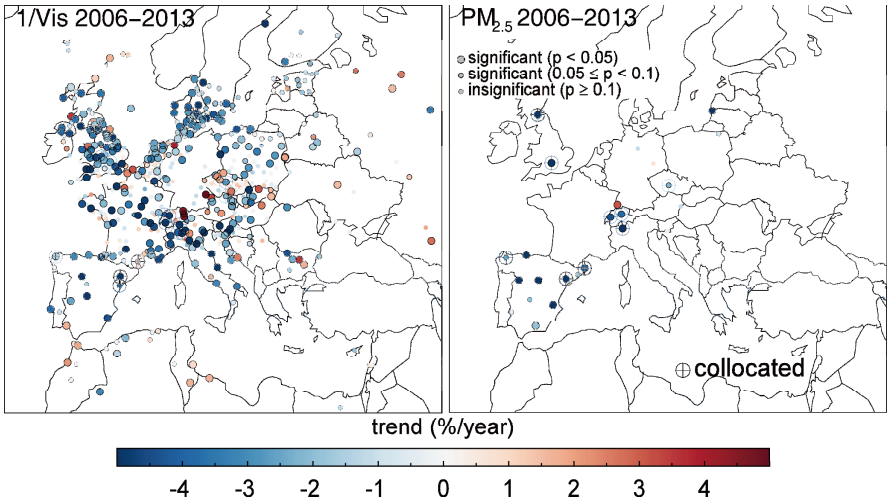

Figure 2-5. Spatial distribution of relative trends in 1/Vis and $PM_{2.5}$ over Europe for 2006-2013. Larger colored points with black outline indicate trends with at least 95% significance, smaller colored points with black outline represent trends with 90%-95% significance, and colored points without outline indicate insignificant trends.Stations with cross and circle symbols are collocated between the ISD and EMEP networks for composite time series analysis in Figure 2-6.

Figure 2-6 (bottom) shows composite time series of $PM_{2.5}$ and 1/Vis of these collocated 1/Vis and $PM_{2.5}$ stations over Europe for 2006-2013. High correlation (0.80) between these two time series indicates consistent seasonal variation. The winter maximum in the composite 1/Vis over Europe well represents the $PM_{2.5}$ seasonality at most collocated EMEP sites, which could be attributable to near surface inversion and low surface winds (Yttri et al., 2006), to greater nitrate aerosol formation (Aas et al., 2012; Yttri et al., 2006), and to higher carbonaceous aerosol emission from residential wood combustion (Denier van der Gon et al., 2015). The CI of the 1/Vis trend (-3.4% yr^{-1}, 95% CI: -4.4, -2.4% yr^{-1}) overlaps with that of the $PM_{2.5}$ trend (-5.8% yr^{-1}, 95% CI: -7.8, -4.2% yr^{-1}), but underestimates the relative decrease of $PM_{2.5}$. In addition to the weak sensitivity of discrete 1/Vis to resolve aerosol variation under clean environment (the collocated EMEP stations are mostly in the cleaner western Europe), the inclusion of Rayleigh scattering in 1/Vis and

the non-linear association between ambient 1/Vis and dry $PM_{2.5}$ (fixed at 50% RH) also contribute to this bias.

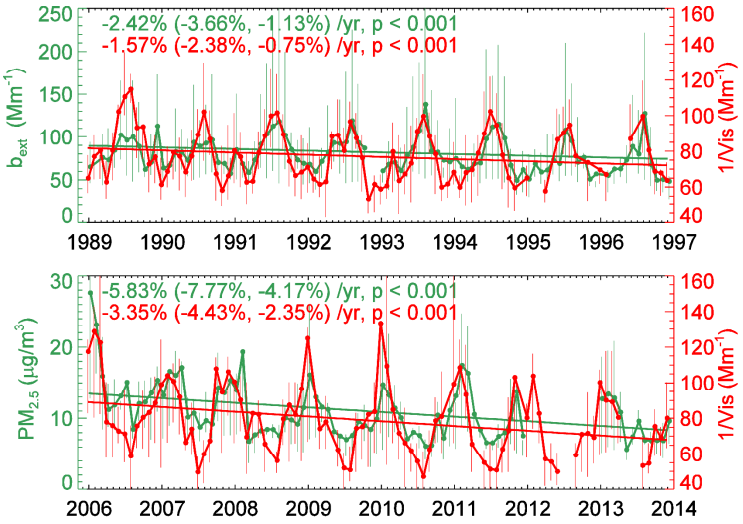

Figure 2-6. Composite time series and trends of (top) 1/Vis and b_{ext} for collocated ISD and IMPROVE stations (Figure 2-4) over 1989-1996 and (bottom) 1/Vis and $PM_{2.5}$ for collocated ISD and EMEP stations (Figure 2-5) over 2006-2013. Only stations with significant trends of >90% confidence are collocated. The long ticks on the horizontal axis indicate the January of the year. Data gaps represent months with less than 75% of the total grids. Error bars show the 25th and 75th percentile of all monthly values of collocated stations.

In summary, 1/Vis exhibits spatially variant K (i.e. relationship with b_{ext}) and data quality that suggests uncertainty in the information of one station especially at clean locations. However the aggregated 1/Vis time series successfully capture the seasonal variation and trends of collocated in situ data. The high correlation between composite time series and the overall consistency of composite trends suggest that the interpretation value of 1/Vis data benefits from averaging over multiple stations.

2.6 Historical Trends of 1/Vis

2.6.1 United States

Figure 2-7 presents the calculated relative trend of 1/Vis of all qualified stations over the US for 1945-1988 (Figure 2-4 contains 1/Vis trends over 1989-2013). Figure 2-8 shows the regionally averaged time series and trends of 1/Vis over the eastern US for 1945-1996,

superimposed with the evolution of SO_2 emission data. Historically, 1/Vis in the eastern US experienced a pronounced decrease (-2.8% yr^{-1}, $p < 0.001$) after World War II until the mid 1950s, a consistent upward trend afterwards (0.9–1.8% yr^{-1}, $p < 0.001$) during the following 2 periods until the early 1970s, variable tendencies during 1973-1980, and a significant decreasing trend (-1.1 to -2.0% yr^{-1}, $p < 0.005$) from the early 1980s until 1996. Over 1954-1973, the long-term trend of 1/Vis is 1.2% yr^{-1} ($p < 0.001$), lying between the separated short-term trends. This 1/Vis trend evolution resembles the SO_2 emission trend. Industrial activity gradually decreased after World War II until the mid 1950s, followed by economic growth until the early 1970s with the emergence of both the oil crisis and the Clean Air Act (Greenstone, 2001). The emission of SO_2 starts to consistently decrease after 1973 for the Smith inventory, and after 1977 for the EDGAR inventory. For the period 1973-1980 the regional 1/Vis is generally consistent with these two inventories except for an anomalous peak of annual 1/Vis in 1977-1979. The NOAA Climate Extremes Index (http://www.ncdc.noaa.gov/extremes/cei/) describes the winters of 1977-1979 as the coldest during 1945-1996 across the US. Increased emissions from domestic heating, as well as stagnant weather may contribute to the 1/Vis peak. After 1978, the three annual time series uniformly exhibit a downward tendency.

Table 2-1 contains the correlation of annual 1/Vis with SO_2 emissions. Annual 1/Vis over the eastern US exhibits a correlation of 0.66 with the Smith SO_2 emissions over the entire US (1946-1995), and of 0.73 with the EDGAR SO_2 emissions over the eastern US (1970-1995). The 1/Vis trends over the western US (where SO_2 emissions are much lower than in the eastern US, organic aerosols dominate in $PM_{2.5}$ and forest fires are more prevalent) are less consistent than over the eastern US with the SO_2 emission data, given the influence of other sources. In summary, the 1/Vis time series successfully capture large-scale haze evolution over the eastern US from 1945 to 1996, which is consistent with changes in SO_2 emissions as well as previous investigations on 1/Vis for this region (Husar and Wilson, 1993; Schichtel et al., 2001).

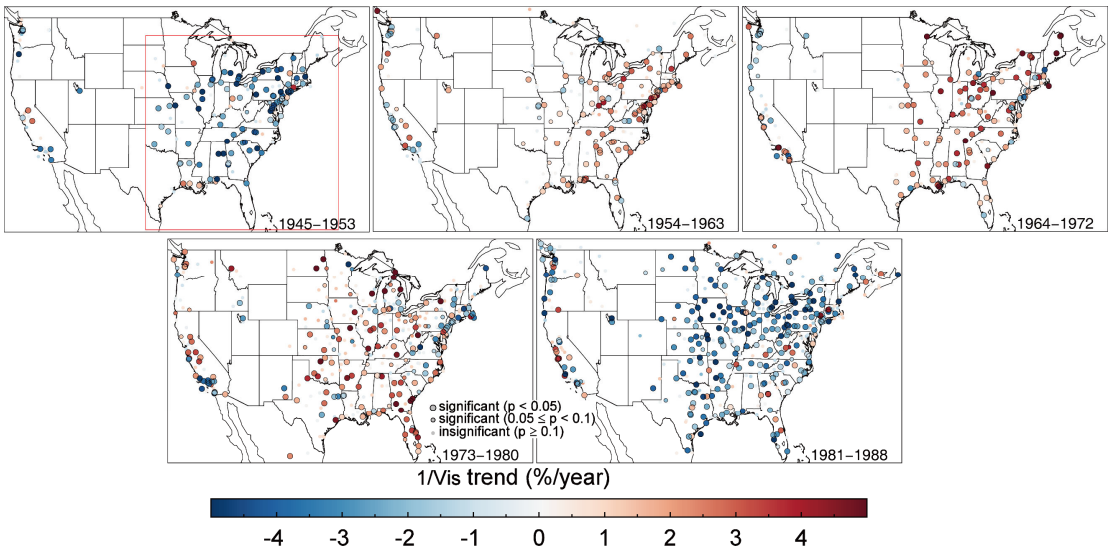

Figure 2-7. Spatial distribution of relative trends in 1/Vis over the US for 1945-1988. Larger colored points with black outline indicate trends with at least 95% significance, smaller colored points with black outline represent trends with 90%-95% significance, and colored points without outline indicate insignificant trends. The red rectangle defines the eastern US region for composite time series analysis in Figure 2-8.

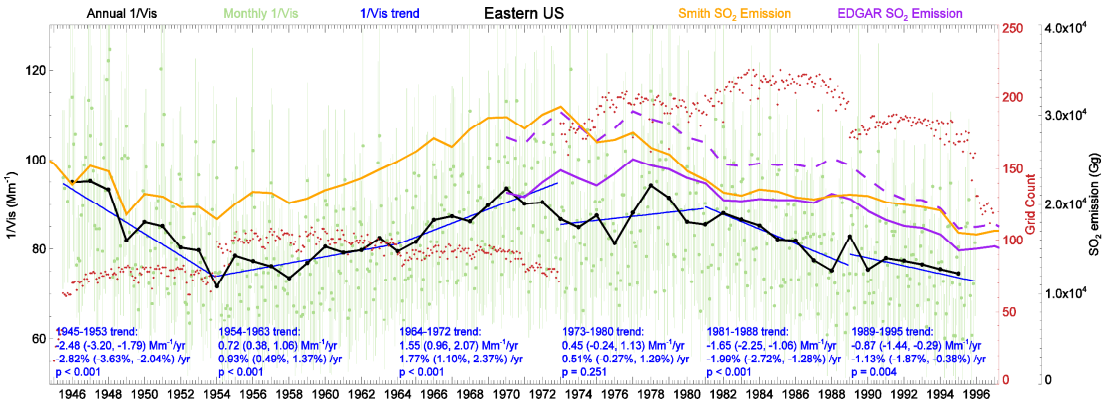

Figure 2-8. Composite time series of 1/Vis and SO_2 emission over the eastern US region. The long ticks on the horizontal axis indicate January of the year, where all annual values are plotted. Light green dots represent the average monthly 1/Vis of all qualified stations (error bars showing the 25th and 75th percentile) in the defined region. Red dots show the number of grid cells for averaging, and data gaps indicate months with less than 75% of the total grids for each period. Blue lines and text represent the 1/Vis trends calculated using the monthly anomalies for each period. Trends in parentheses are the 95% confidence intervals. Black lines are the annual 1/Vis averaged from at least 8 monthly values. SO_2 emissions for the entire US from Smith et al. (2011b) are in orange. Purple indicates EDGAR SO_2 emissions for the entire US (dashed) and for the defined region (solid) in Figure 2-7.

Table 2-1. Summary of Pearson correlation coefficients (r) between annual 1/Vis and SO_2 emissions for five regions.

Inventory	**Period**	**Eastern US**	
Smith	1946-1995	0.66	
EDGAR	1970-2008	0.73	
		Eastern Europe	**Western Europe**
Smith	1973-2005	0.92	0.91
EDGAR	1973-2008	0.92	0.92
		Northern China	**Southern China**
Lu	1996-2010	0.78	0.87
EDGAR	1973-2008	0.91	0.88

Figure 2-S4 shows the calculated 1/Vis trends over the US for two short periods prior to 1945. Although the stations are sparsely distributed, the nearly uniform trends in 1/Vis strongly suggest a prominent decrease over 1929-1934, and then a rapid increase over 1935-1944. This evolution reflects the significant drop in industrial activity following the 1929 Great Depression, and the economic recovery after ~1933 during the New Deal programs and World War II. The Smith SO_2 emissions of the US (Figure 2-S3) also reflect these socioeconomic events.

2.6.2 Europe

Figure 2-9 presents the spatial distribution and temporal evolution of haze trends over Europe as derived from the 1/Vis data for 1973-2005. The historical trend pattern of 1/Vis is quite different between western and eastern Europe. The large-scale 1/Vis trend over western Europe is consistently decreasing for the four periods after 1981 (also in Figure 2-5). Some countries such as the UK and France begin decreasing prior to 1981, consistent with the SO_2 emission decrease over these countries (Figure 2-S3). Prior analysis also indicated Vis improvements after ~1973 for most sites over the UK (Doyle and Dorling, 2002). Meanwhile stations over eastern Europe have significantly increased 1/Vis for 1973-1980, a mostly decreasing trend in its western part for 1981-1988, and then a decrease-dominant trend after 1989.

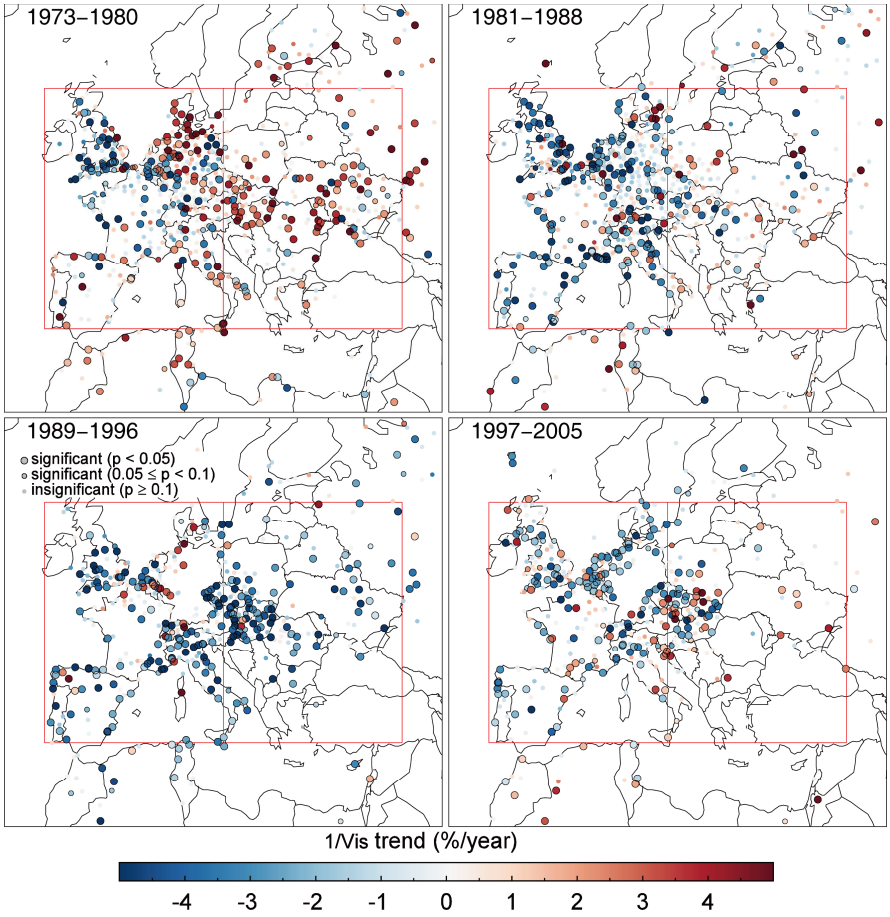

Figure 2-9. Spatial distribution of relative trends in 1/Vis over Europe for 1973-2005. Larger colored points with black outline indicate trends with at least 95% significance, smaller colored points with black outline represent trends with 90%-95% significance, and colored points without outline indicate insignificant trends. Red rectangles define the eastern and western Europe regions for composite time series analysis in Figure 2-10.

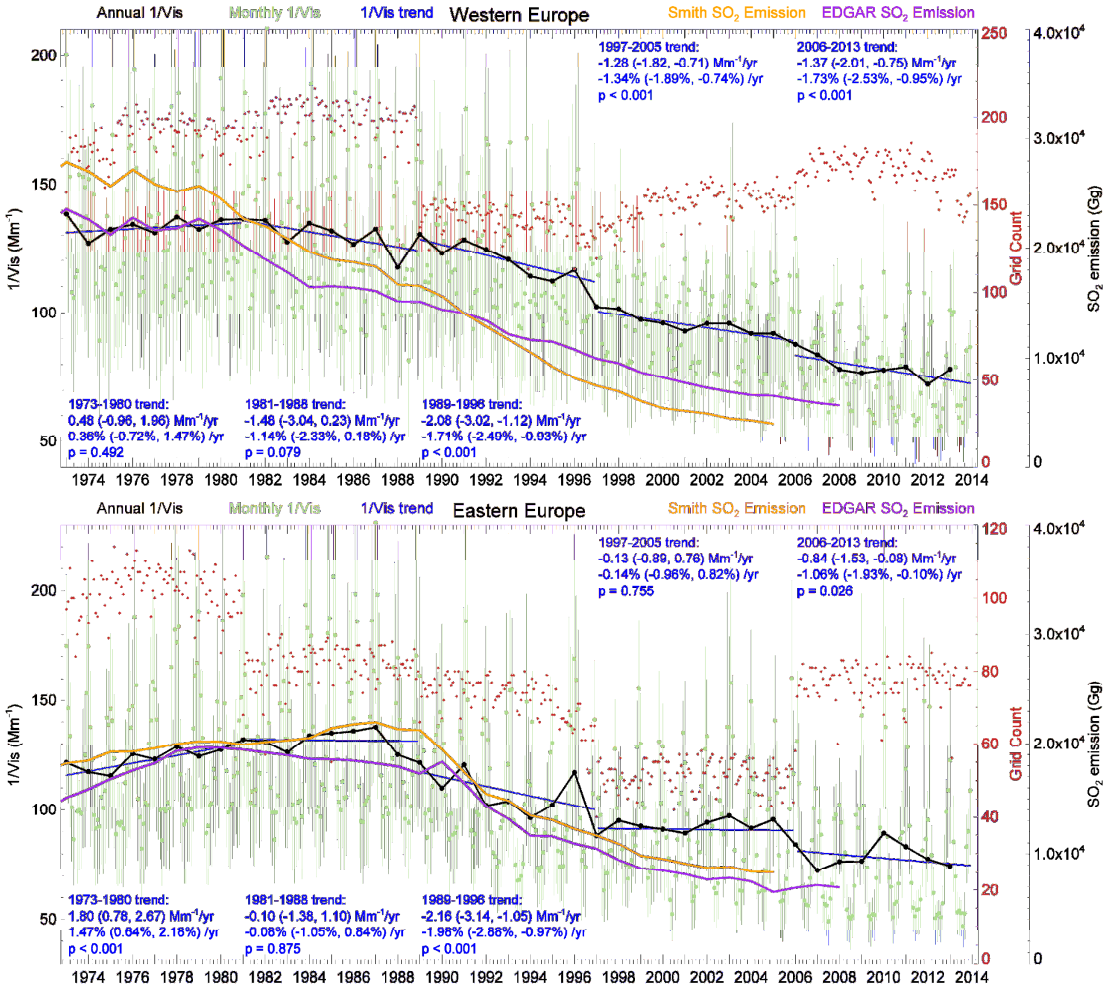

Figure 2-10. Regional time series analysis of 1/Vis and SO_2 emission over western and eastern Europe. The long ticks on the horizontal axis indicate January of the year, where all annual values are plotted. Light green dots represent the average monthly 1/Vis of all qualified stations (error bars showing the 25th and 75th percentile) in the defined region. Red dots show the number of grid cells for averaging, and data gaps indicate months with less than 75% of the total grids for each period. Blue lines and text represent the 1/Vis trends calculated using the monthly anomalies for each period. Trends in parentheses are the 95% confidence intervals. Black lines are the annual 1/Vis averaged from at least 8 monthly values. The Smith SO_2 emissions in orange are the total emission of all countries listed in Table 2-2 for each region. The EDGAR SO_2 emissions in purple are summed from all pixels inside the defined region (Figure 2-9).

Figure 2-10 shows the regionally composite time series of 1/Vis as well as SO_2 emissions over western and eastern Europe for 1973-2013. Table 2-2 lists the specific country names included in the Smith emissions for the two regions. The evolution of 1/Vis over western and eastern Europe is broadly consistent with the SO_2 emissions, and reflects the lag of emission reduction in eastern vs. western Europe. Stjern et al. (2011) similarly

reported later improvement in Vis over eastern vs. western Europe. The SO_2 emission reduction extends from the 1980s to the end of data record for western Europe, and primarily over 1989-2000 for eastern Europe. The composite 1/Vis time series successfully capture the significant reduction of haze over western Europe (-1.1 to -1.7% yr^{-1}, $p < 0.08$). Long term 1/Vis trend over western Europe for 1981-2011 (insufficient qualified stations after 2011) is -1.8% yr^{-1} ($p < 0.001$), consistent with the separate short-term trends. For eastern Europe the decrease of 1/Vis is stronger before 1997 (-2.0% yr^{-1}, $p < 0.001$) than after 2006 (-1.1% yr^{-1}, $p = 0.03$), and the calculated trend over 1997-2005 is insignificant, consistent with the SO_2 emission evolution. There is an obvious peak in 1/Vis from October 1995 to March 1996 especially over eastern Europe, which is consistent with the peak sulfate concentration that Stjern et al. (2011) attributed to the anomalously cold winter of 1996 with stagnant air.

Table 2-1 shows that the annual 1/Vis time series exhibit a correlation of 0.91 (0.92) with the Smith Emissions for 1973-2005, and of 0.92 (0.92) with the EDGAR emissions for 1973-2008 over western (eastern) Europe, respectively. Such high correlations suggest a major role of SO_2 emissions to determine the decadal trends of haze over Europe.

Table 2-2. List of countries included to calculate regional SO_2 emission from the country-level emission data (countries with most parts inside the defined region) of (Smith et al., 2011b).

Region	Countries
Eastern US	United States
Eastern Europe	Albania, Belarus, Bosnia & Herzegovina, Bulgaria, Czech, Croatia, Greece, Hungary, Latvia, Lithuania, Moldova, Poland, Romania, Serbia & Montenegro, Slovakia, Slovenia, Turkey, Ukraine
Western Europe	Austria, Belgium, Denmark, France, Germany, Ireland, Italy, Netherland, Portugal, Spain, Switzerland, United Kingdom

2.6.3 Eastern Asia

Figure 2-11 shows the calculated relative trends of 1/Vis over eastern Asia after 1973. A persistent increasing trend of 1/Vis dominates over eastern China for more than 30 years. A prominent feature in the trends over China is more heterogeneity in the spatial distribution compared to the trend maps over the US and Europe. This could be a result of asynchronous economic development, as several studies reported “lagging” of Vis

impairment in rural sites (from ~1990s) compared to urban sites (from ~1960s) in China (Quan et al., 2011; Wu et al., 2012). The overall increasing trend in 1/Vis reverses in the last period of 2006-2013, when most stations in southern China and many in northern China show a statistically significant decreasing trend of 1/Vis. This is consistent with the implementation of fuel-gas desulfurization facilities in power plants after ~2007. This recent reduction was also supported by satellite observations of SO_2 (Li et al., 2010; Lu et al., 2010; Lu et al., 2011; Wang et al., 2015b; Zhao et al., 2013).

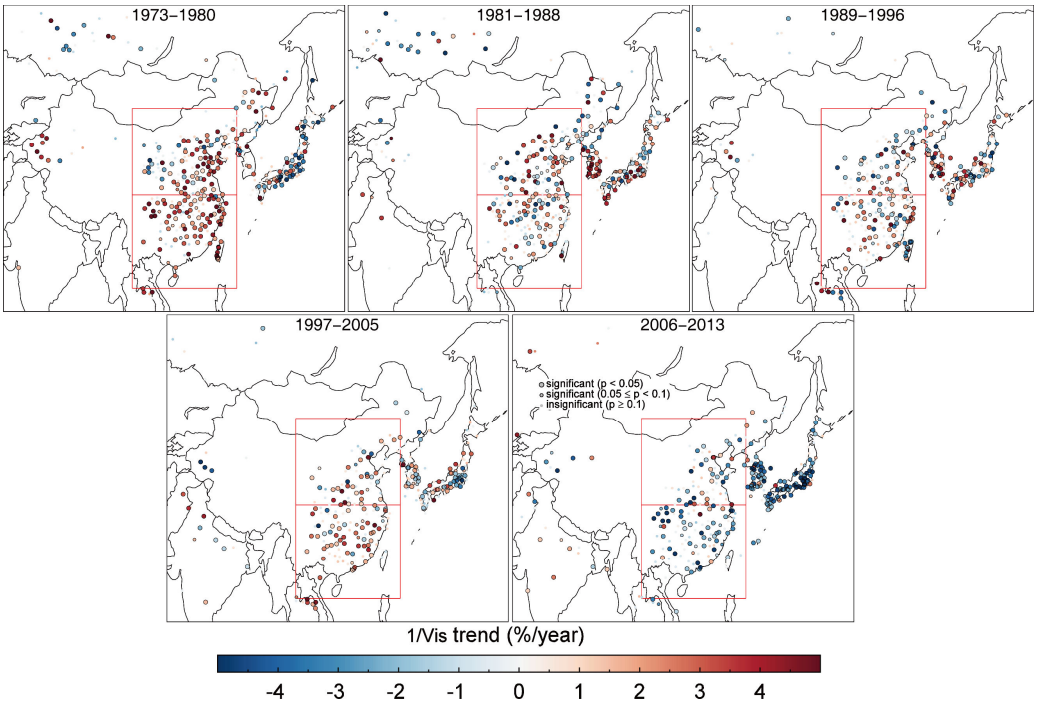

Figure 2-11. Spatial distribution of relative trends in 1/Vis over eastern Asia for 1973-2013. Larger colored points with black outline indicate trends with at least 95% significance, smaller colored points with black outline represent trends with 90%-95% significance, and colored points without outline indicate insignificant trends.Red rectangles define the northern and southern China regions for composite time series analysis in Figure 2-12.

Figure 2-11 also shows a consistent increase of 1/Vis over Korea from 1973 to 1996. After 1997 when the SO_2 emission transits to decrease (Figure 2-S3), the increase in 1/Vis levels off and reverses. The aerosols over China also affect areas downwind through long-range transport (Aikawa et al., 2010). For the 1997-2005 period, most eastern stations of Korea show a downward trend, in contrast with the increasing 1/Vis over the west, which is more strongly influenced by pollutant transport from China. Lee et al. (2015b) also discovered insignificant improvement of Vis over urban areas of Korea after late 1990s

despite the national emission reduction policy launched in early 2000s, which was attributed to the regional transport from upwind continental areas. Long-term aerosol measurement over Gosan Island, Korea showed rapid increase of sulfate and nitrate concentrations from early 2000s to ~2006, which were closely related with the trends of China's emission (Kim et al., 2011). Similarly, stations over the western and coastal areas of Japan consistently exhibit an upward 1/Vis trend before 2006, despite the continuous decrease of local SO_2 emission and concentration since 1970 (Wakamatsu et al., 2013). Aikawa et al. (2010) found a zonal gradient in terms of both the magnitude and trend of measured SO_2 and sulfate concentrations over Japan, and in the modeled contribution from China to the sulfate concentration in Japan. Lu et al. (2010) reported that most EANET (Acid Deposition Monitoring Network in East Asia) stations over Japan and Korea have increasing trends in SO_2 and sulfate aerosols from 2001 to 2007. For the last period 2006-2013, 1/Vis shows a dominant decreasing trend over Japan and Korea that may reflect in part China's SO_2 emission controls. Itahashi et al. (2012) reported a trend reversal of MODIS (Moderate Resolution Imaging Spectroradiometer) fine aerosol optical depth (AOD) over the Sea of Japan from increasing to decreasing at ~2006 that is more consistent with China's SO_2 emission than the local emission. This analysis highlights the sensitivity of 1/Vis to long range transport, and the value of international collaboration for air quality improvement over eastern Asia.

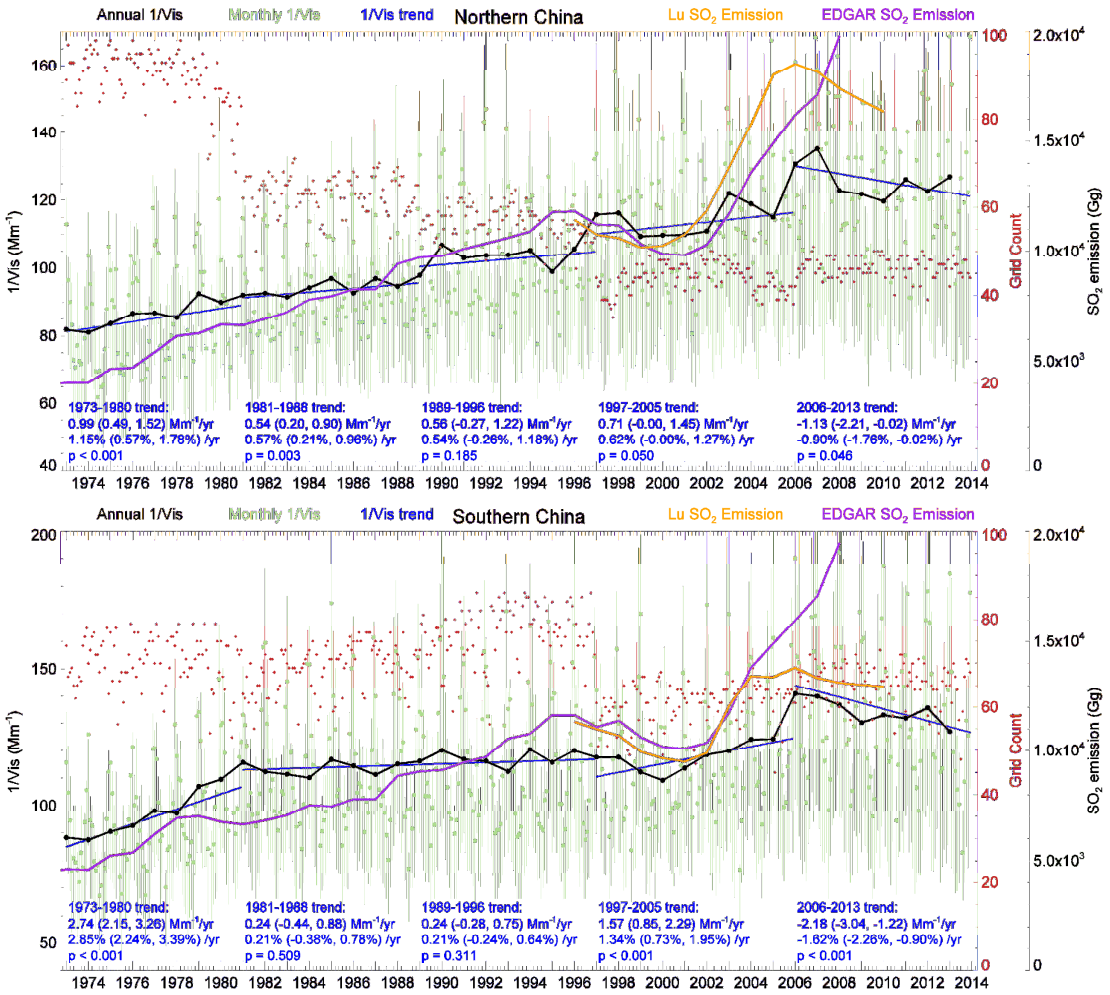

Figure 2-12. Regional time series analysis of 1/Vis and SO_2 emission over southern and northern China. The long ticks on the horizontal axis indicate January of the year, where all annual values are plotted. Light green dots represent the average monthly 1/Vis of all qualified stations (error bars showing the 25th and 75th percentile) in the defined region. Red dots show the number of grid cells for averaging, and data gaps indicate months with less than 75% of the total grids for each period. Blue lines and text represent the 1/Vis trends calculated using the monthly anomalies for each period. Trends in parentheses are the 95% confidence intervals. Black lines are the annual 1/Vis averaged from at least 8 monthly values. The SO_2 emission in Lu et al. (2011) in orange and the EDGAR SO_2 emission in purple are summed from all pixels inside the defined region (Figure 2-11).

Figure 2-12 presents a regional analysis of averaged 1/Vis time series over northern and southern China, and the evolution of SO_2 emissions from two inventories. The overall Vis impairment trend in China for 1973-2005 reflects the consistent SO_2 emission increase. Both the north and south show a steady and significant ($p < 0.001$) increase of haziness for the 1973-1980 period, and southern China shows an even faster impairment (2.9% yr^{-1})

than the north (1.2% yr^{-1}). For the next 2 decades (1980-2000) the 1/Vis increase slows down in both the south and the north, in accordance with other investigations using Vis and SSR data (Chen and Wang, 2015; Luo et al., 2001; Wu et al., 2014). The south exhibits a slower (0.2% yr^{-1}) and less significant ($p > 0.3$) increase than the north (0.5–0.6% yr^{-1}). The long-term trend over 1981-1996 for northern China (0.5% yr^{-1}, $p < 0.001$) also exceeds that for southern China (0.2% yr^{-1}, $p = 0.04$). This difference is determined not only by the slower increase of SO_2 emissions in the south (Lu et al., 2010), but also by more precipitation and ventilation in the south that favors the removal of aerosols and their precursors (Xu, 2001; Ye et al., 2013). The decline of SO_2 emissions from 1996 to 2000 reflects both the 1997 Asian financial crisis, and a decline in coal use and sulfur content (Lu et al., 2011). Both regions show a leveling off or even reversal of 1/Vis increase during this short period, which is again more significant in the south. The period 2000-2006 exhibits significant growth (>1% yr^{-1}) of 1/Vis in both the north and south, resembling the steady growth in SO_2 emissions. The recent reduction of SO_2 emissions is reflected in the Lu emissions while not in the EDGAR emissions. After 2006, significant ($p < 0.05$) decreasing trends in 1/Vis are apparent (-0.9 to -1.6% yr^{-1}) for both northern and southern China, which is more consistent with the Lu emissions. As shown in Table 2-1, the annual 1/Vis time series exhibit a high correlation of 0.78 (0.87) with the Lu emissions (1996-2010), and of 0.91 (0.88) with the EDGAR emissions (1973-2008) over northern (southern) China, respectively.

2.6.4 Connections to SSR and AOD Trends

Long-term records of surface solar radiation (SSR) and columnar aerosol optical depth (AOD) serve as complementary data resources to study and interpret changes in air pollution during the last few decades, especially for regions with fewer ground-based aerosol measurements. SSR is determined by the total columnar extinction of aerosols and clouds while 1/Vis represents the extinction level at the surface. Moreover, the direct scattering and absorption of solar radiation by aerosols could be amplified in less polluted regions or dampened over highly polluted stations, due to aerosol-cloud interaction (Fuzzi et al., 2015; Wild, 2009). Despite these uncertainties, the observed reversals of SSR from “dimming” to “brightening” in 1980-1990 over the US and Europe (Streets et al., 2006;

Turnock et al., 2015; Wild, 2012) generally agree with the reversals around the 1980s of 1/Vis trends in this study. Over China, the recently reported decadal SSR variation shows dimming before the 1990s and no significant trend afterwards (Tang et al., 2011; Wang et al., 2015a). The latter phenomenon may reflect compensation of more aerosol extinction by less cloud cover (Norris and Wild, 2009).

Reliable AOD data over land are limited to the recent 2 decades, but exhibit even greater consistency with 1/Vis trends. The recent decrease in 1/Vis after late-1990s over the US and western Europe in this study is consistent with previous studies on AOD trends based on both ground based (e.g. Li et al., 2014b; Yoon et al., 2012) and satellite (e.g. Chin et al., 2014; Hsu et al., 2012; Pozzer et al., 2015) observations. Over China, several studies on AOD trends in the 2000s showed notable increasing tendency (e.g. Hsu et al., 2012; Pozzer et al., 2015; Yoon et al., 2012), while some recent studies also discovered that separating AOD time series could reflect the plateauing and reversal of trends in recent years due to emission control strategies (Che et al., 2015; He et al., 2016; Lu et al., 2011). $PM_{2.5}$ trends derived from satellite AOD over 1998-2012 have decreasing tendencies over North America and Europe, and increasing tendencies over eastern Asia (Boys et al., 2014; van Donkelaar et al., 2015), similar to the 1/Vis trends found here.

2.7 Conclusion

This study examines Vis observations as a trend indicator of haziness and air quality over the US (1945-1996), Europe (1973-2013), and eastern Asia (1973-2013). We comprehensively process the raw data from over 20,000 stations considering effects from meteorological factors, protocol design, and human errors. We develop filters to exclude relatively clean cases (i.e. months with ≤ 50% records below the threshold Vis, or years with annual 1/Vis ≤ 40 Mm^{-1}) with weaker sensitivity to b_{ext} variation, and apply change point detection and separation to largely reduce the intrinsic discontinuities. Nearly 4000 stations remain after the processing with 753 over the US, 1625 over Europe, and 791 over eastern Asia. The composite time series of 1/Vis over the US for 1989-1996 generally agrees with the collocated IMPROVE b_{ext} in terms of both seasonal variation (r = 0.77) and trends (-1.6% yr^{-1}, 95% CI: -2.4, -0.8% yr^{-1}) in 1/Vis vs. b_{ext} (-2.4% yr^{-1}, 95% CI: -3.7, -

1.1% yr^{-1}). Similarly, for 2006-2013 over Europe, the seasonal variation (r = 0.80) and significant decrease (-5.8% yr^{-1}, 95% CI: -7.8, -4.2% yr^{-1}) in $PM_{2.5}$ are captured by collocated 1/Vis (-3.4% yr^{-1}, 95% CI: -4.4, -2.4% yr^{-1}). This consistency highlights the benefits of thorough data screening to reduce uncertainties brought by the inherent issues in Vis observations such as threshold choices, discreteness and discontinuities. As discussed in Section 2.4.1, the inclusion of unresolved values in the mean 1/Vis and the contaminants of discontinuities could dampen the ability of 1/Vis to correctly resolve aerosol trends. Admittedly, the derived 1/Vis trends are still subject to several uncertainties, e.g. the spatially variant K and data quality, the less robust short-term trends, sampling differences and direct averaging in composite time series. Nevertheless, the interpretation value of 1/Vis data is shown to be enhanced by the comprehensive screening and spatial averaging. Therefore we focus on the trend results that are regionally coherent and aggregated, and avoid drawing strong conclusions based solely on the 1/Vis trends. Although at individual stations the 1/Vis changes might be affected by these above-stated artificial factors, regionally coherent trend signals suggest these derived 1/Vis trends represent actual changes in b_{ext}. Our filtered monthly 1/Vis data are freely available as a public good (http://fizz.phys.dal.ca/~atmos/martin/?page_id=1435).

Analysis of the 1/Vis trends for several short periods reveals haze trend evolution and reversals. These historical 1/Vis trends and their evolution also exhibit compelling consistency with SO_2 emissions and SSR studies. For example, 1/Vis shows statistically significant decreasing trends from the late 1970s to the mid 1990s over the eastern US (-1.1 to -2.0% yr^{-1}), from the early 1980s to 2013 over western Europe (-1.1 to -1.7% yr^{-1}), in the early 1990s (-2.0% yr^{-1}) and after the mid 2000s (-1.1% yr^{-1}) over eastern Europe, and after the mid 2000s over China (-0.9 to -1.6%/yr). These recent decreases in 1/Vis are attributable to emission changes in these populated areas. Reversal points of 1/Vis trends also consistently reflect several historical socioeconomic events e.g. the New Deal programs (from decrease to increase at ~1934), the end of World War II (from increase to decrease at ~1945) and the Clean Air Act (from increase to decrease at ~1979) in the US, the collapse of communism in eastern Europe (from increase to decrease at ~1989), and the 1997 Asian financial crisis.

Therefore, the constructed 1/Vis data are applicable to resolve historical aerosol trends on a regional and annual basis, and provide complementary information about the historical changes in air quality. For instance, the annual 1/Vis time series exhibit high correlations (0.7-0.9) with SO_2 emissions for five large domains (Table 2-1). Apart from verifying the historical 1/Vis trends, this consistency also provides an evaluation of emission inventories. For example, after ~2006 1/Vis trends agree better with Lu et al. (2011) than the EDGAR emissions in capturing the SO_2 emission controls over China. Emission inventories differ significantly (Smith et al., 2011b), and 1/Vis data offer constraints on these inventories.

However, SO_2 emission inventories cannot fully explain the trends in ambient haze due to the influence of other emissions and meteorological factors. Notable reductions in emissions of nitrogen oxides and black carbon have been reported over North America and western Europe (Bond et al., 2007; Lu et al., 2015; US EPA, 2012; Vestreng et al., 2009), while steady increase in emissions of nitrogen oxides, organic carbon and black carbon were identified over China (Lu et al., 2011; Zhao et al., 2013). Observed (Leibensperger et al., 2012; Murphy et al., 2011) and simulated (Lin and McElroy, 2010; Wang et al., 2013) changes in various aerosol chemical species suggest increasing importance of emissions other than SO_2 on air quality trends in recent years. We have also shown that occasional cold winters in the US and Europe, and the long-range transport of China's pollutants into Korea and Japan could affect the association between 1/Vis and local emission. Future work includes applying a chemical transport model to further interpret the observed 1/Vis (b_{ext}) trends, as well as the contribution from meteorology and emissions.

2.8 Acknowledgements

This work is supported by the Natural Science and Engineering Research Council of Canada. C. Li is partially supported by a Killam Predoctoral Scholarship, and an ACEnet Research Fellowship. We thank two anonymous reviewers for their helpful comments. Special thanks to Dr. Jing Li at NASA GISS for instructions and discussion about trend calculation, Dr. Xiaolan Wang and Dr. Yang Feng at Climate Research Division, Environment Canada for maintaining the RHtest software, and Dr. Zifeng Lu at Argonne National Laboratory for guidance in SO_2 emission data. This work primarily relies on the

visibility data provided by NOAA NCEI. The b_{ext} data are from the IMPROVE network. IMPROVE is a collaborative association of state, tribal, and federal agencies, and international partners. US Environmental Protection Agency is the primary funding source, with contracting and research support from the National Park Service. The Air Quality Group at the University of California, Davis is the central analytical laboratory, with ion analysis provided by Research Triangle Institute, and carbon analysis provided by Desert Research Institute. We acknowledge the EMEP measurement networks and the data managers for maintaining the $PM_{2.5}$ data for validating 1/Vis trends over Europe. We also thank NASA SEDAC and EDGAR for making the emission data used in this study publicly available.

2.9 Supporting Information

Four supporting figures are included for complementary interpretation.

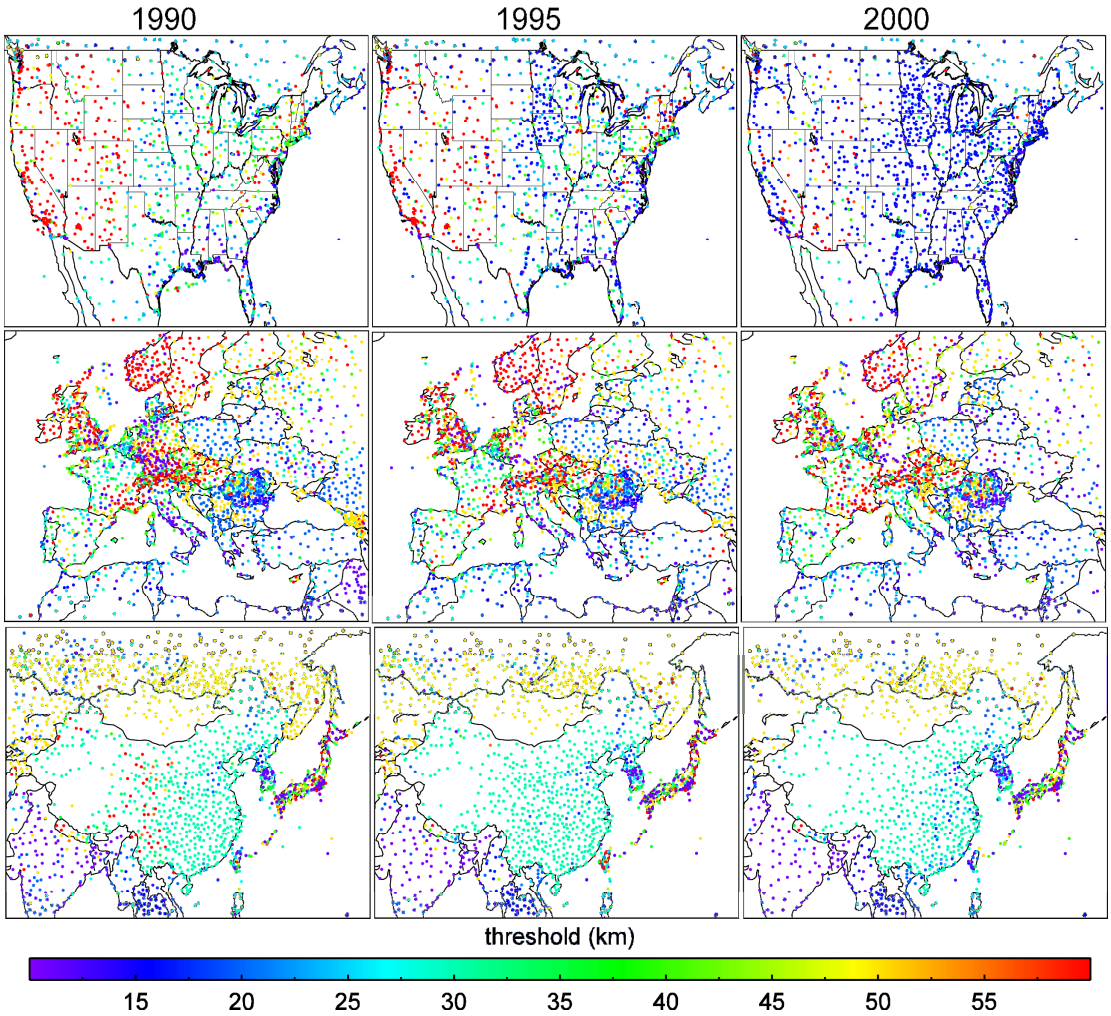

Figure 2-S1. Threshold visibility of ISD stations over the US, Europe and eastern Asia in 1990, 1995 and 2000.

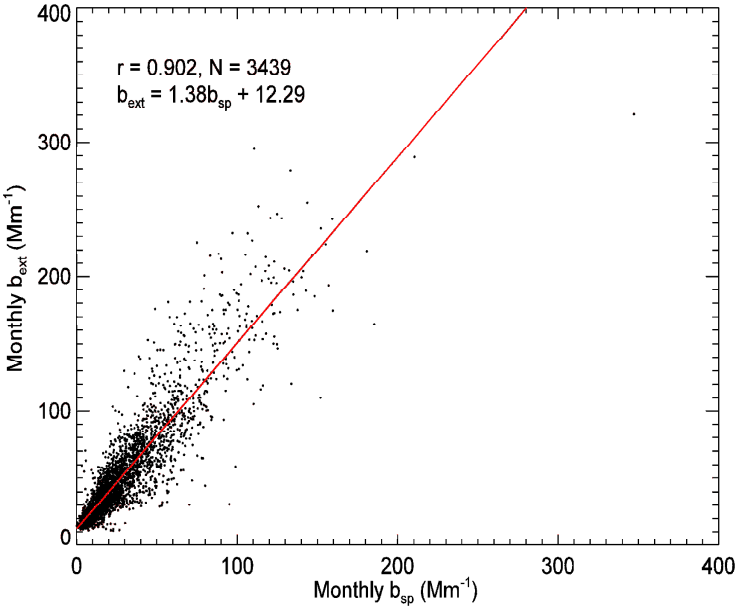

Figure 2-S2. Scatter plot of monthly b_{sp} (measured by nephelometers) and b_{ext} (estimated from aerosol speciation data) from all IMPROVE stations with b_{sp} measurements for 56 IMPROVE sites over 1993-2013. The intercept of ~12 Mm^{-1} corresponds to Reyleigh scattering.

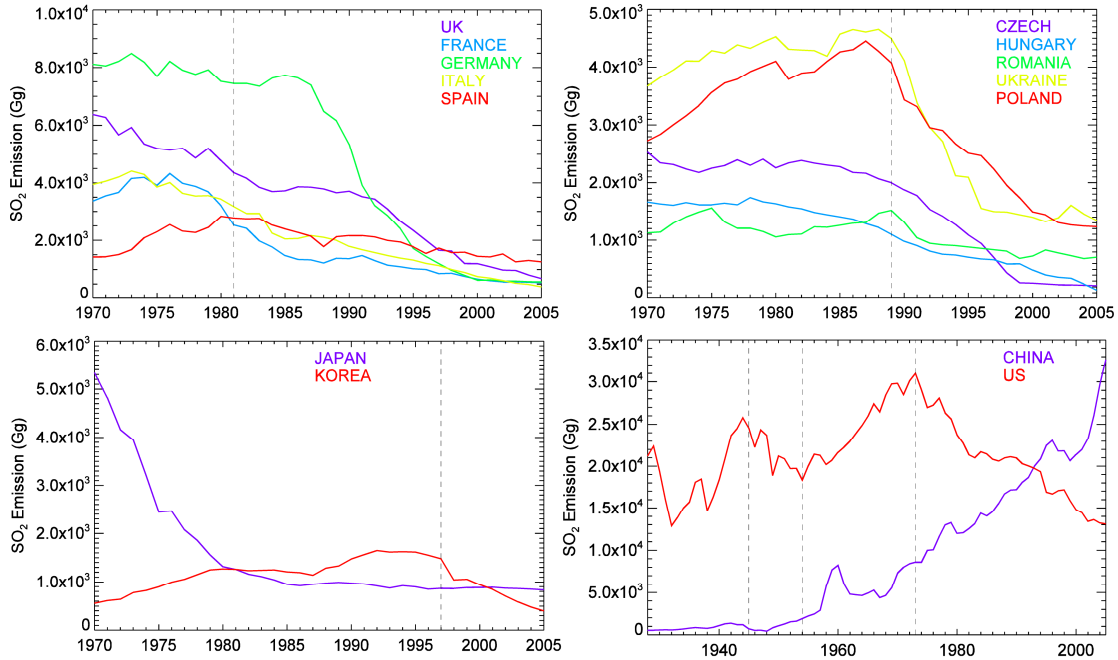

Figure 2-S3. SO_2 emission for several major countries. Data are from Smith et al. (2011b). The top left and top right panels include major countries of western and eastern Europe, respectively. Vertical lines represent division years of the study periods that roughly indicate transition points of emission trend.

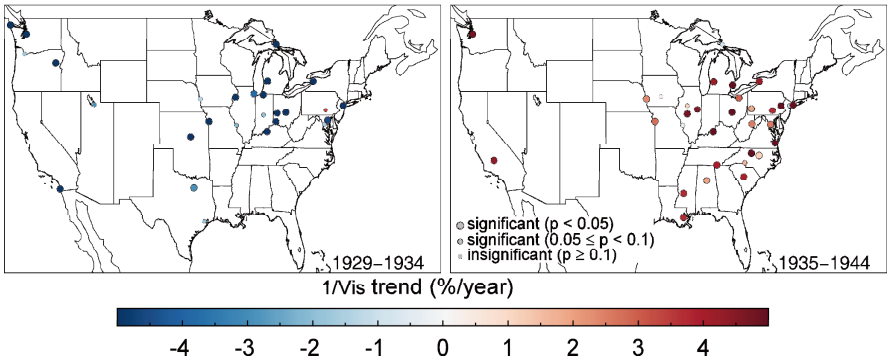

Figure 2-S4. Spatial distribution of relative trends in 1/Vis over the US for 1929-1944. Larger colored points with black outline indicate trends with at least 95% significance, smaller colored points with black outline represent trends with 90%-95% significance, and colored points without outline indicate insignificant trends.

Chapter 3. Decadal Changes in Seasonal Variation of Atmospheric Haze over the Eastern United States: Connections with Anthropogenic Emissions and Implications for Aerosol Composition

Reproduced with permission from "Decadal changes in seasonal variation of atmospheric haze over the eastern United States: connections with anthropogenic emissions and implications for aerosol composition" by Li, C. and Martin, R. V., *Environ. Sci. Technol. Lett.*, 5, 413-418, doi:10.1021/acs.estlett.8b00295, 2018. All text, figures and results were contributed by the first author.

3.1 Abstract

The current seasonal summer maximum in surface fine particulate matter ($PM_{2.5}$) over the eastern United States has been well established. We find that this seasonality has historically changed substantially, based on long-term quality assured inverse visibility (1/Vis) data over 1946-1998. The median summer/winter 1/Vis ratio increased from about 0.8 over both the southeastern and northeastern United States in the late 1940s, to 1.24 over the southeastern United States and to 1.04 over the northeastern United States in the mid-1970s. This ratio exhibits weaker changes in both regions afterwards. The observed $PM_{2.5}$ seasonality after the year 2000 has similar spatial distribution as that in 1/Vis over the mid-1990s, with systematically higher summer/winter ratios which rapidly weaken after the mid-2000s. From 1956 to 1975, stronger increases in 1/Vis occurred in summer than in winter in both regions, associated with increases in sulfur dioxide emissions and reductions in anthropogenic carbonaceous emissions. Over the southeastern United States, the changes in aerosol seasonality, i.e. both the strengthened summer maxima over 1946-1975 and dampened summer maxima after 2007, suggest historical changes in anthropogenic influence on secondary organic aerosol (SOA) formation, and suggest the prospect of reducing summer SOA through controls on anthropogenic emissions.

3.2 Introduction

Atmospheric aerosols (i.e. particulate matter) exert significant impacts on health (Hoek et al., 2013; West et al., 2016), climate (IPCC, 2013), visibility (Wang et al., 2009) and ecosystems (Mercado et al., 2009; Zhang et al., 2012a). Outdoor exposure to fine particulate matter ($PM_{2.5}$) is associated with an estimated 4.2 million global attributable mortalities in 2015 (Cohen et al., 2017a). Fine particles are also efficient in scattering radiation and impairing visibility (Hand et al., 2012a; Malm et al., 1994; Pitchford et al., 2007). The spatial and temporal variation of aerosols and their effects are strongly heterogeneous due to the diversity of aerosol chemical composition (Hand et al., 2012a; Kahn and Gaitley, 2015; Snider et al., 2016; Zhang et al., 2007) as determined by various emission sources and atmospheric processes (Fuzzi et al., 2015). Dense observations of aerosol speciation from long-term in situ networks across the United States (US) have been valuable for understanding aerosol sources and processes (Chen et al., 2010; Kim et al., 2015; Schichtel et al., 2017), long-term trends (Blanchard et al., 2016; Hand et al., 2012b; Malm et al., 2002; Malm et al., 2017), visibility (Hand et al., 2014a), and spatial and seasonal variation (Hand et al., 2012a; Hidy et al., 2014; Malm et al., 1994). From these observations, summertime maxima in $PM_{2.5}$ concentration have been consistently reported over the eastern US for both rural and urban regions (Hand et al., 2012a). These seasonal patterns are affected by the seasonality in ammonium sulfate aerosols, and also by the concurrent seasonality of secondary organic aerosol (SOA) from biogenic carbon over the southeastern US (Goldstein et al., 2009; Hand et al., 2012a; Hidy et al., 2014). However, few observations exist about changes in fine aerosols prior to the 1990s. This gap could be bridged by interpreting alternative observations of aerosol burden, such as atmospheric visibility (Husar et al., 2000; Wang et al., 2009).

Anthropogenic aerosol sources over the eastern US have changed significantly over the last century. Sulfur dioxide (SO_2) emissions reversed trends several times before the 1970s, and decreased afterwards (Li et al., 2016a; Smith et al., 2011b). Nitrogen oxide (NO_x) and ammonia (NH_3) emissions generally increased until the 1980s and decreased recently (Gschwandtner et al., 1986; Hoesly et al., 2018). Organic carbon (OC) and black

carbon (BC) emissions have decreased since the 1930s (Bond et al., 2007; DuBay and Fuldner, 2017; Hoesly et al., 2018). These changes in anthropogenic emissions would have introduced significant trends in sulfate, nitrate, ammonium, primary organic aerosols, BC, and associated aerosol water (Attwood et al., 2014; Blanchard et al., 2013; Hand et al., 2012b; Malm et al., 2017; Murphy et al., 2011; Nguyen et al., 2015; Nguyen et al., 2016; Xing et al., 2015). Indirectly, these emission changes could also affect the SOA yields from biogenic carbon in multiple ways, such as by altering oxidation pathways, gas/particle partitioning, and aqueous-phase reactions (Hoyle et al., 2011; Marais et al., 2016; Pye et al., 2017; Xu et al., 2015a). These anthropogenic influences on major aerosol chemical components offer valuable information to understand the historical seasonality in aerosol extinction and visibility.

In this letter, we analyze a recently developed data record of historical inverse visibility (1/Vis) (Li et al., 2016a) to explore how the aerosol seasonality in the eastern US evolved over five decades. We interpret seasonal contrasts in 1/Vis trends, and use historical emission inventories to understand observed changes in 1/Vis and its seasonality.

3.3 Materials and Methods

Horizontal visibility (Vis) is inversely related with atmospheric extinction, and has been recognized as a proxy of surface aerosol loading (Husar et al., 2000; Li et al., 2016a; Wang et al., 2009). We use a recently developed dataset of quality assured inverse visibility (1/Vis, unit: Mm^{-1}) (Inverse visibility data, 2018; Li et al., 2016a). Starting from global raw synoptic observations, this monthly 1/Vis dataset has been comprehensively screened and processed to reduce effects from cloudy, foggy and high relative humidity (RH > 90%) records, as well as spikes, artificial detection thresholds and discontinuities (Li et al., 2016a). The 1/Vis data were validated against aerosol extinction and $PM_{2.5}$ data over the US and Europe and provided quantitatively insightful information on aerosol seasonal variations and trends (Li et al., 2016a). We use the 1/Vis data for 1946-1998, during which each year contains at least 150 sites over the eastern US. The number of available sites substantially decreased after 1998 because of the Vis reporting thresholds (i.e. Vis higher than 10 miles are not resolved) after adopting instrumentation to replace human

observations; this limits the representativeness of the 1/Vis data for cleaner air quality in recent years (Li et al., 2016a). For 1999-2016, we obtain long-term federal reference method $PM_{2.5}$ data from the US Environmental Protection Agency (EPA) to complement our interpretation of 1/Vis.

For each site and season, we calculate seasonal 1/Vis or $PM_{2.5}$ for each year provided that at least 2 of 3 monthly 1/Vis or $PM_{2.5}$ records are available. We define the aerosol seasonality as the ratio of 1/Vis or $PM_{2.5}$ between summer (JJA) and winter (DJF), and calculate this ratio (subsequently referred to as "summer/winter") for each running 5-year period. In spring or fall, the 1/Vis data generally exist between summer and winter values.

We use historical anthropogenic emissions and meteorological reanalyses to interpret the observed changes in 1/Vis seasonality. We use monthly 70-year (1945-2014) Community Emission Data System (CEDS) anthropogenic emission data (Hoesly et al., 2018) of sulfur dioxides (SO_2), nitrogen oxides (NO_x), organic carbon (OC), black carbon (BC) and ammonia (NH_3) for perspective on historical aerosol sources. We also use long-term (1948-2015) monthly data from NOAA National Center for Environmental Prediction (NCEP) Reanalysis to infer trends in meteorological factors.

We separate the regions of the northeastern and southeastern US following Goldstein et al. (2009) and exploit their strong contrasts in biogenic aerosol sources (Figure 3-S1) to interpret the observed historical changes in 1/Vis seasonality. We focus our analysis on the start (1946-1950), middle (1973-1977) and end (1993-1997) of our dataset, while also examining changes between them. We estimate seasonal percentage trends in 1/Vis, CEDS emissions and NCEP parameters (relative to multi-year mean) in summer and winter using the Sen's slope (Sen, 1968) and determined the significance (i.e. *p* value) from the Mann-Kendall test (Kendall, 1975; Mann, 1945), provided that at least 2/3 of the total years in the calculated periods are available.

3.4 Results and Discussion

3.4.1 Changes in 1/Vis and $PM_{2.5}$ Seasonality

Figure 3-1 shows the calculated summer/winter ratio in 1/Vis over the eastern US. In the late 1940s (1946-1950), the whole domain is characterised by low summer/winter values, with 95% of sites exhibiting a winter maximum (summer/winter<1). The lowest summer/winter ratios (<0.5) are found around the Great Lakes region, and the highest values (>0.9) are over the New England coast. These summer/winter values increase over time. After nearly 3 decades (1973-1977), 63% of sites exhibit a summer maximum with summer/winter>1, except for the Great Lakes region with a winter maximum and the lowest summer/winter ratios across the domain. Summer/winter values over the mid-Atlantic and southeastern US exhibit high values (summer/winter>2). This spatial pattern remains similar two decades later (1993-1997).

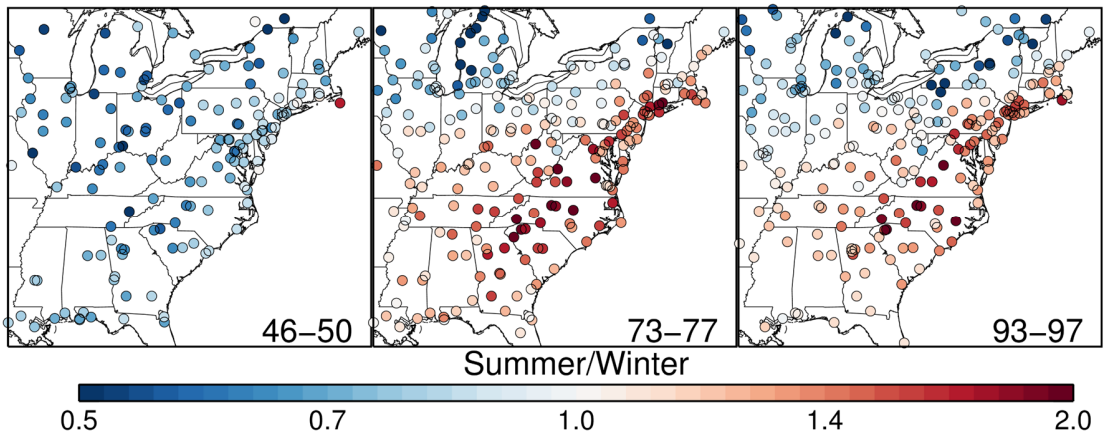

Figure 3-1. Spatial distribution of 5-year summer/winter ratio in 1/Vis over the eastern US.

Figure 3-S2 shows the summer/winter ratios calculated from more recent $PM_{2.5}$ data. The spatial distribution over 1999-2003 is broadly consistent with those in 1/Vis over 1993-1997, with highest summer/winter values across the Appalachian region from New England to Alabama, and lowest values appearing in the north. $PM_{2.5}$ sites with summer/winter>1 extend further west and north, perhaps related to either aerosol hygroscopicity or different time periods. Interestingly, there is a broad reduction in the summer/winter ratios over most eastern US sites in recent years (2012-2016), with many sites over the northeastern US reverting to a winter maximum, and most southeastern sites

exhibiting weaker summer maxima. A recent study also found more measurement sites with wintertime $PM_{2.5}$ maxima over the US appearing after 2009 (Chan et al., 2018).

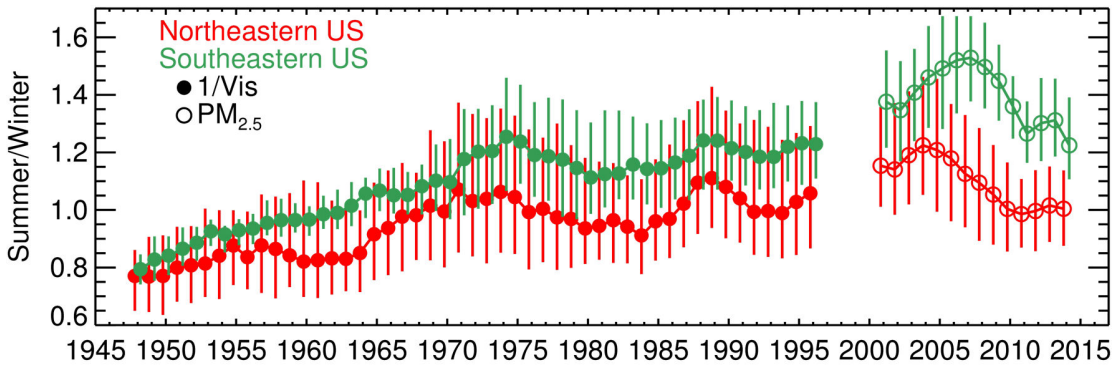

Figure 3-2. Temporal evolution of the summer/winter ratio of 1/Vis (filled) and $PM_{2.5}$ (open) over the northeastern (red) and southeastern (green) US. Regions are defined in Figure 3-S1. Each point represents the multi-site median of the 5-year running mean summer/winter ratios. Error bars indicate the 25th and 75th percentiles of the calculated ratios within each region.

Figure 3-2 shows the historical evolution in multi-site median of the calculated 5-year running mean summer/winter ratios over the northeastern and southeastern US. Both regions have median summer/winter of ~0.8 in 1948 (i.e. representing 1946-1950), which significantly ($p < 0.05$) increase to 1.04 (northeastern US) and 1.24 (southeastern US) in 1975. The changes in regional median summer/winter ratios are not uniform and less pronounced after 1975, exhibiting significant ($p < 0.05$) but slower overall increases (by less than 0.1) during 1976-1996. Over both regions, the summer/winter values in 1/Vis might exhibit a systematic underestimation of those in $PM_{2.5}$, although the measurement gap over 1997-2000 complicates interpretation. Nevertheless, the median summer/winter ratios calculated from $PM_{2.5}$ for recent years generally follow the tendency of these from 1/Vis, with consistently higher median summer/winter over the southeast than the northeast. The recent reductions in summer/winter (weakened seasonality) are evident for both regions. In summary, we find that the dominance of summer maxima broadly observed in $PM_{2.5}$ over the eastern US is also observed in the 1/Vis data after the 1970s, but the 1/Vis seasonality in earlier years is significantly weaker and even reversed in the 1940s, suggesting similar historical evolution of $PM_{2.5}$ seasonality.

3.4.2 Contrasting 1/Vis Trends in Winter and Summer

Figure 3-S3 shows the calculated seasonal 1/Vis trends over each site, and Figure 3-S4 shows the time series of the seasonal 1/Vis over the two regions. There is a 3-phase trend evolution in 1/Vis, i.e. decreases for 1946-1955, increases for 1956-1975, and decreases after 1975. This evolution is most evident in summer and is consistent with annual trends (Li et al., 2016a). Comparing to these summer trends, the winter 1/Vis decreasing trends over 1946-1955 are stronger, and the 1956-1975 increasing trends are weaker over both regions, introducing increases in the summer/winter ratios. After 1975, the decreases in 1/Vis are similar in winter and summer, leading to the weaker changes in summer/winter values.

3.4.3 Linkage to Emissions and Aerosol Composition

Changes in aerosol sources and chemical composition could contribute to these changes in aerosol seasonality. Among the major aerosol species, ammonium sulfate and SOA from biogenic carbon (BSOA) have higher concentrations and higher extinction in summer with more rapid photochemistry and stronger biogenic emissions (Goldstein et al., 2009; Hand et al., 2012a; Hand et al., 2014a). Meanwhile nitrate and carbonaceous aerosols from anthropogenic sources generally exhibit winter maxima due to low temperatures which promote nitrate formation (Hand et al., 2012a; Heald et al., 2012) and carbonaceous emissions from residential heating (Bond et al., 2007; Hand et al., 2012a). This is consistent with the observed recent spatial distribution of summer/winter in $PM_{2.5}$, specifically higher values over the southeast with stronger biogenic emissions and over the Appalachian region with prevalent coal burning, versus lower values over the northern and colder states. The recent reduction in the summer/winter values of $PM_{2.5}$ (Figure 3-2) over the eastern US is attributable to stronger reductions in summertime sulfate and weaker reductions in wintertime nitrate and OA in the 2000s (Chan et al., 2018; Kim et al., 2015; Li et al., 2017a). In contrast, the observed strengthening in summer maxima in 1/Vis over 1946-1975 could be caused either by increases in the mass fraction of sulfate and BSOA, or by decreases in that of nitrate, anthropogenic organic aerosol (OA) and BC. We use historical emission estimates to interpret these observed changes in 1/Vis seasonality.

Table 3-S1 shows winter and summer trends in anthropogenic emissions over both regions, with detailed time series shown in Figure 3-S5. Over 1946-1955, the stronger decreases in 1/Vis in winter than in summer (Figure 3-S3 and 3-S4) over both regions are associated with significant reductions in OC and BC emissions ($p < 0.05$), which have winter emission maxima over this period (Figure 3-S5). These carbonaceous emission reductions are driven by the domestic sector (Figure 3-S5), as the percentage of homes over the US using coal, coke or wood for wintertime residential heating reduced from 77% in 1940 to 16% in 1960 (Historical Census of Housing Tables, 2018). SO_2 emissions also decreased ($p < 0.1$) in both regions and seasons over this period. The consequent decrease in sulfate (with a photochemical summer maximum) does not fully compensate for the effects from OA and BC reductions on increasing the summer/winter. Over 1956-1975, the significantly increasing ($p < 0.05$) SO_2 emissions in both regions, driven by increases in the energy sector, drive the increasing 1/Vis (Figure 3-S3) and the strengthening summer maxima. Meanwhile several sites with negative 1/Vis trends over 1956-1975 in winter over the northeast (Figure 3-S3) suggest additional effects of significant wintertime OC and BC emission reductions ($p < 0.05$) during this period (Figure 3-S5). Over 1976-1995, the SO_2, OC and BC emissions all decrease ($p < 0.05$) following the Clean Air Act and its amendments (Evolution of the Clean Air Act, 2018), and the resultant trends in 1/Vis appear similar in summer and winter (Figure 3-S3), corresponding to relatively constant summer/winter (Figure 3-2). The small decreases in median summer/winter over both regions during 1976-1985 (Figure 3-2) are consistent with the temporary increases in wood burning (Historical Census of Housing Tables, 2018) and OC emissions during the same period (Figure 3-S5). Possible effects of changes in NO_x and NH_3 emissions, as well as in meteorology are discussed in the Supporting Information and expected to be less important.

Although the evolution in anthropogenic emissions is similar over the two regions (Table 3-S1 and Figure 3-S5), the substantial changes in the summer/winter over the southeastern US cannot be solely explained by the effects of increased sulfate and reduced anthropogenic OA and BC. In summer, if BSOA over the southeastern US (currently accounting for >30% of total $PM_{2.5}$) (Kim et al., 2015; Xu et al., 2015b) had not increased significantly, the northeastern US dominated by anthropogenic aerosols would have historically greater relative increases in 1/Vis. However, we find that from 1956 to 1975,

the median 1/Vis in summer increased by 25 Mm^{-1} (29%) over the northeastern US, and by 38 Mm^{-1} (56%) over the southeastern US (Figure 3-S4). This stronger increase over the southeast is insensitive to the RH thresholds used to screen the visibility data (Figure 3-S8 and Figure 3-S11), confirming stronger increases in aerosol mass concentration over the southeast than the northeast where anthropogenic aerosols dominate. Therefore, increases in BSOA likely occurred over the southeastern US during 1956-1975.

Biogenic emissions are not expected to exhibit systematic trends concurrent with anthropogenic emissions (Sindelarova et al., 2014). Numerous recent studies proposed various pathways by which anthropogenic emissions could mediate BSOA formation yields (Carlton et al., 2010; Hoyle et al., 2011; Rollins et al., 2012). Various model developments have emerged recently to describe these processes (Budisulistiorini et al., 2017; Keppel‐Aleks and Washenfelder, 2016; Marais et al., 2016; Pye et al., 2013). Especially over the southeastern US, observational evidence suggests a strong relationship of BSOA with sulfate or SO_2 emissions, and recent decreasing BSOA with concurrent reductions in sulfur and associated aerosol water (Blanchard et al., 2016; Carlton and Turpin, 2013; Malm et al., 2017; Nguyen et al., 2015; Pye et al., 2017; Xu et al., 2015a). The 1/Vis data provide observational evidence that an opposite procedure, i.e. enhanced BSOA formation over the southeastern US following the increase in anthropogenic emissions has occurred historically. In the late 1940s, the similar summer/winter values over both regions (Figure 3-1 and 3-2) indicate similar aerosol composition (i.e. higher anthropogenic OA and BC, lower sulfate and BSOA). Although hard to quantitatively estimate, the previously inhibited BSOA yields could reflect less existing aerosol for gas/particle partitioning (Carlton et al., 2010), less aerosol water due to dominance of carbonaceous aerosols (Nguyen et al., 2015), and less sulfur to facilitate aqueous-phase reactive isoprene uptake to SOA (Xu et al., 2015a). Trends in summertime surface air temperature are insignificant (Figure 3-S12), and thus unlikely to sufficiently increase biogenic emissions to explain the 1/Vis trends. Anthropogenic land use increased biogenic emissions over the southeastern US from the mid-1980s to the mid-1990s (Purves et al., 2004), and might also partially contribute to the increasing BSOA if it occurred over 1946-1975.

Thus, the growing dominance of summer maxima in 1/Vis over the eastern US from the late 1940s to the mid-1970s was likely driven by reductions in OC and BC emissions and increases in SO_2 emissions. The observed changes in 1/Vis seasonality are associated with substantial changes in aerosol sources and composition, with anthropogenic OA and BC becoming less dominant, and sulfate and BSOA being more important. Anthropogenic OA reduction was estimated to save ~0.18 million premature deaths in the US over 1990-2012 (Ridley et al., 2018). Our findings provide indirect observational evidence of longer-term benefits of historical changes in carbonaceous emissions. Over the southeastern US, the winter maxima in 1/Vis before the 1950s, the stronger increase in the summer/winter values compared to the northeast, and the recent weakening of summer maxima all suggest evidence of interaction between anthropogenic emissions and BSOA formation, and co-benefits on reducing BSOA through mitigating anthropogenic emissions.

3.5 Acknowledgement

This work was supported by the Natural Science and Engineering Research Council of Canada. Chi Li was supported by a Killam Predoctoral Scholarship. The visibility data before processing is originally provided by NOAA NCEI (https://www.ncei.noaa.gov/access-ui/data-search?datasetId=global-hourly). The $PM_{2.5}$ data was hosted by the Federal Land Manager Environmental Database (http://views.cira.colostate.edu/fed/DataWizard/). The NCEP reanalysis data is from NOAA (https://www.esrl.noaa.gov/psd/data/gridded/data.ncep.reanalysis.html). We also thank the Input Datasets for Model Intercomparison Projects (https://esgf-node.llnl.gov/projects/input4mips/) for making the emission data used in this study publicly available.

3.6 Supporting Information

3.6.1 Discussion of Other Emission and Meteorological Factors Affecting Observed Changes in 1/Vis

Besides the changes in sulfur and anthropogenic carbon emissions discussed in the main text, aerosol composition and extinction are affected by various other emission and meteorological factors that might contribute to the observed long-term changes in 1/Vis. Here we discuss these effects.

Nitrogen oxides (NO_x) and ammonia (NH_3) emissions increased ($p < 0.05$) across the eastern US in both summer and winter over 1946-1975 (Table 3-S1 and Figure 3-S5). These increases could increase the formation of ammonium nitrate (Holt et al., 2015; Pinder et al., 2008a) and have compensating effects for the increasing summer/winter ratios, especially around the Great Lakes, where nitrate formation is favored (Hand et al., 2012a). However, increasing NO_x emissions could also contribute to the increasing summer/winter in haze through stronger photochemical production of oxidants (Fuglestvedt et al., 1999; Wang and Jacob, 1998) that increase summertime sulfate production rates (Fiore et al., 2012; Shindell et al., 2009). The overall effect from NO_x and NH_3 emission trends is therefore undetermined and requires chemical transport modeling to fully resolve, which is beyond the scope of this study.

Relative humidity is an important parameter that determines aerosol composition and extinction. Ambient aerosol extinction is affected by particle water which would increase its size and scattering ability (Attwood et al., 2014; Pitchford et al., 2007). Generally, inorganic aerosols of sea salt, ammonium sulfate and ammonium nitrate are significantly more hygroscopic than carbonaceous aerosols and dust (Martin et al., 2003b; Pitchford et al., 2007; Snider et al., 2016). Therefore, changes in aerosol composition would modify the overall hygroscopicity and consequently the extinction. Recent studies over the southeastern US indicate that aerosol water decreased by 79% over 2001-2012 in summer (Nguyen et al., 2015), and the weakened aerosol hygroscopicity is responsible for a decrease in aerosol extinction equivalent to 32% of the decreased extinction due to changes in dry aerosol mass (Attwood et al., 2014).

Our 1/Vis data were constructed with screening of high RH records (RH > 90%) in the raw hourly data (Li et al., 2016a) to avoid strong effects on 1/Vis from aerosol water that would mask the representativeness of the 1/Vis data on changes in aerosol loading, as was similarly performed in other related studies (Che et al., 2007; Husar et al., 2000; Lin et al., 2014). We perform sensitivity tests by reprocessing the raw data with stricter screening of records with RH > 80% (Figure 3-S6 – 3-S8) and RH > 70% (Figure 3-S9 – 3-S11). These screenings reduce the number of available monthly 1/Vis records by 30% (for RH > 80%) and 43% (for RH > 70%) relative to the data presented in the main text, and reduce the overall 1/Vis (e.g. comparing Figure 3-S4 with Figure 3-S8 and 3-S11) because of less water contribution to extinction. Aerosol hygroscopicity also reduces the magnitudes of summer/winter ratios, as the median summer/winter in Figure 3-S7 and 3-S10 are higher than these in Figure 3-2, especially after the 1970s when the more hygroscopic sulfate aerosols have increased while less hygroscopic OA and BC have reduced. Nevertheless, the main findings in this paper about historical changes, i.e. increasing summer/winter from the late 1940s to the mid-1970s (Figure 3-S6 and 3-S9), larger increase in median summer/winter over the southeast than over the northeast (Figure 3-S7 and 3-S10), stronger increase in summer 1/Vis over the southeast which indicates additional increase in BSOA than over the northeast (Figure 3-S8 and 3-S11), and steady reductions in winter 1/Vis over the northeast (Figure 3-S8 and 3-S11) corroborating historical reductions in carbonaceous aerosols, are all consistently supported by these sensitivity experiments derived from 1/Vis records less affected by RH. We therefore conclude that the changes in 1/Vis and its seasonality as presented in the main text are insensitive to RH and dominated by changes in the aerosol mass concentration and chemical composition.

Besides changing aerosol water, RH is also associated with aerosol formation yields of some components, e.g. nitrate and SOA (Carlton and Turpin, 2013; Heald et al., 2012; Pye et al., 2017). Any long-term trends in RH would also affect aerosol composition. Figure 3-S12 explores trends in RH and several other key meteorological parameters in NCEP over 1948-2015, including surface air temperature that affects biogenic emissions, chemical reaction rates, and aerosol partitioning of semi-volatile species, cloud cover that affects sulfate and SOA aqueous formation (Carlton and Turpin, 2013; Paulot et al., 2017;

Pye et al., 2017), as well as surface wind speed and precipitation that affect aerosol removal. Strong interannual variability in these parameters results in different signs and significance in the calculated trends for different time periods, seasons and regions. For the 2 regions, 2 seasons and 4 periods, we find that 15 out of the 16 calculated trends in RH and cloud cover agree in their signs (except for the 1948-1955 summer over the northeast while both trends are insignificant with $p > 0.1$). Similarly, the signs of 14 calculated trends in RH and precipitation are consistent (except for the 1996-2015 summer over both regions while only 1 trend is significant at $p < 0.1$). The strong covarying feature among these 3 parameters reflects their variabilities driven by atmospheric water vapor. However, these parameters have compensating effects on aerosols, with RH and cloud cover favoring aerosol formation and hygroscopic growth while precipitation facilitates aerosol scavenging. For wind speed, the only significant trend ($p < 0.05$) before 1975 is the increasing wind speed over the southeastern US in winter for 1948-1955, which could accelerate aerosol ventilation in winter and positively contribute to the increasing summer/winter. Air temperature exhibits insignificant trends ($p > 0.1$) before 1975. The significantly increasing ($p < 0.05$) temperature in winter over 1976-1995 could decrease nitrate particle formation and increase the summer/winter, which might also be compensated by concurrently decreasing wind speed ($p < 0.1$) also occurred over winter. Quantitative evaluation of the meteorological contributions to the observed changes cannot be achieved without numerical simulation, which is beyond the scope of this study. Based on the compensating effects from different parameters, it appears likely that the contributions from anthropogenic emissions to long-term changes in aerosol composition and 1/Vis dominate over the overall effects from climate change, which is consistent with conclusions from recent modeling studies (Fang et al., 2013; Ridley et al., 2018; Westervelt et al., 2016; Yang et al., 2016).

Table 3-S1. Seasonal and regional trends in total anthropogenic emissions (CEDS) for 3 periods. Trends with $p < 0.1$ are followed by one asterisk (*), and trends with $p < 0.05$ are bold and followed by two asterisks (**). Positive trend ($p < 0.1$) are red and negative trends ($p < 0.1$) are green.

Trend (%/yr)	Winter (DJF)			Summer (DJF)		
	46-55	56-75	76-95	46-55	56-75	76-95
Northeastern US						
SO_2	-1.4*	**2.3****	**-1.5****	-1.4*	**3.0****	**-1.4****
NO_x	**2.6****	**3.7****	-0.1	**2.4****	**3.9****	**-0.3****
OC	**-3.5****	**-3.5****	**-1.4****	**-2.3****	**-0.6****	**-0.9****
BC	**-2.3****	**-1.8****	**-2.1****	-0.6	**1.1****	**-1.8****
NH_3	**2.9****	**2.1****	-0.3*	**2.8****	**2.4****	**0.4****
Southeastern US						
SO_2	-1.4*	**2.2****	**-1.3****	-1.5*	**2.9****	**-1.0****
NO_x	**2.5****	**3.4****	**-0.6****	**2.4****	**3.6****	**-0.5****
OC	**-3.2****	**-2.5****	**-0.8****	**-2.4****	**-0.9****	**-0.6****
BC	**-1.7****	**-1.0****	**-1.7****	-0.7	**0.5****	**-1.4****
NH_3	**3.1****	**2.7****	**0.5****	**3.1****	**2.8****	**0.9****

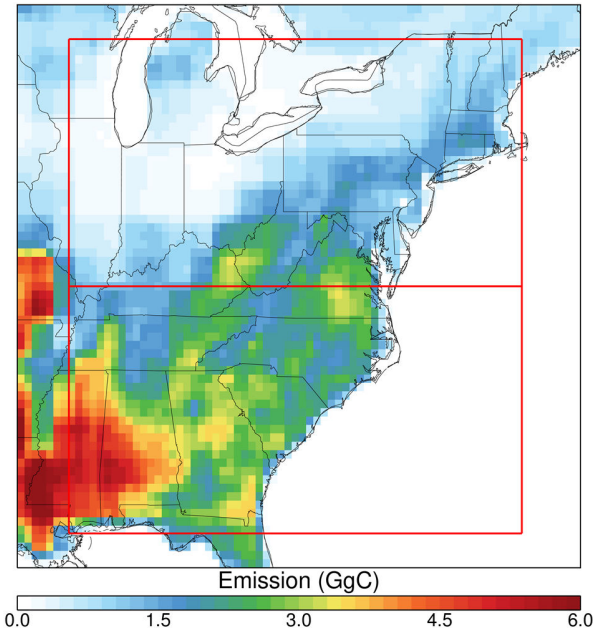

Figure 3-S1. Total emissions of isoprene and monoterpenes over the eastern US in the summer (JJA) of 2013 from MEGAN 2.1 (Guenther et al., 2012). The definitions of the northeastern and southeastern US are indicated by the red rectangles.

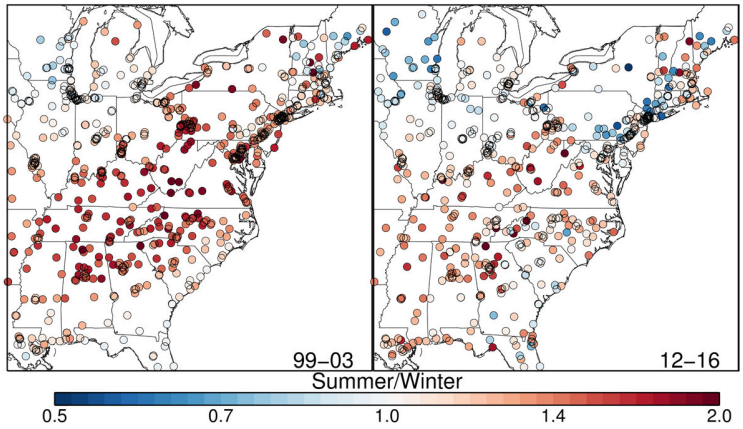

Figure 3-S2. Spatial distribution of 5-year summer/winter ratio in $PM_{2.5}$ over the eastern US.

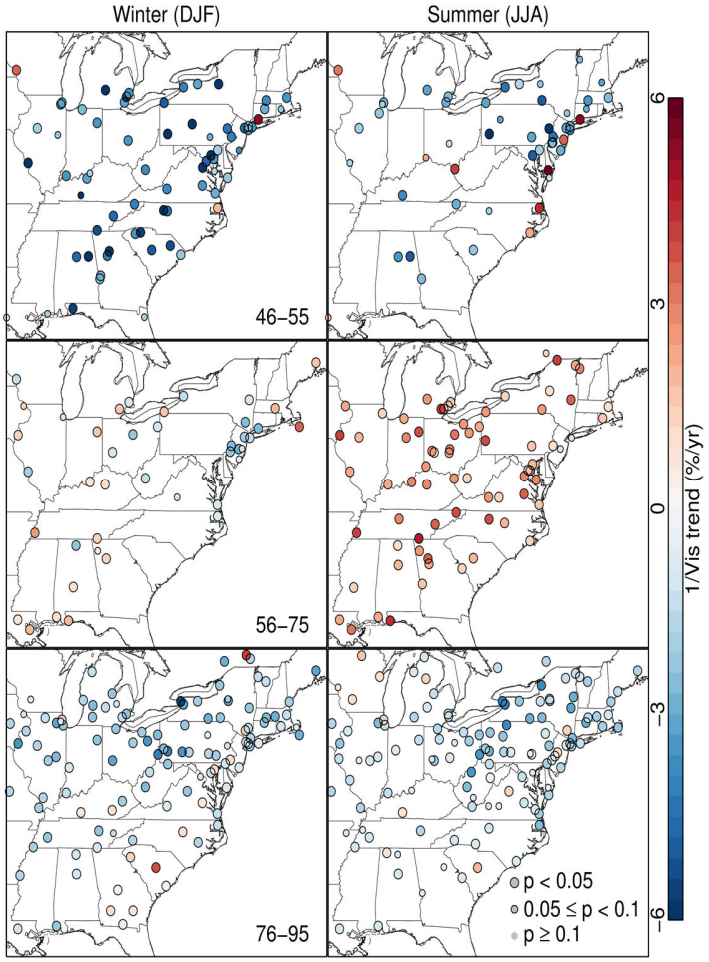

Figure 3-S3. Relative trends in 1/Vis for winter (DJF) and summer (JJA) over 3 periods. Larger points with black outlines indicate significant trends with $p < 0.05$. Smaller points with black outline represent significant trends with $0.05 \leq p < 0.1$. Points without outline indicate insignificant trends.

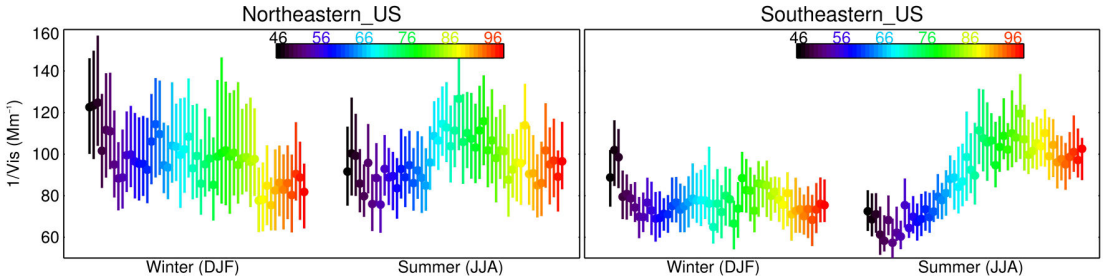

Figure 3-S4. Evolution of 1/Vis over the northeastern (left) and southeastern (right) US in winter (DJF) and summer (JJA). Points indicate median 1/Vis within each region in the year (color coded) and season. Error bars represent the 25th and 75th percentiles.

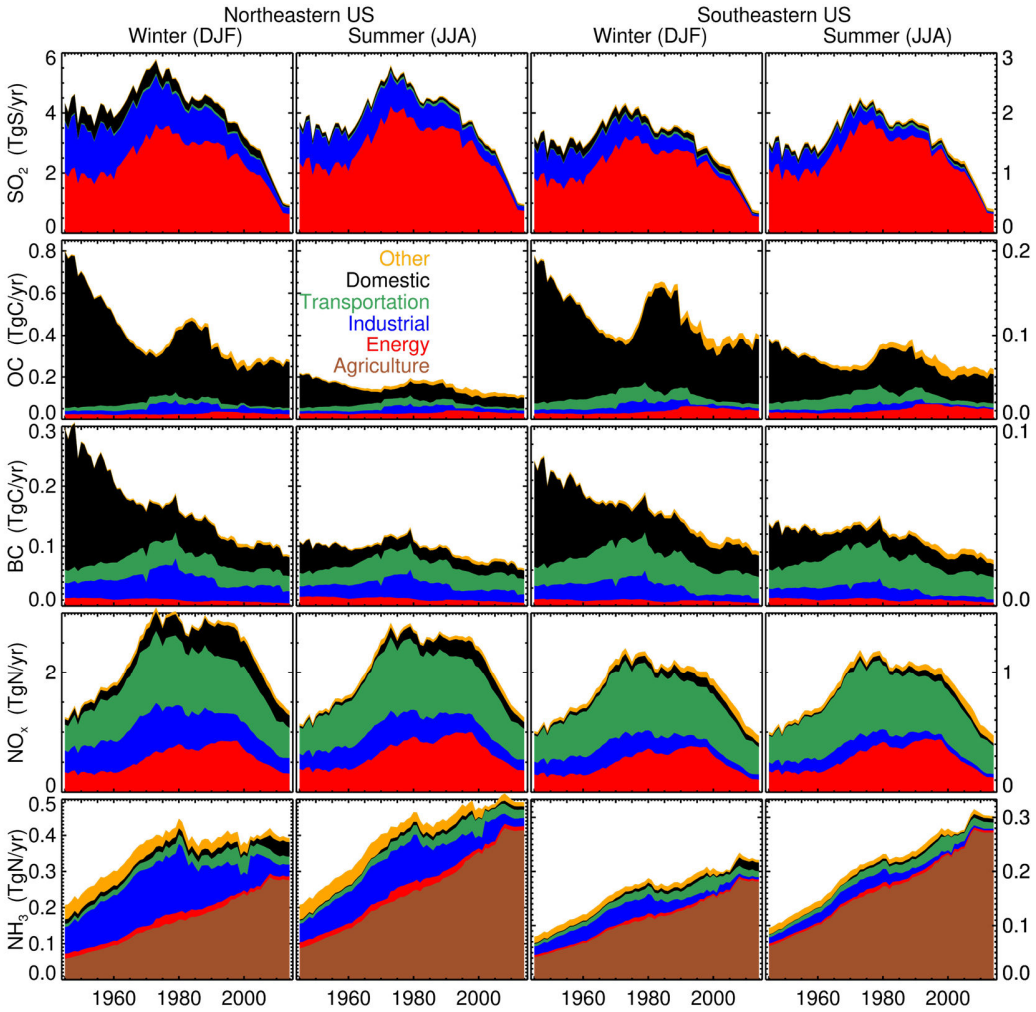

Figure 3-S5. Anthropogenic emissions (1945-2014) of aerosol sources from the CEDS inventory for winter and summer, and over the northeastern and southeastern US. Colors indicate emission sectors.

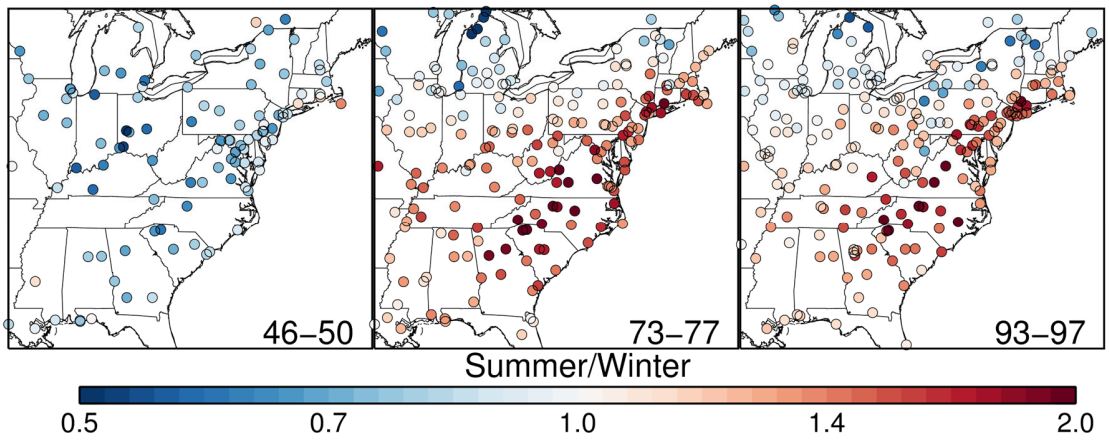

Figure 3-S6. Similar to Figure 3-1 but regenerated by eliminating hourly Vis records with RH > 80%.

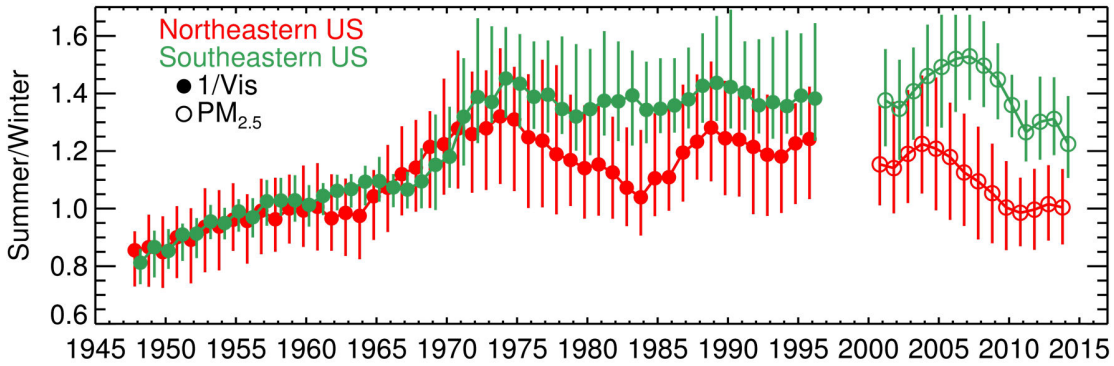

Figure 3-S7. Similar to Figure 3-2 but regenerated by eliminating hourly Vis records with RH > 80%.

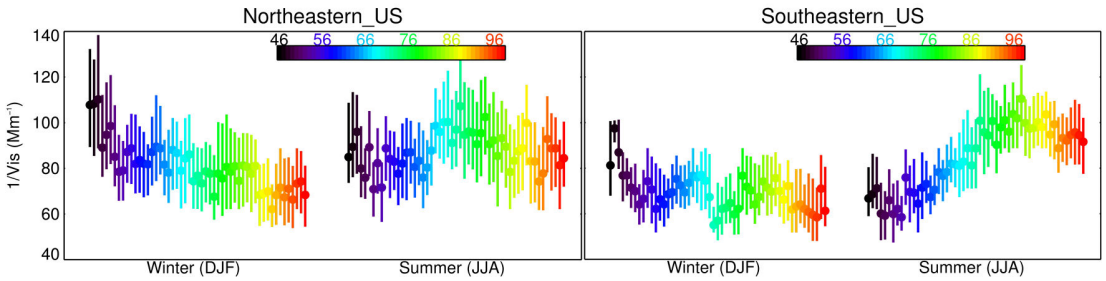

Figure 3-S8. Similar to Figure 3-S4 but regenerated by eliminating hourly Vis records with RH > 80%.

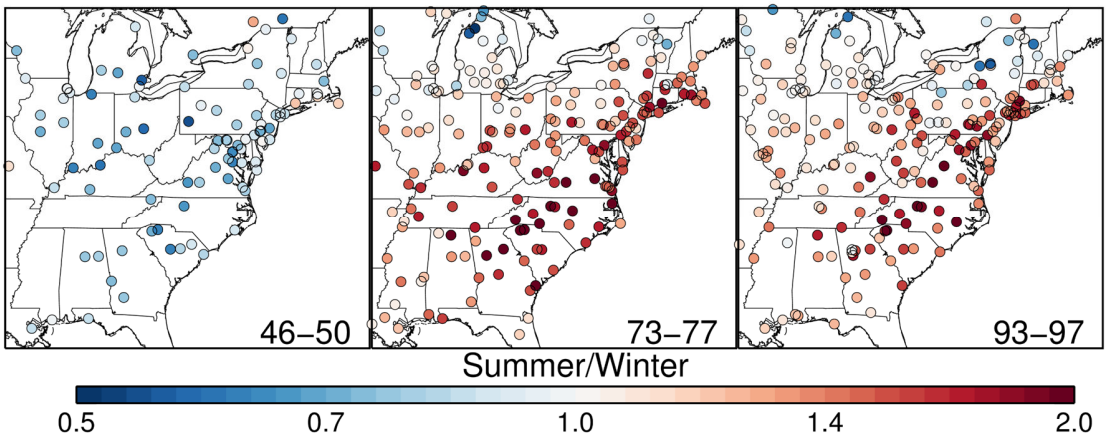

Figure 3-S9. Similar to Figure 3-1 but regenerated by eliminating hourly Vis records with RH > 70%.

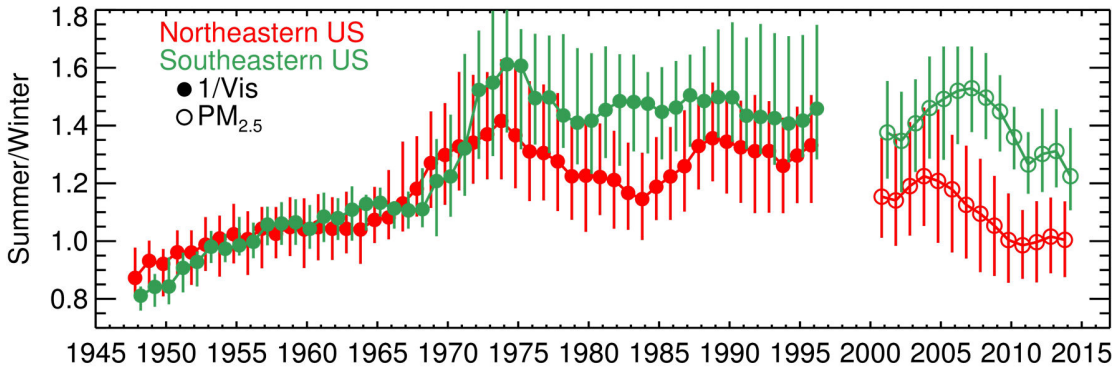

Figure 3-S10. Similar to Figure 3-2 but regenerated by eliminating hourly Vis records with RH > 70%.

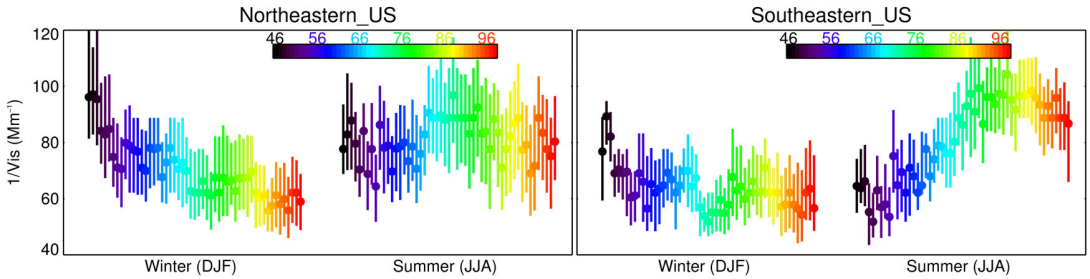

Figure 3-S11. Similar to Figure 3-S4 but regenerated by eliminating hourly Vis records with RH > 70%.

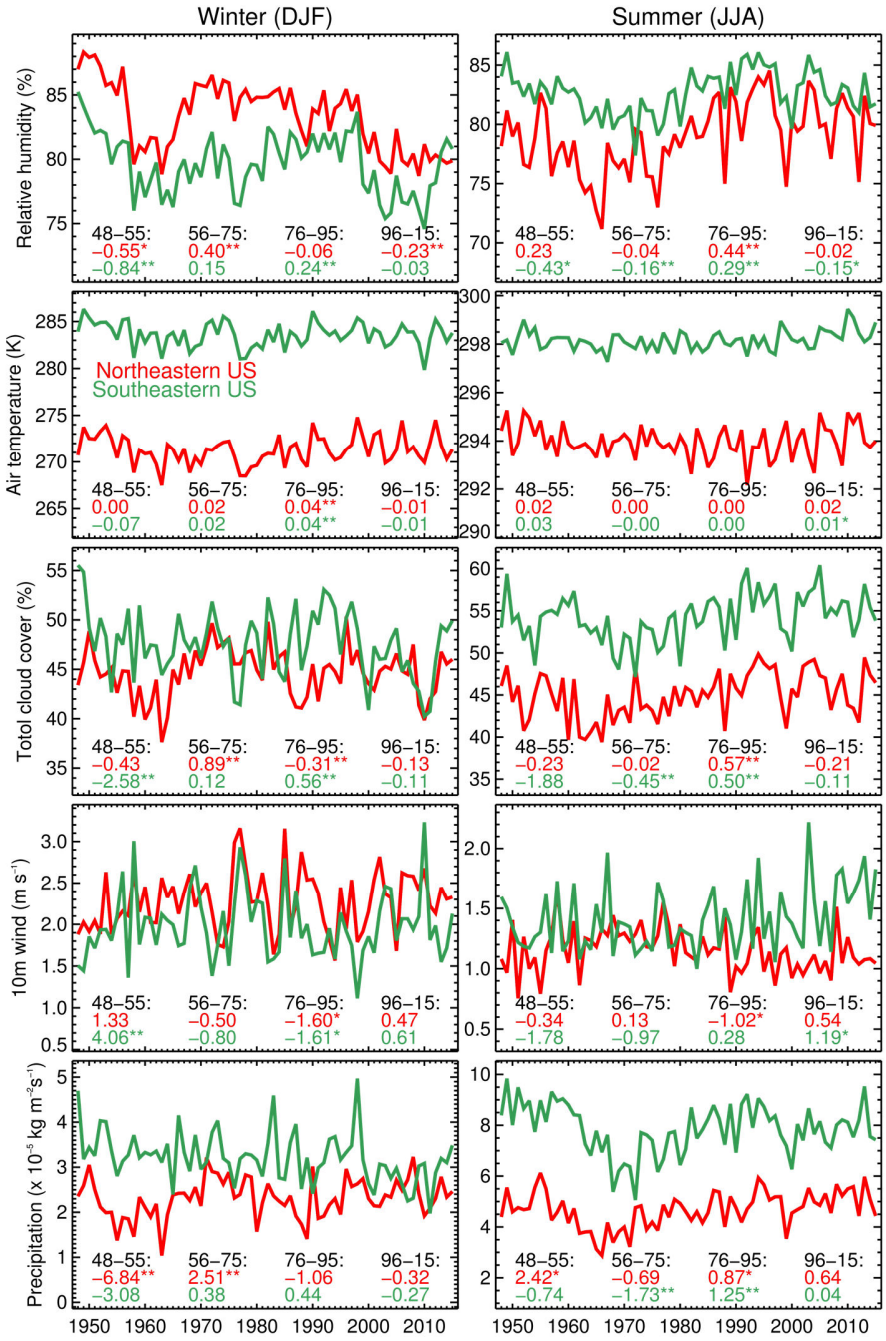

Figure 3-S12. Long-term (1948-2015) variations in NCEP surface relative humidity, surface air temperature, total cloud cover, surface (10m) horizontal wind speed and precipitation rate over winter (left) and summer (right) for the northeastern (red) and southeastern US (green). Relative trends (%/yr) for 4 periods are shown on the bottom of each panel. Trends with $p < 0.1$ are followed by one asterisk (*), and trends with $p < 0.05$ are followed by two asterisks (**).

Chapter 4. Trends in Chemical Composition of Global and Regional Population-Weighted Fine Particulate Matter Estimated for 25 Years

4.1 Abstract

We interpret in situ and satellite observations with a chemical transport model (GEOS-Chem, downscaled to 0.1° × 0.1°) to understand global trends in population-weighted mean chemical composition of fine particulate matter ($PM_{2.5}$). Trends in observed and simulated population-weighted mean $PM_{2.5}$ composition over 1989-2013 are highly consistent for $PM_{2.5}$ (-2.4 vs. -2.4 %/yr), secondary inorganic aerosols (-4.3 vs. -4.1 %/yr), organic aerosols (OA, -3.6 vs. -3.0 %/yr) and black carbon (-4.3 vs. -3.9 %/yr) over North America, as well as for sulfate (-4.7 vs. -5.8 %/yr) over Europe. Simulated trends over 1998-2013 also have overlapping 95% confidence intervals with satellite-derived trends in population-weighted mean $PM_{2.5}$ for 20 of 21 global regions. Over 1989-2013, most (79%) of the simulated increase in global population-weighted mean $PM_{2.5}$ of 0.28 μg $m^{-3}yr^{-1}$ is explained by significantly ($p < 0.05$) increasing OA (0.10 μg $m^{-3}yr^{-1}$), nitrate (0.05 μg $m^{-3}yr^{-1}$), sulfate (0.04 μg $m^{-3}yr^{-1}$) and ammonium (0.03 μg $m^{-3}yr^{-1}$). These four components predominantly drive trends in population-weighted mean $PM_{2.5}$ over populous regions of South Asia (0.94 μg $m^{-3}yr^{-1}$), East Asia (0.66 μg $m^{-3}yr^{-1}$), Western Europe (-0.47 μg $m^{-3}yr^{-1}$) and North America (-0.32 μg $m^{-3}yr^{-1}$). Trends in area-weighted mean and population-weighted mean $PM_{2.5}$ composition differ significantly.

4.2 Introduction

Atmospheric aerosols have major roles in air quality (Fuzzi et al., 2015; West et al., 2016), visibility (Li et al., 2016a; Malm et al., 1994; Wang et al., 2009) and climate (Bellouin et al., 2005; IPCC, 2013; Wild, 2009). Particles with an aerodynamic diameter of 2.5 μm or less ($PM_{2.5}$) are a leading risk factor for global morbidity and mortality (Dockery et al., 1993; US EPA, 2009; Forouzanfar et al., 2016; Hoek et al., 2013). Not only does over 85% of the world's current population live where annual estimated $PM_{2.5}$ is above the World Health Organization (WHO) guideline of 10 μg/m (Brauer et al., 2015; van Donkelaar et al., 2016), but recent cohort studies also reveal an association of mortality rates with long-term exposure to $PM_{2.5}$ concentrations at levels below the WHO guideline (Correia et al., 2013; Crouse et al., 2012; Pinault et al., 2016), implying the need for further mitigation efforts (Apte et al., 2015). Changes in $PM_{2.5}$ mass concentration are driven by changes in its chemical composition due to variations in emissions and atmospheric processes (Chin et al., 2014; Daskalakis et al., 2016; Fuzzi et al., 2015). Understanding trends in $PM_{2.5}$ components can help inform source contributions and future mitigation efforts. Since the 1980s, regulations in developed regions have dramatically reduced emissions of primary particles and precursor gases, while the rapidly growing economies of developing countries have led to steeply rising energy consumption and pollutant emissions (Crippa et al., 2016; Daskalakis et al., 2016; Lu et al., 2011; Vestreng et al., 2007; Xing et al., 2013). Given the established impacts of $PM_{2.5}$ on human health, improved understanding of how these changes affect trends in global $PM_{2.5}$ burden and composition is warranted.

A few regions have long-term in situ measurements of $PM_{2.5}$ and its chemical composition. These measurements revealed regionally coherent decreases over North America in $PM_{2.5}$ (Brook et al., 1999; US EPA, 2016; Wang et al., 2012), ammonium (Leibensperger et al., 2012; Silvern et al., 2017; Xing et al., 2015), sulfate (Brook et al., 1999; Hand et al., 2012b; Leibensperger et al., 2012; Malm et al., 2002; Silvern et al., 2017; Xing et al., 2015), nitrate (Leibensperger et al., 2012; Xing et al., 2015), organic aerosol (Hand et al., 2013; Leibensperger et al., 2012; Marais et al., 2017; Zhang et al., 2017) and black carbon (Hand et al., 2013; Leibensperger et al., 2012; Murphy et al., 2011; Xing et al., 2015), and over Europe in sulfate (Tørseth et al., 2012; Turnock et al., 2015; Xing et

al., 2015), nitrate (Xing et al., 2015) and $PM_{2.5}$ (Li et al., 2016a; Tørseth et al., 2012; Wang et al., 2012). Table 4-S1 summarizes these reported trends. Measurements in these regions, where emissions are relatively well known, offer valuable information to test the representation of $PM_{2.5}$-related atmospheric processes in global models. Over regions without long-term in situ data, alternative proxies of $PM_{2.5}$ provide complementary trend information (Table 4-S2), such as global trends in satellite observations of columnar aerosol optical depth (AOD) (Hsu et al., 2012; Mehta et al., 2016; Yoon et al., 2014). These satellite observations have been related to ground-level $PM_{2.5}$ by chemical transport modeling (Boys et al., 2014; Geng et al., 2017) or statistical models (Hoek et al., 2008; Ma et al., 2016). More broadly, models facilitate interpretation of these ground-based and satellite-based observations to understand sources and processes affecting these trends, and their relation with chemical composition (Chen et al., 2010; Chin et al., 2014).

Chemical transport models (CTMs) have been widely used for global characterization of aerosol spatiotemporal variation, with the ability to quantify the contributions from different chemical composition and sources. Recent regional simulations largely reproduced observed aerosol trends over North America and Europe, affirming their value for interpretation (Leibensperger et al., 2012; Marais et al., 2017; Turnock et al., 2015; Xing et al., 2015). But the current generation of global models suffers from relatively coarse resolution that introduces spatial misalignment between population density and modeled $PM_{2.5}$ that inhibits direct assessment of $PM_{2.5}$ exposure using models alone. Case studies indicate that mortality estimates due to $PM_{2.5}$ at a typical resolution of current global simulations could be systematically lower compared to estimates at finer resolutions (Li et al., 2016c; Punger and West, 2013). Thus in this study we combine the attributes of satellite observations at fine resolution with process-level information offered by CTM simulations. We spatially redistribute the CTM-modeled $PM_{2.5}$ composition with satellite-based $PM_{2.5}$ estimates at 0.1˚ resolution, to produce a 25-year assessment of global population-weighted $PM_{2.5}$ chemical composition from 1989 to 2013. We evaluate this downscaled simulation versus in situ observations where available. Then we apply this downscaled simulation to investigate global changes in population-weighted mean $PM_{2.5}$ chemical composition, to further understand the intrinsic drivers of trends in $PM_{2.5}$ exposure.

4.3 Materials and Methods

4.3.1 Observations and Complementary Data

We collect long-term observation data about $PM_{2.5}$ and its chemical composition over North America and Europe, and the global ground-based $PM_{2.5}$ measurements collected for the Global Burden of Disease Study (GBD) (Brauer et al., 2015). Population data at 0.1˚ × 0.1˚ resolution are also used for exposure estimation. Details on data selection and processing are described in the Supporting Information (SI).

For model downscaling to a resolution more relevant to population exposure, we use the global satellite-based $PM_{2.5}$ estimates at 0.1˚ × 0.1˚ resolution (van Donkelaar et al., 2016) that merged satellite AOD retrievals from 7 different algorithms inversely weighted by their errors against AERONET, converted AOD to $PM_{2.5}$ using simulated $PM_{2.5}$-AOD relationships, and then statistically fused (geographically weighted regression) these $PM_{2.5}$ estimates with ground-based measurements. We use the 5-year average data between 2008-2012 (referred to as $Mean_{sat}$) when more ground-based $PM_{2.5}$ records (over 4000) are available for statistical calibration.

We evaluate simulated trends in global $PM_{2.5}$ using mostly independent satellite-based $PM_{2.5}$ trends (referred to as $Trend_{sat}$). The 1998-2013 annual variations in global $PM_{2.5}$ were inferred from the SeaWiFS and MISR sensors that have long-term calibration stability (Boys et al., 2014; van Donkelaar et al., 2015). $PM_{2.5}$ trends for 1999-2012 from these estimates show unbiased consistency with in situ measurements over the eastern US (Boys et al., 2014). The absolute concentrations of $Trend_{sat}$ are also calibrated to $Mean_{sat}$ to match the 2008-2012 mean while preserving the original trends. The annual mean $PM_{2.5}$ data to calculate $Mean_{sat}$ and $Trend_{sat}$ are obtained directly from the publicly available archive (Global Estimates of Surface $PM_{2.5}$, 2017). Although $Mean_{sat}$ and $Trend_{sat}$ contain some common elements (e.g. both using AOD from SeaWiFS and MISR, and $PM_{2.5}$-AOD relationship in GEOS-Chem), we attempt to isolate their independent information by focusing on the spatial distribution of absolute concentrations from $Mean_{sat}$, and on temporal variation from $Trend_{sat}$ to evaluate the downscaled simulation.

4.3.2 GEOS-Chem Simulation and Downscaling

We use the GEOS-Chem CTM (version 11-01; http://www.geos-chem.org), including updated emission inventories and meteorological data from a consistent reanalysis (MERRA-2), to simulate the global evolution of $PM_{2.5}$ chemical composition over 1989-2013. More details about the simulation and historical emissions are provided in the SI.

The current generation of global models does not sufficiently resolve spatial variation in $PM_{2.5}$ to adequately estimate population exposure (Li et al., 2016c; Punger and West, 2013). Thus we follow Lee et al. (2015a) to downscale the simulation to $0.1^\circ \times 0.1^\circ$ resolution to match the $PM_{2.5}$ magnitude and spatial variation in the 2008-2012 $Mean_{sat}$. This downscaled simulation (referred to as Sim_{ds}) does not modify the modeled fraction or the simulated relative temporal variation of $PM_{2.5}$ composition, since we apply to all years the same scale factors (namely, the $0.1^\circ \times 0.1^\circ$ spatial map of ratios in the 2008-2012 mean of $Mean_{sat}$ versus the simulation). Table 4-S3 contains a comparison of annual $PM_{2.5}$ from Sim_{ds} versus the global ground-based database collected for GBD. Globally and regionally, fine-scale information from $Mean_{sat}$ improves the spatial representation of $PM_{2.5}$ in Sim_{ds} compared to the pure simulation.

4.3.3 Trend Analysis and Evaluation

We summarize time series as linear trends to aid presentation. Following commonly adopted methods in previous studies (e.g. Tables 4-S1 and 4-S2), we analyze data over a long time period (i.e. over ~10 years) to reduce random errors and to detect systematic trends. In addition to trends over 1989-2013, short-term trends over 2002-2013 are included to summarize more recent trends during the periods of denser in situ observations, and these over 1998-2013 are also calculated to facilitate comparison with $Trend_{sat}$. Details on the trend analysis are contained in the SI.

4.4 Results and Discussion

4.4.1 Emission Trends

Figure 4-S2 shows time series of annual area-weighted mean emissions of major aerosol and precursor species over GBD regions, and Table 4-S5 lists trends in these regional emissions over 1989-2013. Substantial reductions in anthropogenic and total emissions of SO_2, NO_x, OC and BC are found over North America, Asia-Pacific and Europe, whereas increases in these species are substantial over Asia. Reductions are dramatic in SO_2, OC and BC emissions before ~1996, with a transitional slow down afterwards over Central Asia, Central Europe and Eastern Europe (Crippa et al., 2016; Vestreng et al., 2007). SO_2 emissions over East Asia also show a transition from increasing to decreasing at ~2006 (Lu et al., 2011; Wang et al., 2015b). NH_3 emissions generally have increasing or insignificant trends except over Europe where NH_3 emissions decrease. Strong inter-annual variation in OC and BC emissions occurs over biomass burning regions such as Eastern Europe (including Siberia), Southeast Asia, Tropical Latin America and Central Sub−Saharan Africa, and in mineral dust emissions from desert regions.

4.4.2 In Situ Trends

Figure 4-1 shows the spatial distribution over North America of annual trends in $PM_{2.5}$ and its composition from the downscaled simulation (Sim_{ds}), overlaid with observed trends for two periods. The observations show significant ($p < 0.05$) decrease in population-weighted mean (PWM) $PM_{2.5}$ of -0.26 μg $m^{-3}yr^{-1}$ over 1989-2013, increasing in magnitude to -0.44 μg $m^{-3}yr^{-1}$ over 2002-2013, with larger decreases in the east than in the western interior. The collocated Sim_{ds} well reproduces the composite PWM trends within 0.06 μg $m^{-3}yr^{-1}$. Steeper reductions in PWM sulfate, nitrate and ammonium at measurement sites over 2002-2013 than over 1989-2013 are indicated by both the observations and Sim_{ds}, due to inclusion of more urban sites from EPA_CSN as well as stronger emission reductions in recent years (Figure 4-S2). These secondary inorganic aerosols (SIA) largely drive the $PM_{2.5}$ decreases over North America, with significant decreases ($p < 0.05$) in PWM concentration over 1989-2013 in both the observations (-0.31 μg $m^{-3}yr^{-1}$ or -4.3 %/yr) and Sim_{ds} (-0.28 μg $m^{-3}yr^{-1}$ or -4.1 %/yr), and more pronounced decreases over 2002-2013 in

both the observations and Sim_{ds}. The Sim_{ds} shows relatively weaker performance for nitrate trends, similar to recent simulations (Leibensperger et al., 2012; Xing et al., 2015), possibly due to bias in simulated HNO_3 (Heald et al., 2012; Zhang et al., 2012a), uncertainties in NH_3 emissions (Zhu et al., 2013), and non-linear sensitivity of nitrate partitioning to SO_2, NO_x and NH_3 emissions (Holt et al., 2015; Pinder et al., 2008a). The observed and simulated annual decreases in $PM_{2.5}$ and SIA are largely consistent with trends in winter and summer (Figure 4-S3 & 4-S4). Steeper decreases in sulfate and ammonium are observed in summer than in winter, a seasonal variation that is captured by Sim_{ds}, reflecting faster photochemistry in summer that more closely connects emission changes to local concentration changes (Paulot et al., 2017). Meanwhile nitrate generally has higher concentration and stronger absolute decreases in winter when colder temperatures favor its formation (Pinder et al., 2008a).

Observed significant ($p < 0.05$) reductions in PWM OA partially drive the $PM_{2.5}$ trends, and are consistent with the collocated Sim_{ds} (-0.16 vs. -0.11 $\mu g\ m^{-3}yr^{-1}$) over 1989-2013. This reduction in OA reflects different seasonal mechanisms in Sim_{ds}. Over winter (Figure 4-S3), natural OA sources are weak and simulated OA trends are similar to the annual trends, driven by reductions in anthropogenic OC emissions (Figure 4-S2). Over summer (Figure 4-S4), observed decreases in OA over the southeastern US are well represented in Sim_{ds}, due primarily to inclusion of an aqueous formation mechanism of isoprene SOA (Marais et al., 2016), which yields an SOA decrease driven by reductions in sulfate (Marais et al., 2017), consistent with observational evidence (Blanchard et al., 2016; Xu et al., 2015b). Meanwhile over 2002-2013, Sim_{ds} underestimates observed PWM OA trends, driven by weaker wintertime OA trends in the simulation relative to observations (Figure 4-S3), due to increasing anthropogenic wood burning (US EPA, 2015) and OC emissions in the east after 2008.

BC has significant ($p < 0.05$) decreases (-2.5 – -4.3 %/yr) in both the observations and Sim_{ds} because of reductions in BC emission, despite small absolute changes. Finally, weak and mostly insignificant trends in PWM dust and sea salt are observed and simulated.

Figure 4-S5 shows the spatial distribution of trends in sulfate and $PM_{2.5}$ over Europe. Significant ($p < 0.05$) reductions in annual PWM sulfate observed over 1989-2013 (-0.15

μg $m^{-3}yr^{-1}$) and over 2002-2013 (-0.12 μg $m^{-3}yr^{-1}$) are seasonally consistent with Sim_{ds}. The slower sulfate decline and fewer significant trends over 2002-2013 in both the observations and Sim_{ds} reflect slower SO_2 emission reductions (Figure 4-S2), consistent with previous investigations (Tørseth et al., 2012; Turnock et al., 2015). The PWM $PM_{2.5}$ over all sites trend downward at $p < 0.1$ in observations and Sim_{ds} over 2002-2013, driven mostly by sites over western Europe while most eastern sites have insignificant trends. The stronger reductions in observed PWM $PM_{2.5}$ are disproportionately influenced by a single site near the Po Valley of Italy (IT0004R), and the paucity of sites across Europe. Excluding this site reduces the observed annual PWM trends by 75% (-0.15 μg $m^{-3}yr^{-1}$ or -1.4 %/yr), yielding better agreement with the collocated Sim_{ds} (-0.23 μg $m^{-3}yr^{-1}$ or -1.6 %/yr).

Table 4-S6 summarizes the network-composite PWM concentrations and trends between Sim_{ds} and in situ data after spatial and temporal collocation. Observed and simulated PWM trends agree within their 95% confidence intervals (CIs) for 33 of the 35 cases. All components except dust and sea salt have decreasing and significant trends in observations, which are mostly well reproduced by Sim_{ds}. The importance of SIA and OA in driving PWM $PM_{2.5}$ trends over North America is apparent in both observations and Sim_{ds}. The Sim_{ds} underestimates observed OA and its trends in IMPROVE and NAPS, which is an unresolved issue in current CTMs, likely due to missing anthropogenic sources and uncertainties in SOA modeling (Tsigaridis et al., 2014). The Sim_{ds} also underestimates PWM BC, partially due to heterogeneity of BC (Hand et al., 2014b) not resolved in Sim_{ds}. Our estimates of OA and BC contribution to PWM $PM_{2.5}$ and its trends likely represent lower bounds.

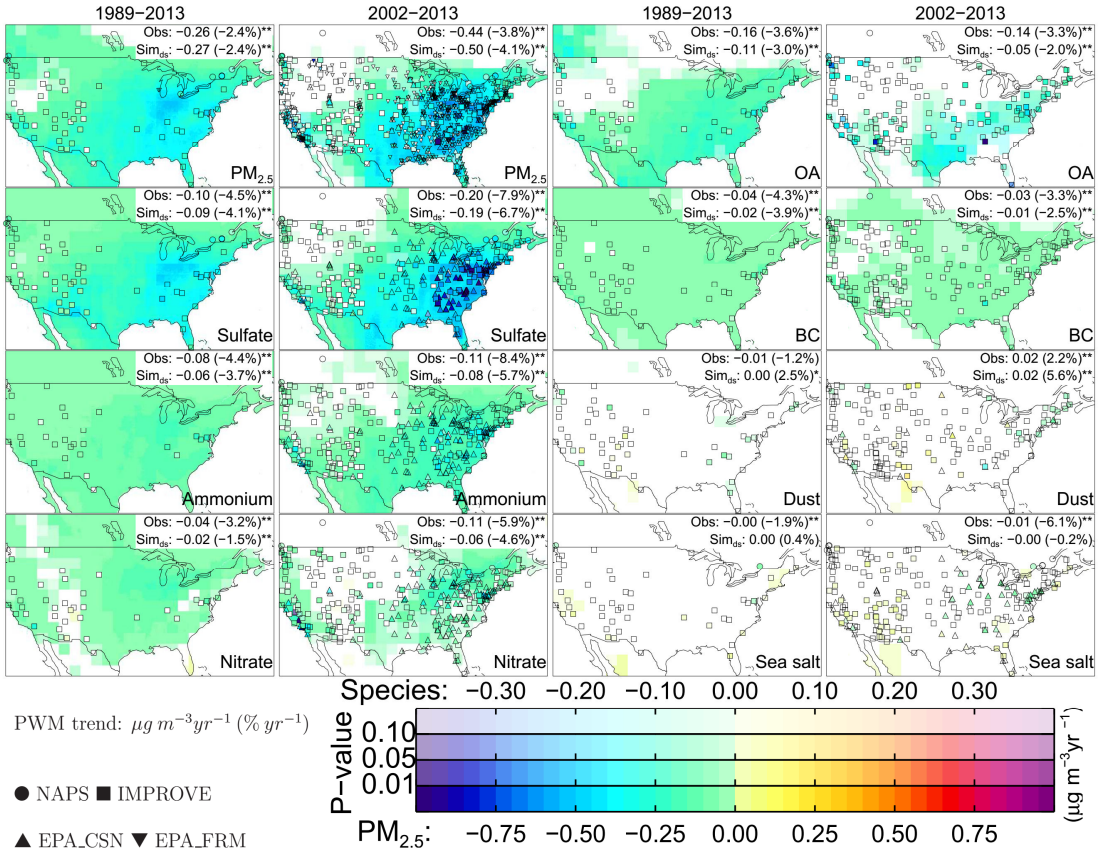

Figure 4-1. Spatial distribution of long-term (1989-2013) and short-term (2002-2013) annual trends in $PM_{2.5}$ and its chemical composition from the downscaled simulation (Sim_{ds}, background) and in situ observations (symbols, with different shapes representing different networks). The significance (i.e. *p* value) of derived trends over land is indicated by the opaqueness of the colors. The color scale of trends for $PM_{2.5}$ (saturated at ± 1.0 μg $m^{-3}yr^{-1}$) and its chemical composition (saturated at ± 0.4 μg $m^{-3}yr^{-1}$) differ. $PM_{2.5}$ is simulated at 35% RH and its individual components are presented without aerosol water, for consistency with observational protocols. Composite trends (in μg $m^{-3}yr^{-1}$, with relative trends in %/yr in brackets) in population-weighted mean concentration from all sites are shown for observations (Obs) and spatiotemporally collocated Sim_{ds}. Trends with >90% significance ($p < 0.1$) are followed by one asterisk (*), and those with >95% significance ($p < 0.05$) are followed by two asterisks (**).

In summary, Sim_{ds} generally well represents observed trends in $PM_{2.5}$ and its composition across North America and Europe, where emissions are relatively well known. We find greater OA influence than in previous GEOS-Chem simulations (Boys et al., 2014; Leibensperger et al., 2012) due to stronger trends in OC emissions (Ridley et al., 2018; Xing et al., 2013), and to an aqueous isoprene SOA mechanism (Marais et al., 2017). The overall consistency of Sim_{ds} with measurements supports its applicability to represent

atmospheric processes to understand the chemical components driving $PM_{2.5}$ trends. We next evaluate the performance of Sim_{ds} where emissions are less well known.

4.4.3 Global Trends in $PM_{2.5}$

Figure 4-S6 shows global $PM_{2.5}$ trends over 1998-2013 in $Trend_{sat}$ and Sim_{ds}. The two datasets exhibit a high degree of consistency in the spatial distribution of trends and significance. Both datasets show significant ($p < 0.1$) increases over eastern Africa, India, China and the Middle East, and decreases over North America, western Africa and Europe. Regional mismatches are found from forest fires over boreal Canada and Russia, with little impact on regional PWM trends due to low population. The spatial distribution of trends from the two datasets are significantly correlated (r = 0.67, slope = 0.75), with even higher correlation (r = 0.85, slope = 0.76) where both datasets suggest significant trends at $p < 0.1$. Both $Trend_{sat}$ and Sim_{ds} show significant ($p < 0.05$) increases in global PWM $PM_{2.5}$ (0.53 vs. 0.37 $\mu g\ m^{-3}yr^{-1}$), with overlapping 95% CIs.

Table 4-S7 lists the annual PWM $PM_{2.5}$ and trends over 21 GBD regions for 1998-2013. The downscaling substantially improves the accuracy of PWM $PM_{2.5}$ over several regions e.g. South Asia, Southern Latin America and Central Asia, where the original simulated PWM $PM_{2.5}$ underestimates the satellite-based estimates by more than a factor of 2. This improvement reinforces the value of bringing together the satellite observations and simulation. The annual trends from $Trend_{sat}$ and Sim_{ds} have overlapping 95% CIs for 20 regions (except Oceania with ~0.1% of global population), and consistency in their significance (at 90% confidence) for the first 15 regions that comprise 91% of the global population. Both datasets also suggest the most pronounced and significant ($p < 0.05$) increases over South Asia (0.97 vs. 0.99 $\mu g\ m^{-3}yr^{-1}$) and East Asia (1.32 vs. 0.86 $\mu g\ m^{-3}yr^{-1}$), in contrast with decreases over High-income North America (-0.31 vs. -0.39 $\mu g\ m^{-3}yr^{-1}$), Western Europe (-0.23 vs. -0.23 $\mu g\ m^{-3}yr^{-1}$) and Central Europe (-0.23 vs. -0.30 $\mu g\ m^{-3}yr^{-1}$). Increases over the densely populated regions of East and South Asia drive increases in global PWM $PM_{2.5}$. Two other developing regions (Southeast Asia and Southern Sub-Saharan Africa) and two arid regions (Eastern Sub-Saharan Africa & North Africa and Middle East) also show significant and consistent increases ($p < 0.1$) in both datasets. This overall agreement in regional PWM trends provides further confidence in the ability of

Sim_{ds} to resolve trends on a global scale. We further extend the analysis of Sim_{ds} to long-term global trends in $PM_{2.5}$ composition in the context of $Trend_{sat}$.

4.4.4 Global Trends in $PM_{2.5}$ Composition

Figure 4-2 shows trends in $PM_{2.5}$ mass and composition from Sim_{ds} over 1989-2013. The spatial pattern of simulated $PM_{2.5}$ trends is similar (r = 0.81) to that over the shorter 1998-2013 period, with a slightly weaker global PWM trend of 0.28 μg $m^{-3}yr^{-1}$, driven by stronger reductions over Europe and weaker increases over Asia in the 1990s. OA makes the largest individual contribution to the increase in global PWM $PM_{2.5}$, with a significant PWM trend of 0.10 μg $m^{-3}yr^{-1}$, driven by substantial increases (> 0.2 μg $m^{-3}yr^{-1}$) over eastern China and India. This is despite substantial decreases (< -0.2 μg $m^{-3}yr^{-1}$) in OA over less populous tropical biomass burning regions driven by trends in the fire inventory (Figure 4-S2). Sulfate and ammonium have similar spatial distribution (r = 0.93) in annual trends, with pronounced increases (> 0.1 μg $m^{-3}yr^{-1}$) over India and China and pronounced decreases (< -0.1 μg $m^{-3}yr^{-1}$) over North America and Europe, driven by trends in regional SO_2 emissions (Figure 4-S2). The global PWM trends in sulfate (0.04 μg $m^{-3}yr^{-1}$) and ammonium (0.03 μg $m^{-3}yr^{-1}$) are also driven by densely populated regions of South and East Asia. The global PWM nitrate trend of 0.05 μg $m^{-3}yr^{-1}$ exhibits the most pronounced increases (> 0.1 μg $m^{-3}yr^{-1}$) over China and northern India, and decreases (< -0.1μg $m^{-3}yr^{-1}$) over the US and Europe. BC trends have similar spatial distribution (r = 0.78) with OA trends, with smaller yet significant contribution (0.02 μg $m^{-3}yr^{-1}$) to global PWM $PM_{2.5}$ trends. Dust trends exhibit a dipole with decreases over the western Sahara (< -0.2 μg $m^{-3}yr^{-1}$) and increases over the eastern Sahara and Arabic Peninsula (> 0.3 μg $m^{-3}yr^{-1}$); its global PWM trend of 0.03 μg $m^{-3}yr^{-1}$ reflects these compensating effects. Sea salt trends are minor and insignificant. Trends in $PM_{2.5}$ composition are similar over the period of satellite observations (Figure 4-S7), with largely consistent global PWM trends albeit smaller areas of significant trends.

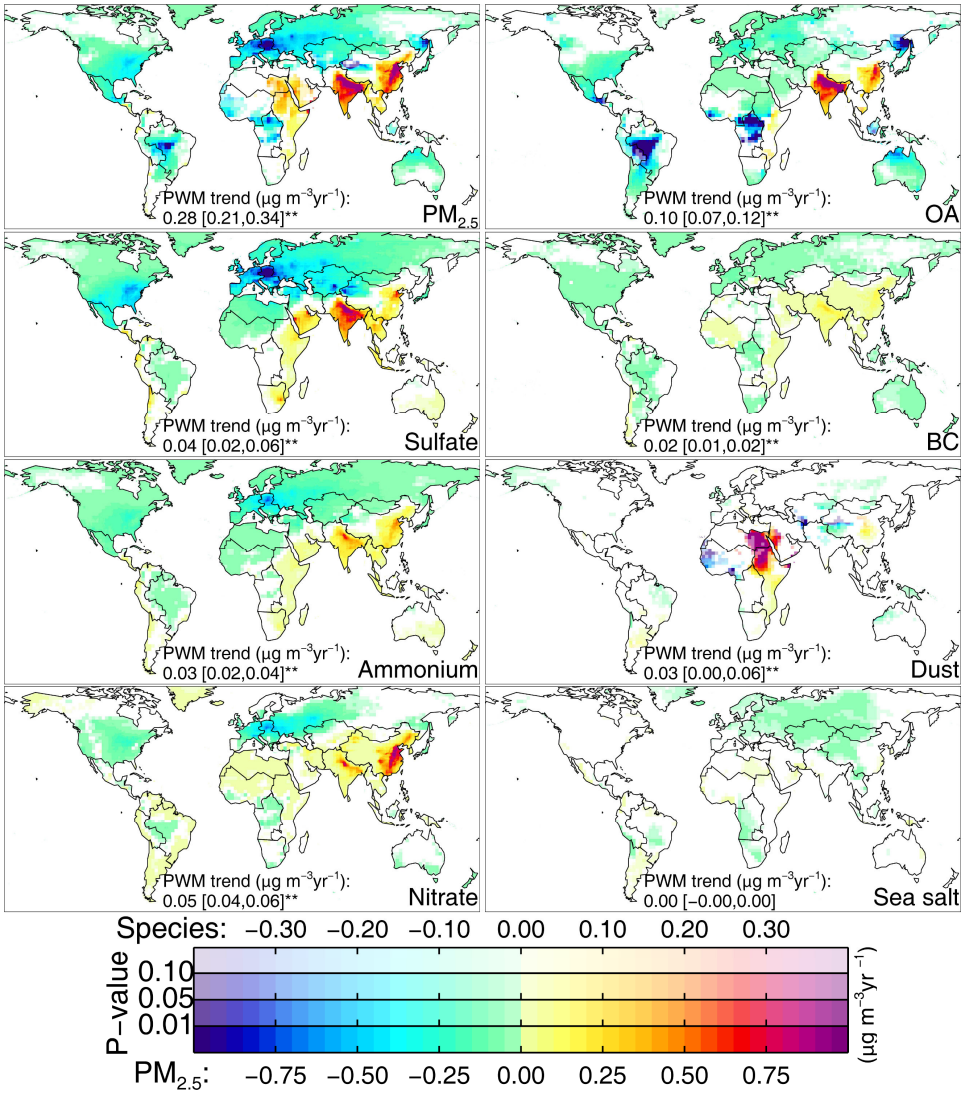

Figure 4-2. Annual trends in global $PM_{2.5}$ and its chemical composition over 1989-2013 from the downscaled simulation. Aerosol water is associated with each chemical component at 35% RH. The significance (i.e. *p* value) of derived trends over land is indicated by the opaqueness of the colors. The color scale of trends for $PM_{2.5}$ (saturated at ± 1.0 μg $m^{-3}yr^{-1}$) and its chemical composition (saturated at ± 0.4 μg $m^{-3}yr^{-1}$) differ. Global population-weighted mean trends (95% confidence intervals in the square brackets) are shown, and trends with >95% significance ($p < 0.05$) are followed by two asterisks (**). Boundaries in the maps correspond to the 21 GBD regions in Figure 4-S1.

Sim_{ds} shows an increase in global PWM $PM_{2.5}$ from 26.7 μg m^{-3} in 1990 to 32.0 μg m^{-3} in 2013, consistent with the GBD 2013 study (26.4 μg m^{-3} in 1990 and 31.8 μg m^{-3} in 2013) (Brauer et al., 2015). These trends are primarily of anthropogenic origin, consistent with recent studies on $PM_{2.5}$ air quality (Boys et al., 2014; Daskalakis et al., 2016; Lelieveld et al., 2015; Silva et al., 2016) and AOD (Chin et al., 2014; Pozzer et al., 2015). SIA and

OA account for 79% of the significant increase in global PWM $PM_{2.5}$ (0.28 μg $m^{-3}yr^{-1}$), and drive PWM $PM_{2.5}$ trends over densely populated regions (North America, Europe and Asia). In contrast, $PM_{2.5}$ trends are driven by OA from open fires over tropical rainforests and by mineral dust over North Africa and the Arabic Peninsula. Reddington et al. (2015) reported recent air quality improvements driven by decreasing OA due to fewer deforestation fires over the Amazon. Boys et al. (2014) attributed the satellite-based $PM_{2.5}$ trends over the Arabic Peninsula to dust. We further examine the regional driving components based on analysis of regional time series in the next section.

4.4.5 Regional Trends in Populated-Weighted Mean $PM_{2.5}$ Composition

Figure 4-3 summarizes annual concentrations and trends in PWM $PM_{2.5}$ and its composition over 21 GBD regions from the downscaled simulation and satellite-based estimates. Below we discuss regional trends over 1989-2013.

4.4.5.1 Densely Populated Regions

The regions of South and East Asia have the largest increases in PWM $PM_{2.5}$, consistent with long-term increases in aerosol loading from satellite AOD (Hsu et al., 2012; Yoon et al., 2014) and visibility observations (Che et al., 2007; Jaswal et al., 2013) (Tables 4-S1 and 4-S2). SIA and OA account for over 90% of these increases. OA is the leading contributor to PWM $PM_{2.5}$ increases over South Asia and the second largest contributor over East Asia. The OA trends over these two regions largely determines its role as the leading contributor to global PWM $PM_{2.5}$ increases.

Over South Asia, OA makes the largest contribution to the annual PWM $PM_{2.5}$ concentration (38%) and trends (43%), consistent with measurements of high OA fractions in $PM_{2.5}$ (Ram et al., 2012; Snider et al., 2016), reflecting the extensive agricultural and biofuel burning in this region. The residential sector, primarily biofuel burning, accounts for the largest (39%) sectoral fraction of energy consumption in India (Lu et al., 2011). Lacey et al. (2017) estimated that eliminating residential solid fuel use in India and Bangladesh could avoid ~60 thousand premature deaths from outdoor $PM_{2.5}$ each year, ~90% of which is associated with OA, illustrating the value of reducing OC emissions across this region (Ram et al., 2012; Venkataraman et al., 2005).

Over East Asia, nitrate has the largest trends, contributing to 35% of the annual increase in PWM $PM_{2.5}$, due to continuously increasing NO_x and NH_3 emissions and to decreasing SO_2 emissions since 2006 (Figure 4-S2). Over 2006-2013, PWM $PM_{2.5}$ in East Asia insignificantly ($p > 0.1$) decreases in $Trend_{sat}$ and Sim_{ds}, despite significantly ($p < 0.05$) increasing nitrate (0.28 μg $m^{-3}yr^{-1}$). This recent reversal of $PM_{2.5}$ trends over China is consistent with other investigations (Ma et al., 2016; Tang et al., 2017) (Tables 4-S1 and 4-S2), and implies the role of nitrate in driving recent and future $PM_{2.5}$ trends over China (Li et al., 2016b; Matsui and Koike, 2016; Wang et al., 2013) after recent reductions in SO_2 and sulfate (Wang et al., 2015b). China has made progress in reducing NO_x emissions after 2011 as observed by satellite observations (de Foy et al., 2016), but reducing nitrate could also benefit from reductions in NH_3 emissions (Backes et al., 2016; Holt et al., 2015; Pinder et al., 2008b; Wang et al., 2013).

Southeast Asia also has significant increases in $PM_{2.5}$ especially over the Mainland (e.g. Figure 4-S6). Sulfate and ammonium drive the PWM $PM_{2.5}$ trends, accounting for over 65% of the simulated PWM $PM_{2.5}$ increase, consistent with the steady increases in fuel consumption (e.g. 275% increase in coal burning from 1990 to 2003), and in SO_2 and NH_3 emissions over this region (Li et al., 2017b; Ohara et al., 2007). OA accounts for 45% of PWM $PM_{2.5}$, revealing the importance of open and residential burning (Cohen et al., 2017b). But OA trends are insignificant due to strong meteorologically driven inter-annual variation of fires (Marlier et al., 2013).

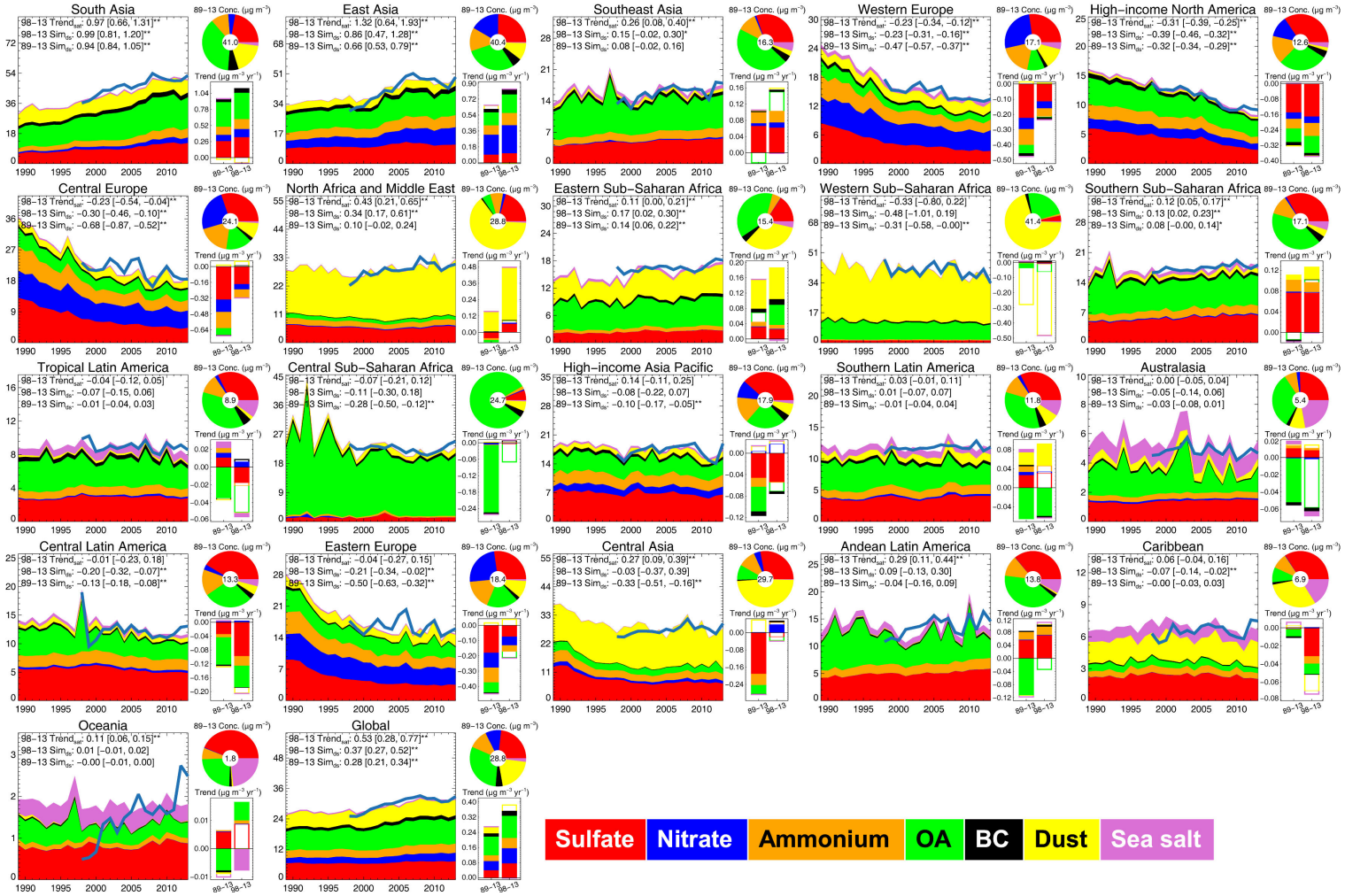

Figure 4-3 (caption on the next page).

Figure 4-3. Regional and global variations in annual population-weighted mean (PWM) $PM_{2.5}$ and its composition in the downscaled simulation (Sim_{ds}), with time series in satellite-based $PM_{2.5}$ estimates ($Trend_{sat}$) shown as thick blue lines. Different colors indicate different chemical composition. Aerosol water is associated with each chemical component at 35% RH. The PWM $PM_{2.5}$ trends (95% confidence intervals in the square brackets) with >90% significance ($p < 0.1$) are followed by one asterisk (*), and those with >95% significance ($p < 0.05$) are followed by two asterisks (**). For each region, the pie chart shows the 1989-2013 mean PWM concentrations in each composition with the mean $PM_{2.5}$ concentrations in the middle, and the two bar plots show the trends of each chemical species over 1989-2013 and 1998-2013, respectively. Statistically significant trends ($p < 0.1$) are presented with filled bars while insignificant trends ($p \geq 0.1$) are indicated by blank bars.

Three populous regions have significant decreases in PWM $PM_{2.5}$ in both the simulation and satellite-based estimates: Western Europe, High-income North America and Central Europe. Over the two European regions, more than 80% of PWM $PM_{2.5}$ trends are explained by SIA, with especially pronounced decreases in the 1990s when SO_2 emissions decreased more rapidly (Figure 4-S2). Nitrate is a prominent component over Europe that comprises over 25% of PWM $PM_{2.5}$ concentrations. Simulations and observations also indicate that the nitrate contribution to particle mass over Europe usually is similar to sulfate except during summer (Putaud et al., 2010; Schaap et al., 2004; Xing et al., 2015). Simultaneous reductions in NO_x and NH_3 emissions (Figure 4-S2) yield a pronounced nitrate decrease, accounting for 15-19% of PWM $PM_{2.5}$ trends. Over High-income North America, the driving roles of sulfate and OA, accounting for 69% of PWM $PM_{2.5}$ decreases, are consistent with our previous discussions based on in situ data, and with an extensive body of literature (Table 4-S1).

For these 6 populated regions, $PM_{2.5}$ chemical components generally exhibit consistent contributions to PWM $PM_{2.5}$ trends in all seasons due to seasonally consistent emission changes (Figure 4-S8 – 4-S11). Dust invasion in spring and summer to South Asia, and in spring to East Asia results in seasonal enhancements in the dust fraction in PWM $PM_{2.5}$ concentration, but makes insignificant contribution to its trends. East Asia has higher PWM $PM_{2.5}$ and OA concentrations and increases in winter with intensive coal and wood burning for domestic heating, and in fall with enhanced agricultural burning (Zhang et al., 2008; Zhang et al., 2012b). Europe has the highest PWM $PM_{2.5}$ in winter driven by higher nitrate. North America has higher $PM_{2.5}$ in summer associated with OA and sulfate.

4.4.5.2 Arid Regions

Trends in SIA and OA are weak or variable over the two largest desert regions (North Africa and Middle East, and Western Sub-Saharan Africa), where dust explains most of the annual PWM $PM_{2.5}$ concentrations (> 65%) and trends (> 75%). The opposite regional trends and significance levels are well captured by Sim_{ds} over 1998-2013, and are consistent with prior trend analysis of dust (Ganor et al., 2010; Shao et al., 2013) and AOD (Klingmüller et al., 2016; Ridley et al., 2014) over these two regions (Table 4-S2). Over Eastern Sub-Saharan Africa, dust remains dominant but its importance is less pronounced (accounting for 33% of PWM $PM_{2.5}$ and 57% of its increase) due to steady increases in SIA, OA and BC associated with anthropogenic emissions (Figure 4-S2). Over Southern Sub-Saharan Africa with weaker dust emissions and stronger increases in anthropogenic emissions, the dust contribution is negligible compared to the driving role of ammoniated sulfate.

Dust exhibits strong meteorologically driven inter-annual variation and seasonality, thus its trends exhibit varying significance levels and contributions to PWM $PM_{2.5}$ trends in different periods and seasons over these 4 regions (Figure 4-S8 – 4-S11). For example, the simulation indicates highest dust intensity in winter and lowest in summer over Eastern Sub-Saharan Africa, where dust is the dominant driver of PWM $PM_{2.5}$ increases in winter, while OA becomes the leading contributor in summer.

4.4.5.3 Tropical Biomass Burning Regions

PWM $PM_{2.5}$ changes over Tropical Latin America and Central Sub-Saharan Africa are driven by OA from biogenic sources and biomass burning. Insignificantly ($p > 0.1$) decreasing PWM $PM_{2.5}$ in the satellite-based estimates over 1998-2013 are reproduced by the simulation, consistent with recent decreases in AOD (Bevan et al., 2009; Reddington et al., 2015) (Table 4-S2) and burning intensities (Andela and van der Werf, 2014; Giglio et al., 2013; Reddington et al., 2015) over these regions. Similar to the desert regions, strong inter-annual variation of fire intensity (Duncan et al., 2003; Giglio et al., 2013) leads to variable tendencies in different periods in PWM $PM_{2.5}$ and OA over these two regions. Trends in OA and $PM_{2.5}$ over 1989-2013 are more uncertain for regions with $PM_{2.5}$

dominated by open fire sources, due to weaker constraints on fire emissions from satellite observations in early years (1989-1996) (Schultz et al., 2008). The PWM $PM_{2.5}$ trends are solely driven by OA over Central Sub-Saharan Africa for all seasons, while SIA plays the dominant role over Tropical Latin America in winter (Figure 4-S8) and spring (Figure 4-S9) when the intensity of burning is low.

4.4.5.4 Other Regions

Insignificant PWM $PM_{2.5}$ trends are consistently indicated by both the satellite-based estimates and the simulation over High-income Asia Pacific, Southern Latin America and Australasia. Increasing pollutant transport from China (Aikawa et al., 2010; Itahashi et al., 2012; Li et al., 2016a) compensates for the effects of decreasing local emissions (Figure 4-S2) and partially explains the insignificant trends over High-income Asia Pacific in recent years. Over the two small dust source regions in the Southern Hemisphere, Sim_{ds} attributes the insignificant trends in PWM $PM_{2.5}$ to counteracting effects of different components, i.e. increasing SIA and dust in Southern Latin America and increasing SIA in Australasia counteracts decreasing OA driven by recent decreases in open burning (Giglio et al., 2013; Shao et al., 2013).

The remaining 6 regions, containing 9% of the global population, exhibit less consistency in the magnitude and significance (at $p < 0.1$) of PWM $PM_{2.5}$ trends in $Trend_{sat}$ and Sim_{ds}. Over Central Latin America and Eastern Europe, mismatches in certain years (e.g. 1999-2000 over Central Latin America and 2005-2006 over Eastern Europe) are partially explained by uncertainties in open fire inventories. Over Central Asia and Andean Latin America, the satellite-based estimates suggest significant increases ($p < 0.05$) in PWM $PM_{2.5}$ over 1998-2013, consistent with significant SIA increases in the simulation over both regions. Meanwhile the simulation has insignificant trends in total PWM $PM_{2.5}$ due to compensating effects of other components (e.g. dust over Central Asia and OA over Andean Latin America). The Caribbean and Oceania have strong influences from external transport in Sim_{ds}. For example, the high dust fraction (31%) in annual PWM $PM_{2.5}$ over the Caribbean reflects transport from the western African coast in spring and summer (Prospero and Lamb, 2003; Ridley et al., 2014).

4.4.5.5 Contrasts with Area-Weighted Trends

Many long-term analyses of regional aerosol composition have focused on area-weighted mean (AWM) or multi-station mean values (Chin et al., 2014; Hand et al., 2012b; US EPA, 2016; Turnock et al., 2015; Xing et al., 2015). We find significantly different concentrations and trends in PWM (Figure 4-3) and AWM (Figure 4-S12) $PM_{2.5}$ composition over the 21 GBD regions. Over populated regions, all PWM trends exceed AWM trends, since higher $PM_{2.5}$ concentrations generally coexist with higher population densities. For example, PWM $PM_{2.5}$ concentrations and trends are about twice those of AWM $PM_{2.5}$ over High-income North America and Eastern Europe. Similarly, SIA generally has higher contributions to PWM $PM_{2.5}$ and trends than in the AWM case over most regions. In contrast, the contribution of natural dust to PWM $PM_{2.5}$ concentration is smaller than in the AWM case, especially over regions with both broad desert and populated cities (e.g. Australasia and the African arid regions), because the dustiest regions generally have lower population density. Similarly, the contributions of OA to PWM $PM_{2.5}$ and its trends are also smaller in the PWM cases than in the AWM cases over biomass burning regions (e.g. Tropical Latin America). The global AWM $PM_{2.5}$ trend of 0.06 $\mu g\ m^{-3}yr^{-1}$ is distinctively weaker than the significant PWM trends of 0.53 $\mu g\ m^{-3}yr^{-1}$ in $Trend_{sat}$. In summary, population weighting yields significant differences from area weighting, with implications for conclusions about the dominant $PM_{2.5}$ components and their contributions to $PM_{2.5}$ trends.

Overall, we found that Sim_{ds} reproduced the significant reductions in PWM concentrations of $PM_{2.5}$ chemical composition across North America and Europe, and exhibited consistency with satellite-based estimates of $PM_{2.5}$ trends. Globally, population weighting, along with updated emission inventories and OA processes contributed to our finding that OA is the leading contributor to the global increase in PWM $PM_{2.5}$ over 1989-2013, followed by nitrate and sulfate. Our analysis also identified regional differences in $PM_{2.5}$ trends and its key drivers, implying the need for ongoing attention to regional variation in emissions and chemistry. Despite the insights from this study, further work is needed in key areas. Finer resolution simulations would better resolve fine-scale and nonlinear processes affecting $PM_{2.5}$ production and loss. Outstanding issues in current CTMs e.g. underestimation of OA (Tsigaridis et al., 2014), uncertainties in inter-annual

variation in open fire emissions, and regional biases in dust (Ridley et al., 2016) and nitrate (Heald et al., 2012) continue to warrant attention. Ongoing work to reduce uncertainties in emission inventories, especially beyond North America and Europe would further improve the accuracy of trends in $PM_{2.5}$ composition and their contributions to $PM_{2.5}$ trends. Future developments of satellite remote sensing of aerosol properties and accumulation of long-term data in emerging global $PM_{2.5}$ speciation networks (Snider et al., 2016) would offer valuable observational constraints.

4.5 Acknowledgement

This work was supported by the Natural Science and Engineering Research Council of Canada. Chi Li was partially supported by a Killam Predoctoral Scholarship, and an ACEnet Research Fellowship. We acknowledge the Federal Land Manager Environmental Database (http://views.cira.colostate.edu/fed/DataWizard/), the Environment and Climate Change Canada (http://maps-cartes.ec.gc.ca/rnspa-naps/data.aspx?lang=en) and the World Data Centre for Aerosol (http://ebas.nilu.no) for hosting the in situ data. We also thank the developers of the emission inventories and meteorological data used in this study.

4.6 Supporting Information

4.6.1 Description of Compiled Observational Aerosol Trends from Literatures

We collect literature results about observed trends in $PM_{2.5}$ and its chemical composition, as tabulated in Table 4-S1. We focus on results at spatially coherent regional scales, but also include several studies over particular sites. Significant reductions are observed since the early 1990s for total $PM_{2.5}$, secondary inorganic and carbonaceous aerosols over the US, Canada and Europe, as summarized in Table 4-S1. Outside these regions, regional trends derived from satellite aerosol optical depth (AOD) reveal persistent increases in $PM_{2.5}$ over South Asia and the Middle East. Over China, a transition from increase to decrease is reported around 2006-2008.

We also include studies on long-term trends in other indirect observations, e.g. satellite- and ground-based aerosol optical depth (AOD) and horizontal visibility, to evaluate our trend results outside North America and Europe. Table 4-S2 indicates persistent increasing trends in these $PM_{2.5}$ proxies over India and Middle East and decreases over Western Africa. Over China, the transition from increasing aerosol loading to decreases at around ~2007 is further supported. Trends in aerosols over Australia are affected by large inter-annual variation in biomass burning and/or dust. Over Brazil, an overall decreasing trend since late 1990s is suggested, with a temporary increase due to fires during 2001-2005.

4.6.2 Description of In Situ and Complementary Data

In this study, employed in situ measurements in densely populated areas of North America include $PM_{2.5}$ data from the US EPA based on the federal reference method (EPA_FRM) and the chemical speciation network (EPA_CSN), as well as the National Air Pollution Surveillance program over Canada (NAPS). Networks designed to represent the regional background include the US IMPROVE and the European EMEP. These datasets have been extensively described and evaluated (Dabek-Zlotorzynska et al., 2011; Hand et al., 2012a; Tørseth et al., 2012). We do not use the organic carbon (OC) and black carbon (BC) data from EPA_CSN due to a protocol change of carbonaceous aerosol measurements during 2007-2010 (Hand et al., 2012a; Hand et al., 2014b). From EMEP, we only use

sulfate and filter-based gravimetric $PM_{2.5}$ data due to the scarcity (< 5) of long-term sites and variations in protocols (Tørseth et al., 2012) for other components. NAPS data of ammonium and nitrate before 2003 are not used due to concerns about volatilization losses (Brook et al., 1999; Dabek-Zlotorzynska et al., 2011). We also avoid the IMPROVE sulfate data before April 1989 and nitrate data between 1996-2000 due to concerns about data quality (http://vista.cira.colostate.edu/IMPROVE/data/QA_QC/Advisory.htm). All the data are screened based on available data quality flags, and averaged monthly provided at least 4 qualified observations are available for a month.

To examine modeled $PM_{2.5}$ concentration over broader areas, we also make use of global annual mean $PM_{2.5}$ database (2008-2013) from surface monitors, collected for the Global Burden of Disease (GBD) (Brauer et al., 2015). Annual mean $PM_{2.5}$ from the original and downscaled simulation are collocated with each record in the database. Statistics are calculated globally and for several regions with sufficient collocation pairs (Table 4-S3).

We use gridded population estimates from the Socioeconomic Data and Applications Center (SEDAC, version 4, regridded to $0.1^\circ \times 0.1^\circ$) to calculate population-weighted mean (PWM) $PM_{2.5}$ for Global Burden of Disease Study (GBD) regions (Figure 4-S1). We estimate population for each year using linear interpolation from the original data that provides population estimates in 5-year intervals. The calculated PWM $PM_{2.5}$ composition and trends are similar whether using time-varying or single-year population for all GBD regions. For example, over parts of Asia with strong population growth and domestic migration during urbanization, the PWM $PM_{2.5}$ trends (and 95% confidence interval) in $Trend_{sat}$ based on time-varying population vs. the 2010 population are 1.32 (0.64, 1.93) vs. 1.31 (0.61, 1.86) $\mu g\ m^{-3}yr^{-1}$ over East Asia and 0.97 (0.66, 1.31) vs. 0.92 (0.61, 1.27) $\mu g\ m^{-3}yr^{-1}$ over South Asia. This weak sensitivity of PWM trends to population change is consistent with prior findings for $PM_{2.5}$ (van Donkelaar et al., 2015) and NO_2 (Geddes et al., 2016). We show results with time-varying population.

4.6.3 Description of GEOS-Chem Simulation

GEOS-Chem treats fully coupled tropospheric oxidant–aerosol chemistry (Bey et al., 2001; Park et al., 2004), including black carbon (Park et al., 2003; Wang et al., 2011; Wang et al., 2014a), mineral dust (Duncan Fairlie et al., 2007; Zhang et al., 2013), sea salt (Jaeglé et al., 2011), the sulfate–nitrate–ammonium system (Park et al., 2004), as well as primary (Pye and Seinfeld, 2010) and secondary (Pye et al., 2010) organic aerosols (OA). We update the original semi-volatile partitioning of secondary OA (SOA) formed from isoprene with the irreversible aqueous uptake scheme in Marais et al. (2016) The local ratio between OA and OC mass (OM/OC) in the model and in situ measurements varies spatiotemporally based on conventional literature values of 1.4 for primary OA, and 2.3 for oxidized OA (Canagaratna et al., 2015; Philip et al., 2014a; Turpin and Lim, 2001). We include recent updates in dry (Fisher et al., 2011) and wet (Liu et al., 2001; Wang et al., 2011; Wang et al., 2014a) deposition. The ISORROPIA II thermodynamic module (Fountoukis and Nenes, 2007) performs aerosol–gas partitioning as implemented by Pye et al. (2009) Aerosol uptake of N_2O_5 is given by Evans and Jacob (2005). HNO_3 concentrations are reduced following Heald et al. (2012) for better consistency with observations. Aerosol optics affect photolysis rates as described by Martin et al. (2003b) with updates on aerosol size distribution (Drury et al., 2010), dust optics (Ridley et al., 2012) and brown carbon (Hammer et al., 2016). For consistency with common measurement protocols, simulated $PM_{2.5}$ is at 35% relative humidity (RH), except for comparison with EMEP observations where $PM_{2.5}$ is given at 50% RH to comply with European measurement protocols. Concentrations of simulated $PM_{2.5}$ composition are also reported at 35% RH, except when comparing with measurements where aerosol water is completely excluded.

We conduct simulations at a horizontal resolution of 2˚ × 2.5˚ with 47 vertical levels, driven by assimilated meteorology from the Modern-Era Retrospective analysis for Research and Applications, Version 2 (MERRA-2). This recent reanalysis from the Global Modeling and Assimilation Office offers a consistent assimilation from 1980, including updates in both the Goddard Earth Observing System Model and the assimilation system (Molod et al., 2015). We include a non-local boundary layer mixing scheme (Lin and McElroy, 2010). We follow the recommendations of Philip et al. (2016) to use a chemical

and transport operator duration of 20 min and 10 min, respectively, for computationally efficient operator splitting. We spin up the model for 1 month before each simulation to remove the effects of initial conditions.

4.6.4 Description of Historical Emissions

Emissions are handled in GEOS-Chem via the HEMCO module (Keller et al., 2014). We use the GEOS-Chem default emission inventories for lightning (Murray et al., 2012; Price and Rind, 1992), biogenic (Guenther et al., 2012; Hu et al., 2015; Tai et al., 2013), soil NO_x (Hudman et al., 2012), volcano (Fisher et al., 2011), dust (Duncan Fairlie et al., 2007; Zhang et al., 2013), sea spray (Jaeglé et al., 2011), aircraft (Stettler et al., 2011) and ship (Lee et al., 2011) sources.

Global anthropogenic emissions are based on EDGAR v4.3.1 (Crippa et al., 2016) except for speciated volatile organic compounds (VOCs) which are from RETRO (Schultz, 2007). These global inventories are overwritten with regional inventories as summarized in Table 4-S4. None of these inventories cover exactly the simulation period, thus we also collect available information to scale emissions to each year (Table 4-S4, Column 4). The global scale factors are from EDGAR v4.3.1, with available regional information over the US, Canada, Europe and Asia. The original emission summaries from the NEI (US) and APEI (Canada) do not provide BC or OC emissions. We apply the sector-specific OC to $PM_{2.5}$ emission ratios based on data in the EPA SPECIATE database (Reff et al., 2009) to calculate OC emission trends from the available primary $PM_{2.5}$ emissions over the US and Canada, following the approach in Ridley et al. (2018) for the US. Since most estimates of emission sources over the US use thermal optical methods to estimate BC as elemental carbon (EC), we use the EC to $PM_{2.5}$ emission ratio in SPECIATE to infer annual variations in BC emissions.

The default open fire emissions are from GFED-4 (Giglio et al., 2013), covering the years 1997-2014. For the prior years of 1989-1996, we apply the annual variation from the RETRO fire emission inventory (Schultz et al., 2008) while preserving the seasonality in GFED-4. For each grid cell, each emission species and each month, we scale RETRO

emissions to match GFED-4 for the overlapping years 1997-2000. We fill RETRO grids without emissions with climatological mean monthly GFED-4 data over 1997-2000.

4.6.5 Description of Trend Analysis and Evaluation

Linear trend slopes and significance levels are calculated from annual or seasonal mean time series, based on the Theil-Sen slope (Sen, 1968) and the Mann-Kendall test (Mann, 1945). Relative trends are expressed as normalized to the multi-year mean. We focus on annual trends while also provide information on seasonal trends for additional insight. Following Li et al. (2016a), a valid trend requires 2/3 of the total years in the specified period, with each record averaged from at least 6 months per year for annual trends and 2 months per year for seasonal trends. Network- or region- composite PWM trends are calculated by firstly aggregating measurements to $0.1^{\circ} \times 0.1^{\circ}$ grids before population-weighted averaging. We require each site to contain at least 2/3 of total years for each study period, and each annual record to be averaged from at least 75% of the total sites to ensure the spatial and temporal representativeness of the composite time series.

Table 4-S1. Summary of literature results of trends in $PM_{2.5}$ and its chemical composition. Results are based on in situ measurements except for the last 3 studies over China which are based on estimates from satellite aerosol optical depth (AOD). Increasing trends are colored in red and decreases in green. If mentioned in the paper, statistically significant trends are bolded and insignificant trends are slant. Only results in Geng et al. (2017) are based on population-weighted mean concentrations.

City/Region	Trend (No. of sites if available), μg $m^{-3}yr^{-1}$ (%yr^{-1} if absolute trend not available)						Period	Reference
	$PM_{2.5}$	Sulfate	Nitrate	Ammonium	OA	BC		
US (IMPROVE)		**-0.033 (27)**	*-0.003 (27)*			**-0.006 (26)**	1990-2010	(Xing et al., 2015)
US (CASTNET)		**-0.099 (38)**	*-0.006 (38)*	**-0.026 (38)**				
US		**-2.7% (53)**					1990-2010	(Hand et al., 2012b)
US		**-4.6% (157)**					2001-2010	
US					**Negative (total carbon)**		1990-2010	(Hand et al., 2013)
US						-2.2% (50)	1990-2004	(Murphy et al., 2011)
US	**-1.4%**						1990-2015	(US EPA, 2016)
US	-1.8% (406)						1998-2010	(Wang et al., 2012)
US (summer)		**-8.0%**		**-8.5%**			2003-2013	(Silvern et al., 2017)
Southeast US (summer)		**-9.2%**		**-9.1%**				
Eastern US		-2.1% (54)	-1.1% (54)	-1.9% (41)	-1.7% (15)	-2.5% (15)	1990-2009	(Leibensperger et al., 2012)
Southeast US		**-0.21 (8)**	*-0.01 (8)*	**-0.05 (8)**	**-0.17 (8)**		2004-2012	(Saylor et al., 2015) (median trend)
Southeast US	**-0.40 (8)**	**-0.19 (8)**	*-0.01 (8)*	**-0.08 (8)**	**-0.18 (8)**	**-0.05 (8)**	1999-2010	(Blanchard et al., 2013)
Southeast US (IMPROVE, summer)		**-2.8%**			**-1.6%**		1991-2013	(Marais et al., 2017)
Southeast US (SEARCH, summer)		**-4.0%**			**-1.9%**		1998-2013	
Southeast US (IMPROVE, summer)		-4.5%			-1.5%		1992-2013	(Attwood et al., 2014)
Southeast US (SEARCH, summer)		-6.7%			-0.9%		1998-2013	
Canada	**-0.6 (10)**	*-0.05 (10)*					1986-1995	(Brook et al., 1999)
Canada	-0.8% (56)						1995-2009	(Wang et al., 2012)
Europe		**-0.104 (39)**	*-0.008 (12)*	*0.005 (6)*			1990-2010	(Xing et al., 2015)
Europe (winter)		**-0.19**					1978-2009	(Turnock et al., 2015)
Europe (summer)		**-0.17**						

Europe	-0.9% (98)						1998-2009	(Wang et al., 2012)
Europe	**-5.8% (10)**						2006-2013	(Li et al., 2016a)
Europe	**-2.7% (13)**						2000-2009	(Tørseth et al., 2012)
Europe		**-2.8% (30)**					1990-2009	
California, US						-2.5%	1989-2008	(Bahadur et al., 2011)
Los Angeles, US					-0.25	-0.09	1970-2010	(McDonald et al., 2015)
Edmonton, Canada	*−0.05*	***-0.01***	*0.004*	*-0.005*	**-0.14 (OC)**	**-0.15**	2007-2014	(Bari and Kindzierski, 2016)
Montseny, Spain	**-0.65**	**-0.09**	**-0.04**	**-0.06**	**-0.14 (OC)**	*-0.001*	2002-2010	(Cusack et al., 2012)
Po Valley, Italy	**-0.82 (24)**						2006-2014	(Bigi and Ghermandi, 2016) (median trend)
Spain	**-0.30 (9)**						2001–2012	(Querol et al., 2014) (median trend)
Beijing, China	**-3.18**						2005-2013	(Zhang et al., 2015)
Wanqingsha, Guangdong, China (Fall and Winter)	**-8.58**	**-1.72**	**0.79**		**-1.10 (OC)**		2007-2011	(Fu et al., 2014)
Tokyo, Japan	**-5.0% (4)**						2001-2010	(Hara et al., 2013)
Seol, Korea	*-0.55*						2004-2013	(Ahmed et al., 2015)
China	-0.28%						2005-2012	(Geng et al., 2017) (derived from satellite AOD)
China	18.19%						2005-2007	
China	-2.67%						2008-2012	
China	**1.97**						2004-2007	(Ma et al., 2016) (derived from satellite AOD)
China	**-0.46**						2008-2013	
East China	**0.79**						1998-2012	(Boys et al., 2014) (derived from satellite AOD)
India	**0.93**							
Middle East	**0.81**							

Table 4-S2. Summary of literature results of trends in $PM_{2.5}$ proxies over broad regions outside North America and Europe. Trends indicating increasing aerosol loading are colored in red and those representing decreasing aerosols in green. If mentioned in the paper, statistically significant trends are bolded and insignificant trends are slant.

Variable, unit[a]	Trend, unit yr^{-1} ($\%yr^{-1}$ if absolute trend not available)						Period	Reference
	China	India	Western Africa	Middle East	Brazil	Australia		
AOD	**0.004**	**0.006**	*0.005*	**0.009**			1998-2010	(Hsu et al., 2012)
AOD (Multi-sensor)	**1.45-5.66%**	**1.52-4.77%**		**1.63-3.84%**			1998-2010	(Yoon et al., 2014)
AOD (AERONET)	*-1%*	*0.5%*		**2%**	**-10%**	**3%**	1993-2013	(Yoon et al., 2016)
AOD (MODIS&MISR)	**negative**	**positive**		*positive*	*negative*		2001–2014	(Mehta et al., 2016)
AOD		**0.01–0.04**					2000-2010	(Dey and Di Girolamo, 2011)
AOD (ARFINET)[b]		**2.97%**					2001-2012	(Babu et al., 2013)
AOD				**0.014**			2000-2015	(Klingmüller et al., 2016)
AOD	**0.004**						2002-2007	(He et al., 2016)
AOD	*-0.006*						2008-2015	
Local AOD[c]	**0.003**						2001-2007	(Sun and Chen, 2017)
Local AOD	**-0.002**						2008-2015	
AOD (Aug-Nov)					**0.02**		2000-2005	(Koren et al., 2007)
AOD (Aug-Oct)					**-0.026**		2001-2012	(Reddington et al., 2015)
AOD (dry season)					negative		1995-2000	(Bevan et al., 2009)
AOD (dry season)					positive		2000-2005	
AOD			**-0.004**				1980-2006	(Foltz and McPhaden, 2008)
Dust AOD (Dec -Mar)			**-0.003**				1982-2008	(Ridley et al., 2014)
Dust AOD (Apr -Sep)			**-0.005**					
AOD (sun photometer network)						18 of 22 sites insignificant, **negative over tropical northwest**	2000-2015	(Mitchell et al., 2017)
Visibility, km	**-0.21**						1990-2005	(Che et al., 2007)
	1%						1981-2005	

Extinction (b_{ext}) estimated from visibility, km^{-1}	1.5%						2000-2011	(Wang et al., 2012)
AOD estimated from visibility	**0.002**						1990-2005	(Tang et al., 2017)
	-0.007						2006-2010	
	0.002						1996-2009	(Wu et al., 2014)
Annual haze days (days/year)	**0.27**						1961-2012	(Han et al., 2016)
Winter haze days (days/year)	**0.26**						1980-2012	(Yang et al., 2016)
Afternoon good Visibility days		**-0.86%**					1961-2008	(Jaswal et al., 2013)
Morning poor Visibility days		**0.33%**						
Dust estimated from visibility, $\mu g/m^3$			**-1.08**	*0.10*		*0.002*	1984-2012	(Shao et al., 2013)
Dust days (days/yr)				0.27			1958-2006	(Ganor et al., 2010)

a. AOD is unitless, and refers to single-sensor satellite data if not specified.

b. Median trend of 9 stations, among which 8 show significant positive trends

c. Defined as average from AODs below the median value of all valid AODs during one period (e.g. a month), based on the assumption that localized aerosol emissions are persistent on both clear and polluted days.

Table 4-S3. Comparison between annual mean $PM_{2.5}$ from the downscaled and original (in brackets) simulation and from ground monitors collected for the GBD (2008-2013). For comparisons over each region, the number of collocated pairs (N), slope (k) of reduced major axis regression, correlation coefficient (R), and root mean square difference (RMSD, relative to the average of in situ data) are shown.

Region	Direct $PM_{2.5}$ measurements				$PM_{2.5}$ estimated from PM_{10}			
	N	k	R	RMSD	N	k	R	RMSD
Global	1855	0.77 (0.58)	0.91 (0.80)	48% (76%)	2227	1.06 (1.06)	0.81 (0.67)	43% (59%)
North America	793	0.92 (1.27)	0.72 (0.45)	24% (42%)	231	0.57 (0.77)	0.48 (0.19)	47% (69%)
Europe[a]	729	0.85 (0.53)	0.83 (0.62)	25% (43%)	1123	0.82 (0.48)	0.76 (0.55)	28% (43%)
East Asia	99	0.70 (0.65)	0.84 (0.69)	35% (47%)	304	1.33 (1.88)	0.58 (0.36)	31% (50%)
South Asia	18	0.77 (0.15)	0.64 (0.70)	39% (75%)	185	1.16 (0.44)	0.61 (0.38)	59% (54%)
Middle East and Africa[b]	34	0.85 (0.61)	0.64 (0.24)	42% (68%)	135	0.77 (0.25)	0.69 (0.45)	39% (72%)
Other regions	182	0.74 (0.38)	0.73 (0.47)	55% (89%)	249	0.97 (0.71)	0.51 (0.44)	51% (59%)

a. Includes all 3 European GBD regions, where $PM_{2.5}$ is simulated at 50% RH for consistency with protocols, whereas $PM_{2.5}$ at 35% RH is used for other regions.

b. Including GBD regions of Central Asia, North Africa and Middle East and 4 sub-Saharan regions.

Table 4-S4. Summary of anthropogenic emission inventories used in this study.

Region	Inventory (coverage)	Used species	Annual scale factor[a]	Reference
World	EDGAR v4.3.1 (1970-2010)	CO, NO_x, SO_2, NH_3, OC, BC	N/A	(Crippa et al., 2016)
	RETRO (2000)	VOCs	from EDGAR v4.3.1, 1970-2010	(Schultz, 2007)
US	EPA NEI (2011)	CO, NO_x, SO_2, NH_3, OC, BC, VOCs	NEI historical emission, 1990-2014[b]	US Environmental Protection Agency[e]
Canada	CAC (2002-2008)	CO, NO_x, SO_2, NH_3, OC, BC	APEI, 1990-2014[c]	Environment Canada[f]
Mexico	BRAVO (1999)	CO, NO_x, SO_2	from EDGAR v4.3.1, 1970-2010	(Kuhns et al., 2005)
Europe	EMEP (1990-2012)	CO, NO_x, SO_2, NH_3	N/A	Centre on Emission Inventories and Projections[g]
Asia	MIX (2008-2012)	CO, NO_x, SO_2, NH_3, OC, BC, VOCs	CO, NO_x, NH_3, VOCs from EDGAR v4.3.1, SO_2, OC, BC from Lu et al. (2011)	(Li et al., 2017b)

a. Annual scale factors are applied only when the emission inventory lacks data for a certain year. These scale factors are all spatially resolved. Data in the closest available year is used if outside of the available range.

b. https://www.epa.gov/air-emissions-inventories/national-emissions-inventory-nei, state level. NH_3 scale factors are not used due to methodological changes in 2000 (US EPA, 2001) and weak trends in NH_3 emissions during the investigated period (Xing et al., 2013). Annual variation in OC/BC emission is calculated from $PM_{2.5}$ emission based on Reff et al. (2009).

c. http://ec.gc.ca/inrp-npri/donnees-data/ap/index.cfm?lang=En, province level. Annual variation in OC/BC emission is calculated from $PM_{2.5}$ emission based on Reff et al. (2009).

d. http://edgar.jrc.ec.europa.eu/overview.php?v=431

e. https://www.epa.gov/air-emissions-inventories/2011-national-emissions-inventory-nei-data

f. https://www.ec.gc.ca/air/default.asp?lang=En&n=7C43740B-1

g. http://www.ceip.at/webdab-emission-database

Table 4-S5. Summary of relative trends in $PM_{2.5}$ related emissions over 21 GBD regions. Only statistically significant trends with >90% significance ($p < 0.1$) are shown, and trends with >95% significance ($p < 0.05$) are bolded.

Region	Trend (% yr^{-1}, left: total emission; right: anthropogenic emission)										
	SO_2		NO_x		NH_3		OC		BC		Dust[a]
South Asia	**3.4**	**3.4**	**3.0**	**3.0**	**1.3**	**1.4**	**1.6**	**1.7**	**1.9**	**2.0**	**-1.3**
East Asia	**1.2**	**1.2**	**4.3**	**4.3**	**0.4**	**0.5**	**0.8**	**1.1**	**1.3**	**1.3**	
Southeast Asia	**1.3**	**1.8**		**2.8**	**1.0**	**1.6**	-1.4	**0.8**		**1.0**	
Western Europe	**-7.4**	**-7.4**	**-3.1**	**-3.1**	**-1.0**	**-1.1**	**-3.3**	**-3.5**	**-3.7**	**-3.7**	**2.0**
High-income North America	**-4.7**	**-4.8**	**-2.4**	**-2.7**		**0.02**		**-2.2**	**-2.5**	**-3.2**	
Central Europe	**-6.0**	**-6.0**	**-2.2**	**-2.3**	**-1.6**	**-1.8**	**-1.7**	**-1.5**			
North Africa and Middle East	**2.2**	**2.2**	**2.7**	**2.7**	**2.0**	**2.3**			**1.7**	**1.7**	
Eastern Sub-Saharan Africa	**1.1**	**2.6**		**3.8**	**1.5**	**2.8**		**1.9**	**0.6**	**2.7**	**2.1**
Western Sub-Saharan Africa		**1.3**		**3.1**	**1.2**	**2.6**	**-0.9**	**1.5**		**2.4**	**-0.8**
Southern Sub-Saharan Africa	**1.6**	**1.7**	**0.6**	**1.1**	**0.8**	**1.4**	**-0.9**	**0.6**	**-0.9**		
Tropical Latin America	**-1.1**		**-1.5**	**2.0**	**0.7**	**2.1**	**-4.4**	**1.1**	**-3.2**		
Central Sub-Saharan Africa	**-0.7**	**2.6**	**-1.1**	**4.0**	**-0.5**	**2.8**	**-1.2**	**2.3**	**-1.0**	**3.2**	**-3.3**
High-income Asia Pacific	**-4.8**	**-4.8**	**-1.2**	**-1.2**	**-0.4**	**-0.4**	**-4.8**	**-5.5**	**-3.1**	**-3.1**	
Southern Latin America			**1.2**	**1.7**	**1.7**	**2.3**	**-1.2**	**0.9**		**0.9**	
Australasia		**1.0**	**-2.7**	**-0.9**		**2.1**	**-4.1**	**-3.0**	**-4.4**	**-1.9**	
Central Latin America	**-1.8**	**-1.7**	**0.7**	**1.5**	**0.7**	**1.3**	**-2.8**	**-0.6**	**-1.6**	0.2	2.5
Eastern Europe	**-3.6**	**-3.6**	**-1.9**	**-1.8**	**-2.2**	**-3.6**		**-4.5**	**-2.4**	**-1.9**	
Central Asia	**-3.0**	**-3.0**			-0.3			-1.6			
Andean Latin America		**1.3**		**3.2**	**0.8**	**3.0**	**-3.5**		**-2.7**	**1.9**	
Caribbean	**0.7**	**0.8**	**-0.8**		**-0.7**	**-0.6**	**-4.0**	**-4.2**	**-3.8**	**-3.1**	
Oceania	**1.2**	**4.8**	**-2.4**	**3.9**	**-0.9**	**1.7**	**-3.9**	**1.3**	**-3.5**	**1.7**	

a. No anthropogenic dust emission is included in this simulation.

Table 4-S6. Summary of annual network-composite population-weighted mean concentrations and trends in $PM_{2.5}$ and its chemical composition over North America and Europe. The downscaled simulation (Sim_{ds}) is temporally and spatially collocated with each in situ network before comparison. The 4th column (N) indicates the number of collocated grids. The Sim_{ds} $PM_{2.5}$ is given at 35% and 50% RH, to be compared with observations over North America and Europe, respectively, while its composition is in dry mass concentration. Absolute and relative (normalized to the multi-year mean concentration) trends (95% confidence intervals in the square brackets) with >90% significance ($p < 0.1$) are followed by one asterisk (*), and those with >95% significance ($p < 0.05$) are followed by two asterisks (**).

Table 4-S6 (continued, caption in the previous page)

Period	Species	Network	N	Mean (μg m^{-3})		Trend (μg $m^{-3}yr^{-1}$)		Relative trend (% yr^{-1})	
				In situ	Sim_{ds}	In situ	Sim_{ds}	In situ	Sim_{ds}
1989 - 2013	$PM_{2.5}$	IMPROVE	58	12.00	13.90	-0.517 [-0.586, -0.450]**	-0.523 [-0.588, -0.440]**	-4.3 [-4.9, -3.8]**	-3.8 [-4.2, -3.2]**
		NAPS	7	9.68	9.83	-0.199 [-0.264, -0.122]**	-0.269 [-0.319, -0.214]**	-2.1 [-2.7, -1.3]**	-2.7 [-3.2, -2.2]**
	Sulfate	EMEP	46	3.12	3.37	-0.148 [-0.179, -0.099]**	-0.194 [-0.236, -0.151]**	-4.7 [-5.7, -3.2]**	-5.8 [-7.0, -4.5]**
		IMPROVE	58	3.76	3.88	-0.197 [-0.226, -0.163]**	-0.190 [-0.232, -0.161]**	-5.2 [-6.0, -4.3]**	-4.9 [-6.0, -4.1]**
		NAPS	6	2.06	1.71	-0.063 [-0.090, -0.045]**	-0.053 [-0.064, -0.042]**	-3.0 [-4.4, -2.2]**	-3.1 [-3.7, -2.5]**
	Ammonium	IMPROVE	29	1.86	1.68	-0.082 [-0.106, -0.058]**	-0.063 [-0.077, -0.049]**	-4.4 [-5.7, -3.1]**	-3.8 [-4.6, -2.9]**
	Nitrate		38	1.21	1.09	-0.041 [-0.051, -0.026]**	-0.016 [-0.028, -0.006]**	-3.4 [-4.2, -2.2]**	-1.4 [-2.6, -0.5]**
	OA		53	4.32	3.75	-0.156 [-0.199, -0.122]**	-0.111 [-0.140, -0.061]**	-3.6 [-4.6, -2.8]**	-3.0 [-3.7, -1.6]**
	BC		53	0.88	0.49	-0.037 [-0.054, -0.024]**	-0.019 [-0.021, -0.016]**	-4.3 [-6.2, -2.8]**	-3.9 [-4.4, -3.3]**
	Dust		59	0.70	0.18	-0.009 [-0.018, 0.003]	0.004 [-0.002, 0.009]*	-1.2 [-2.5, 0.5]	2.5 [-0.9, 4.9]*
	Sea salt		52	0.16	0.11	-0.002 [-0.008, 0.005]	0.001 [-0.000, 0.002]*	-1.1 [-4.9, 3.1]	0.8 [-0.1, 1.4]*
2002 - 2013	$PM_{2.5}$	EMEP	21	14.7	17.7	-0.596 [-1.198, -0.104]**	-0.269 [-0.626, 0.008]*	-4.1 [-8.1, -0.7]**	-1.5 [-3.5, 0.0]*
		EPA_CSN	151	12.7	12.10	-0.532 [-0.796, -0.302]**	-0.571 [-0.667, -0.440]**	-4.2 [-6.3, -2.4]**	-4.7 [-5.5, -3.6]**
		IMPROVE	154	9.92	11.60	-0.226 [-0.437, -0.012]**	-0.319 [-0.547, -0.144]**	-2.3 [-4.4, -0.1]**	-2.8 [-4.7, -1.2]**
		EPA_FRM	737	11.60	12.10	-0.431 [-0.548, -0.398]**	-0.506 [-0.604, -0.397]**	-3.7 [-4.7, -3.4]**	-4.2 [-5.0, -3.3]**
		NAPS	14	8.81	8.42	-0.221 [-0.418, -0.143]**	-0.199 [-0.299, -0.094]**	-2.5 [-4.7, -1.6]**	-2.4 [-3.5, -1.1]**
	Sulfate	EMEP	49	2.54	2.60	-0.118 [-0.192, -0.064]**	-0.134 [-0.175, -0.085]**	-4.7 [-7.5, -2.5]**	-5.2 [-6.7, -3.3]**
		EPA_CSN	151	2.71	2.98	-0.215 [-0.323, -0.161]**	-0.200 [-0.248, -0.146]**	-7.9 [-11.9, -5.9]**	-6.7 [-8.3, -4.9]**
		IMPROVE	154	2.03	2.90	-0.168 [-0.191, -0.142]**	-0.132 [-0.185, -0.082]**	-8.3 [-9.4, -7.0]**	-4.6 [-6.4, -2.8]**
		NAPS	13	1.70	1.58	-0.117 [-0.158, -0.085]**	-0.109 [-0.174, -0.049]**	-6.9 [-9.3, -5.0]**	-6.9 [-11.0, -3.1]**
	Ammonium	EPA_CSN	150	1.33	1.43	-0.119 [-0.170, -0.085]**	-0.084 [-0.102, -0.073]**	-8.9 [-12.8, -6.4]**	-5.9 [-7.1, -5.1]**
		IMPROVE	153	1.13	1.16	-0.092 [-0.134, -0.048]**	-0.056 [-0.074, -0.041]**	-8.1 [-11.9, -4.2]**	-4.8 [-6.4, -3.5]**
		NAPS	5	0.73	1.01	-0.038 [-0.069, -0.022]**	-0.044 [-0.062, -0.020]**	-5.2 [-9.5, -3.0]**	-4.4 [-6.2, -2.0]**
	Nitrate	EPA_CSN	150	1.88	1.27	-0.101 [-0.128, -0.082]**	-0.057 [-0.089, -0.034]**	-5.4 [-6.8, -4.3]**	-4.5 [-7.0, -2.7]**
		IMPROVE	153	1.52	0.77	-0.084 [-0.136, 0.029]*	-0.038 [-0.067, -0.022]**	-5.5 [-8.9, 1.9]*	-5.0 [-8.7, -2.8]**
		NAPS	5	0.89	1.48	-0.030 [-0.091, 0.006]**	-0.012 [-0.066, 0.014]	-3.3 [-10.2, 0.7]**	-0.8 [-4.4, 1.0]
	OA	IMPROVE	154	4.57	3.01	-0.138 [-0.229, -0.027]**	-0.037 [-0.095, 0.036]	-3.0 [-5.0, -0.6]**	-1.2 [-3.2, 1.2]
		NAPS	5	3.64	2.36	-0.095 [-0.194, -0.010]**	-0.018 [-0.118, 0.054]	-2.6 [-5.3, -0.3]**	-0.8 [-5.0, 2.3]
	BC	IMPROVE	154	0.74	0.52	-0.018 [-0.066, -0.002]**	-0.006 [-0.026, 0.008]	-2.5 [-8.9, -0.2]**	-1.2 [-5.0, 1.5]
		NAPS	5	0.87	0.29	-0.044 [-0.061, -0.032]**	-0.010 [-0.016, -0.005]**	-5.1 [-7.1, -3.6]**	-3.3 [-5.5, -1.6]**
	Dust	EPA_CSN	23	1.09	0.55	0.018 [-0.004, 0.056]	0.009 [-0.015, 0.049]	1.7 [-0.3, 5.1]	1.6 [-2.7, 8.9]
		IMPROVE	154	1.41	0.61	0.011 [-0.057, 0.055]	0.011 [-0.047, 0.047]	0.8 [-4.1, 3.9]	1.9 [-7.8, 7.7]
	Sea salt	EPA_CSN	77	0.12	0.22	-0.008 [-0.014, -0.002]**	0.001 [-0.005, 0.008]	-6.7 [-11.7, -2.0]**	0.4 [-2.5, 3.7]
		IMPROVE	153	0.22	0.30	-0.002 [-0.008, 0.007]	0.005 [-0.013, 0.018]	-0.8 [-3.6, 3.0]	1.8 [-4.3, 5.9]
		NAPS	12	0.16	0.10	-0.001 [-0.008, 0.006]	0.001 [-0.003, 0.004]	-0.9 [-5.3, 3.8]	0.6 [-3.2, 4.2]

Table 4-S7. Regional and global population in 2010, mean and trends in annual population weighted mean (PWM) $PM_{2.5}$ over 1998-2013 from satellite-based estimates ($Trend_{sat}$), the downscaled simulation (Sim_{ds}) and the original simulation (Sim). Trends (95% confidence intervals in the square brackets) with >90% significance ($p < 0.1$) are followed by one asterisk (*), and those with >95% significance ($p < 0.05$) are followed by two asterisks (**). The first 15 regions show consistency in the significance level (at 90% confidence) of trends in both datasets, which are grouped in consistency with Sect 3.4.1-3.4.4 and sorted by population in each group. Regions with significant ($p < 0.1$) trends in $Trend_{sat}$ are bold, and those also with significant ($p < 0.1$) trends in Sim_{ds} are underlined.

Region	Population (Million)	PWM $PM_{2.5}$ ($\mu g\ m^{-3}$)			1998-2013 trend ($\mu g\ m^{-3}yr^{-1}$)		
		$Trend_{sat}$	Sim_{ds}	Sim	$Trend_{sat}$	Sim_{ds}	Sim
South Asia	1607	46.4	45.2	29.1	0.97 [0.66, 1.31]**	0.99 [0.81, 1.20]**	0.62 [0.54, 0.77]**
East Asia	1387	42.5	43.3	49.8	1.32 [0.64, 1.93]**	0.86 [0.47, 1.28]**	0.87 [0.46, 1.31]**
Southeast Asia	614	15.8	16.2	12.9	0.26 [0.08, 0.40]**	0.15 [-0.02, 0.30]*	0.13 [0.01, 0.27]**
Western Europe	417	14.8	14.6	11.2	-0.23 [-0.34, -0.12]**	-0.23 [-0.31, -0.16]**	-0.18 [-0.24, -0.12]**
High-income North America	344	11.2	11.3	10.5	-0.31 [-0.39, -0.25]**	-0.39 [-0.46, -0.32]**	-0.37 [-0.43, -0.29]**
Central Europe	117	21.0	20.3	14.4	-0.23 [-0.54, -0.04]**	-0.30 [-0.46, -0.10]**	-0.21 [-0.33, -0.08]**
North Africa and Middle East	445	28.3	28.9	18.4	0.43 [0.21, 0.65]**	0.34 [0.17, 0.61]**	0.18 [0.09, 0.35]**
Eastern Sub-Saharan Africa	363	16.5	16.0	11.6	0.11 [0.00, 0.21]**	0.17 [0.02, 0.30]**	0.12 [-0.00, 0.22]*
Western Sub-Saharan Africa	339	40.8	40.5	47.0	-0.33 [-0.80, 0.22]	-0.48 [-1.01, 0.19]	-0.55 [-1.13, 0.20]
Southern Sub-Saharan Africa	72	17.4	17.3	9.89	0.12 [0.05, 0.17]**	0.13 [0.02, 0.23]**	0.06 [-0.00, 0.12]*
Tropical Latin America	204	8.99	8.95	6.36	-0.04 [-0.12, 0.05]	-0.07 [-0.15, 0.06]	-0.07 [-0.12, 0.04]
Central Sub-Saharan Africa	98	22.6	22.2	28.1	-0.07 [-0.21, 0.12]	-0.11 [-0.30, 0.18]	-0.23 [-0.47, 0.17]
High-income Asia Pacific	176	17.1	17.3	15.6	0.14 [-0.11, 0.25]	-0.08 [-0.22, 0.07]	-0.07 [-0.20, 0.06]
Southern Latin America	61	11.8	11.9	4.62	0.03 [-0.01, 0.11]	0.01 [-0.07, 0.07]	0.00 [-0.04, 0.03]
Australasia	26	4.83	5.34	3.88	0.00 [-0.05, 0.04]	-0.05 [-0.14, 0.06]	-0.04 [-0.11, 0.06]
Central Latin America	234	12.4	13.0	8.47	-0.01 [-0.23, 0.18]	-0.20 [-0.32, -0.07]**	-0.11 [-0.19, -0.03]**
Eastern Europe	208	16.5	16.0	11.0	-0.04 [-0.27, 0.15]	-0.21 [-0.34, -0.02]**	-0.15 [-0.24, -0.02]**
Central Asia	81	27.3	28.1	11.7	0.27 [0.09, 0.39]**	-0.03 [-0.37, 0.39]	-0.03 [-0.16, 0.11]
Andean Latin America	53	13.6	13.5	5.37	0.29 [0.11, 0.44]**	0.09 [-0.13, 0.30]	0.03 [-0.14, 0.11]
Caribbean	27	6.55	6.98	5.11	0.06 [-0.04, 0.16]	-0.07 [-0.14, -0.02]**	-0.06 [-0.10, -0.01]**
Oceania	7	1.52	1.79	2.83	0.11 [0.06, 0.15]**	0.01 [-0.01, 0.02]	0.03 [-0.01, 0.05]*
Global	6880	29.9	29.9	25.5	0.53 [0.28, 0.77] **	0.37 [0.27, 0.52]**	0.28 [0.18, 0.45]**

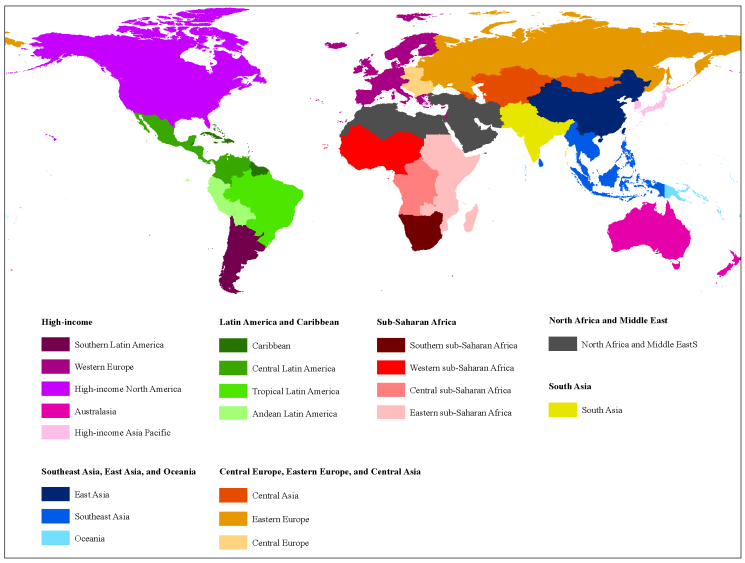

Figure 4-S1. Definition of GBD regions (adapted from http://www.healthdata.org/gbd/faq).

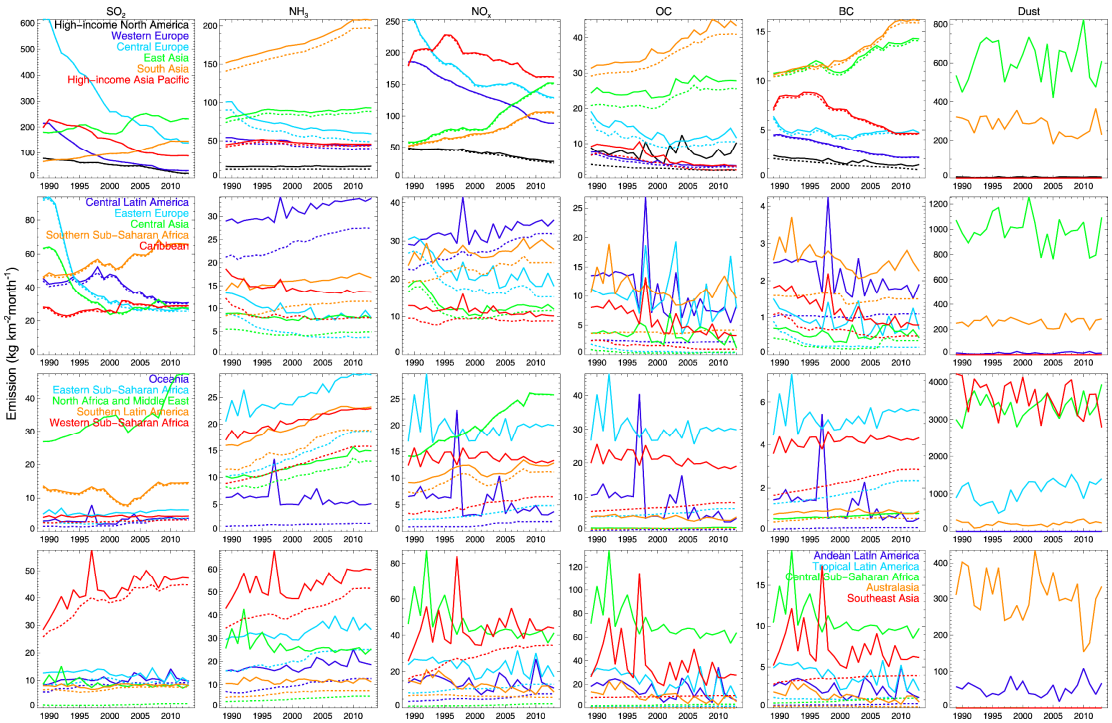

Figure 4-S2. Anthropogenic (dashed) and total (solid) time series of annual mean emission over the 21 GBD regions. Volcanic, ship and aircraft emissions are not included. Different regions are indicated by colors. Regions with similar magnitudes of emissions are grouped for visualization clarity.

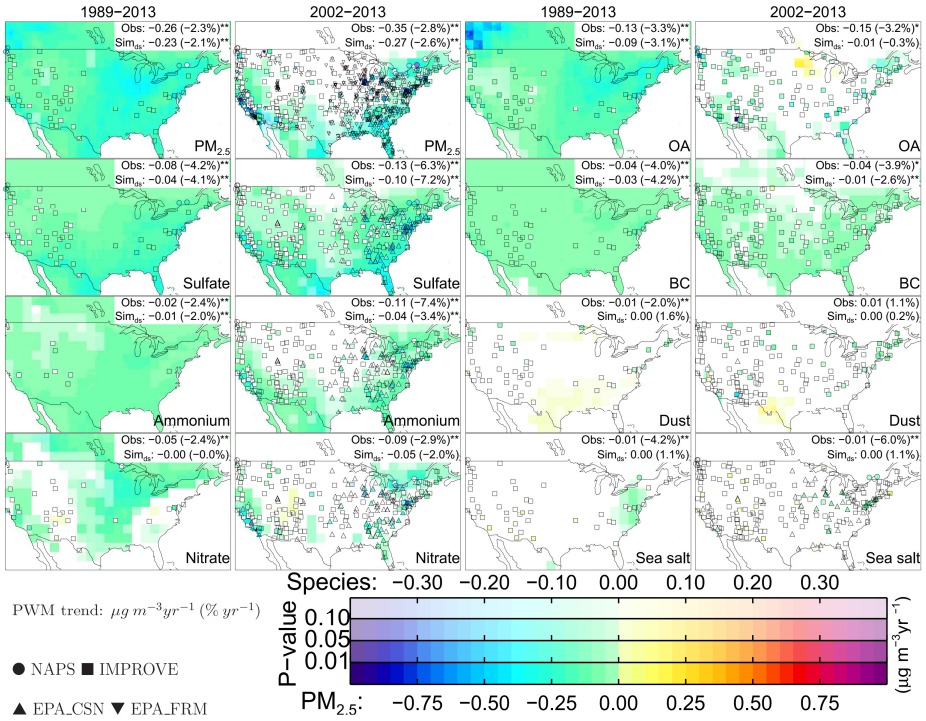

Figure 4-S3. Similar to Figure 4-1 but for wintertime (DJF) trends.

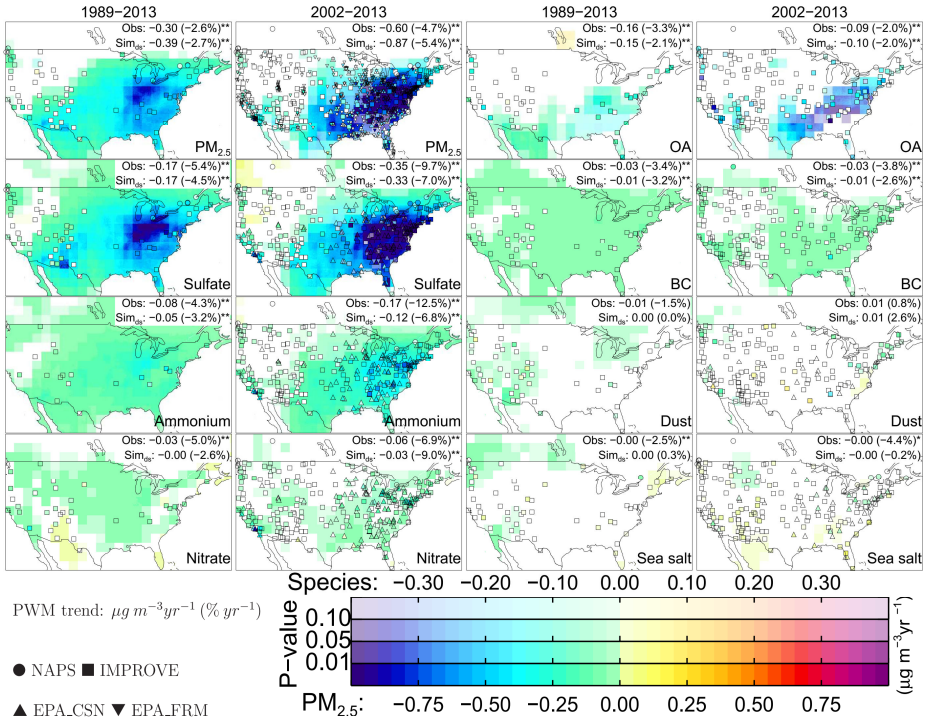

Figure 4-S4. Similar to Figure 4-1 but for summertime (JJA) trends.

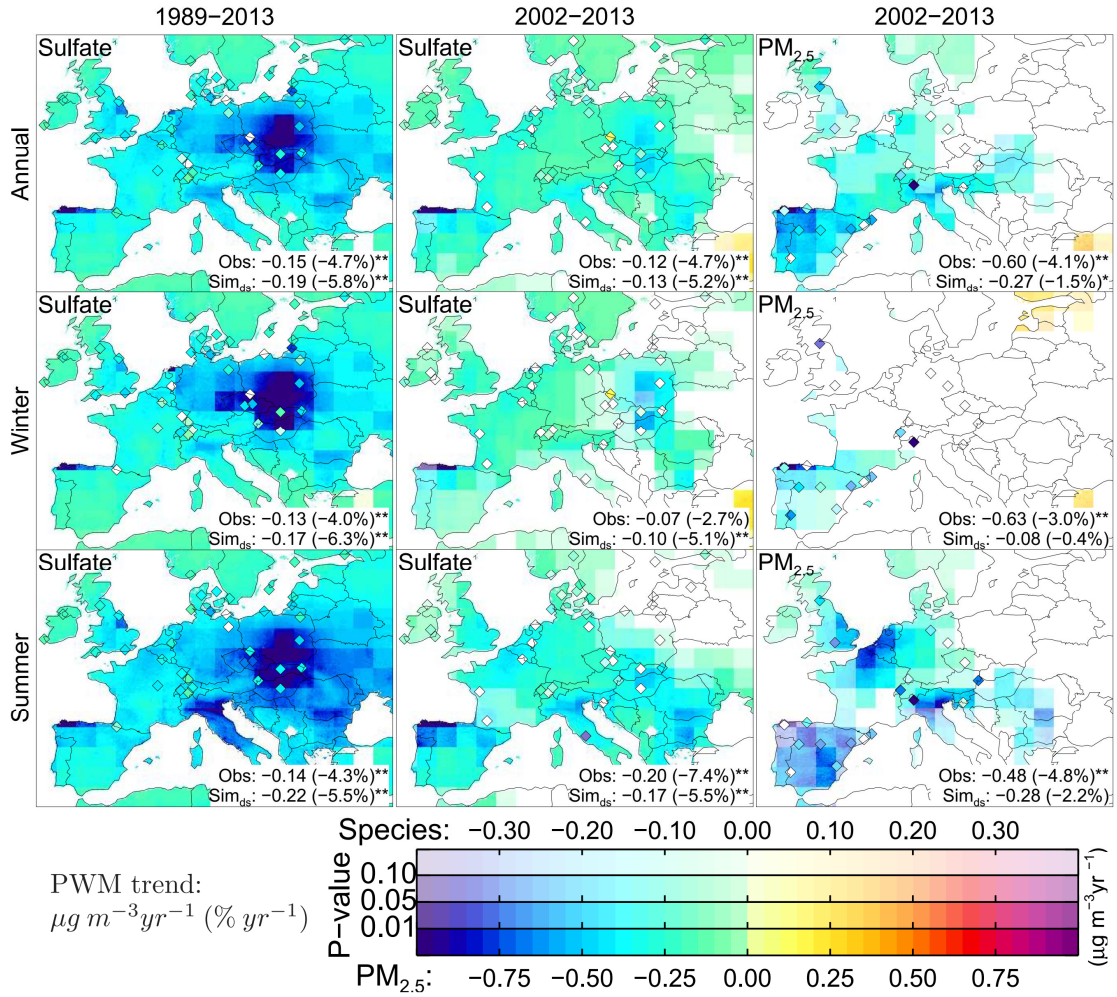

Figure 4-S5. Spatial distribution of long-term (1989-2013) and short-term (2002-2013) annual and seasonal trends in $PM_{2.5}$ and sulfate from the downscaled simulation (Sim_{ds}, background) and EMEP observations (diamond symbols). The significance (i.e. *p* value) of derived trends over land is indicated by the opaqueness of the colors. The color scale of trends for $PM_{2.5}$ (saturated at ±1.0 μg $m^{-3}yr^{-1}$) and its chemical composition (saturated at ±0.4 μg $m^{-3}yr^{-1}$) differ. $PM_{2.5}$ is simulated at 50% RH and sulfate is presented without aerosol water, for consistency with observational protocols. Composite trends (in μg $m^{-3}yr^{-1}$, with relative trends in % yr^{-1} in brackets) in population-weighted mean concentration from all sites are shown for observations (Obs) and spatiotemporally collocated Sim_{ds}. Trends with >90% significance ($p < 0.1$) are followed by one asterisk (*), and those with >95% significance ($p < 0.05$) are followed by two asterisks (**).

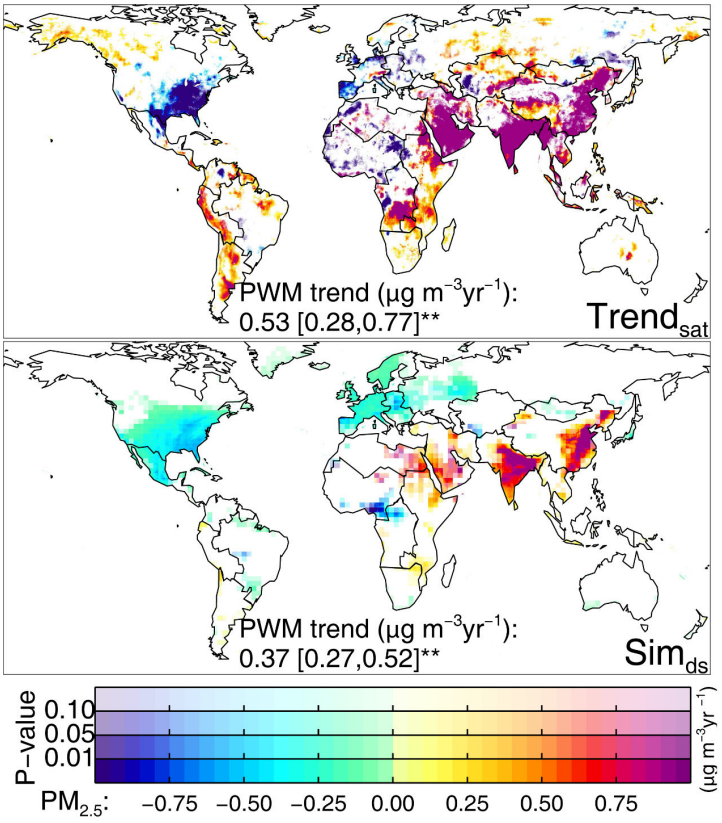

Figure 4-S6. Annual $PM_{2.5}$ trends (at 35% RH) over 1998-2013 from satellite-based estimates (upper) and downscaled simulation (lower). The significance (i.e. *p* value) of derived trends over land is indicated by the opaqueness of the colors. Global population-weighted mean trends (95% confidence intervals in the square brackets) in $PM_{2.5}$ are shown, and trends with >95% significance ($p < 0.05$) are followed by two asterisks (**). Boundaries in the maps correspond to the 21 GBD regions in Figure 4-S1.

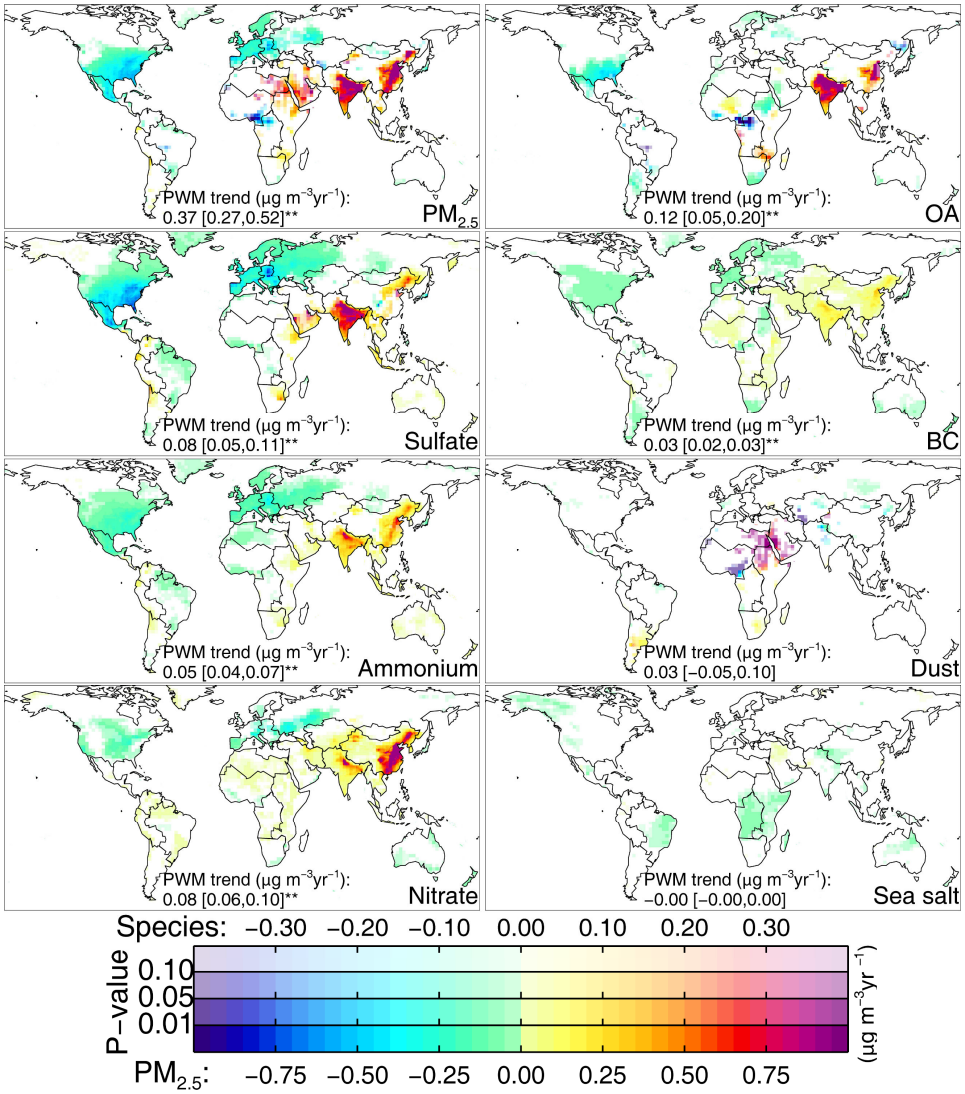

Figure 4-S7. Similar to Figure 4-2 but for annual trends over 1998-2013.

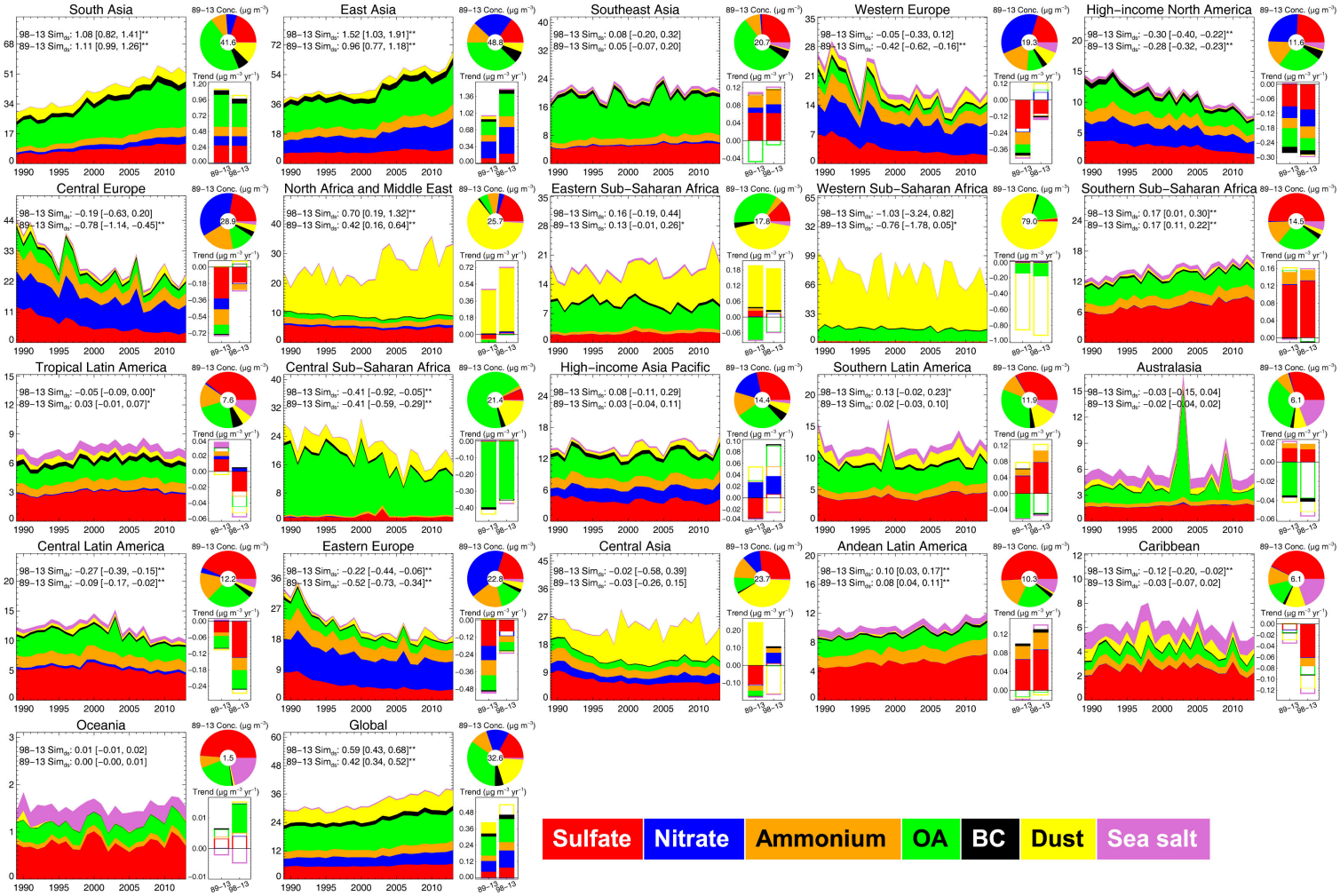

Figure 4-S8. Similar to Figure 4-3 but for analysis of wintertime (DJF).

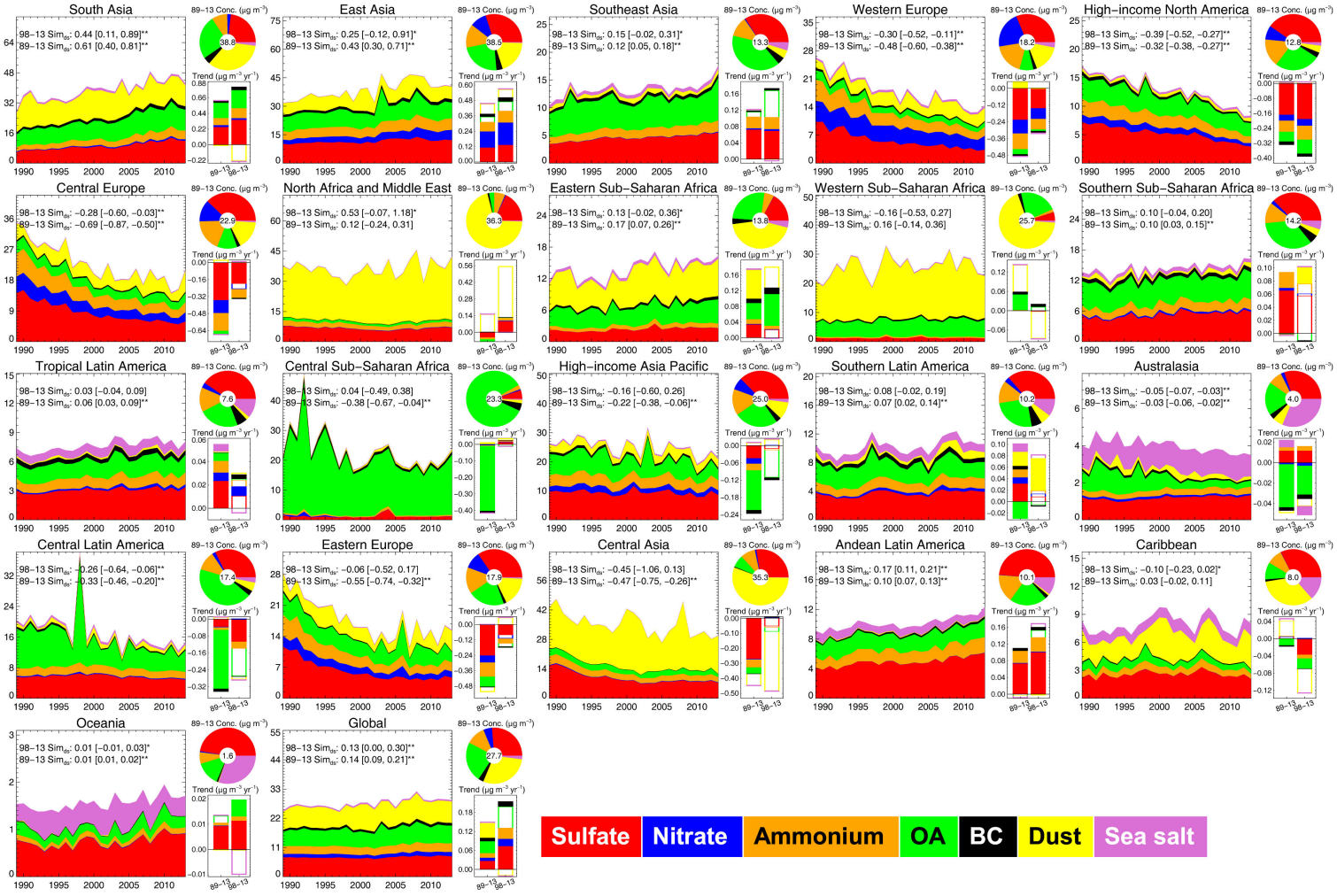

Figure 4-S9. Similar to Figure 4-3 but for analysis of springtime (MAM).

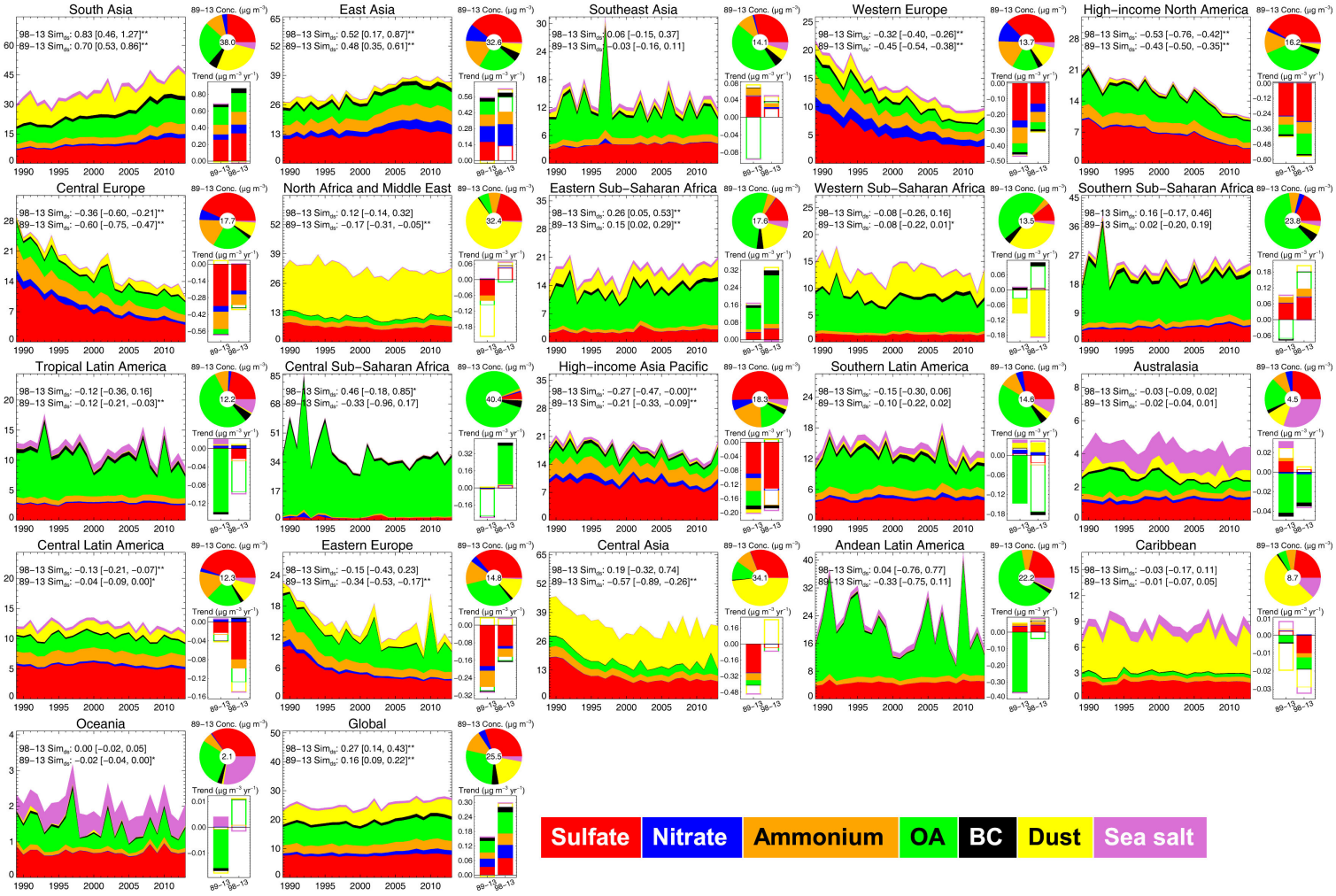

Figure 4-S10. Similar to Figure 4-3 but for analysis of summertime (JJA).

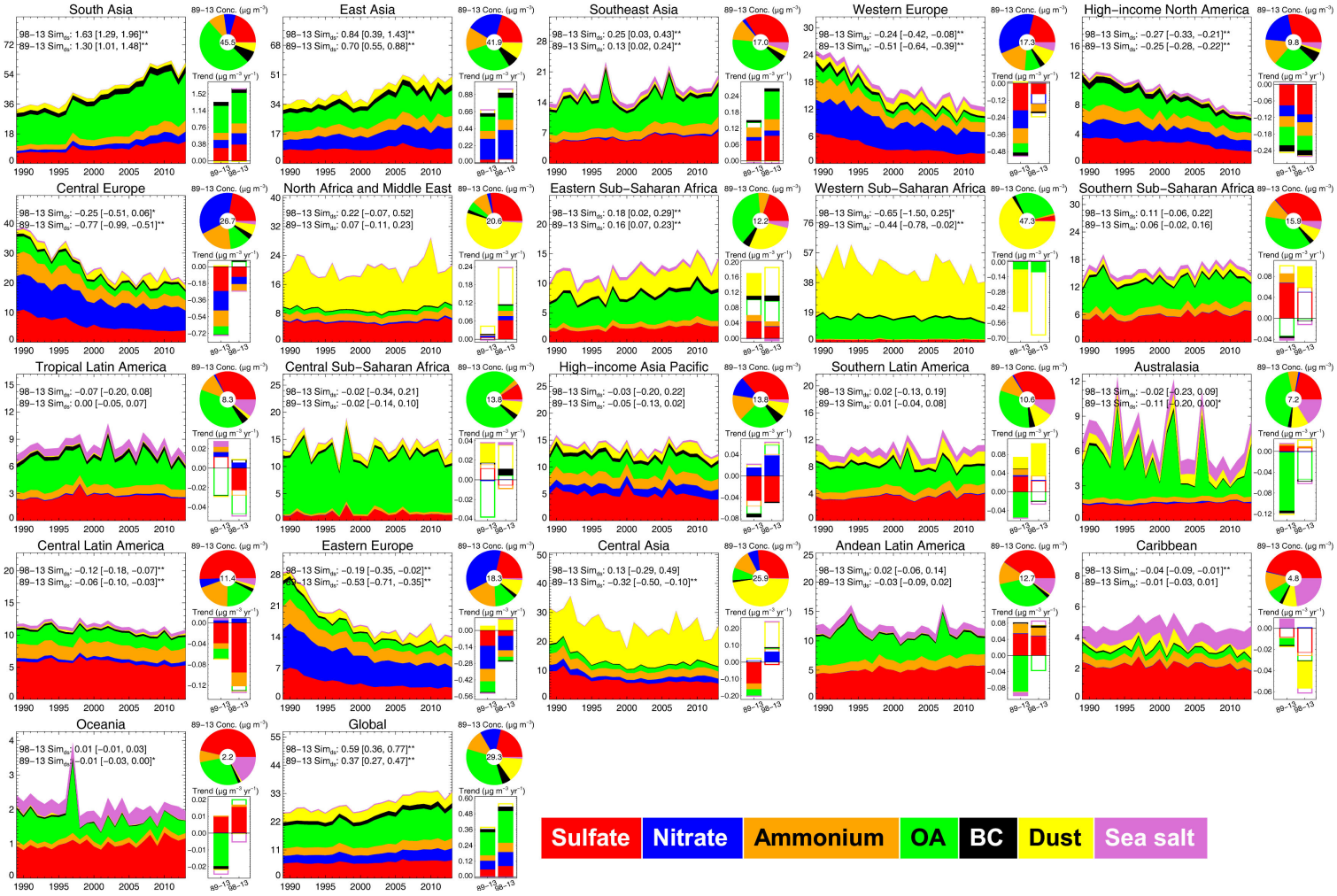

Figure 4-S11. Similar to Figure 4-3 but for analysis of fall time (SON).

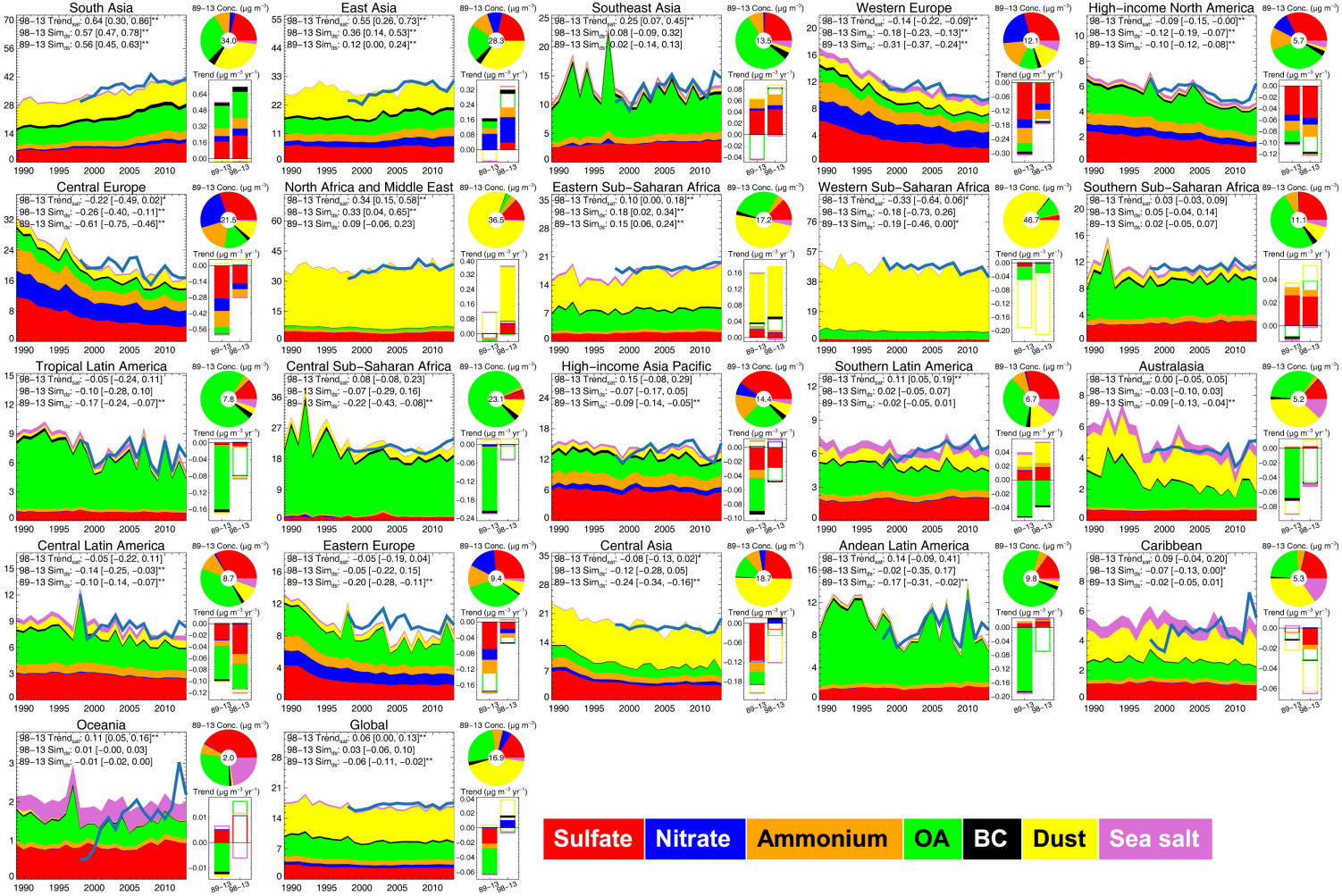

Figure 4-S12. Similar to Figure 4-3 but for analysis of area-weighted mean $PM_{2.5}$ and its composition.

Chapter 5. Assessing the Ability of Iterative Finite Difference Mass Balance and 4D-Var Methods to Retrieve Ammonia Emissions over North America Using Synthetic Cross-track Infrared Sounder Observations

5.1 Abstract

The recent emergence of satellite retrievals of ammonia (NH_3) offers promise to constrain NH_3 emissions. Here we evaluate two inverse modeling methods by conducting inversion experiments using the GEOS-Chem chemical transport model and its adjoint. We simulate pseudo observations of NH_3 column density as observed by the Cross-track Infrared Sounder over North America to test the ability of the iterative finite difference mass balance (IFDMB) and the four-dimensional variational assimilation (4D-Var) methods to recover known NH_3 emissions. Comparing to the more rigorous 4D-Var method, the IFDMB approach requires fewer iterations (~10 vs. ~25) to yield similar or smaller errors (12-17% vs. 17-26%) in the top-down inventories at 2˚ × 2.5˚ resolution, but consistently exhibits larger errors (44-69% vs. 30-45%) at 0.25˚ × 0.31˚ resolution. Analysis of simulated differences in NH_3 columns and in NH_3 emissions suggests stronger misalignments at the finer resolution. Adjoint calculations further indicate that the adjacent grids needed to account for >70% emission contributions to the local columnar NH_3 abundance over an NH_3 source site increase from ~1 at 2˚ × 2.5˚ to ~10 at 0.25˚ × 0.31˚, leading to increased errors in IFDMB. Applying the inversion results from 2˚ × 2.5˚ resolution to update the *a priori* emissions at 0.25˚ × 0.31˚ resolution could improve the accuracy of IFDMB inversions, and reduce the number of iterations needed in the 4D-Var by ~10.

5.2 Introduction

Ammonia (NH_3) is the most abundant alkaline gas in the atmosphere with major implications. Ammonia contributes significantly to atmospheric aerosols and in turn their

associated health effects and radiative forcing (Henze et al., 2012; IPCC, 2013; Lelieveld et al., 2015). NH_3 is critical to the formation of new particles (Croft et al., 2016; Kirkby et al., 2011). NH_3 is the dominant acid-neutralizing component in aerosols, and thus alters aerosol acidity (Guo et al., 2017; Weber et al., 2016) and associated properties (e.g. Holt et al., 2015; Jang et al., 2002; Xu et al., 2015a). Dry and wet deposition of NH_3 and ammonium significantly affect soil properties and vegetation wellness (Fangmeier et al., 1994; Stevens et al., 2004). Quantifying NH_3 sources is a prerequisite for a better understanding of these environmental effects.

Ammonia emissions are complex. The largest contribution to global NH_3 emissions is from the agricultural sector (Bouwman et al., 1997), with emission rates of NH_3 through farming and livestock production that depend on numerous geo-environmental factors that are highly variable in space and time (Huang et al., 2012; Paulot et al., 2014; Zhang et al., 2018b), making "bottom-up" emission estimation challenging. Uncertainties in current bottom-up estimates of NH_3 emission over North America have been attributed as a source of errors in modeled ammonium nitrate aerosols (Heald et al., 2012; Pye et al., 2009; Walker et al., 2012). Recent satellite remote sensing instruments provide unprecedented observations of columnar NH_3 abundance with global coverage (Shephard et al., 2011; Shephard and Cady-Pereira, 2015; Van Damme et al., 2014; Warner et al., 2016; Zhu et al., 2015b). In addition to providing evaluation opportunities, these observations also enable inferring NH_3 emissions using "top-down" inverse modelling approaches (Jacob et al., 2016; McLinden et al., 2016; Streets et al., 2013). Prior to applications to inversions with real data, it is essential to evaluate existing inversion methods using pseudo observations simulated from known emissions.

Several recent studies applied the four-dimensional variational (4D-Var) assimilation approach to constrain NH_3 emissions from satellite observations (Zhang et al., 2018b; Zhu et al., 2013). The 4D-Var method calculates the gradients of a cost function with respect to spatially resolved emissions in a forward model (e.g. a chemical transport model) and adjusts emissions to minimize the cost function based on the calculated gradients. The calculation of the gradients is efficient using the adjoint of the forward model (Henze et al., 2007), where the sensitivities of observations to emissions through processes in the forward model (e.g. transport, chemistry and deposition) are explicitly accounted for. An alternative

and more computationally efficient approach, i.e. the mass balance method (Lamsal et al., 2011; Martin et al., 2003a), simplifies the problem by treating the difference between the concentration from observations and from a forward model as linearly related with local emissions. This assumption may be inappropriate for long-lived species (Jacob et al., 2016; Streets et al., 2013) or finer resolutions (Turner et al., 2012), while these effects might be reduced by iterative processing (Ghude et al., 2013; Zhao and Wang, 2009). Using pseudo observations, a recent study (Cooper et al., 2017) found that for a short-lived species (NO_x), the iterative finite difference mass balance method had similar errors in the emission estimates compared to the 4D-Var approach at coarse (4˚ × 5˚ and 2˚ × 2.5˚) resolutions. However, no prior studies have investigated the mass balance approach for NH_3 emission inversion. Moreover, no comparison of these two methods has been performed at finer resolutions using pseudo observations, even though more recent studies have utilized regional inverse modeling to resolve spatially heterogeneous emissions at resolutions finer than 1˚ (e.g. Cui et al., 2017; Kaiser et al., 2018; Sheng et al., 2018; Turner et al., 2015; Zhang et al., 2018b).

In this study, we evaluate the iterative finite difference mass balance (IFDMB) and the 4D-Var methods using synthetic satellite observations of NH_3 column created from known emissions over North America. We compare the two approaches at coarse (2˚ × 2.5˚) and fine (0.25˚ × 0.3125˚) resolutions to contrast their applicability. Section 5.3 introduces the modeling tools used and inversion methods tested in this study. Comparison of inversion results are presented in Section 5.4, with discussions on the implications for realistic inversions. Conclusions are drawn in Section 5.5.

5.3 Data and Methods

5.3.1 GEOS-Chem and its Adjoint

We use the GEOS-Chem chemical transport model and its adjoint to simulate NH_3 processes and sensitivities to NH_3 emissions. Specifically, we use version 35k of the adjoint model for the 4D-Var inversion, and use the identical forward model to test the mass balance approach to facilitate comparison of these two methods. The forward model

simulates a detailed tropospheric ozone–NO_x–hydrocarbon–aerosol chemistry (Bey et al., 2001; Park et al., 2004). Although bi-directional exchange of NH_3 flux could be significant and affect emission estimates (Wentworth et al., 2014; Zhu et al., 2015a), NH_3 emission is treated as one-way in the current model version. Partitioning of NH_3 gas and ammonium aerosol phases is calculated from the ISORROPIA II thermodynamic module (Fountoukis and Nenes, 2007). Removal of ammonia and ammonium aerosols are through wet (Liu et al., 2001; Wang et al., 2011) and dry (Wesely, 1989; Zhang et al., 2001) deposition. The GEOS-Chem adjoint includes the adjoint calculation of model processes of convection, advection, chemistry, turbulent mixing, wet removal and aerosol thermodynamics (Henze et al., 2007). The calculated sensitivities of modeled observations (e.g. column density) to emissions have been extensively applied to inverse modeling of aerosol sources (e.g. Paulot et al., 2014; Qu et al., 2017; Xu et al., 2013; Zhang et al., 2018b; Zhu et al., 2013).

We conduct the simulations at coarse (2˚ × 2.5˚) and fine (0.25˚ × 0.3125˚) resolutions. The coarse resolution simulation is performed globally while the fine resolution simulation is applied to a nested-grid domain of 26.25˚ × 23.44˚ around the Great Lakes region of North America. The nested simulation domain is 105 × 75 grids around the Great Lakes. We discard 5 columns (rows) of grids at each boarder of the nested region for analysis to avoid impacts from the buffer zone (3 columns and rows) of one-way nesting. The simulations are performed for April, July and October in 2013, driven by assimilated GEOS-FP meteorology data (native resolution: 0.25˚ × 0.3125˚) from the Goddard Earth Observing System of the NASA Global Modeling and Assimilation Office. Natural and anthropogenic emissions of NH_3 are from the Global Emissions InitiAtive (GEIA) inventory (Bouwman et al., 1997) unless stated otherwise, and open fire emissions are from Global Fire Emissions Database version 3 (van der Werf et al., 2010).

5.3.2 Pseudo Observations

We use synthetic observations to test the accuracy of the inversion methods to recover "true" emissions for satellite observing scenarios. We obtain NH_3 retrievals from the Cross-track Infrared Sounder (CrIS) (Shephard and Cady-Pereira, 2015) over North America. CrIS is a Fourier Transform Spectrometer onboard the Suomi National Polar-orbiting Partnership satellite. CrIS has a spatial resolution of 14 km at nadir, and a spectral

resolution of 0.625 cm^{-1} over the main NH_3 absorbing spectral region (960-970 cm^{-1}). CrIS is in a sun-synchronous orbit, with a mean local overpass time of 01:30 and 13:30 and twice daily global coverage. We only use the daytime retrievals with quality flag = 4 (highest quality) to represent typical sampling scenarios in inversions. CrIS retrievals of NH_3 are based on an optimal estimation method as described in Shephard and Cady-Pereira (2015). These retrievals compute the sensitivities of the retrievals to the true atmospheric state (i.e. average kernels), which are used to compute the CrIS "retrieved" NH_3 from the GEOS-Chem simulations. The trace of the averaging kernel matrix gives the number of degrees of freedom for signal (DOFS).

We first run the forward model with the "true" NH_3 emissions (i.e. base simulations) to simulate hourly NH_3 fields. Emissions, meteorology data and initial conditions in these base simulations are identical with the descriptions in Section 5.3.1 except that anthropogenic emissions of NH_3 are overwritten with the 2008 U.S. National Emissions Inventory (NEI) over the US, and with the Criteria Air Contaminants (CAC) inventories over Canada (van Donkelaar et al., 2008). Simulated NH_3 profiles collocated with the sampling time and locations are converted to the profile and column density (Ω) as "retrieved" using the *a priori* profiles and average kernels of CrIS. Two weeks of pseudo observations are prepared for each month and resolution.

We apply these NH_3 columns as pseudo observations to simulations using the *a priori* anthropogenic NH_3 emissions (from GEIA) to evaluate two inversion approaches. We use normalized mean error (NME) and Pearson correlation (r) vs. the "true" emissions as standards to evaluate the emission estimates. The expression of NME is:

$$NME = \frac{\Sigma|x-y|}{\Sigma y} \tag{5-1}$$

where x represents estimates and y represents the truth.

5.3.3 Inversion Methods

The iterative finite difference mass balance (IFDMB) approach is described elsewhere (Cooper et al., 2017; Lamsal et al., 2011). Briefly, the sensitivity of the column density (Ω) to emission (E) of NH_3 over each grid box is linearized around an *a priori* concentration

obtained from a forward model. Then top-down emission estimates (E_t) in one iteration can be calculated as:

$$E_t = E_a(1 + \frac{\Omega_o - \Omega_a}{\beta \Omega_a}) \quad (5\text{-}2)$$

where $\beta = \frac{\Delta\Omega/\Omega}{\Delta E/E}$. E_a is the *a priori* emission, corresponding to a simulated column Ω_a, and Ω_o is the observed column. The sensitivity (β) of fraction changes in NH_3 column to those in NH_3 emission can be determined from a simulation with E_a perturbed by 10%. The top-down emission E_t can be used as E_a in the next iteration. The iteration is interpreted as converged if consecutive iterations yields emission estimates with small normalized mean error (NME < 2%). We follow Cooper et al. (2017) to limit β values to the range 0.1–10 to avoid unrealistically large sensitivities and emission adjustments. We also briefly examine the performance of the iterative basic mass balance (IBMB) method (Martin et al., 2013a) in which β equals unity.

The emission optimization in 4D-Var starts with defining a cost function (J) that considers the error-weighted difference between the simulated and observed NH_3 column:

$$J(\boldsymbol{x}) = \left(\boldsymbol{\Omega}_o - \boldsymbol{\Omega}(\boldsymbol{x})\right)^T \boldsymbol{S}_o^{-1}\left(\boldsymbol{\Omega}_o - \boldsymbol{\Omega}(\boldsymbol{x})\right) + \gamma(\boldsymbol{\sigma} - \mathbf{1})^T \boldsymbol{S}_a^{-1}(\boldsymbol{\sigma} - \mathbf{1}) \quad (5\text{-}3)$$

where $\boldsymbol{\Omega}_o$ is the vector of observed column, $\boldsymbol{\Omega}(\mathbf{x})$ is the vector of simulated column, and $\mathbf{x}$ is the vector of emissions to be adjusted by scaling factors $\boldsymbol{\sigma}$. $\mathbf{S}_o$ and $\mathbf{S}_a$ are the error covariance matrices in the observations and *a priori*, respectively. γ is the regularization parameter that determines the weighting of the cost function toward observations or *a priori* emissions. According to evaluation with surface remote sensing products (Dammers et al., 2017), a 35% random error is assumed to represent typical CrIS retrieval uncertainties, overwritten by an absolute error of 5×10^{15} molecules/cm^2 to low-NH_3 records ($\Omega < 1.43\times10^{16}$ molecules/cm^2). The minimum absolute error is assumed to account for the increasing uncertainties in CrIS data under low-NH_3 environments (Dammers et al., 2017; Kharol et al., 2018). We assume errors in each observation record are independent (i.e. $\mathbf{S}_o$ is diagonal).

The GEOS-Chem adjoint model calculates the gradients of the cost function with respect to the distribution of emissions and uses the imbedded 4D-Var module to iteratively

adjust emissions to minimize the cost function. In this work, we focus on how well the inversion methods can reproduce the "true" emissions. Therefore, we do not include a weighted balance between observations and the *a priori* to generate the *a posteriori* estimates, but rather evaluate the top-down inversion results (e.g. Equation 5-2). For the 4D-Var, this is done by setting $\gamma=0$, namely ignoring the right term in Equation 5-3.

5.4 Results and Discussion

5.4.1 Inversions at Coarse Resolution Using Ideal Pseudo Observations

Figure 5-1 shows the results of inversion experiments at 2˚ × 2.5˚ resolution in April, July and October, 2013. The "true" NH_3 emissions from NEI and CAC exhibit consistently high emissions over agricultural regions, e.g. southwestern California and the midwestern states. The *a priori* emissions from GEIA underestimate the domain-total emissions by 20-70%. This underestimation is most significant in April, when the emissions have a maximum in NEI&CAC and a minimum in GEIA among the 3 months, highlighting the uncertainties in different bottom-up inventories. After inverting 2 weeks of pseudo observations, the IFDMB inversions reduce the NME of the *a priori* emissions from 53-77% to 12-17%, and the 4D-Var tests reduce the NME to 17-26%. Both methods generally recover the domain-wide spatial distribution ($r>0.95$) of NH_3 emissions.

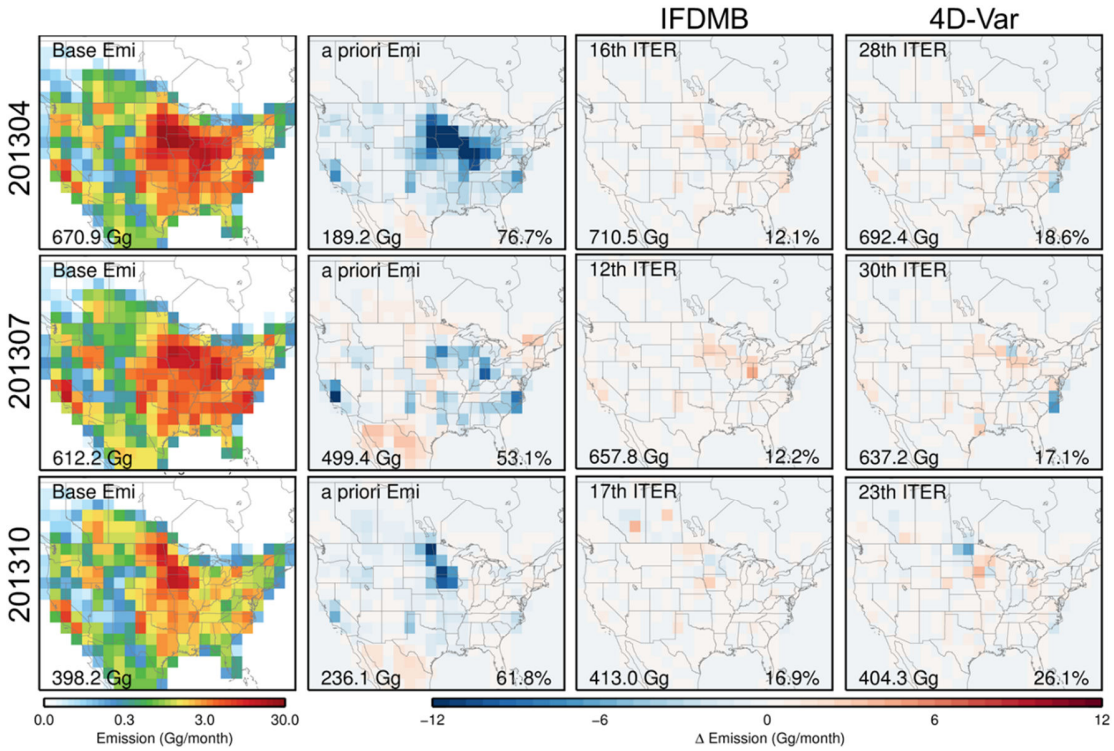

Figure 5-1. Evaluation of top-down emission estimates at 2˚ × 2.5˚ resolution from iterative finite difference mass balance (IFDMB) method and from 4D-Var inversion. The left column shows "true" anthropogenic NH_3 emissions. The other columns show the difference vs. the true emissions of the *a priori* emissions and the top-down emission estimates from IFDMB method and from 4D-Var inversion. Experiments are conducted for April (upper), July (middle) and October (lower) 2013. For each panel, total emission over the domain is shown at the bottom-left, normalized mean error vs. the "true" emissions is indicated at the bottom-right, and the number of iterations is indicated at the top-left.

Figure 5-2 shows the evolution of the accuracy of the top-down estimates. Despite the similar or better performance, the computation burden in IFDMB inversions are significantly smaller, as indicated by the steeper reductions in NME, faster increases in the correlation, and the fewer number of iterations needed (~10 in IFDMB vs. ~25 in 4D-Var) to reach convergence. A maximum number of 30 iterations is conducted in the 4D-Var experiments, although the July case might not have converged.

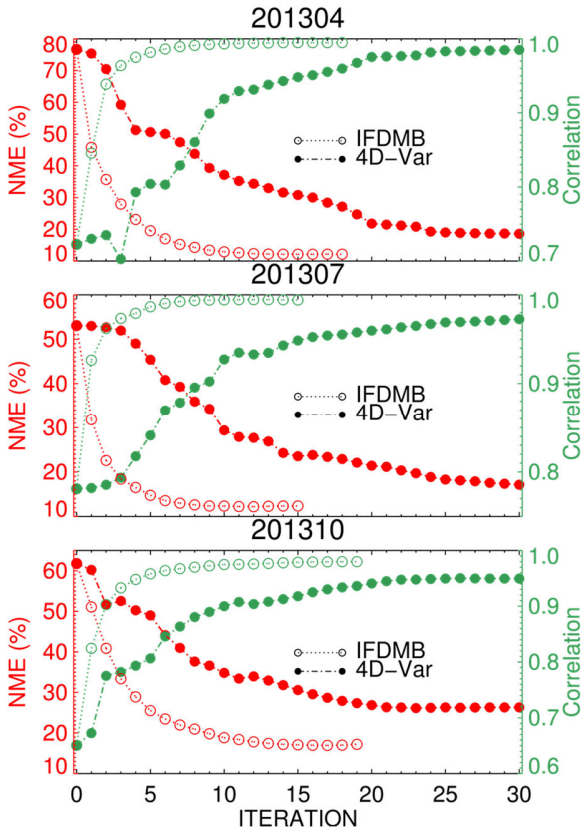

Figure 5-2. Evolution of normalized mean error (red) and correlation (green) of top-down emission estimates from iterative finite difference mass balance method (blank circles) and 4D-Var inversion (filled circles) for April (top), July (middle) and October (bottom), at 2˚ × 2.5˚ resolution.

5.4.2 Inversions at Fine Resolution Using Ideal Pseudo Observations

Figure 5-3 shows the performance of two inversion methods at 0.25˚ × 0.3125˚ resolution. At this fine resolution, the effects of transport become more apparent and both methods yield larger NME and smaller correlations with the "true" emissions compared to the inversions at coarse resolution. The IFDMB method nonetheless improves the emission estimates and reproduces the domain-wide total emissions. However, the 4D-Var estimates (NME=30-45%, r=0.85-0.95) exhibit significantly better skill in reproducing the spatial distribution of emissions than the IFDMB inversions (NME=44-69%, r=0.7-0.9).

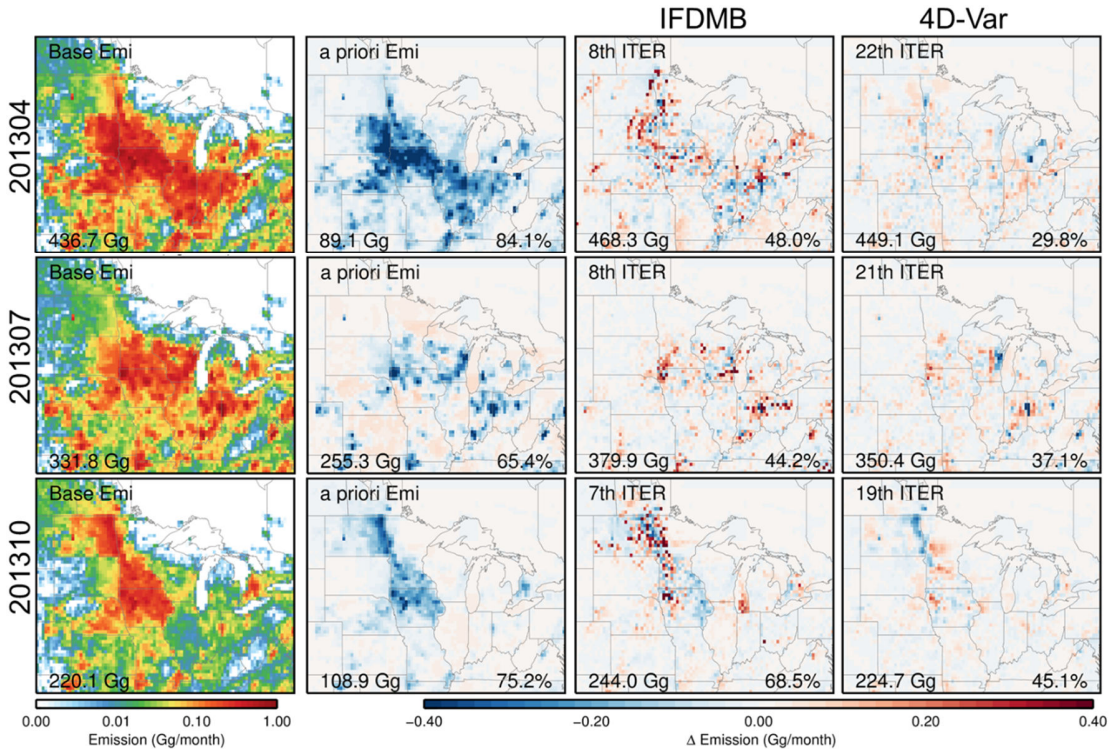

Figure 5-3. Similar to Figure 5-1 but for experiments at 0.25˚ × 0.3125˚ resolution over a nested domain around the Great Lakes.

Figure 5-4 shows the accuracy of top-down estimates after each iteration at the fine resolution. Fewer iterations are needed in the IFDMB (~10) than in the 4D-Var (~20) for convergence at the fine resolution, but the accuracy of the 4D-Var quickly exceeds that of the IFDMB. Both methods yield larger NME in the October inversions than in the other two months at both resolutions.

Table 5-1 provides information on the base simulation and pseudo observations. April exhibits the strongest horizontal wind and the largest sensitivity (e.g. averaged DOFS) of CrIS observations. The strongest sensitivity (i.e. weaker reliance on the *a priori* NH_3 profiles) is consistent with the highest observed NH_3 column in April (Shephard and Cady-Pereira, 2015), which compensate the expected stronger "smearing effects" due to transport. Meanwhile October has the smallest observed NH_3 emissions and CrIS sensitivities, which might be the main cause of the larger errors of inversion in this month. Figure 5-S1 shows that using the iterative basic mass balance (IBMB) methods (i.e. β fixed to 1) yields unstable inversion for October at fine resolution, while provides similar estimates as the IFDMB in other months.

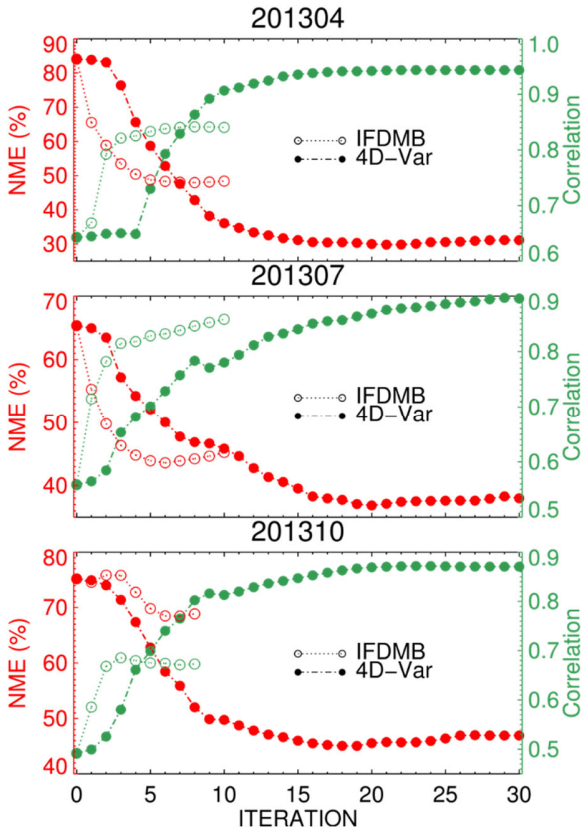

Figure 5-4. Similar to Figure 5-2 but for experiments at 0.25˚ × 0.3125˚ resolution.

Table 5-1. Description of pseudo observations in the base simulation. For each resolution, total number of observations (N), mean Degree of Freedom (DOFS), mean 10-m horizontal wind speed (W10, m/s) and mean NH_3 column of all observations (Ω, $\times 10^{15}$ molecule/cm^2) are shown for the domains of Figure 5-1 and Figure 5-3.

Month	2˚ × 2.5˚				0.25˚ × 0.3125˚			
	N	DOFS	Ω	W10	N	DOFS	Ω	W10
201304	157684	0.82	8.4	4.5	29982	0.89	16	4.0
201307	184359	0.77	5.9	3.4	50039	0.86	9.3	3.3
201310	217115	0.75	3.4	3.5	44315	0.78	4.8	3.5

Overall, our results at 2˚ × 2.5˚ resolution indicate that mass balance inversions with iterations provide similar accuracy as the more complex 4D-Var assimilation approach while requiring fewer iterations and computational resources, at least in the configurations applying CrIS sampling and sensitivities provided in this study. These are consistent with the conclusions for nitrogen oxides (NO_x) emission inversions in Cooper et al. (2017), and suggesting promising application of the IFDMB for inversions at such coarse resolution. However, the 4D-Var exhibits greater skill at 0.25˚ × 0.3125˚ resolution if sufficient computational resources are available.

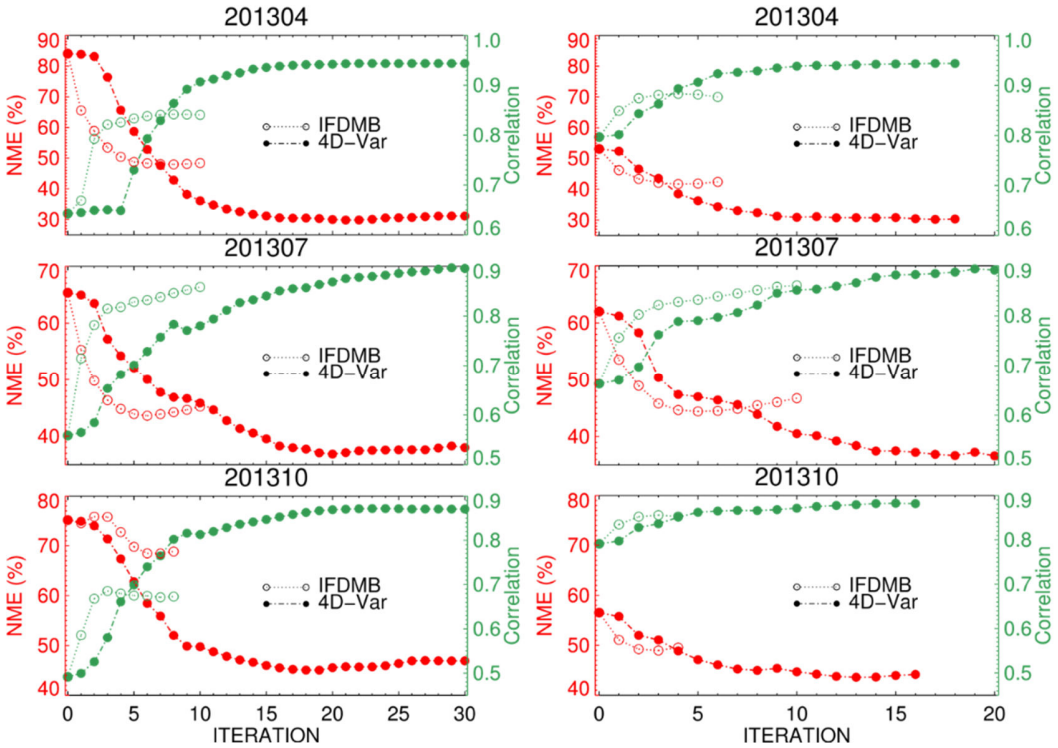

Figure 5-5. Comparison of inversion results at 0.25˚ × 0.3125˚ resolution, using the *a priori* emissions (left) and using the *a priori* emissions scaled with the IFDMB inversion results at 2 × 2.5˚ resolution (right).

We also conduct sensitivity inversions at 0.25˚ × 0.3125˚ resolution by updating the *a priori* emissions with the scaling factors derived from the IFDMB inversions at 2˚ × 2.5˚. Figure 5-5 shows that the *a priori* emissions have reduced errors after the scaling, and the IFDMB inversions show improvements in both the NMEs and the correlations with the updated *a priori* emissions. The improvements are nearly negligible in July, and are most significant in October when the NME of the inversion results reduce from 69% to 49%. The dependence of IFDMB inversions on the accuracy of the *a priori* emissions indicates the weaker robustness of the inversion capability at the fine resolution. Meanwhile the NMEs and correlations of 4D-Var inversions are similar with the two *a priori* emissions, and are consistently better than the IFDMB inversions, indicating robust performance insensitive to the input *a priori*. It is noteworthy that using the updated *a priori* emissions that are closer to the "true" emissions could reduce the number of iterations to reach convergence (i.e. from ~20 to 10-15) in the 4D-Var inversions. This suggests that an initial inversion at coarse resolution (i.e. using the IFDMB method) could help reduce the computational resources needed for 4D-Var inversions at fine resolution.

5.4.3 Nonnegligible Effects from Transport at Fine Resolution

The core assumption in the IFDMB approach is that the changes in NH_3 column are driven by changes in local emissions in each grid. For NH_3, violation of this assumption is mostly due to contribution to the observed column changes from non-local emissions via transport. Here we discuss the extent of such violation at coarse and fine resolution.

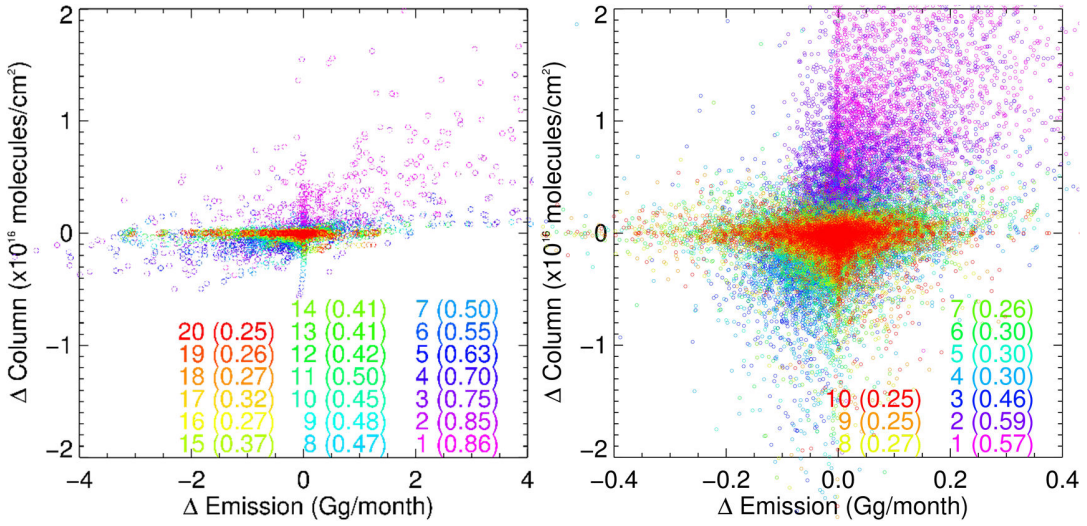

Figure 5-6. Scatterplots between the difference (truth – simulation) of NH_3 column density and that of NH_3 emissions in the IFDMB inversions in April 2013, at 2˚ × 2.5˚ (left) and 0.25˚ × 0.3125˚ (right) resolutions. Correlations are in brackets following the number of iterations indicated by colors.

Figure 5-6 shows scatter plots of the column difference (ΔΩ) vs. emission difference (ΔE) between the base and *a priori* simulations in each grid for April 2013 during the iterations in IFDMB. The fine resolution case exhibits weaker correlation (0.57) than at coarse resolution (0.86) in the *a priori* (i.e. first iteration) simulation, characterized by a cluster of points around the Y-axis (i.e. large ΔΩ but nearly zero ΔE). The stronger misalignments between ΔΩ and ΔE clearly indicate stronger influence from non-local emission changes at fine resolution. As emission estimates improve for subsequent iterations, ΔΩ values reduce, and so does their correlation with ΔE. The iterations converge at both resolutions when the correlation between local ΔΩ and ΔE are reduced to ~0.25, and the scatter of the points are clustered around the X-axis (i.e. large ΔE but nearly zero ΔΩ), indicating residual misalignments between local ΔΩ and ΔE that cannot be resolved by further iterations. Although ΔΩ has been significantly reduced after the iterations, there

are more severe residual misalignments between $\Delta\Omega$ and ΔE at fine resolution than at coarse resolution, indicating important effects from transport at finer grid size.

To quantitatively assess the influence of non-local emissions to the observed NH_3 abundance, we calculate the gradient of the total columnar mass (M) of NH_3 at a grid box to the fractional changes in anthropogenic NH_3 emissions using the GEOS-Chem adjoint model. We then follow Turner et al. (2012) to calculate the fraction of the total gradient within a distance of the grid center to represent the cumulative emission influence on M.

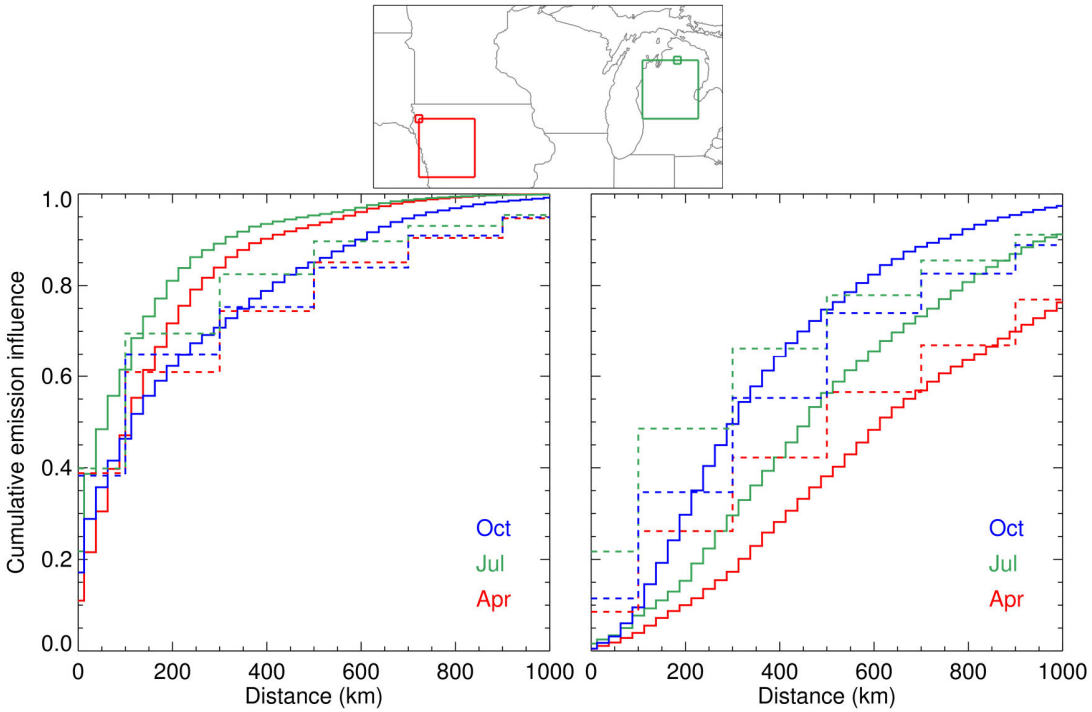

Figure 5-7. Emission influence of grids within a certain distance on total columnar mass of NH_3 at a grid box normalized to the total influence from all grids. Results are given for a source (red grids and plot on the left) and a recipient (green grids and plot on the right) site at 2˚ × 2.5˚ (large grids and dashed line) and 0.25˚ × 0.3125˚ (small grids and solid line) resolutions. We approximate the width of a 2˚ × 2.5˚ grid as 200 km, and that of a 0.25˚ × 0.3125˚ grid as 25 km.

Figure 5-7 shows the increase of calculated emission influence following the distance for a source and a recipient grid at both resolutions. For the source site in Iowa, the local grid (within 100 km) contributes to ~40% of total NH_3 burden, which increases to 60-70% after adding only one adjacent grid at each side (within 300 km) at 2˚ × 2.5˚ resolution. Our experiment suggests that the IFDMB method is capable of accounting for one adjacent grid after iterations and resolve the spatial distribution of emissions at such ~200 km scale.

At 0.25˚ × 0.3125˚ resolution, the local emission (within 12.5 km) of the Iowa site only contributes 10-20% to the NH_3 columnar mass. The adjoint calculations at finer resolution reveal more details of source contribution from adjacent grids, and suggest that 5-10 adjacent grids at each side (i.e. 100-400 total grids) are needed to accumulate the contribution to ~70%. The IFDMB method poorly accounts for interactions between hundreds of grids within that distance, thus fails to resolve emission distributions at the fine resolution according to our tests.

The example recipient site at northern Michigan has much smaller NH_3 emissions (Figure 5-1 and 5-3) and has weaker local contributions (< 22% at 2˚ × 2.5˚ and < 3% at 0.25˚ × 0.3125˚) as well as slower accumulation with distance of the emission contribution than the source site. The calculation at 0.25˚ × 0.3125˚ resolution suggests that a 70% contribution should include all grids within 400-900 km around the site. The IFDMB method cannot correctly find the local emissions with such low local sensitivities. Thus although the iterative emission corrections over the other source regions gradually reduce $\Delta\Omega$, the resultant local emissions are erroneous as illustrated in Figure 5-6 by the clustering of points around the X-axis (wrong emission estimates despite reduced $\Delta\Omega$).

In summary, our experiments indicate that the stronger effects of transport at finer spatial scales increase the adjacent grids needed to account for >70% emission contributions to local columnar mass from ~1 at 2˚ × 2.5˚ to ~10 at 0.25˚ × 0.3125˚. The IFDMB method poorly accounts for complicated transport effects of hundreds of grids. In contrast, the 4D-Var assimilation explicitly calculates these source influences by tracking processes including transport, thus has better skill in retrieving the spatial distribution of emissions at 0.25˚ × 0.3125˚ resolution.

5.5 Conclusion

We assessed the ability of two well-established inversion methods to retrieve top-down NH_3 emissions from satellite observations of NH_3 column density over North America. Based on inversion results using pseudo observations, the iterative finite difference mass balance (IFDMB) approach requires fewer iterations (~10 vs. ~25) than the mathematically more rigorous four-dimensional variational assimilation (4D-Var) to

reach similar or lower inversion errors (NME of 12-17% vs. 17-26%) at 2˚ × 2.5˚ resolution. Meanwhile, the 4D-Var estimates (NME=30-45%, r=0.85-0.95) yield significantly improved inversions than the IFDMB (NME=44-69%, r=0.7-0.9) and exhibit more robustness against the input *a priori* emissions at 0.25˚ × 0.3125˚ resolution. The large errors of IFDMB at 0.25˚ × 0.3125˚ resolution are attributed to enhanced effects of transport. Nevertheless, applying the inversion results from 2˚ × 2.5˚ resolution to update the *a priori* emissions at 0.25˚ × 0.3125˚ resolution could improve the accuracy of IFDMB inversions and reduce the number of iterations needed in the 4D-Var by ~10. Our results suggest promising application of the more computationally efficient IFDMB method for top-down NH_3 emission inversions at coarse resolution, as well as for refining the *a priori* emissions to accelerate the 4D-Var inversions at fine resolution.

5.6 Supporting Information

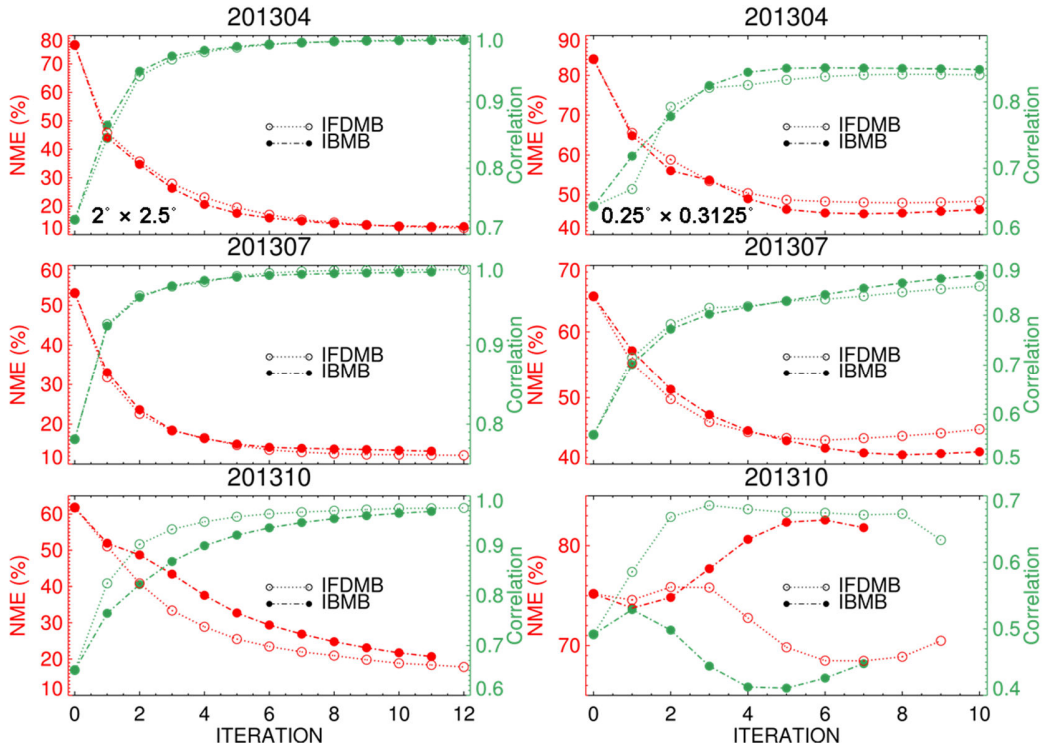

Figure 5-S1. Comparison between the iterative finite difference mass balance (IFDMB) and the iterative basic mass balance (IBMB) inversion methods at 2˚ × 2.5˚ (left) and 0.25˚ × 0.3125˚ (right) resolutions.

Chapter 6. Conclusions

6.1 Summary

Aerosols exert significant effects on the global environment, human health and climate change. The current state of understanding of aerosols and their effects is limited due to complicated sources and processes that dynamically alter their size, composition and abundance. This study exploits a large suite of observation data and a chemical transport model (CTM) for characterizing global and regional aerosol trends and sources.

In Chapter 2, decades of visibility data from ~30,000 global stations are collected to inform trends in haze, which reflect trends in surface aerosol extinction contributed dominantly by fine particulate matter ($PM_{2.5}$). Despite the intuitively straightforward relationship between inverse visibility (1/Vis) and surface atmospheric extinction (b_{ext}), we find that a critical step for such purpose is a comprehensive data filtering process. Besides eliminating records with high humidity and spikes as is conventionally performed in other studies, there is a tendency of weaker representativeness of aerosol variation by 1/Vis under cleaner environment. This tendency is revealed by the higher correlations ($r > 0.5$) between monthly 1/Vis and b_{ext} data from the Interagency Monitoring of PROtected Visual Environments (IMPROVE) network over the eastern US and the two most polluted metropolitan areas in California than over other sites (Figure 2-3). The manual reporting of discrete visibility with a maximum threshold is the main contributor to the weakened representativeness. We consider this factor in our filtering algorithm, and further examine and separate discontinuities in the time series of 1/Vis. The quality assured 1/Vis data exhibit over less than 4000 sites after screening, and reveal trends (95% confidence intervals in brackets) that are consistent with collocated b_{ext} trend over the US in 1989-1996 (1/Vis: -1.6% [-2.4, -0.8] yr^{-1}; b_{ext}: -2.4% [-3.7, -1.1] yr^{-1}), and with collocated $PM_{2.5}$ trend over Europe in 2016-2013 (1/Vis: -3.4% [-4.4, -2.4] yr^{-1}; $PM_{2.5}$: -5.8% [-7.8, -4.2] yr^{-1}). This consistency supports the applicability of the screened 1/Vis dataset for historical and regional haze trend studies.

Application of the screened 1/Vis data to calculate regional trends over several separating periods reveals historical haze pollution during six decades (1929-1996) over the eastern US, and during four decades (1973-2013) over Europe and eastern Asia. Several reversal points of 1/Vis trends are largely consistent with transitions in sulfur dioxide (SO_2) emission trends, reflecting historical socioeconomic events and environmental regulations. Some inconsistencies between SO_2 and 1/Vis evolution may be contributed by anomalies in meteorology and other aerosol sources.

In Chapter 3, we further interpret historical changes in the seasonality of 1/Vis over the eastern US with a recently published historical emission inventory of major anthropogenic aerosol sources during 1946-1998. We find that the regional dominance of summer maxima in $PM_{2.5}$ as observed from aerosol chemical composition network in 1999-2009 was reversed historically. This region was characterized by winter maxima in 1/Vis before the 1950s, and the summer/winter ratio in 1/Vis increased steadily over 1946-1975. This reversed seasonality is attributable to increasing SO_2 emissions (increasing sulfate and strengthening summer maxima) since the mid 1950s and decreasing organic carbon (OC) and black carbon (BC) emissions (decreasing primary organic aerosols and black carbon and reducing winter maxima) since the 1940s. We also find that summer 1/Vis exhibits faster increase over the southeastern US than over the northeastern US during 1956-1975 despite the greater sulfate dominance in $PM_{2.5}$ over the northeast, suggesting that secondary organic aerosols (SOA) should have increased concurrently with increasing sulfate. These findings highlight the ability of combining 1/Vis data and historical emissions to qualitatively reveal historical changes in major aerosol composition.

In Chapter 4, evolutions in surface $PM_{2.5}$ and its chemical composition over 1989-2013 are simulated using the GEOS-Chem CTM at $2^\circ \times 2.5^\circ$ resolution. We collect available global and regional emission inventories and their historical evolution for the study period to supply the simulation, and use satellite-derived global $PM_{2.5}$ to further downscale the simulation to a resolution ($0.1^\circ \times 0.1^\circ$) relevant to population exposure studies. The downscaled simulation not only increases the correlation vs. global in situ measured $PM_{2.5}$ from 0.80 (original simulation) to 0.91, but also successfully reproduces observed trends (1989-2013) in population-weighted mean (PWM) $PM_{2.5}$ (observation vs. downscaled simulation: -2.4 vs. -2.4 %/yr), secondary inorganic aerosols (-4.3 vs. -

4.1 %/yr), organic aerosols (OA, -3.6 vs. -3.0 %/yr) and black carbon (-4.3 vs. -3.9 %/yr) over North America, and in PWM sulfate (-4.7 vs. -5.8 %/yr) over Europe. The successful reproduction of OA trends over North America in both winter and summer is a model improvement, benefiting from reasonable trends in OC emissions and recent updates in SOA yields.

Showing statistically overlapping trends in PWM $PM_{2.5}$ vs. trends in satellite-derived $PM_{2.5}$ over 20 of the 21 Global Burden of Disease Study regions, the downscaled simulation attributes nearly 80% of the significant ($p < 0.05$) increase in global PWM $PM_{2.5}$ (0.28 μg $m^{-3}yr^{-1}$) over 25 years to significantly ($p < 0.05$) increasing OA (0.10 μg $m^{-3}yr^{-1}$), nitrate (0.05 μg $m^{-3}yr^{-1}$), sulfate (0.04 μg $m^{-3}yr^{-1}$) and ammonium (0.03 μg $m^{-3}yr^{-1}$), reflecting the dominant contribution of anthropogenic emissions to changes in population exposure to $PM_{2.5}$. Unlike the populated regions of North America, Europe, South Asia and East Asia where these four species also predominantly drive the steady trends in PWM $PM_{2.5}$, the inter-annual evolutions in PWM $PM_{2.5}$ are with dominant influences from dust over desert regions in Africa, and from organic aerosols due to biomass burning over African and Amazon forests. We also find that global trend in area-weighted mean $PM_{2.5}$ is much weaker (0.06 μg $m^{-3}yr^{-1}$) in the satellite-derived $PM_{2.5}$, distinctly different from the trend in PWM $PM_{2.5}$ (0.58 μg $m^{-3}yr^{-1}$).

In Chapter 5, we use the GEOS-Chem model and its adjoint to evaluate how satellite observations of ammonia (NH_3) abundance can improve our understanding of NH_3 emissions. We create synthetic NH_3 column density as observed by the Cross-track Infrared Sounder with known emissions and apply two inversion methods to infer top-down NH_3 emissions from these pseudo observations. We find that the iterative finite difference mass balance (IFDMB) approach requires fewer iterations (~10 vs. ~25) than the four-dimensional variational assimilation (4D-Var) to reach similar or lower normalized mean errors (NME, 12-17% vs. 17-26%) in the inversions at 2˚ × 2.5˚ resolution. However, the 4D-Var estimates (NME=30-45%, r=0.85-0.95) exhibit pronounced advantages over the IFDMB (NME=44-69%, r=0.7-0.9) at 0.25˚ × 0.3125˚ resolution. At 0.25˚ × 0.3125˚, simulated differences in NH_3 column and in NH_3 emission exhibit strong misalignments and the local emission contribution to columnar NH_3 abundance is less than 20%, explaining the large errors because of reduced representativeness of transport in IFDMB.

We also find that the IFDMB inversion at 2˚ × 2.5˚ resolution could be used to improve the *a priori* emissions at 0.25˚ × 0.3125˚ resolution and consequently reduce the number of iterations needed in the 4D-Var by ~10. These inversion experiments suggest promising application of the more computationally efficient IFDMB method for top-down NH_3 emission inversions.

6.2 Studies Utilizing this Work

The GEOS-Chem simulation in Chapter 4 featured a collection of recent updates in emission inventories and model capabilities. Hammer et al. (2018) used the aerosol data archived in this simulation to calculate and interpret observed trends in Ultraviolet Aerosol Index (UVAI) from the Ozone Monitoring Instrument (OMI) over 2005-2015. Absorption of mineral dust or brown carbon were found to dominantly contribute to the trends in UVAI over North Africa, Middle East, Australia, Central South America and West Africa, while significant trends in UVAI over the eastern US and eastern India were determined by opposite trends in scattering of secondary inorganic aerosols. This simulation served as boundary conditions of a nested (0.5˚ × 0.625˚) simulation using the same emissions and model processes over North America, which contributed to a historical estimates of surface $PM_{2.5}$ over 1980-2016 (Meng et al., 2018). Future estimates of global $PM_{2.5}$ based on satellite remote sensing of aerosol optical depth (AOD) will also incorporate the modelled AOD profile and $PM_{2.5}$ from global and regional nested simulations using the emissions and chemical mechanisms in this work.

6.3 Future Directions

The 1/Vis dataset developed in Chapter 2 showed promising applicability for regional aerosol trend studies. Besides the populated regions discussed in Section 2.6, information of 1/Vis evolution over other areas with fewer aerosol measurements, e.g. South Asia, Africa, Australia and South America are valuable. As discussed in this thesis, the reduced number of sites available over these regions after screening usually impedes generalization of spatially coherent information. Therefore, evaluation against available measurements

similar to Section 2.5 is prerequisite for such future applications. This thesis focuses on using 1/Vis to probe long-term evolution of mean 1/Vis state, such as trends (e.g. Chapter 2) and seasonal variations (e.g. Chapter 3). Extremes in visibility without high humidity are related with strong haze pollution and have outstanding health and climate implications (Gao et al., 2017; Li et al., 2018b). Similar to recent studies on winter haze over China (Wang and Chen, 2016; Yang et al., 2016; Yin et al., 2017; Zou et al., 2017), future analysis of visibility with measurements of aerosols, emissions and meteorological parameters, as well as model processes to interpret their associations would help elucidate causes of extreme haze events.

The historical changes in aerosol seasonality over the eastern US as revealed by the 1/Vis data in Chapter 3 warrant further quantitative assessment using model simulations. The quantified historical effects on $PM_{2.5}$ of e.g. significant reduction in carbonaceous aerosol emissions, possible enhanced SOA yields due to anthropogenic emissions, and potential enhancement in atmospheric oxidation following NO_x emissions, would be insightful for current environmental policies.

As outlined in Chapter 4, future developments in chemical transport models and emergence of new observations will improve our current understanding of changes in $PM_{2.5}$ and its chemical composition. The GEOS-Chem model has recently introduced a high-performance capability (GCHP) utilizing a distributed-memory framework for massive parallelization (Eastham et al., 2018), which would enable global simulations with full chemistry at 10-km resolution scale and online coupling with processes in earth system models (Hu et al., 2018). Besides new satellite missions, developments of AOD retrieval algorithm from historical radiance observations of Advanced Very High Radiometer (AVHRR) are promising to provide constraints on trends since the late 1970s (Hsu et al., 2017; Sayer et al., 2017). Finally, this global study reveals strong connections of trends in population exposure to $PM_{2.5}$ components with associated emissions. Meanwhile this connection is expected to be modulated by changes in meteorology and chemistry. For example, a GEOS-Chem simulation constrained with aircraft measurements identified strengthened formation yields of wintertime sulfate over the eastern US in recent years due to relaxed oxidant deficiency as its concentration decreases (Shah et al., 2018). Future work

employing detailed analysis of model processes with measurement data would provide more insights on non-emission effects and regulation policies.

More work is needed to consolidate and extend the conclusions of Chapter 5. The comparison in this work idealizes errors in the observations, e.g. these from forward modeling, from satellite retrievals and from the *a priori* emissions. Future evaluation of the inversion methods using pseudo observations containing such errors will give more insights on their robustness to errors in realistic inversions. Sensitivity of the inversion accuracy to sampling frequency is also of interest, regarding future launch of geostationary satellite missions (Zhu et al., 2015b) that would significantly increase the number of available retrievals. These experiments could also be performed at more intermediate resolutions to determine the critical spatial scale that IFDMB could resolve. At fine resolution, the large dimensionality of state vector (**x**) at native resolution in 4D-Var might not be optimal regarding available density of sampling, which could severely affect the inversion (Jacob et al., 2016; Wecht et al., 2014). Choices of state vector aggregation and their influence on both methods (e.g. Turner and Jacob, 2015) warrant more investigation. Finally, this research would contribute to advancing the top-down constraints of NH_3 emissions using realistic satellite observations.

References

Aas, W., Tsyro, S., Bieber, E., Bergström, R., Ceburnis, D., Ellermann, T., Fagerli, H., Frölich, M., Gehrig, R., Makkonen, U., Nemitz, E., Otjes, R., Perez, N., Perrino, C., Prévôt, A. S. H., Putaud, J. P., Simpson, D., Spindler, G., Vana, M., and Yttri, K. E.: Lessons learnt from the first EMEP intensive measurement periods, Atmos. Chem. Phys., 12, 8073-8094, 2012.

Ahmed, E., Kim, K.-H., Shon, Z.-H., and Song, S.-K.: Long-term trend of airborne particulate matter in Seoul, Korea from 2004 to 2013, Atmos. Environ., 101, 125-133, 2015.

Aikawa, M., Ohara, T., Hiraki, T., Oishi, O., Tsuji, A., Yamagami, M., Murano, K., and Mukai, H.: Significant geographic gradients in particulate sulfate over Japan determined from multiple-site measurements and a chemical transport model: Impacts of transboundary pollution from the Asian continent, Atmos. Environ., 44, 381-391, 2010.

Andela, N., and van der Werf, G. R.: Recent trends in African fires driven by cropland expansion and El Nino to La Nina transition, Nat. Clim. Change, 4, 791-795, 2014.

Apte, J. S., Marshall, J. D., Cohen, A. J., and Brauer, M.: Addressing Global Mortality from Ambient PM2.5, Environ. Sci. Technol., 49, 8057-8066, 2015.

Attwood, A., Washenfelder, R., Brock, C., Hu, W., Baumann, K., Campuzano-Jost, P., Day, D., Edgerton, E., Murphy, D., and Palm, B.: Trends in sulfate and organic aerosol mass in the Southeast US: Impact on aerosol optical depth and radiative forcing, Geophys. Res. Lett., 41, 7701-7709, 2014.

Babu, S. S., Manoj, M. R., Moorthy, K. K., Gogoi, M. M., Nair, V. S., Kompalli, S. K., Satheesh, S. K., Niranjan, K., Ramagopal, K., Bhuyan, P. K., and Singh, D.: Trends in aerosol optical depth over Indian region: Potential causes and impact indicators, J. Geophys. Res., 118, 11,794-711,806, doi:10.1002/2013JD020507, 2013.

Backes, A. M., Aulinger, A., Bieser, J., Matthias, V., and Quante, M.: Ammonia emissions in Europe, part II: How ammonia emission abatement strategies affect secondary aerosols, Atmos. Environ., 126, 153-161, 2016.

Bahadur, R., Feng, Y., Russell, L. M., and Ramanathan, V.: Impact of California's air pollution laws on black carbon and their implications for direct radiative forcing, Atmos. Environ., 45, 1162-1167, doi:http://dx.doi.org/10.1016/j.atmosenv.2010.10.054, 2011.

Bari, M. A., and Kindzierski, W. B.: Eight-year (2007–2014) trends in ambient fine particulate matter (PM2.5) and its chemical components in the Capital Region of Alberta, Canada, Environ. Int., 91, 122-132, 2016.

Bellouin, N., Boucher, O., Haywood, J., and Reddy, M. S.: Global estimate of aerosol direct radiative forcing from satellite measurements, Nature, 438, 1138-1141, 2005.

Bevan, S. L., North, P. R. J., Grey, W. M. F., Los, S. O., and Plummer, S. E.: Impact of atmospheric aerosol from biomass burning on Amazon dry-season drought, J. Geophys. Res., 114, doi:10.1029/2008JD011112, 2009.

Bey, I., Jacob, D. J., Yantosca, R. M., Logan, J. A., Field, B. D., Fiore, A. M., Li, Q., Liu, H. Y., Mickley, L. J., and Schultz, M. G.: Global modeling of tropospheric chemistry with assimilated meteorology: Model description and evaluation, J. Geophys. Res., 106, 23073-23095, 2001.

Bigi, A., and Ghermandi, G.: Trends and variability of atmospheric PM2.5 and PM10–2.5 concentration in the Po Valley, Italy, Atmos. Chem. Phys., 16, 15777-15788, 2016.

Blanchard, C. L., Hidy, G. M., Tanenbaum, S., Edgerton, E. S., and Hartsell, B. E.: The Southeastern Aerosol Research and Characterization (SEARCH) study: Temporal trends in gas and PM concentrations and composition, 1999–2010, J. Air Waste Manag. Assoc., 63, 247-259, 2013.

Blanchard, C. L., Hidy, G. M., Shaw, S., Baumann, K., and Edgerton, E. S.: Effects of emission reductions on organic aerosol in the southeastern United States, Atmos. Chem. Phys., 16, 215-238, doi:10.5194/acp-16-215-2016, 2016.

Bond, T. C., Habib, G., and Bergstrom, R. W.: Limitations in the enhancement of visible light absorption due to mixing state, J. Geophys. Res., 111, doi:10.1029/2006JD007315, 2006.

Bond, T. C., Bhardwaj, E., Dong, R., Jogani, R., Jung, S., Roden, C., Streets, D. G., and Trautmann, N. M.: Historical emissions of black and organic carbon aerosol from energy-related combustion, 1850–2000, Global Biogeochem. Cycles, 21, doi:10.1029/2006GB002840, 2007.

Bouwman, A. F., Lee, D. S., Asman, W. A. H., Dentener, F. J., Van Der Hoek, K. W., and Olivier, J. G. J.: A global high-resolution emission inventory for ammonia, Global Biogeochem. Cycles, 11, 561-587, doi:10.1029/97GB02266, 1997.

Boys, B., Martin, R., van Donkelaar, A., MacDonell, R., Hsu, N., Cooper, M., Yantosca, R., Lu, Z., Streets, D. G., and Zhang, Q.: Fifteen-Year Global Time Series of Satellite-Derived Fine Particulate Matter, Environ. Sci. Technol., 48, 11109-11118, 2014.

Brauer, M., Amann, M., Burnett, R. T., Cohen, A., Dentener, F., Ezzati, M., Henderson, S. B., Krzyzanowski, M., Martin, R. V., Van Dingenen, R., van Donkelaar, A., and Thurston, G. D.: Exposure Assessment for Estimation of the Global Burden of Disease Attributable to Outdoor Air Pollution, Environ. Sci. Technol., 46, 652-660, 2012.

Brauer, M., Freedman, G., Frostad, J., Van Donkelaar, A., Martin, R. V., Dentener, F., Dingenen, R. v., Estep, K., Amini, H., and Apte, J. S.: Ambient air pollution exposure estimation for the global burden of disease 2013, Environ. Sci. Technol., 50, 79-88, 2015.

Brook, J. R., Dann, T. F., and Bonvalot, Y.: Observations and Interpretations from the Canadian Fine Particle Monitoring Program, J. Air Waste Manag. Assoc., 49, 35-44, 1999.

Budisulistiorini, S. H., Li, X., Bairai, S. T., Renfro, J., Liu, Y., Liu, Y. J., McKinney, K. A., Martin, S. T., McNeill, V. F., Pye, H. O. T., Nenes, A., Neff, M. E., Stone, E. A., Mueller, S., Knote, C., Shaw, S. L., Zhang, Z., Gold, A., and Surratt, J. D.: Examining the effects of anthropogenic emissions on isoprene-derived secondary organic aerosol formation during the 2013 Southern Oxidant and Aerosol Study (SOAS) at the Look Rock, Tennessee ground site, Atmos. Chem. Phys., 15, 8871-8888, doi:10.5194/acp-15-8871-2015, 2015.

Budisulistiorini, S. H., Nenes, A., Carlton, A. G., Surratt, J. D., McNeill, V. F., and Pye, H. O. T.: Simulating Aqueous-Phase Isoprene-Epoxydiol (IEPOX) Secondary Organic Aerosol Production During the 2013 Southern Oxidant and Aerosol Study (SOAS), Environ. Sci. Technol., 51, 5026-5034, doi:10.1021/acs.est.6b05750, 2017.

Canagaratna, M. R., Jimenez, J. L., Kroll, J. H., Chen, Q., Kessler, S. H., Massoli, P., Hildebrandt Ruiz, L., Fortner, E., Williams, L. R., Wilson, K. R., Surratt, J. D., Donahue, N. M., Jayne, J. T., and Worsnop, D. R.: Elemental ratio measurements of organic compounds using aerosol mass spectrometry: characterization, improved calibration, and implications, Atmos. Chem. Phys., 15, 253-272, doi:10.5194/acp-15-253-2015, 2015.

Carlton, A. G., Pinder, R. W., Bhave, P. V., and Pouliot, G. A.: To What Extent Can Biogenic SOA be Controlled?, Environ. Sci. Technol., 44, 3376-3380, 2010.

Carlton, A. G., and Turpin, B. J.: Particle partitioning potential of organic compounds is highest in the Eastern US and driven by anthropogenic water, Atmos. Chem. Phys., 13, 10203-10214, 2013.

Chan, E. A. W., Gantt, B., and McDow, S.: The reduction of summer sulfate and switch from summertime to wintertime PM2.5 concentration maxima in the United States, Atmos. Environ., 175, 25-32, doi:https://doi.org/10.1016/j.atmosenv.2017.11.055, 2018.

Che, H., Zhang, X., Li, Y., Zhou, Z., and Qu, J. J.: Horizontal visibility trends in China 1981–2005, Geophys. Res. Lett., 34, doi:10.1029/2007GL031450, 2007.

Che, H., Zhang, X. Y., Xia, X., Goloub, P., Holben, B., Zhao, H., Wang, Y., Zhang, X. C., Wang, H., Blarel, L., Damiri, B., Zhang, R., Deng, X., Ma, Y., Wang, T., Geng, F., Qi, B., Zhu, J., Yu, J., Chen, Q., and Shi, G.: Ground-based aerosol climatology of China: aerosol optical depths from the China Aerosol Remote Sensing Network (CARSNET) 2002–2013, Atmos. Chem. Phys., 15, 7619-7652, doi:10.5194/acp-15-7619-2015, 2015.

Chen, H., and Wang, H.: Haze Days in North China and the associated atmospheric circulations based on daily visibility data from 1960 to 2012, J. Geophys. Res., 120, doi:10.1002/2015JD023225, 2015.

Chen, L. W.-A., Watson, J. G., Chow, J. C., DuBois, D. W., and Herschberger, L.: Chemical mass balance source apportionment for combined PM2.5 measurements from U.S. non-urban and urban long-term networks, Atmos. Environ., 44, 4908-4918, 2010.

Chen, Y., Zheng, M., Edgerton, E. S., Ke, L., Sheng, G., and Fu, J.: PM2.5 source apportionment in the southeastern U.S.: Spatial and seasonal variations during 2001–2005, J. Geophys. Res., 117, doi:10.1029/2011JD016572, 2012.

Chin, M., Jacob, D. J., Gardner, G. M., Foreman-Fowler, M. S., Spiro, P. A., and Savoie, D. L.: A global three-dimensional model of tropospheric sulfate, J. Geophys. Res., 101, 18667-18690, doi:10.1029/96JD01221, 1996.

Chin, M., Diehl, T., Tan, Q., Prospero, J. M., Kahn, R. A., Remer, L. A., Yu, H., Sayer, A. M., Bian, H., Geogdzhayev, I. V., Holben, B. N., Howell, S. G., Huebert, B. J., Hsu, N. C., Kim, D., Kucsera, T. L., Levy, R. C., Mishchenko, M. I., Pan, X., Quinn, P. K., Schuster, G. L., Streets, D. G., Strode, S. A., Torres, O., and Zhao, X. P.: Multi-decadal aerosol variations from 1980 to 2009: a perspective from observations and a global model, Atmos. Chem. Phys., 14, 3657-3690, 2014.

Cohen, A. J., Brauer, M., Burnett, R., Anderson, H. R., Frostad, J., Estep, K., Balakrishnan, K., Brunekreef, B., Dandona, L., Dandona, R., Feigin, V., Freedman, G., Hubbell, B., Jobling, A., Kan, H., Knibbs, L., Liu, Y., Martin, R., Morawska, L., Pope, C. A., III, Shin, H., Straif, K., Shaddick, G., Thomas, M., van Dingenen, R., van Donkelaar, A., Vos, T., Murray, C. J. L., and Forouzanfar, M. H.: Estimates and 25-year trends of the global burden of disease attributable to ambient air pollution: an analysis of data from the Global Burden of Diseases Study 2015, The Lancet, 389, 1907-1918, 2017a.

Cohen, J. B., Lecoeur, E., and Hui Loong Ng, D.: Decadal-scale relationship between measurements of aerosols, land-use change, and fire over Southeast Asia, Atmos. Chem. Phys., 17, 721-743, doi:10.5194/acp-17-721-2017, 2017b.

Collaud Coen, M., Andrews, E., Asmi, A., Baltensperger, U., Bukowiecki, N., Day, D., Fiebig, M., Fjaeraa, A., Flentje, H., and Hyvärinen, A.: Aerosol decadal trends–Part 1: In-situ optical measurements at GAW and IMPROVE stations, Atmos. Chem. Phys., 13, 869-894, 2013.

Cooper, M., Martin, R. V., Padmanabhan, A., and Henze, D. K.: Comparing mass balance and adjoint methods for inverse modeling of nitrogen dioxide columns for global nitrogen oxide emissions, J. Geophys. Res., 122, 4718-4734, doi:10.1002/2016JD025985, 2017.

Correia, A. W., Pope, C. A., Dockery, D. W., Wang, Y., Ezzati, M., and Dominici, F.: The Effect of Air Pollution Control on Life Expectancy in the United States: An Analysis of 545 US counties for the period 2000 to 2007, Epidemiology (Cambridge, Mass.), 24, 23-31, 2013.

Costa, A. C., and Soares, A.: Homogenization of climate data: review and new perspectives using geostatistics, Math. Geol., 41, 291-305, 2009.

Crippa, M., Janssens-Maenhout, G., Dentener, F., Guizzardi, D., Sindelarova, K., Muntean, M., Van Dingenen, R., and Granier, C.: Forty years of improvements in European air quality: regional policy-industry interactions with global impacts, Atmos. Chem. Phys., 16, 3825-3841, 2016.

Croft, B., Pierce, J. R., and Martin, R. V.: Interpreting aerosol lifetimes using the GEOS-Chem model and constraints from radionuclide measurements, Atmos. Chem. Phys., 14, 4313-4325, 2014.

Croft, B., Wentworth, G. R., Martin, R. V., Leaitch, W. R., Murphy, J. G., Murphy, B. N., Kodros, J. K., Abbatt, J. P. D., and Pierce, J. R.: Contribution of Arctic seabird-colony ammonia to atmospheric particles and cloud-albedo radiative effect, Nat. Commun., 7, 13444, doi:10.1038/ncomms13444, 2016.

Crouse, D. L., Peters, P. A., van Donkelaar, A., Goldberg, M. S., Villeneuve, P. J., Brion, O., Khan, S., Atari, D. O., Jerrett, M., and Pope III, C. A.: Risk of Nonaccidental and Cardiovascular Mortality in Relation to Long-term Exposure to Low Concentrations of Fine Particulate Matter: A Canadian National-Level Cohort Study, Environ. Health Perspect., 120, 708-714, 2012.

Cui, Y. Y., Brioude, J., Angevine, W. M., Peischl, J., McKeen, S. A., Kim, S.-W., Neuman, J. A., Henze, D. K., Bousserez, N., Fischer, M. L., Jeong, S., Michelsen, H. A., Bambha, R. P., Liu, Z., Santoni, G. W., Daube, B. C., Kort, E. A., Frost, G. J., Ryerson, T. B., Wofsy, S. C., and Trainer, M.: Top-down estimate of methane emissions in California using a mesoscale inverse modeling technique: The San Joaquin Valley, J. Geophys. Res., 122, 3686-3699, 2017.

Cusack, M., Alastuey, A., Pérez, N., Pey, J., and Querol, X.: Trends of particulate matter ($PM_{2.5}$) and chemical composition at a regional background site in the Western Mediterranean over the last nine years (2002–2010), Atmos. Chem. Phys., 12, 8341-8357, 2012.

Dabek-Zlotorzynska, E., Dann, T. F., Kalyani Martinelango, P., Celo, V., Brook, J. R., Mathieu, D., Ding, L., and Austin, C. C.: Canadian National Air Pollution Surveillance (NAPS) PM2.5 speciation program: Methodology and PM2.5 chemical composition for the years 2003–2008, Atmos. Environ., 45, 673-686, 2011.

Dammers, E., Shephard, M. W., Palm, M., Cady-Pereira, K., Capps, S., Lutsch, E., Strong, K., Hannigan, J. W., Ortega, I., Toon, G. C., Stremme, W., Grutter, M., Jones, N., Smale, D., Siemons, J., Hrpcek, K., Tremblay, D., Schaap, M., Notholt, J., and Erisman, J. W.: Validation of the CrIS fast physical NH3 retrieval with ground-based FTIR, Atmos. Meas. Tech., 10, 2645-2667, 2017.

Daskalakis, N., Tsigaridis, K., Myriokefalitakis, S., Fanourgakis, G. S., and Kanakidou, M.: Large gain in air quality compared to an alternative anthropogenic emissions scenario, Atmos. Chem. Phys., 16, 9771-9784, doi:10.5194/acp-16-9771-2016, 2016.

Daum, P. H., Schwartz, S. E., and Newman, L.: Acidic and related constituents in liquid water stratiform clouds, J. Geophys. Res., 89, 1447-1458, 1984.

de Foy, B., Lu, Z., and Streets, D. G.: Satellite NO2 retrievals suggest China has exceeded its NOx reduction goals from the twelfth Five-Year Plan, Sci. Rep., 6, 35912, doi:10.1038/srep35912, 2016.

Denier van der Gon, H. A. C., Bergström, R., Fountoukis, C., Johansson, C., Pandis, S. N., Simpson, D., and Visschedijk, A. J. H.: Particulate emissions from residential wood combustion in Europe – revised estimates and an evaluation, Atmos. Chem. Phys., 15, 6503-6519, 2015.

Dey, S., and Di Girolamo, L.: A decade of change in aerosol properties over the Indian subcontinent, Geophys. Res. Lett., 38, doi:10.1029/2011GL048153, 2011.

Dockery, D. W., Pope, C. A., Xu, X., Spengler, J. D., Ware, J. H., Fay, M. E., Ferris Jr, B. G., and Speizer, F. E.: An association between air pollution and mortality in six US cities, New England journal of medicine, 329, 1753-1759, 1993.

Dominici, F., Peng, R. D., Bell, M. L., and et al.: Fine particulate air pollution and hospital admission for cardiovascular and respiratory diseases, JAMA, 295, 1127-1134, 2006.

Doyle, M., and Dorling, S.: Visibility trends in the UK 1950–1997, Atmos. Environ., 36, 3161-3172, doi:10.1016/S1352-2310(02)00248-0, 2002.

Drury, E., Jacob, D. J., Spurr, R. J. D., Wang, J., Shinozuka, Y., Anderson, B. E., Clarke, A. D., Dibb, J., McNaughton, C., and Weber, R.: Synthesis of satellite (MODIS), aircraft (ICARTT), and surface (IMPROVE, EPA-AQS, AERONET) aerosol observations over eastern North America to improve MODIS aerosol retrievals and constrain surface aerosol concentrations and sources, J. Geophys. Res., 115, doi:10.1029/2009JD012629, 2010.

DuBay, S. G., and Fuldner, C. C.: Bird specimens track 135 years of atmospheric black carbon and environmental policy, Proc. Natl. Acad. Sci. U.S.A., 114, 11321-11326, 2017.

Dubovik, O., Holben, B., Eck, T. F., Smirnov, A., Kaufman, Y. J., King, M. D., Tanré, D., and Slutsker, I.: Variability of absorption and optical properties of key aerosol types observed in worldwide locations, J. Atmospheric Sci., 59, 590-608, 2002.

Dubovik, O., Sinyuk, A., Lapyonok, T., Holben, B. N., Mishchenko, M., Yang, P., Eck, T. F., Volten, H., Muñoz, O., Veihelmann, B., van der Zande, W. J., Leon, J. F., Sorokin, M., and Slutsker, I.: Application of spheroid models to account for aerosol particle nonsphericity in remote sensing of desert dust, J. Geophys. Res., 111, doi:10.1029/2005JD006619, 2006.

Duncan, B. N., Martin, R. V., Staudt, A. C., Yevich, R., and Logan, J. A.: Interannual and seasonal variability of biomass burning emissions constrained by satellite observations, J. Geophys. Res., 108, doi:10.1029/2002JD002378, 2003.

Duncan Fairlie, T., Jacob, D. J., and Park, R. J.: The impact of transpacific transport of mineral dust in the United States, Atmos. Environ., 41, 1251-1266, 2007.

Eastham, S. D., Long, M. S., Keller, C. A., Lundgren, E., Yantosca, R. M., Zhuang, J., Li, C., Lee, C. J., Yannetti, M., Auer, B. M., Clune, T. L., Kouatchou, J., Putman, W. M., Thompson, M. A., Trayanov, A. L., Molod, A. M., Martin, R. V., and Jacob, D. J.: GEOS-Chem High Performance (GCHP v11-02c): a next-generation implementation of the GEOS-Chem chemical transport model for massively parallel applications, Geosci. Model Dev., 11, 2941-2953, 2018.

Evans, M. J., and Jacob, D. J.: Impact of new laboratory studies of N2O5 hydrolysis on global model budgets of tropospheric nitrogen oxides, ozone, and OH, Geophys. Res. Lett., 32, doi:10.1029/2005GL022469, 2005.

Evolution of the Clean Air Act. https://www.epa.gov/clean-air-act-overview/evolution-clean-air-act, accessed March 25, 2018.

Fang, Y., Mauzerall, D. L., Liu, J., Fiore, A. M., and Horowitz, L. W.: Impacts of 21st century climate change on global air pollution-related premature mortality, Clim. Change, 121, 239-253, doi:10.1007/s10584-013-0847-8, 2013.

Fangmeier, A., Hadwiger-Fangmeier, A., Van der Eerden, L., and Jäger, H.-J.: Effects of atmospheric ammonia on vegetation—A review, Environ. Pollut., 86, 43-82, 1994.

Fiore, A. M., Naik, V., Spracklen, D. V., Steiner, A., Unger, N., Prather, M., Bergmann, D., Cameron-Smith, P. J., Cionni, I., Collins, W. J., Dalsoren, S., Eyring, V., Folberth, G. A., Ginoux, P., Horowitz, L. W., Josse, B., Lamarque, J.-F., MacKenzie, I. A., Nagashima, T., O'Connor, F. M., Righi, M., Rumbold, S. T., Shindell, D. T., Skeie, R. B., Sudo, K., Szopa, S., Takemura, T., and Zeng, G.: Global air quality and climate, Chem. Soc. Rev., 41, 6663-6683, 2012.

Fisher, J. A., Jacob, D. J., Wang, Q., Bahreini, R., Carouge, C. C., Cubison, M. J., Dibb, J. E., Diehl, T., Jimenez, J. L., Leibensperger, E. M., Lu, Z., Meinders, M. B. J., Pye, H. O. T., Quinn, P. K., Sharma, S., Streets, D. G., van Donkelaar, A., and Yantosca, R. M.: Sources, distribution, and acidity of sulfate–ammonium aerosol in the Arctic in winter–spring, Atmos. Environ., 45, 7301-7318, 2011.

Foltz, G. R., and McPhaden, M. J.: Trends in Saharan dust and tropical Atlantic climate during 1980–2006, Geophys. Res. Lett., 35, doi:10.1029/2008GL035042, 2008.

Forouzanfar, M. H., Afshin, A., Alexander, L. T., Anderson, H. R., Bhutta, Z. A., Biryukov, S., et al.: Global, regional, and national comparative risk assessment of 79 behavioural, environmental and occupational, and metabolic risks or clusters of risks, 1990–2015: a systematic analysis for the Global Burden of Disease Study 2015, The Lancet, 388, 1659-1724, 2016.

Founda, D., Kazadzis, S., Mihalopoulos, N., Gerasopoulos, E., Lianou, M., and Raptis, P. I.: Long-term visibility variation in Athens (1931–2013): a proxy for local and regional atmospheric aerosol loads, Atmos. Chem. Phys., 16, 11219-11236, 2016.

Fountoukis, C., and Nenes, A.: ISORROPIA II: a computationally efficient thermodynamic equilibrium model for K^+-Ca^{2+}-Mg^{2+}-NH_4^+-Na^+-SO_4^{2-}-NO_3^--Cl^--H_2O aerosols, Atmos. Chem. Phys., 7, 4639-4659, doi:10.5194/acp-7-4639-2007, 2007.

Fu, X., Wang, X., Guo, H., Cheung, K., Ding, X., Zhao, X., He, Q., Gao, B., Zhang, Z., Liu, T., and Zhang, Y.: Trends of ambient fine particles and major chemical components in the Pearl River Delta region: Observation at a regional background site in fall and winter, Sci. Total Environ., 497, 274-281, 2014.

Fuglestvedt, J. S., Berntsen, T. K., Isaksen, I. S. A., Mao, H., Liang, X.-Z., and Wang, W.-C.: Climatic forcing of nitrogen oxides through changes in tropospheric ozone and methane; global 3D model studies, Atmos. Environ., 33, 961-977, 1999.

Fuzzi, S., Baltensperger, U., Carslaw, K., Decesari, S., Denier van der Gon, H., Facchini, M. C., Fowler, D., Koren, I., Langford, B., Lohmann, U., Nemitz, E., Pandis, S., Riipinen, I., Rudich, Y., Schaap, M., Slowik, J. G., Spracklen, D. V., Vignati, E., Wild, M., Williams, M., and Gilardoni, S.: Particulate matter, air quality and climate: lessons learned and future needs, Atmos. Chem. Phys., 15, 8217-8299, doi:10.5194/acp-15-8217-2015, 2015.

Gakidou, E., Afshin, A., Abajobir, A. A., Abate, K. H., Abbafati, C., Abbas, K. M., et al.: Global, regional, and national comparative risk assessment of 84 behavioural, environmental and occupational, and metabolic risks or clusters of risks, 1990–2016: a systematic analysis for the Global Burden of Disease Study 2016, The Lancet, 390, 1345-1422, 2017.

Ganor, E., Osetinsky, I., Stupp, A., and Alpert, P.: Increasing trend of African dust, over 49 years, in the eastern Mediterranean, J. Geophys. Res., 115, doi:10.1029/2009JD012500, 2010.

Gao, M., Saide, P. E., Xin, J., Wang, Y., Liu, Z., Wang, Y., Wang, Z., Pagowski, M., Guttikunda, S. K., and Carmichael, G. R.: Estimates of Health Impacts and Radiative Forcing in Winter Haze in Eastern China through Constraints of Surface PM2.5 Predictions, Environ. Sci. Technol., 51, 2178-2185, doi:10.1021/acs.est.6b03745, 2017.

Geddes, J., Martin, R., Boys, B., and van Donkelaar, A.: Long-term trends worldwide in ambient NO_2 concentrations inferred from satellite observations, Environ. Health Perspect., 124, 281-289, 2016.

Geng, G., Zhang, Q., Tong, D., Li, M., Zheng, Y., Wang, S., and He, K.: Chemical composition of ambient $PM_{2.5}$ over China and relationship to precursor emissions during 2005–2012, Atmos. Chem. Phys., 17, 9187-9203, 2017.

Ghude, S. D., Pfister, G. G., Jena, C., van der A, R. J., Emmons, L. K., and Kumar, R.: Satellite constraints of nitrogen oxide (NOx) emissions from India based on OMI observations and WRF-Chem simulations, Geophys. Res. Lett., 40, 423-428, 2013.

Giglio, L., Randerson, J. T., and van der Werf, G. R.: Analysis of daily, monthly, and annual burned area using the fourth-generation global fire emissions database (GFED4), J. Geophys. Res., 118, 317-328, doi:10.1002/jgrg.20042, 2013.

Ginoux, P., Chin, M., Tegen, I., Prospero, J. M., Holben, B., Dubovik, O., and Lin, S.-J.: Sources and distributions of dust aerosols simulated with the GOCART model, J. Geophys. Res., 106, 20255-20273, doi:10.1029/2000JD000053, 2001.

Global Estimates of Surface $PM_{2.5}$. Atmospheric Composition Analysis Group, http://fizz.phys.dal.ca/~atmos/martin/?page_id=140, accessed March 13, 2018.

Goldstein, A. H., Koven, C. D., Heald, C. L., and Fung, I. Y.: Biogenic carbon and anthropogenic pollutants combine to form a cooling haze over the southeastern United States, Proc. Natl. Acad. Sci. U.S.A., 106, doi:10.1073/pnas.0904128106, 2009.

Greenstone, M.: The Impacts of Environmental Regulations on Industrial Activity: Evidence from the 1970 and 1977 Clean Air Act Amendments and the Census of Manufactures, J. Polit. Econ., 2001.

Griffing, G. W.: Relations between the prevailing visibility, nephelometer scattering coefficient and sunphotometer turbidity coefficient, Atmos. Environ., 14, 577-584, 1980.

Grythe, H., Ström, J., Krejci, R., Quinn, P., and Stohl, A.: A review of sea-spray aerosol source functions using a large global set of sea salt aerosol concentration measurements, Atmos. Chem. Phys., 14, 1277-1297, doi:10.5194/acp-14-1277-2014, 2014.

Gschwandtner, G., Gschwandtner, K., Eldridge, K., Mann, C., and Mobley, D.: Historic Emissions of Sulfur and Nitrogen Oxides in the United States from 1900 to 1980, J. Air Pollut. Control Assoc., 36, 139-149, doi:10.1080/00022470.1986.10466052, 1986.

Guenther, A. B., Jiang, X., Heald, C. L., Sakulyanontvittaya, T., Duhl, T., Emmons, L. K., and Wang, X.: The Model of Emissions of Gases and Aerosols from Nature version 2.1 (MEGAN2.1): an extended and updated framework for modeling biogenic emissions, Geosci. Model Dev., 5, 1471-1492, doi:10.5194/gmd-5-1471-2012, 2012.

Guo, H., Liu, J., Froyd, K. D., Roberts, J. M., Veres, P. R., Hayes, P. L., Jimenez, J. L., Nenes, A., and Weber, R. J.: Fine particle pH and gas–particle phase partitioning of inorganic species in Pasadena, California, during the 2010 CalNex campaign, Atmos. Chem. Phys., 17, 5703-5719, doi:10.5194/acp-17-5703-2017, 2017.

Hammer, M. S., Martin, R. V., van Donkelaar, A., Buchard, V., Torres, O., Ridley, D. A., and Spurr, R. J. D.: Interpreting the ultraviolet aerosol index observed with the OMI satellite instrument to understand absorption by organic aerosols: implications for atmospheric oxidation and direct radiative effects, Atmos. Chem. Phys., 16, 2507-2523, doi:10.5194/acp-16-2507-2016, 2016.

Hammer, M. S., Martin, R. V., Li, C., Torres, O., Manning, M., and Boys, B. L.: Insight into global trends in aerosol composition from 2005 to 2015 inferred from the OMI Ultraviolet Aerosol Index, Atmos. Chem. Phys., 18, 8097-8112, 2018.

Han, R., Wang, S., Shen, W., Wang, J., Wu, K., Ren, Z., and Feng, M.: Spatial and temporal variation of haze in China from 1961 to 2012, J. Environ. Sci., 46, 134-146, 2016.

Hand, J., Schichtel, B., Pitchford, M., Malm, W., and Frank, N.: Seasonal composition of remote and urban fine particulate matter in the United States, J. Geophys. Res., 117, doi:10.1029/2011JD017122, 2012a.

Hand, J. L., Schichtel, B. A., Malm, W. C., and Pitchford, M. L.: Particulate sulfate ion concentration and SO_2 emission trends in the United States from the early 1990s through 2010, Atmos. Chem. Phys., 12, 10353-10365, doi:10.5194/acp-12-10353-2012, 2012b.

Hand, J. L., Schichtel, B. A., Malm, W. C., and Frank, N. H.: Spatial and Temporal Trends in PM2.5 Organic and Elemental Carbon across the United States, Adv. Meteorol., 2013, doi:10.1155/2013/367674, 2013.

Hand, J. L., Schichtel, B. A., Malm, W. C., Copeland, S., Molenar, J. V., Frank, N., and Pitchford, M.: Widespread reductions in haze across the United States from the early 1990s through 2011, Atmos. Environ., 94, 671-679, 2014a.

Hand, J. L., Schichtel, B. A., Malm, W. C., Pitchford, M., and Frank, N. H.: Spatial and seasonal patterns in urban influence on regional concentrations of speciated aerosols across the United States. J. Geophys. Res., 119, 12,832-12,849, 2014b.

Hara, K., Homma, J., Tamura, K., Inoue, M., Karita, K., and Yano, E.: Decreasing trends of suspended particulate matter and PM2.5 concentrations in Tokyo, 1990–2010, J. Air Waste Manag. Assoc., 63, 737-748, doi:10.1080/10962247.2013.782372, 2013.

He, Q., Zhang, M., and Huang, B.: Spatio-temporal variation and impact factors analysis of satellite-based aerosol optical depth over China from 2002 to 2015, Atmos. Environ., 129, 79-90, doi:http://dx.doi.org/10.1016/j.atmosenv.2016.01.002, 2016.

Heald, C. L., Collett Jr, J. L., Lee, T., Benedict, K. B., Schwandner, F. M., Li, Y., Clarisse, L., Hurtmans, D. R., Van Damme, M., Clerbaux, C., Coheur, P. F., Philip, S., Martin, R. V., and Pye, H. O. T.: Atmospheric ammonia and particulate inorganic nitrogen over the United States, Atmos. Chem. Phys., 12, 10295-10312, 2012.

Henze, D. K., Hakami, A., and Seinfeld, J. H.: Development of the adjoint of GEOS-Chem, Atmos. Chem. Phys., 7, 2413-2433, doi:10.5194/acp-7-2413-2007, 2007.

Henze, D. K., Shindell, D. T., Akhtar, F., Spurr, R. J. D., Pinder, R. W., Loughlin, D., Kopacz, M., Singh, K., and Shim, C.: Spatially Refined Aerosol Direct Radiative Forcing Efficiencies, Environ. Sci. Technol., 46, 9511-9518, doi:10.1021/es301993s, 2012.

Hidy, G. M., Blanchard, C. L., Baumann, K., Edgerton, E., Tanenbaum, S., Shaw, S., Knipping, E., Tombach, I., Jansen, J., and Walters, J.: Chemical climatology of the southeastern United States, 1999-2013, Atmos. Chem. Phys., 14, 11893-11914, doi:10.5194/acp-14-11893-2014, 2014.

Historical Census of Housing Tables, https://www.census.gov/hhes/www/housing/census/historic/fuels.html, accessed March 25, 2018.

Hoek, G., Beelen, R., de Hoogh, K., Vienneau, D., Gulliver, J., Fischer, P., and Briggs, D.: A review of land-use regression models to assess spatial variation of outdoor air pollution, Atmos. Environ., 42, 7561-7578, 2008.

Hoek, G., Krishnan, R. M., Beelen, R., Peters, A., Ostro, B., Brunekreef, B., and Kaufman, J. D.: Long-term air pollution exposure and cardio-respiratory mortality: a review, Environ. Health, 12, doi:10.1186/1476-069X-12-43, 2013.

Hoesly, R. M., Smith, S. J., Feng, L., Klimont, Z., Janssens-Maenhout, G., Pitkanen, T., Seibert, J. J., Vu, L., Andres, R. J., Bolt, R. M., Bond, T. C., Dawidowski, L., Kholod, N., Kurokawa, J. I., Li, M., Liu, L., Lu, Z., Moura, M. C. P., O'Rourke, P. R., and Zhang, Q.: Historical (1750–2014) anthropogenic emissions of reactive gases and aerosols from the Community Emissions Data System (CEDS), Geosci. Model Dev., 11, 369-408, 2018.

Holt, J., Selin, N. E., and Solomon, S.: Changes in Inorganic Fine Particulate Matter Sensitivities to Precursors Due to Large-Scale US Emissions Reductions, Environ. Sci. Technol., 49, 4834-4841, doi:10.1021/acs.est.5b00008, 2015.

Hoyle, C. R., Boy, M., Donahue, N. M., Fry, J. L., Glasius, M., Guenther, A., Hallar, A. G., Huff Hartz, K., Petters, M. D., Petäjä, T., Rosenoern, T., and Sullivan, A. P.: A review of the anthropogenic influence on biogenic secondary organic aerosol, Atmos. Chem. Phys., 11, 321-343, doi:10.5194/acp-11-321-2011, 2011.

Hsu, N. C., Gautam, R., Sayer, A. M., Bettenhausen, C., Li, C., Jeong, M. J., Tsay, S.-C., and Holben, B. N.: Global and regional trends of aerosol optical depth over land and ocean using SeaWiFS measurements from 1997 to 2010, Atmos. Chem. Phys., 12, 8037-8053, 2012.

Hsu, N. C., Lee, J., Sayer, A. M., Carletta, N., Chen, S.-H., Tucker, C. J., Holben, B. N., and Tsay, S.-C.: Retrieving near-global aerosol loading over land and ocean from AVHRR, J. Geophys. Res., 122, 9968-9989, doi:10.1002/2017JD026932, 2017.

Hu, L., Millet, D. B., Baasandorj, M., Griffis, T. J., Turner, P., Helmig, D., Curtis, A. J., and Hueber, J.: Isoprene emissions and impacts over an ecological transition region in the U.S. Upper Midwest inferred from tall tower measurements, J. Geophys. Res., 120, 3553-3571, 2015.

Hu, L., Keller, C. A., Long, M. S., Sherwen, T., Auer, B., Da Silva, A., Nielsen, J. E., Pawson, S., Thompson, M. A., Trayanov, A. L., Travis, K. R., Grange, S. K., Evans, M. J., and Jacob, D. J.: Global simulation of tropospheric chemistry at 12.5 km resolution: performance and evaluation of the GEOS-Chem chemical module (v10-1) within the NASA GEOS Earth System Model (GEOS-5 ESM), Geosci. Model Dev. Discuss., 2018, 1-32, doi:10.5194/gmd-2018-111, 2018.

Huang, X., Song, Y., Li, M., Li, J., Huo, Q., Cai, X., Zhu, T., Hu, M., and Zhang, H.: A high-resolution ammonia emission inventory in China, Global Biogeochem. Cycles, 26, doi:10.1029/2011GB004161, 2012.

Hudman, R. C., Moore, N. E., Mebust, A. K., Martin, R. V., Russell, A. R., Valin, L. C., and Cohen, R. C.: Steps towards a mechanistic model of global soil nitric oxide emissions: implementation and space based-constraints, Atmos. Chem. Phys., 12, 7779-7795, 2012.

Husar, R. B., Holloway, J. M., Patterson, D. E., and Wilson, W. E.: Spatial and temporal pattern of eastern US haziness: a summary, Atmos. Environ., 15, 1919-1928, 1981.

Husar, R. B., Patterson, D. E., and Wilson, W. E.: Haze climate of the United States, US Environmental Protection Agency, Atmospheric Sciences Research Laboratory, 1987.

Husar, R. B., and Wilson, W. E.: Haze and sulfur emission trends in the eastern United States, Environ. Sci. Technol., 27, 12-16, 1993.

Husar, R. B., Husar, J. D., and Martin, L.: Distribution of continental surface aerosol extinction based on visual range data, Atmos. Environ., 34, 5067-5078, 2000.

Intergovernmental Panel on Climate Change (IPCC), Climate Change 2013: The Physical Science Basis, Cambridge University Press, Cambridge, UK and New York, NY, USA, 2013.

Inverse visibility data. Atmospheric Composition Analysis Group, http://fizz.phys.dal.ca/~atmos/martin/?page_id=1435, accessed March 20, 2018.

Itahashi, S., Uno, I., Yumimoto, K., Irie, H., Osada, K., Ogata, K., Fukushima, H., Wang, Z., and Ohara, T.: Interannual variation in the fine-mode MODIS aerosol optical depth and its relationship to the changes in sulfur dioxide emissions in China between 2000 and 2010, Atmos. Chem. Phys., 12, 2631-2640, 2012.

Jacob, D. J., Crawford, J. H., Maring, H., Clarke, A. D., Dibb, J. E., Emmons, L. K., Ferrare, R. A., Hostetler, C. A., Russell, P. B., Singh, H. B., Thompson, A. M., Shaw, G. E., McCauley, E., Pederson, J. R., and Fisher, J. A.: The Arctic Research of the Composition of the Troposphere from Aircraft and Satellites (ARCTAS) mission: design, execution, and first results, Atmos. Chem. Phys., 10, 5191-5212, doi:10.5194/acp-10-5191-2010, 2010.

Jacob, D. J., Turner, A. J., Maasakkers, J. D., Sheng, J., Sun, K., Liu, X., Chance, K., Aben, I., McKeever, J., and Frankenberg, C.: Satellite observations of atmospheric methane and their value for quantifying methane emissions, Atmos. Chem. Phys., 16, 14371-14396, 2016.

Jaeglé, L., Quinn, P. K., Bates, T. S., Alexander, B., and Lin, J. T.: Global distribution of sea salt aerosols: new constraints from in situ and remote sensing observations, Atmos. Chem. Phys., 11, 3137-3157, doi:10.5194/acp-11-3137-2011, 2011.

Jang, M., Czoschke, N. M., Lee, S., and Kamens, R. M.: Heterogeneous Atmospheric Aerosol Production by Acid-Catalyzed Particle-Phase Reactions, Science, 298, 814-817, 2002.

Jaswal, A. K., Kumar, N., Prasad, A. K., and Kafatos, M.: Decline in horizontal surface visibility over India (1961–2008) and its association with meteorological variables, Natural Hazards, 68, 929-954, doi:10.1007/s11069-013-0666-2, 2013.

Jethva, H., Torres, O., and Ahn, C.: Global assessment of OMI aerosol single-scattering albedo using ground-based AERONET inversion, J. Geophys. Res., 119, 9020-9040, 2014.

Johannes, Q., Olivier, B., Nicolas, B., and Stefan, K.: Satellite-based estimate of the direct and indirect aerosol climate forcing, J. Geophys. Res., 113, doi:10.1029/2007JD008962, 2008.

Kahn, R. A., and Gaitley, B. J.: An analysis of global aerosol type as retrieved by MISR, J. Geophys. Res., 120, 4248–4281, 2015.

Kaiser, J., Jacob, D. J., Zhu, L., Travis, K. R., Fisher, J. A., González Abad, G., Zhang, L., Zhang, X., Fried, A., Crounse, J. D., St. Clair, J. M., and Wisthaler, A.: High-resolution inversion of OMI formaldehyde columns to quantify isoprene emission on ecosystem-relevant scales: application to the southeast US, Atmos. Chem. Phys., 18, 5483-5497, 2018.

Kaufman, Y. J., Tanré, D., and Boucher, O.: A satellite view of aerosols in the climate system, Nature, 419, 215-223, 2002.

Keller, C. A., Long, M. S., Yantosca, R. M., Da Silva, A. M., Pawson, S., and Jacob, D. J.: HEMCO v1.0: a versatile, ESMF-compliant component for calculating emissions in atmospheric models, Geosci. Model Dev., 7, 1409-1417, 2014.

Kendall, M. G.: Rank correlation methods, Griffin, London, 1975.

Keppel-Aleks, G., and Washenfelder, R. A.: The effect of atmospheric sulfate reductions on diffuse radiation and photosynthesis in the United States during 1995–2013, Geophys. Res. Lett., 43, 9984-9993, doi:10.1002/2016GL070052, 2016.

Kessner, A. L., Wang, J., Levy, R. C., and Colarco, P. R.: Remote sensing of surface visibility from space: A look at the United States East Coast, Atmos. Environ., 81, 136-147, 2013.

Kettle, A. J., Andreae, M. O., Amouroux, D., Andreae, T. W., Bates, T. S., Berresheim, H., Bingemer, H., Boniforti, R., Curran, M. A. J., DiTullio, G. R., Helas, G., Jones, G. B., Keller, M. D., Kiene, R. P., Leck, C., Levasseur, M., Malin, G., Maspero, M., Matrai, P., McTaggart, A. R., Mihalopoulos, N., Nguyen, B. C., Novo, A., Putaud, J. P., Rapsomanikis, S., Roberts, G., Schebeske, G., Sharma, S., Simó, R., Staubes, R., Turner, S., and Uher, G.: A global database of sea surface dimethylsulfide (DMS) measurements and a procedure to predict sea surface DMS as a function of latitude, longitude, and month, Global Biogeochem. Cycles, 13, 399-444, 1999.

Khalizov, A. F., Zhang, R., Zhang, D., Xue, H., Pagels, J., and McMurry, P. H.: Formation of highly hygroscopic soot aerosols upon internal mixing with sulfuric acid vapor, J. Geophys. Res., 114, doi:10.1029/2008JD010595, 2009.

Kharol, S. K., Shephard, M. W., McLinden, C. A., Zhang, L., Sioris, C. E., O'Brien, J. M., Vet, R., Cady-Pereira, K. E., Hare, E., Siemons, J., and Krotkov, N. A.: Dry Deposition of Reactive Nitrogen From Satellite Observations of Ammonia and Nitrogen Dioxide Over North America, Geophys. Res. Lett., 45, 1157-1166, doi:10.1002/2017GL075832, 2018.

Kim, D., Chin, M., Remer, L. A., Diehl, T., Bian, H., Yu, H., Brown, M. E., and Stockwell, W. R.: Role of surface wind and vegetation cover in multi-decadal variations of dust emission in the Sahara and Sahel, Atmos. Environ., 148, 282-296, 2017.

Kim, N. K., Kim, Y. P., and Kang, C. H.: Long-term trend of aerosol composition and direct radiative forcing due to aerosols over Gosan: TSP, PM10, and PM2.5 data between 1992 and 2008, Atmos. Environ., 45, 6107-6115, 2011.

Kim, P. S., Jacob, D. J., Fisher, J. A., Travis, K., Yu, K., Zhu, L., Yantosca, R. M., Sulprizio, M. P., Jimenez, J. L., Campuzano-Jost, P., Froyd, K. D., Liao, J., Hair, J. W., Fenn, M. A., Butler, C. F., Wagner, N. L., Gordon, T. D., Welti, A., Wennberg, P. O., Crounse, J. D., St. Clair, J. M., Teng, A. P., Millet, D. B., Schwarz, J. P., Markovic, M. Z., and Perring, A. E.: Sources, seasonality, and trends of southeast US aerosol: an integrated analysis of surface, aircraft, and satellite observations with the GEOS-Chem chemical transport model, Atmos. Chem. Phys., 15, 10411-10433, 2015.

Kirkby, J., Curtius, J., Almeida, J., Dunne, E., Duplissy, J., Ehrhart, S., et al.: Role of sulphuric acid, ammonia and galactic cosmic rays in atmospheric aerosol nucleation, Nature, 476, 429-433, 2011.

Klingmüller, K., Pozzer, A., Metzger, S., Stenchikov, G. L., and Lelieveld, J.: Aerosol optical depth trend over the Middle East, Atmos. Chem. Phys., 16, 5063-5073, 2016.

Koren, I., Remer, L. A., and Longo, K.: Reversal of trend of biomass burning in the Amazon, Geophys. Res. Lett., 34, doi:10.1029/2007GL031530, 2007.

Kristiansen, N. I., Stohl, A., Olivié, D. J. L., Croft, B., Søvde, O. A., Klein, H., Christoudias, T., Kunkel, D., Leadbetter, S. J., Lee, Y. H., Zhang, K., Tsigaridis, K., Bergman, T., Evangeliou, N., Wang, H., Ma, P. L., Easter, R. C., Rasch, P. J., Liu, X., Pitari, G., Di Genova, G., Zhao, S. Y., Balkanski, Y., Bauer, S. E., Faluvegi, G. S., Kokkola, H., Martin, R. V., Pierce, J. R., Schulz, M., Shindell, D., Tost, H., and Zhang, H.: Evaluation of observed and modelled aerosol lifetimes using radioactive tracers of opportunity and an ensemble of 19 global models, Atmos. Chem. Phys., 16, 3525-3561, 2016.

Kuhns, H., Knipping, E. M., and Vukovich, J. M.: Development of a United States–Mexico Emissions Inventory for the Big Bend Regional Aerosol and Visibility Observational (BRAVO) Study, J. Air Waste Manag. Assoc., 55, 677-692, 2005.

Kulmala, M., Asmi, A., Lappalainen, H. K., Baltensperger, U., Brenguier, J. L., Facchini, M. C., et al.: General overview: European Integrated project on Aerosol Cloud Climate and Air Quality interactions (EUCAARI) – integrating aerosol research from nano to global scales, Atmos. Chem. Phys., 11, 13061-13143, doi:10.5194/acp-11-13061-2011, 2011.

Lacey, F. G., Henze, D. K., Lee, C. J., van Donkelaar, A., and Martin, R. V.: Transient climate and ambient health impacts due to national solid fuel cookstove emissions, Proc. Natl. Acad. Sci. U.S.A., 114, 1269-1274, 2017.

Lack, D. A., and Cappa, C. D.: Impact of brown and clear carbon on light absorption enhancement, single scatter albedo and absorption wavelength dependence of black carbon, Atmos. Chem. Phys., 10, 4207-4220, doi:10.5194/acp-10-4207-2010, 2010.

Lamsal, L. N., Martin, R. V., Padmanabhan, A., van Donkelaar, A., Zhang, Q., Sioris, C. E., Chance, K., Kurosu, T. P., and Newchurch, M. J.: Application of satellite observations for timely updates to global anthropogenic NOx emission inventories, Geophys. Res. Lett., 38, doi:10.1029/2010GL046476, 2011.

Lee, C., Martin, R. V., van Donkelaar, A., Lee, H., Dickerson, R. R., Hains, J. C., Krotkov, N., Richter, A., Vinnikov, K., and Schwab, J. J.: SO2 emissions and lifetimes: Estimates from inverse modeling using in situ and global, space-based (SCIAMACHY and OMI) observations, J. Geophys. Res., 116, doi:10.1029/2010JD014758, 2011.

Lee, C. J., Martin, R. V., Henze, D. K., Brauer, M., Cohen, A., and van Donkelaar, A.: Response of Global Particulate-Matter-Related Mortality to Changes in Local Precursor Emissions, Environ. Sci. Technol., 49, 4335-4344, doi:10.1021/acs.est.5b00873, 2015a.

Lee, H.-J., Kang, J.-E., and Kim, C.-H.: Forty-year (1971–2010) semiquantitative observations of visibility-cloud-precipitation in Korea and its implication for aerosol effects on regional climate, J. Air Waste Manag. Assoc., 65, 788-799, 2015b.

Leibensperger, E. M., Mickley, L. J., Jacob, D. J., Chen, W. T., Seinfeld, J. H., Nenes, A., Adams, P. J., Streets, D. G., Kumar, N., and Rind, D.: Climatic effects of 1950 – 2050 changes in US anthropogenic aerosols – Part 1: Aerosol trends and radiative forcing, Atmos. Chem. Phys., 12, 3333-3348, doi:10.5194/acp-12-3333-2012, 2012.

Lelieveld, J., Evans, J. S., Fnais, M., Giannadaki, D., and Pozzer, A.: The contribution of outdoor air pollution sources to premature mortality on a global scale, Nature, 525, 367-371, 2015.

Lesins, G., Chylek, P., and Lohmann, U.: A study of internal and external mixing scenarios and its effect on aerosol optical properties and direct radiative forcing, J. Geophys. Res., 107, doi:10.1029/2001JD000973, 2002.

Levelt, P. F., Joiner, J., Tamminen, J., Veefkind, J. P., Bhartia, P. K., Stein Zweers, D. C., Duncan, B. N., Streets, D. G., Eskes, H., van der A, R., McLinden, C., Fioletov, V., Carn, S., de Laat, J., DeLand, M., Marchenko, S., McPeters, R., Ziemke, J., Fu, D., Liu, X., Pickering, K., Apituley, A., González Abad, G., Arola, A., Boersma, F., Chan Miller, C., Chance, K., de Graaf, M., Hakkarainen, J., Hassinen, S., Ialongo, I., Kleipool, Q., Krotkov, N., Li, C., Lamsal, L., Newman, P., Nowlan, C., Suleiman, R., Tilstra, L. G., Torres, O., Wang, H., and Wargan, K.: The Ozone Monitoring Instrument: overview of 14 years in space, Atmos. Chem. Phys., 18, 5699-5745, 2018.

Levy, R. C., Munchak, L. A., Mattoo, S., Patadia, F., Remer, L. A., and Holz, R. E.: Towards a long-term global aerosol optical depth record: applying a consistent aerosol retrieval algorithm to MODIS and VIIRS-observed reflectance, Atmos. Meas. Tech., 8, 4083-4110, 2015.

Li, C., Zhang, Q., Krotkov, N. A., Streets, D. G., He, K., Tsay, S. C., and Gleason, J. F.: Recent large reduction in sulfur dioxide emissions from Chinese power plants observed by the Ozone Monitoring Instrument, Geophys. Res. Lett., 37, doi:10.1029/2010GL042594, 2010.

Li, C., Xue, Y., von Hoyningen-Huene, W., Zhang, J., and Pan, P.: Quantitative evaluation of uncertainties in satellite retrieval of dust-like aerosols induced by spherical assumption, J. Quant. Spectrosc. Radiat. Transfer, 136, 45-57, 2014a.

Li, C., Martin, R. V., Boys, B. L., van Donkelaar, A., and Ruzzante, S.: Evaluation and application of multi-decadal visibility data for trend analysis of atmospheric haze, Atmos. Chem. Phys., 16, 2435-2457, doi:10.5194/acp-16-2435-2016, 2016a.

Li, C., Martin, R. V., van Donkelaar, A., Boys, B. L., Hammer, M. S., Xu, J.-W., Marais, E. A., Reff, A., Strum, M., Ridley, D. A., Crippa, M., Brauer, M., and Zhang, Q.: Trends in Chemical Composition of Global and Regional Population-Weighted Fine Particulate Matter Estimated for 25 Years, Environ. Sci. Technol., 51, 11185-11195, 2017a.

Li, H., Zhang, Q., Zheng, B., Chen, C., Wu, N., Guo, H., Zhang, Y., Zheng, Y., Li, X., and He, K.: Nitrate-driven urban haze pollution during summertime over the North China Plain, Atmos. Chem. Phys., 18, 5293-5306, doi:10.5194/acp-18-5293-2018, 2018a.

Li, J., Carlson, B. E., Dubovik, O., and Lacis, A. A.: Recent trends in aerosol optical properties derived from AERONET measurements, Atmos. Chem. Phys., 14, 12271-12289, 2014b.

Li, J., Li, C., and Zhao, C.: Different trends in extreme and median surface aerosol extinction coefficients over China inferred from quality-controlled visibility data, Atmos. Chem. Phys., 18, 3289-3298, doi:10.5194/acp-18-3289-2018, 2018b.

Li, K., Liao, H., Zhu, J., and Moch, J. M.: Implications of RCP emissions on future PM2.5 air quality and direct radiative forcing over China, J. Geophys. Res., 121, 12,985-913,008, 2016b.

Li, M., Zhang, Q., Kurokawa, J. I., Woo, J. H., He, K., Lu, Z., Ohara, T., Song, Y., Streets, D. G., Carmichael, G. R., Cheng, Y., Hong, C., Huo, H., Jiang, X., Kang, S., Liu, F., Su, H., and Zheng, B.: MIX: a mosaic Asian anthropogenic emission inventory under the international collaboration framework of the MICS-Asia and HTAP, Atmos. Chem. Phys., 17, 935-963, 2017b.

Li, Y., Henze, D. K., Jack, D., and Kinney, P. L.: The influence of air quality model resolution on health impact assessment for fine particulate matter and its components, Air Qual. Atmos. Health, 9, 51-68, doi:10.1007/s11869-015-0321-z, 2016c.

Li, Z., Zhao, X., Kahn, R., Mishchenko, M., Remer, L., Lee, K. H., Wang, M., Laszlo, I., Nakajima, T., and Maring, H.: Uncertainties in satellite remote sensing of aerosols and impact on monitoring its long-term trend: a review and perspective, Ann. Geophys., 27, 2755-2770, 2009.

Li, Z., Gu, X., Wang, L., Li, D., Xie, Y., Li, K., Dubovik, O., Schuster, G., Goloub, P., Zhang, Y., Li, L., Ma, Y., and Xu, H.: Aerosol physical and chemical properties retrieved from ground-based remote sensing measurements during heavy haze days in Beijing winter, Atmos. Chem. Phys., 13, 10171-10183, doi:10.5194/acp-13-10171-2013, 2013.

Lim, S. S., Vos, T., Flaxman, A. D., Danaei, G., Shibuya, K., Adair-Rohani, H., et al.: A comparative risk assessment of burden of disease and injury attributable to 67 risk factors and risk factor clusters in 21 regions, 1990 – 2010: a systematic analysis for the Global Burden of Disease Study 2010, The Lancet, 380, 2224-2260, 2012.

Lin, J.-T., and McElroy, M. B.: Impacts of boundary layer mixing on pollutant vertical profiles in the lower troposphere: Implications to satellite remote sensing, Atmos. Environ., 44, 1726-1739, doi:http://dx.doi.org/10.1016/j.atmosenv.2010.02.009, 2010.

Lin, J., van Donkelaar, A., Xin, J., Che, H., and Wang, Y.: Clear-sky aerosol optical depth over East China estimated from visibility measurements and chemical transport modeling, Atmos. Environ., 95, 258-267, 2014.

Liu, H., Jacob, D. J., Bey, I., and Yantosca, R. M.: Constraints from 210Pb and 7Be on wet deposition and transport in a global three-dimensional chemical tracer model driven by assimilated meteorological fields, J. Geophys. Res., 106, 12109-12128, 2001.

Logan, T., Xi, B., Dong, X., Obrecht, R., Li, Z., and Cribb, M.: A study of Asian dust plumes using satellite, surface, and aircraft measurements during the INTEX-B field experiment, J. Geophys. Res., 115, doi:10.1029/2010JD014134, 2010.

Lu, Z., Streets, D. G., Zhang, Q., Wang, S., Carmichael, G. R., Cheng, Y. F., Wei, C., Chin, M., Diehl, T., and Tan, Q.: Sulfur dioxide emissions in China and sulfur trends in East Asia since 2000, Atmos. Chem. Phys., 10, 6311-6331, 2010.

Lu, Z., Zhang, Q., and Streets, D. G.: Sulfur dioxide and primary carbonaceous aerosol emissions in China and India, 1996–2010, Atmos. Chem. Phys., 11, 9839-9864, 2011.

Lu, Z., Streets, D. G., de Foy, B., Lamsal, L. N., Duncan, B. N., and Xing, J.: Emissions of nitrogen oxides from US urban areas: estimation from Ozone Monitoring Instrument retrievals for 2005–2014, Atmos. Chem. Phys., 15, 10367-10383, 2015.

Luo, Y., Lu, D., Zhou, X., Li, W., and He, Q.: Characteristics of the spatial distribution and yearly variation of aerosol optical depth over China in last 30 years, J. Geophys. Res., 106, 14501-14513, 2001.

Ma, Q., Cai, S., Wang, S., Zhao, B., Martin, R. V., Brauer, M., Cohen, A., Jiang, J., Zhou, W., Hao, J., Frostad, J., Forouzanfar, M. H., and Burnett, R. T.: Impacts of coal burning on ambient PM2.5 pollution in China, Atmos. Chem. Phys., 17, 4477-4491, 2017.

Ma, Z., Hu, X., Sayer, A. M., Levy, R., Zhang, Q., Xue, Y., Tong, S., Bi, J., Huang, L., and Liu, Y.: Satellite-based spatiotemporal trends in PM2. 5 concentrations: China, 2004–2013, Environ. Health Perspect., 124, doi:10.1289/ehp.1409481, 2016.

Mahowald, N., Ballantine, J., Feddema, J., and Ramankutty, N.: Global trends in visibility: implications for dust sources, Atmos. Chem. Phys., 7, 3309-3339, 2007.

Malm, W. C., Sisler, J. F., Huffman, D., Eldred, R. A., and Cahill, T. A.: Spatial and seasonal trends in particle concentration and optical extinction in the United States, J. Geophys. Res., 99, 1347-1370, doi:10.1029/93JD02916, 1994.

Malm, W. C., Schichtel, B. A., Ames, R. B., and Gebhart, K. A.: A 10-year spatial and temporal trend of sulfate across the United States, J. Geophys. Res., 107, doi:10.1029/2002JD002107, 2002.

Malm, W. C., Schichtel, B. A., Hand, J. L., and Collett, J. L.: Concurrent Temporal and Spatial Trends in Sulfate and Organic Mass Concentrations Measured in the IMPROVE Monitoring Program, J. Geophys. Res., 122, 10,462-410,476, 2017.

Mann, H. B.: Nonparametric Tests Against Trend, Econometrica, 13, 245-259, 1945.

Marais, E. A., Jacob, D. J., Jimenez, J. L., Campuzano-Jost, P., Day, D. A., Hu, W., Krechmer, J., Zhu, L., Kim, P. S., Miller, C. C., Fisher, J. A., Travis, K., Yu, K., Hanisco, T. F., Wolfe, G. M., Arkinson, H. L., Pye, H. O. T., Froyd, K. D., Liao, J., and McNeill, V. F.: Aqueous-phase mechanism for secondary organic aerosol formation from isoprene: application to the southeast United States and co-benefit of SO2 emission controls, Atmos. Chem. Phys., 16, 1603-1618, 2016.

Marais, E. A., Jacob, D., Turner, J., and Mickley, L.: Evidence of 1991-2013 decrease of biogenic secondary organic aerosol in response to SO_2 emission controls, Environ. Res. Lett., doi:10.1088/1748-9326/aa69c8, 2017.

Marlier, M. E., DeFries, R. S., Voulgarakis, A., Kinney, P. L., Randerson, J. T., Shindell, D. T., Chen, Y., and Faluvegi, G.: El Nino and health risks from landscape fire emissions in southeast Asia, Nat. Clim. Change, 3, 131-136, 2013.

Martin, R. V., Jacob, D. J., Chance, K., Kurosu, T. P., Palmer, P. I., and Evans, M. J.: Global inventory of nitrogen oxide emissions constrained by space-based observations of NO2 columns, J. Geophys. Res., 108, doi:10.1029/2003JD003453, 2003a.

Martin, R. V., Jacob, D. J., Yantosca, R. M., Chin, M., and Ginoux, P.: Global and regional decreases in tropospheric oxidants from photochemical effects of aerosols, J. Geophys. Res., 108, doi:10.1029/2002JD002622, 2003b.

Martin, S. T., Andreae, M. O., Althausen, D., Artaxo, P., Baars, H., Borrmann, S., Chen, Q., Farmer, D. K., Guenther, A., Gunthe, S. S., Jimenez, J. L., Karl, T., Longo, K., Manzi, A., Müller, T., Pauliquevis, T., Petters, M. D., Prenni, A. J., Pöschl, U., Rizzo, L. V., Schneider, J., Smith, J. N., Swietlicki, E., Tota, J., Wang, J., Wiedensohler, A., and Zorn, S. R.: An overview of the Amazonian Aerosol Characterization Experiment 2008 (AMAZE-08), Atmos. Chem. Phys., 10, 11415-11438, 2010a.

Martin, S. T., Andreae, M. O., Artaxo, P., Baumgardner, D., Chen, Q., Goldstein, A. H., Guenther, A., Heald, C. L., Mayol-Bracero, O. L., McMurry, P. H., Pauliquevis, T., Pöschl, U., Prather, K. A., Roberts, G. C., Saleska, S. R., Silva, D. M. A., Spracklen, D. V., Swietlicki, E., and Trebs, I.: Sources and properties of Amazonian aerosol particles, Rev. Geophys., 48, doi:10.1029/2008RG000280, 2010b.

Matsui, H., and Koike, M.: Enhancement of aerosol responses to changes in emissions over East Asia by gas-oxidant-aerosol coupling and detailed aerosol processes, J. Geophys. Res., 121, 7161-7171, doi:10.1002/2015JD024671, 2016.

McDonald, B. C., Goldstein, A. H., and Harley, R. A.: Long-Term Trends in California Mobile Source Emissions and Ambient Concentrations of Black Carbon and Organic Aerosol, Environ. Sci. Technol., 49, 5178-5188, doi:10.1021/es505912b, 2015.

McLinden, C. A., Fioletov, V., Shephard, M. W., Krotkov, N., Li, C., Martin, R. V., Moran, M. D., and Joiner, J.: Space-based detection of missing sulfur dioxide sources of global air pollution, Nat. Geosci., 9, 496, doi:10.1038/ngeo2724, 2016.

Mehta, M., Singh, R., Singh, A., Singh, N., and Anshumali: Recent global aerosol optical depth variations and trends — A comparative study using MODIS and MISR level 3 datasets, Remote Sens. Environ., 181, 137-150, 2016.

Meng, J., Martin, R. V., Li, C., van Donkelaar, A., Hystad, P., Brauer, M., Estimated long-term historical (1981-2016) concentrations of ambient fine particulate matter over north america from chemical transport modeling, satellite remote sensing and ground-based measurements, manuscript in preparation for Environ. Sci. Technol., 2018.

Meng, Z., Yang, P., Kattawar, G. W., Bi, L., Liou, K. N., and Laszlo, I.: Single-scattering properties of tri-axial ellipsoidal mineral dust aerosols: A database for application to radiative transfer calculations, J. Aerosol Sci., 41, 501-512, 2010.

Mercado, L. M., Bellouin, N., Sitch, S., Boucher, O., Huntingford, C., Wild, M., and Cox, P. M.: Impact of changes in diffuse radiation on the global land carbon sink, Nature, 458, 1014, 2009.

Mitchell, R. M., Forgan, B. W., and Campbell, S. K.: The Climatology of Australian Aerosol, Atmos. Chem. Phys., 17, 5131-5154, doi:10.5194/acp-17-5131-2017, 2017.

Molod, A., Takacs, L., Suarez, M., and Bacmeister, J.: Development of the GEOS-5 atmospheric general circulation model: evolution from MERRA to MERRA2, Geosci. Model Dev., 8, 1339-1356, doi:10.5194/gmd-8-1339-2015, 2015.

Murphy, D. M., Chow, J. C., Leibensperger, E. M., Malm, W. C., Pitchford, M., Schichtel, B. A., Watson, J. G., and White, W. H.: Decreases in elemental carbon and fine particle mass in the United States, Atmos. Chem. Phys., 11, 4679-4686, 2011.

Murray, L. T., Jacob, D. J., Logan, J. A., Hudman, R. C., and Koshak, W. J.: Optimized regional and interannual variability of lightning in a global chemical transport model constrained by LIS/OTD satellite data, J. Geophys. Res., 117, doi:10.1029/2012JD017934, 2012.

Myhre, G., Aas, W., Cherian, R., Collins, W., Faluvegi, G., Flanner, M., Forster, P., Hodnebrog, Ø., Klimont, Z., Lund, M. T., Mülmenstädt, J., Lund Myhre, C., Olivié, D., Prather, M., Quaas, J., Samset, B. H., Schnell, J. L., Schulz, M., Shindell, D., Skeie, R. B., Takemura, T., and Tsyro, S.: Multi-model simulations of aerosol and ozone radiative forcing due to anthropogenic emission changes during the period 1990–2015, Atmos. Chem. Phys., 17, 2709-2720, 2017.

Ng, N. L., Chhabra, P. S., Chan, A. W. H., Surratt, J. D., Kroll, J. H., Kwan, A. J., McCabe, D. C., Wennberg, P. O., Sorooshian, A., Murphy, S. M., Dalleska, N. F., Flagan, R. C., and Seinfeld, J. H.: Effect of NO_x level on secondary organic aerosol (SOA) formation from the photooxidation of terpenes, Atmos. Chem. Phys., 7, 5159-5174, 2007.

Nguyen, T. K. V., Capps, S. L., and Carlton, A. G.: Decreasing Aerosol Water Is Consistent with OC Trends in the Southeast U.S, Environ. Sci. Technol., 49, 7843-7850, 2015.

Nguyen, T. K. V., Ghate, V. P., and Carlton, A. G.: Reconciling satellite aerosol optical thickness and surface fine particle mass through aerosol liquid water, Geophys. Res. Lett., 43, 11,903-911,912, doi:10.1002/2016GL070994, 2016.

Norris, J. R., and Wild, M.: Trends in aerosol radiative effects over China and Japan inferred from observed cloud cover, solar "dimming," and solar "brightening", J. Geophys. Res., 114, doi:10.1029/2008JD011378, 2009.

O'Neill, N. T., Eck, T. F., Smirnov, A., Holben, B. N., and Thulasiraman, S.: Spectral discrimination of coarse and fine mode optical depth, J. Geophys. Res., 108, doi:10.1029/2002JD002975, 2003.

Ohara, T., Akimoto, H., Kurokawa, J., Horii, N., Yamaji, K., Yan, X., and Hayasaka, T.: An Asian emission inventory of anthropogenic emission sources for the period 1980 – 2020, Atmos. Chem. Phys., 7, 4419-4444, 2007.

Olivier, J., Bouwman, A., Van der Maas, C., and Berdowski, J.: Emission database for global atmospheric research (EDGAR), Environ. Monit. Assess., 31, 93-106, 1994.

Pöschl, U.: Atmospheric aerosols: composition, transformation, climate and health effects, Angew. Chem. Int. Ed. Engl., 44, 7520-7540, 2005.

Papadimas, C. D., Hatzianastassiou, N., Mihalopoulos, N., Querol, X., and Vardavas, I.: Spatial and temporal variability in aerosol properties over the Mediterranean basin based on 6-year (2000–2006) MODIS data, J. Geophys. Res., 113, doi:10.1029/2007JD009189, 2008.

Park, R. J., Jacob, D. J., Chin, M., and Martin, R. V.: Sources of carbonaceous aerosols over the United States and implications for natural visibility, J. Geophys. Res., 108, doi:10.1029/2002JD003190, 2003.

Park, R. J., Jacob, D. J., Field, B. D., Yantosca, R. M., and Chin, M.: Natural and transboundary pollution influences on sulfate-nitrate-ammonium aerosols in the United States: Implications for policy, J. Geophys. Res., 109, doi:10.1029/2003JD004473, 2004.

Paul, G., M., P. J., E., G. T., Christina, H. N., and Ming, Z.: Global-scale attribution of anthropogenic and natural dust sources and their emission rates based on MODIS Deep Blue aerosol products, Rev. Geophys., 50, doi:10.1029/2012RG000388, 2012.

Paulot, F., Jacob, D. J., Pinder, R. W., Bash, J. O., Travis, K., and Henze, D. K.: Ammonia emissions in the United States, European Union, and China derived by high-resolution inversion of ammonium wet deposition data: Interpretation with a new agricultural emissions inventory (MASAGE_NH3), J. Geophys. Res., 119, 4343-4364, 2014.

Paulot, F., Fan, S., and Horowitz, L. W.: Contrasting seasonal responses of sulfate aerosols to declining SO2 emissions in the Eastern U.S.: Implications for the efficacy of SO2 emission controls, Geophys. Res. Lett., 44, 455-464, doi:10.1002/2016GL070695, 2017.

Philip, S., Martin, R. V., Pierce, J. R., Jimenez, J. L., Zhang, Q., Canagaratna, M. R., Spracklen, D. V., Nowlan, C. R., Lamsal, L. N., Cooper, M. J., and Krotkov, N. A.: Spatially and seasonally resolved estimate of the ratio of organic mass to organic carbon, Atmos. Environ., 87, 34-40, doi:http://dx.doi.org/10.1016/j.atmosenv.2013.11.065, 2014a.

Philip, S., Martin, R. V., van Donkelaar, A., Lo, J. W.-H., Wang, Y., Chen, D., Zhang, L., Kasibhatla, P. S., Wang, S., and Zhang, Q.: Global chemical composition of ambient fine particulate matter for exposure assessment, Environ. Sci. Technol., 48, 13060-13068, 2014b.

Philip, S., Martin, R. V., and Keller, C. A.: Sensitivity of chemistry-transport model simulations to the duration of chemical and transport operators: a case study with GEOS-Chem v10-01, Geosci. Model Dev., 9, 1683-1695, doi:10.5194/gmd-9-1683-2016, 2016.

Philip, S., Martin, R. V., Snider, G., Weagle, C. L., Donkelaar, A. v., Brauer, M., Henze, D. K., Klimont, Z., Venkataraman, C., Guttikunda, S. K., and Zhang, Q.: Anthropogenic fugitive, combustion and industrial dust is a significant, underrepresented fine particulate matter source in global atmospheric models, Environ. Res. Lett., 12, 044018, 2017.

Pinault, L., Tjepkema, M., Crouse, D. L., Weichenthal, S., van Donkelaar, A., Martin, R. V., Brauer, M., Chen, H., and Burnett, R. T.: Risk estimates of mortality attributed to low concentrations of ambient fine particulate matter in the Canadian community health survey cohort, Environ. Health, 15, doi:10.1186/s12940-016-0111-6, 2016.

Pinder, R. W., Dennis, R. L., and Bhave, P. V.: Observable indicators of the sensitivity of PM2.5 nitrate to emission reductions—Part I: Derivation of the adjusted gas ratio and applicability at regulatory-relevant time scales, Atmos. Environ., 42, 1275-1286, 2008a.

Pinder, R. W., Gilliland, A. B., and Dennis, R. L.: Environmental impact of atmospheric NH3 emissions under present and future conditions in the eastern United States, Geophys. Res. Lett., 35, doi:10.1029/2008GL033732, 2008b.

Pitchford, M., Malm, W., Schichtel, B., Kumar, N., Lowenthal, D., and Hand, J.: Revised algorithm for estimating light extinction from IMPROVE particle speciation data, J. Air Waste Manag. Assoc., 57, 1326-1336, 2007.

Pozzer, A., de Meij, A., Yoon, J., Tost, H., Georgoulias, A. K., and Astitha, M.: AOD trends during 2001–2010 from observations and model simulations, Atmos. Chem. Phys., 15, 5521-5535, doi:10.5194/acp-15-5521-2015, 2015.

Price, C., and Rind, D.: A simple lightning parameterization for calculating global lightning distributions, J. Geophys. Res., 97, 9919-9933, doi:10.1029/92JD00719, 1992.

Prospero, J. M., and Lamb, P. J.: African Droughts and Dust Transport to the Caribbean: Climate Change Implications, Science, 302, 1024-1027, 2003.

Punger, E. M., and West, J. J.: The effect of grid resolution on estimates of the burden of ozone and fine particulate matter on premature mortality in the USA, Air Qual. Atmos. Health, 6, 563-573, doi:10.1007/s11869-013-0197-8, 2013.

Purves, D. W., Caspersen, J. P., Moorcroft, P. R., Hurtt, G. C., and Pacala, S. W.: Human-induced changes in US biogenic volatile organic compound emissions: evidence from long-term forest inventory data, Glob. Change Biol., 10, 1737-1755, 2004.

Putaud, J. P., Van Dingenen, R., Alastuey, A., Bauer, H., Birmili, W., Cyrys, J., Flentje, H., Fuzzi, S., Gehrig, R., Hansson, H. C., Harrison, R. M., Herrmann, H., Hitzenberger, R., Hüglin, C., Jones, A. M., Kasper-Giebl, A., Kiss, G., Kousa, A., Kuhlbusch, T. A. J., Löschau, G., Maenhaut, W., Molnar, A., Moreno, T., Pekkanen, J., Perrino, C., Pitz, M., Puxbaum, H., Querol, X., Rodriguez, S., Salma, I., Schwarz, J., Smolik, J., Schneider, J., Spindler, G., ten Brink, H., Tursic, J., Viana, M., Wiedensohler, A., and Raes, F.: A European aerosol phenomenology – 3: Physical and chemical characteristics of particulate matter from 60 rural, urban, and kerbside sites across Europe, Atmos. Environ., 44, 1308-1320, doi:http://dx.doi.org/10.1016/j.atmosenv.2009.12.011, 2010.

Pye, H. O. T., Liao, H., Wu, S., Mickley, L. J., Jacob, D. J., Henze, D. K., and Seinfeld, J. H.: Effect of changes in climate and emissions on future sulfate-nitrate-ammonium aerosol levels in the United States, J. Geophys. Res., 114, doi:10.1029/2008JD010701, 2009.

Pye, H. O. T., Chan, A. W. H., Barkley, M. P., and Seinfeld, J. H.: Global modeling of organic aerosol: the importance of reactive nitrogen (NO_x and NO_3), Atmos. Chem. Phys., 10, 11261-11276, doi:10.5194/acp-10-11261-2010, 2010.

Pye, H. O. T., and Seinfeld, J. H.: A global perspective on aerosol from low-volatility organic compounds, Atmos. Chem. Phys., 10, 4377-4401, 2010.

Pye, H. O. T., Pinder, R. W., Piletic, I. R., Xie, Y., Capps, S. L., Lin, Y.-H., Surratt, J. D., Zhang, Z., Gold, A., Luecken, D. J., Hutzell, W. T., Jaoui, M., Offenberg, J. H., Kleindienst, T. E., Lewandowski, M., and Edney, E. O.: Epoxide Pathways Improve Model Predictions of Isoprene Markers and Reveal Key Role of Acidity in Aerosol Formation, Environ. Sci. Technol., 47, 11056-11064, doi:10.1021/es402106h, 2013.

Pye, H. O. T., Murphy, B. N., Xu, L., Ng, N. L., Carlton, A. G., Guo, H., Weber, R., Vasilakos, P., Appel, K. W., Budisulistiorini, S. H., Surratt, J. D., Nenes, A., Hu, W., Jimenez, J. L., Isaacman-VanWertz, G., Misztal, P. K., and Goldstein, A. H.: On the implications of aerosol liquid water and phase separation for organic aerosol mass, Atmos. Chem. Phys., 17, 343-369, 2017.

Qu, W., Wang, J., Gao, S., and Wu, T.: Effect of the strengthened western Pacific subtropical high on summer visibility decrease over eastern China since 1973, J. Geophys. Res., 118, 7142-7156, 2013.

Qu, Z., Henze, D. K., Capps, S. L., Wang, Y., Xu, X., Wang, J., and Keller, M.: Monthly top-down NOx emissions for China (2005–2012): A hybrid inversion method and trend analysis, J. Geophys. Res., 122, 4600-4625, doi:10.1002/2016JD025852, 2017.

Quan, J., Zhang, Q., He, H., Liu, J., Huang, M., and Jin, H.: Analysis of the formation of fog and haze in North China Plain (NCP), Atmos. Chem. Phys., 11, 8205-8214, 2011.

Querol, X., Alastuey, A., Pandolfi, M., Reche, C., Pérez, N., Minguillón, M. C., Moreno, T., Viana, M., Escudero, M., Orio, A., Pallarés, M., and Reina, F.: 2001–2012 trends on air quality in Spain, Sci. Total Environ., 490, 957-969, 2014.

Ram, K., Sarin, M. M., and Tripathi, S. N.: Temporal Trends in Atmospheric PM2.5, PM10, Elemental Carbon, Organic Carbon, Water-Soluble Organic Carbon, and Optical Properties: Impact of Biomass Burning Emissions in The Indo-Gangetic Plain, Environ. Sci. Technol., 46, 686-695, doi:10.1021/es202857w, 2012.

Ramanathan, V., Crutzen, P. J., Kiehl, J. T., and Rosenfeld, D.: Aerosols, Climate, and the Hydrological Cycle, Science, 294, 2119-2124, doi:10.1126/science.1064034, 2001.

Reddington, C. L., Butt, E. W., Ridley, D. A., Artaxo, P., Morgan, W. T., Coe, H., and Spracklen, D. V.: Air quality and human health improvements from reductions in deforestation-related fire in Brazil, Nat. Geosci., 8, 768-771, doi:10.1038/ngeo2535, 2015.

Reeves, J., Chen, J., Wang, X. L., Lund, R., and Lu, Q. Q.: A review and comparison of changepoint detection techniques for climate data, J. Appl. Meteorol. Climatol., 46, 900-915, 2007.

Reff, A., Bhave, P. V., Simon, H., Pace, T. G., Pouliot, G. A., Mobley, J. D., and Houyoux, M.: Emissions Inventory of PM2.5 Trace Elements across the United States, Environ. Sci. Technol., 43, 5790-5796, doi:10.1021/es802930x, 2009.

Ridley, D. A., Heald, C. L., and Ford, B.: North African dust export and deposition: A satellite and model perspective, J. Geophys. Res., 117, doi:10.1029/2011JD016794, 2012.

Ridley, D. A., Heald, C. L., and Prospero, J. M.: What controls the recent changes in African mineral dust aerosol across the Atlantic?, Atmos. Chem. Phys., 14, 5735-5747, 2014.

Ridley, D. A., Heald, C. L., Kok, J. F., and Zhao, C.: An observationally constrained estimate of global dust aerosol optical depth, Atmos. Chem. Phys., 16, 15097-15117, 2016.

Ridley, D. A., Heald, C. L., Ridley, K. J., and Kroll, J. H.: Causes and consequences of decreasing atmospheric organic aerosol in the United States, Proc. Natl. Acad. Sci. U.S.A., 115, 290-295, 2018.

Rodgers, C. D.: Inverse methods for atmospheric sounding: theory and practice, edited by: Taylor, F. W., World Scientific, 2000.

Rollins, A. W., Browne, E. C., Min, K.-E., Pusede, S. E., Wooldridge, P. J., Gentner, D. R., Goldstein, A. H., Liu, S., Day, D. A., Russell, L. M., and Cohen, R. C.: Evidence for NO_x Control over Nighttime SOA Formation, Science, 337, 1210-1212, 2012.

Rosenfeld, D., Dai, J., Yu, X., Yao, Z., Xu, X., Yang, X., and Du, C.: Inverse relations between amounts of air pollution and orographic precipitation, Science, 315, 1396-1398, 2007.

Rosenfeld, D., Sherwood, S., Wood, R., and Donner, L.: Climate Effects of Aerosol-Cloud Interactions, Science, 343, 379-380, doi:10.1126/science.1247490, 2014.

Sayer, A. M., Hsu, N. C., Lee, J., Carletta, N., Chen, S.-H., and Smirnov, A.: Evaluation of NASA Deep Blue/SOAR aerosol retrieval algorithms applied to AVHRR measurements, J. Geophys. Res., 122, 9945-9967, doi:10.1002/2017JD026934, 2017.

Saylor, R., Myles, L., Sibble, D., Caldwell, J., and Xing, J.: Recent trends in gas-phase ammonia and PM2.5 ammonium in the Southeast United States, J. Air Waste Manag. Assoc., 65, 347-357, doi:10.1080/10962247.2014.992554, 2015.

Schaap, M., van Loon, M., ten Brink, H. M., Dentener, F. J., and Builtjes, P. J. H.: Secondary inorganic aerosol simulations for Europe with special attention to nitrate, Atmos. Chem. Phys., 4, 857-874, doi:10.5194/acp-4-857-2004, 2004.

Schichtel, B. A., Husar, R. B., Falke, S. R., and Wilson, W. E.: Haze trends over the United States, 1980–1995, Atmos. Environ., 35, 5205-5210, 2001.

Schichtel, B. A., Hand, J. L., Barna, M. G., Gebhart, K. A., Copeland, S., Vimont, J., and Malm, W. C.: Origin of Fine Particulate Carbon in the Rural United States, Environ. Sci. Technol., 51, 9846-9855, doi:10.1021/acs.est.7b00645, 2017.

Schultz, M.: Emission data sets and methodologies for estimating emissions, Reanalysis of the tropospheric chemical composition over the past 40 years—A long-term global modeling study of tropospheric chemistry funded under the 5th EU Framework Programme, EU contract EVK2-CT-2002-00170, Work Package 1, Eur. Comm., Brussels, in, 2007.

Schultz, M. G., Heil, A., Hoelzemann, J. J., Spessa, A., Thonicke, K., Goldammer, J. G., Held, A. C., Pereira, J. M. C., and van het Bolscher, M.: Global wildland fire emissions from 1960 to 2000, Global Biogeochem. Cycles, 22, doi:10.1029/2007GB003031, 2008.

Sen, P. K.: Estimates of the Regression Coefficient Based on Kendall's Tau, J. Am. Stat. Assoc., 63, 1379-1389, 1968.

Shah, V., Jaeglé, L., Thornton, J. A., Lopez-Hilfiker, F. D., Lee, B. H., Schroder, J. C., Campuzano-Jost, P., Jimenez, J. L., Guo, H., Sullivan, A. P., Weber, R. J., Green, J. R., Fiddler, M. N., Bililign, S., Campos, T. L., Stell, M., Weinheimer, A. J., Montzka, D. D., and Brown, S. S.: Chemical feedbacks weaken the wintertime response of particulate sulfate and nitrate to emissions reductions over the eastern United States, Proc. Natl. Acad. Sci. U.S.A., doi:10.1073/pnas.1803295115, 2018.

Shao, Y., Klose, M., and Wyrwoll, K.-H.: Recent global dust trend and connections to climate forcing, J. Geophys. Res., 118, 11,107-111,118, doi:10.1002/jgrd.50836, 2013.

Sheng, J. X., Jacob, D. J., Turner, A. J., Maasakkers, J. D., Sulprizio, M. P., Bloom, A. A., Andrews, A. E., and Wunch, D.: High-resolution inversion of methane emissions in the Southeast US using SEAC4RS aircraft observations of atmospheric methane: anthropogenic and wetland sources, Atmos. Chem. Phys., 18, 6483-6491, 2018.

Shephard, M. W., Cady-Pereira, K. E., Luo, M., Henze, D. K., Pinder, R. W., Walker, J. T., Rinsland, C. P., Bash, J. O., Zhu, L., Payne, V. H., and Clarisse, L.: TES ammonia retrieval strategy and global observations of the spatial and seasonal variability of ammonia, Atmos. Chem. Phys., 11, 10743-10763, doi:10.5194/acp-11-10743-2011, 2011.

Shephard, M. W., and Cady-Pereira, K. E.: Cross-track Infrared Sounder (CrIS) satellite observations of tropospheric ammonia, Atmos. Meas. Tech., 8, 1323-1336, 2015.

Shi, Y., Zhang, J., Reid, J. S., Holben, B., Hyer, E. J., and Curtis, C.: An analysis of the collection 5 MODIS over-ocean aerosol optical depth product for its implication in aerosol assimilation, Atmos. Chem. Phys., 11, 557-565, doi:10.5194/acp-11-557-2011, 2011.

Shilling, J. E., Zaveri, R. A., Fast, J. D., Kleinman, L., Alexander, M. L., Canagaratna, M. R., Fortner, E., Hubbe, J. M., Jayne, J. T., Sedlacek, A., Setyan, A., Springston, S., Worsnop, D. R., and Zhang, Q.: Enhanced SOA formation from mixed anthropogenic and biogenic emissions during the CARES campaign, Atmos. Chem. Phys., 13, 2091-2113, doi:10.5194/acp-13-2091-2013, 2013.

Shindell, D. T., Faluvegi, G., Koch, D. M., Schmidt, G. A., Unger, N., and Bauer, S. E.: Improved Attribution of Climate Forcing to Emissions, Science, 326, 716-718, 2009.

Silva, R. A., Adelman, Z., Fry, M. M., and West, J. J.: The impact of individual anthropogenic emissions sectors on the global burden of human mortality due to ambient air pollution, Environ. Health Perspect., 124, 1776-1784, 2016.

Silvern, R. F., Jacob, D. J., Kim, P. S., Marais, E. A., Turner, J. R., Campuzano-Jost, P., and Jimenez, J. L.: Inconsistency of ammonium–sulfate aerosol ratios with thermodynamic models in the eastern US: a possible role of organic aerosol, Atmos. Chem. Phys., 17, 5107-5118, 2017.

Sindelarova, K., Granier, C., Bouarar, I., Guenther, A., Tilmes, S., Stavrakou, T., Müller, J. F., Kuhn, U., Stefani, P., and Knorr, W.: Global data set of biogenic VOC emissions calculated by the MEGAN model over the last 30 years, Atmos. Chem. Phys., 14, 9317-9341, 2014.

Smith, A., Lott, N., and Vose, R.: The integrated surface database: Recent developments and partnerships, Bull. Am. Meteorol. Soc., 92, 704-708, 2011a.

Smith, S. J., Aardenne, J. v., Klimont, Z., Andres, R. J., Volke, A., and Delgado Arias, S.: Anthropogenic sulfur dioxide emissions: 1850–2005, Atmos. Chem. Phys., 11, 1101-1116, 2011b.

Smith, S. J., van Aardenne, J., Klimont, Z., Andres, R. J., Volke, A., and Delgado Arias, S.: Anthropogenic Sulfur Dioxide Emissions, 1850-2005: National and Regional Data Set by Source Category, Version 2.86, in, NASA Socioeconomic Data and Applications Center (SEDAC), Palisades, NY, 2011c.

Snider, G., Weagle, C. L., Murdymootoo, K. K., Ring, A., Ritchie, Y., Stone, E., Walsh, A., Akoshile, C., Anh, N. X., Balasubramanian, R., Brook, J., Qonitan, F. D., Dong, J., Griffith, D., He, K., Holben, B. N., Kahn, R., Lagrosas, N., Lestari, P., Ma, Z., Misra, A., Norford, L. K., Quel, E. J., Salam, A., Schichtel, B., Segev, L., Tripathi, S., Wang, C., Yu, C., Zhang, Q., Zhang, Y., Brauer, M., Cohen, A., Gibson, M. D., Liu, Y., Martins, J. V., Rudich, Y., and Martin, R. V.: Variation in global chemical composition of PM2.5: emerging results from SPARTAN, Atmos. Chem. Phys., 16, 9629-9653, 2016.

Stern, D. I.: Reversal of the trend in global anthropogenic sulfur emissions, Global Environmental Change, 16, 207-220, 2006.

Stettler, M. E. J., Eastham, S., and Barrett, S. R. H.: Air quality and public health impacts of UK airports. Part I: Emissions, Atmos. Environ., 45, 5415-5424, 2011.

Stevens, B., and Feingold, G.: Untangling aerosol effects on clouds and precipitation in a buffered system, Nature, 461, doi:10.1038/nature08281, 2009.

Stevens, C. J., Dise, N. B., Mountford, J. O., and Gowing, D. J.: Impact of Nitrogen Deposition on the Species Richness of Grasslands, Science, 303, 1876-1879, 2004.

Stjern, C. W., Stohl, A., and Kristjánsson, J. E.: Have aerosols affected trends in visibility and precipitation in Europe?, J. Geophys. Res., 116, doi:10.1029/2010JD014603, 2011.

Streets, D. G., Wu, Y., and Chin, M.: Two-decadal aerosol trends as a likely explanation of the global dimming/brightening transition, Geophys. Res. Lett., 33, doi:10.1029/2006GL026471, 2006.

Streets, D. G., Canty, T., Carmichael, G. R., de Foy, B., Dickerson, R. R., Duncan, B. N., Edwards, D. P., Haynes, J. A., Henze, D. K., Houyoux, M. R., Jacob, D. J., Krotkov, N. A., Lamsal, L. N., Liu, Y., Lu, Z., Martin, R. V., Pfister, G. G., Pinder, R. W., Salawitch, R. J., and Wecht, K. J.: Emissions estimation from satellite retrievals: A review of current capability, Atmos. Environ., 77, 1011-1042, 2013.

Sun, K., and Chen, X.: Spatio-temporal distribution of localized aerosol loading in China: A satellite view, Atmos. Environ., 163, 35-43, 2017.

Tørseth, K., Aas, W., Breivik, K., Fjæraa, A. M., Fiebig, M., Hjellbrekke, A. G., Lund Myhre, C., Solberg, S., and Yttri, K. E.: Introduction to the European Monitoring and Evaluation Programme (EMEP) and observed atmospheric composition change during 1972 – 2009, Atmos. Chem. Phys., 12, 5447-5481, doi:10.5194/acp-12-5447-2012, 2012.

Tai, A. P. K., Mickley, L. J., Heald, C. L., and Wu, S.: Effect of CO2 inhibition on biogenic isoprene emission: Implications for air quality under 2000 to 2050 changes in climate, vegetation, and land use, Geophys. Res. Lett., 40, 3479-3483, doi:10.1002/grl.50650, 2013.

Tang, W., Yang, K., Qin, J., Niu, X., Lin, C., and Jing, X.: A revisit to decadal change of aerosol optical depth and its impact on global radiation over China, Atmos. Environ., 150, 106-115, 2017.

Tang, W. J., Yang, K., Qin, J., Cheng, C. C. K., and He, J.: Solar radiation trend across China in recent decades: a revisit with quality-controlled data, Atmos. Chem. Phys., 11, 393-406, 2011.

Tiitta, P., Vakkari, V., Croteau, P., Beukes, J. P., van Zyl, P. G., Josipovic, M., Venter, A. D., Jaars, K., Pienaar, J. J., Ng, N. L., Canagaratna, M. R., Jayne, J. T., Kerminen, V. M., Kokkola, H., Kulmala, M., Laaksonen, A., Worsnop, D. R., and Laakso, L.: Chemical composition, main sources and temporal variability of PM_1 aerosols in southern African grassland, Atmos. Chem. Phys., 14, 1909-1927, doi:10.5194/acp-14-1909-2014, 2014.

Trivitayanurak, W., Adams, P. J., Spracklen, D. V., and Carslaw, K. S.: Tropospheric aerosol microphysics simulation with assimilated meteorology: model description and intermodel comparison, Atmos. Chem. Phys., 8, 3149-3168, 2008.

Tsigaridis, K., Daskalakis, N., Kanakidou, M., Adams, P. J., Artaxo, P., Bahadur, R., Balkanski, Y., Bauer, S. E., Bellouin, N., Benedetti, A., Bergman, T., Berntsen, T. K., Beukes, J. P., Bian, H., Carslaw, K. S., Chin, M., Curci, G., Diehl, T., Easter, R. C., Ghan, S. J., Gong, S. L., Hodzic, A., Hoyle, C. R., Iversen, T., Jathar, S., Jimenez, J. L., Kaiser, J. W., Kirkevåg, A., Koch, D., Kokkola, H., Lee, Y. H., Lin, G., Liu, X., Luo, G., Ma, X., Mann, G. W., Mihalopoulos, N., Morcrette, J. J., Müller, J. F., Myhre, G., Myriokefalitakis, S., Ng, N. L., O'Donnell, D., Penner, J. E., Pozzoli, L., Pringle, K. J., Russell, L. M., Schulz, M., Sciare, J., Seland, Ø., Shindell, D. T., Sillman, S., Skeie, R. B., Spracklen, D., Stavrakou, T., Steenrod, S. D., Takemura, T., Tiitta, P., Tilmes, S., Tost, H., van Noije, T., van Zyl, P. G., von Salzen, K., Yu, F., Wang, Z., Wang, Z., Zaveri, R. A., Zhang, H., Zhang, K., Zhang, Q., and Zhang, X.: The AeroCom evaluation and intercomparison of organic aerosol in global models, Atmos. Chem. Phys., 14, 10845-10895, 2014.

Turner, A. J., Henze, D. K., Martin, R. V., and Hakami, A.: The spatial extent of source influences on modeled column concentrations of short-lived species, Geophys. Res. Lett., 39, doi:10.1029/2012GL051832, 2012.

Turner, A. J., and Jacob, D. J.: Balancing aggregation and smoothing errors in inverse models, Atmos. Chem. Phys., 15, 7039-7048, doi:10.5194/acp-15-7039-2015, 2015.

Turner, A. J., Jacob, D. J., Wecht, K. J., Maasakkers, J. D., Lundgren, E., Andrews, A. E., Biraud, S. C., Boesch, H., Bowman, K. W., Deutscher, N. M., Dubey, M. K., Griffith, D. W. T., Hase, F., Kuze, A., Notholt, J., Ohyama, H., Parker, R., Payne, V. H., Sussmann, R., Sweeney, C., Velazco, V. A., Warneke, T., Wennberg, P. O., and Wunch, D.: Estimating global and North American methane emissions with high spatial resolution using GOSAT satellite data, Atmos. Chem. Phys., 15, 7049-7069, 2015.

Turnock, S. T., Spracklen, D. V., Carslaw, K. S., Mann, G. W., Woodhouse, M. T., Forster, P. M., Haywood, J., Johnson, C. E., Dalvi, M., Bellouin, N., and Sanchez-Lorenzo, A.: Modelled and observed changes in aerosols and surface solar radiation over Europe between 1960 and 2009, Atmos. Chem. Phys., 15, 9477-9500, 2015.

Turpin, B. J., and Lim, H.-J.: Species Contributions to PM2.5 Mass Concentrations: Revisiting Common Assumptions for Estimating Organic Mass, Aerosol Science and Technology, 35, 602-610, doi:10.1080/02786820119445, 2001.

US EPA, Procedures Document For National Emission Inventory, Criteria Air Pollutants 1985-1999, US Environmental Protection Agency, Research Triangle Park, NC, 2001.

US EPA, Integrated science assessment for particulate matter, US Environmental Protection Agency Washington, DC, 2009.

US EPA: Our Nation's Air – Status and Trends Through 2010, US Environmental Protection Agency, Washington, DC, 2012.

US EPA, 2011 National Emissions Inventory, version 2 Technical Support Document, US Environmental Protection Agency, Research Triangle Park, NC, 2015.

US EPA, Our Nation's Air – Status and Trends Through 2015, US Environmental Protection Agency, Washington, DC, 2016.

Van Damme, M., Clarisse, L., Heald, C. L., Hurtmans, D., Ngadi, Y., Clerbaux, C., Dolman, A. J., Erisman, J. W., and Coheur, P. F.: Global distributions, time series and error characterization of atmospheric ammonia (NH_3) from IASI satellite observations, Atmos. Chem. Phys., 14, 2905-2922, doi:10.5194/acp-14-2905-2014, 2014.

van der Werf, G. R., Randerson, J. T., Giglio, L., Collatz, G. J., Mu, M., Kasibhatla, P. S., Morton, D. C., DeFries, R. S., Jin, Y., and van Leeuwen, T. T.: Global fire emissions and the contribution of deforestation, savanna, forest, agricultural, and peat fires (1997–2009), Atmos. Chem. Phys., 10, 11707-11735, doi:10.5194/acp-10-11707-2010, 2010.

van Donkelaar, A., Martin, R. V., Leaitch, W. R., Macdonald, A. M., Walker, T. W., Streets, D. G., Zhang, Q., Dunlea, E. J., Jimenez, J. L., Dibb, J. E., Huey, L. G., Weber, R., and Andreae, M. O.: Analysis of aircraft and satellite measurements from the Intercontinental Chemical Transport Experiment (INTEX-B) to quantify long-range transport of East Asian sulfur to Canada, Atmos. Chem. Phys., 8, 2999-3014, doi:10.5194/acp-8-2999-2008, 2008.

van Donkelaar, A., Martin, R. V., Brauer, M., and Boys, B. L.: Use of satellite observations for long-term exposure assessment of global concentrations of fine particulate matter, Environ. Health Perspect., 123, doi:10.1289/ehp.1408646, 2015.

van Donkelaar, A., Martin, R. V., Brauer, M., Hsu, N. C., Kahn, R. A., Levy, R. C., Lyapustin, A., Sayer, A. M., and Winker, D. M.: Global Estimates of Fine Particulate Matter using a Combined Geophysical-Statistical Method with Information from Satellites, Models, and Monitors, Environ. Sci. Technol., 50, 3762-3772, 2016.

Vautard, R., Yiou, P., and van Oldenborgh, G. J.: Decline of fog, mist and haze in Europe over the past 30 years, Nat. Geosci., 2, 115-119, 2009.

Venkataraman, C., Habib, G., Eiguren-Fernandez, A., Miguel, A. H., and Friedlander, S. K.: Residential Biofuels in South Asia: Carbonaceous Aerosol Emissions and Climate Impacts, Science, 307, 1454-1456, doi:10.1126/science.1104359, 2005.

Vestreng, V., Myhre, G., Fagerli, H., Reis, S., and Tarrasón, L.: Twenty-five years of continuous sulphur dioxide emission reduction in Europe, Atmos. Chem. Phys., 7, 3663-3681, 2007.

Vestreng, V., Ntziachristos, L., Semb, A., Reis, S., Isaksen, I. S. A., and Tarrasón, L.: Evolution of NO_x emissions in Europe with focus on road transport control measures, Atmos. Chem. Phys., 9, 1503-1520, doi:10.5194/acp-9-1503-2009, 2009.

Vet, R., Artz, R. S., Carou, S., Shaw, M., Ro, C.-U., Aas, W., Baker, A., Bowersox, V. C., Dentener, F., Galy-Lacaux, C., Hou, A., Pienaar, J. J., Gillett, R., Forti, M. C., Gromov, S., Hara, H., Khodzher, T., Mahowald, N. M., Nickovic, S., Rao, P. S. P., and Reid, N. W.: A global assessment of precipitation chemistry and deposition of sulfur, nitrogen, sea salt, base cations, organic acids, acidity and pH, and phosphorus, Atmos. Environ., 93, 3-100, 2014.

Wakamatsu, S., Morikawa, T., and Ito, A.: Air pollution trends in Japan between 1970 and 2012 and impact of urban air pollution countermeasures, Asian Journal of Atmos. Environ., 7, 177-190, 2013.

Walker, J., Philip, S., Martin, R., and Seinfeld, J.: Simulation of nitrate, sulfate, and ammonium aerosols over the United States, Atmos. Chem. Phys., 12, 11213-11227, 2012.

Wang, H. J., and Chen, H. P.: Understanding the recent trend of haze pollution in eastern China: roles of climate change, Atmos. Chem. Phys., 16, 4205-4211, 2016.

Wang, K., Dickinson, R. E., and Liang, S.: Clear sky visibility has decreased over land globally from 1973 to 2007, Science, 323, 1468-1470, 2009.

Wang, K., Dickinson, R., Su, L., and Trenberth, K.: Contrasting trends of mass and optical properties of aerosols over the Northern Hemisphere from 1992 to 2011, Atmos. Chem. Phys., 12, 9387-9398, 2012.

Wang, K., Ma, Q., Li, Z., and Wang, J.: Decadal variability of surface incident solar radiation over China: Observations, satellite retrievals, and reanalyses, J. Geophys. Res., 120, 6500-6514, 2015a.

Wang, Q., Jacob, D. J., Fisher, J. A., Mao, J., Leibensperger, E. M., Carouge, C. C., Le Sager, P., Kondo, Y., Jimenez, J. L., Cubison, M. J., and Doherty, S. J.: Sources of carbonaceous aerosols and deposited black carbon in the Arctic in winter-spring: implications for radiative forcing, Atmos. Chem. Phys., 11, 12453-12473, 2011.

Wang, Q., Jacob, D. J., Spackman, J. R., Perring, A. E., Schwarz, J. P., Moteki, N., Marais, E. A., Ge, C., Wang, J., and Barrett, S. R. H.: Global budget and radiative forcing of black carbon aerosol: Constraints from pole-to-pole (HIPPO) observations across the Pacific, J. Geophys. Res., 119, 195-206, doi:10.1002/2013JD020824, 2014a.

Wang, R., Tao, S., Shen, H., Huang, Y., Chen, H., Balkanski, Y., Boucher, O., Ciais, P., Shen, G., Li, W., Zhang, Y., Chen, Y., Lin, N., Su, S., Li, B., Liu, J., and Liu, W.: Trend in Global Black Carbon Emissions from 1960 to 2007, Environ. Sci. Technol., 48, 6780-6787, 2014b.

Wang, S., Zhang, Q., Martin, R. V., Philip, S., Liu, F., Li, M., Jiang, X., and He, K.: Satellite measurements oversee China's sulfur dioxide emission reductions from coal-fired power plants, Environ. Res. Lett., 10, doi:10.1088/1748-9326/10/11/114015, 2015b.

Wang, X. L., Wen, Q. H., and Wu, Y.: Penalized maximal t test for detecting undocumented mean change in climate data series, J. Appl. Meteorol. Climatol., 46, 916-931, 2007.

Wang, X. L.: Accounting for autocorrelation in detecting mean shifts in climate data series using the penalized maximal t or F test, J. Appl. Meteorol. Climatol., 47, 2423-2444, 2008a.

Wang, X. L.: Penalized maximal F test for detecting undocumented mean shift without trend change, Journal of Atmospheric and Oceanic Technology, 25, 368-384, 2008b.

Wang, Y., and Jacob, D. J.: Anthropogenic forcing on tropospheric ozone and OH since preindustrial times, J. Geophys. Res., 103, 31123-31135, 1998.

Wang, Y., Zhang, Q. Q., He, K., Zhang, Q., and Chai, L.: Sulfate-nitrate-ammonium aerosols over China: response to 2000–2015 emission changes of sulfur dioxide, nitrogen oxides, and ammonia, Atmos. Chem. Phys., 13, 2635-2652, 2013.

Warneke, C., Bahreini, R., Brioude, J., Brock, C. A., de Gouw, J. A., Fahey, D. W., Froyd, K. D., Holloway, J. S., Middlebrook, A., Miller, L., Montzka, S., Murphy, D. M., Peischl, J., Ryerson, T. B., Schwarz, J. P., Spackman, J. R., and Veres, P.: Biomass burning in Siberia and Kazakhstan as an important source for haze over the Alaskan Arctic in April 2008, Geophys. Res. Lett., 36, doi:10.1029/2008GL036194, 2009.

Warner, J. X., Wei, Z., Strow, L. L., Dickerson, R. R., and Nowak, J. B.: The global tropospheric ammonia distribution as seen in the 13-year AIRS measurement record, Atmos. Chem. Phys., 16, 5467-5479, doi:10.5194/acp-16-5467-2016, 2016.

Weagle, C. L., Snider, G., Li, C., van Donkelaar, A., Philip, S., Bissonnette, P., et al., Global sources of fine particulate matter: interpretation of PM2.5 chemical composition observed by the surface particulate matter network using a global chemical transport model, Environ. Sci. Technol., doi:10.1021/acs.est.8b01658, 2018.

Weatherhead, E. C., Reinsel, G. C., Tiao, G. C., Meng, X. L., Choi, D., Cheang, W. K., Keller, T., DeLuisi, J., Wuebbles, D. J., and Kerr, J. B.: Factors affecting the detection of trends: Statistical considerations and applications to environmental data, J. Geophys. Res., 103, 17149-17161, 1998.

Webb, N. P., and Pierre, C.: Quantifying Anthropogenic Dust Emissions, Earth's Future, 6, 286-295, 2016.

Weber, R. J., Guo, H., Russell, A. G., and Nenes, A.: High aerosol acidity despite declining atmospheric sulfate concentrations over the past 15 years, Nat. Geosci., 9, 282, doi:10.1038/ngeo2665, 2016.

Wecht, K. J., Jacob, D. J., Frankenberg, C., Jiang, Z., and Blake, D. R.: Mapping of North American methane emissions with high spatial resolution by inversion of SCIAMACHY satellite data, J. Geophys. Res., 119, 7741-7756, doi:10.1002/2014JD021551, 2014.

Wentworth, G. R., Murphy, J. G., Gregoire, P. K., Cheyne, C. A. L., Tevlin, A. G., and Hems, R.: Soil–atmosphere exchange of ammonia in a non-fertilized grassland: measured emission potentials and inferred fluxes, Biogeosciences, 11, 5675-5686, 2014.

Wesely, M. L.: Parameterization of surface resistances to gaseous dry deposition in regional-scale numerical models, Atmos. Environ., 23, 1293-1304, 1989.

West, J. J., Cohen, A., Dentener, F., Brunekreef, B., Zhu, T., Armstrong, B., Bell, M. L., Brauer, M., Carmichael, G., Costa, D. L., Dockery, D. W., Kleeman, M., Krzyzanowski, M., Künzli, N., Liousse, C., Lung, S.-C. C., Martin, R. V., Pöschl, U., Pope, C. A., Roberts, J. M., Russell, A. G., and Wiedinmyer, C.: "What We Breathe Impacts Our Health: Improving Understanding of the Link between Air Pollution and Health", Environ. Sci. Technol., 50, 4895-4904, 2016.

Westervelt, D. M., Horowitz, L. W., Naik, V., Tai, A. P. K., Fiore, A. M., and Mauzerall, D. L.: Quantifying PM2.5-meteorology sensitivities in a global climate model, Atmos. Environ., 142, 43-56, doi:https://doi.org/10.1016/j.atmosenv.2016.07.040, 2016.

Wild, M., Gilgen, H., Roesch, A., Ohmura, A., Long, C. N., Dutton, E. G., Forgan, B., Kallis, A., Russak, V., and Tsvetkov, A.: From dimming to brightening: Decadal changes in solar radiation at Earth's surface, Science, 308, 847-850, 2005.

Wild, M.: Global dimming and brightening: A review, J. Geophys. Res., 114, doi:10.1029/2008JD011470, 2009.

Wild, M.: Enlightening Global Dimming and Brightening, Bull. Am. Meteorol. Soc., 93, 27-37, doi:10.1175/bams-d-11-00074.1, 2012.

Willett, K. M., Williams Jr, C. N., Dunn, R. J., Thorne, P. W., Bell, S., Podesta, M. d., Jones, P. D., and Parker, D. E.: HadISDH: an updateable land surface specific humidity product for climate monitoring, Clim. Past, 9, 657-677, 2013.

WMO: Guide to Meteorological Instruments and Methods of Observation. Chapter 9. Measurement of Visibility, I.9-1–I.9- 15, WMO-No. 8, World Meteorological Organization, Geneva, Switzerland, 2008.

Wong, E. Y., Gohlke, J., Griffith, W. C., Farrow, S., and Faustman, E. M.: Assessing the health benefits of air pollution reduction for children, Environ. Health Perspect., 112, 226-232, 2004.

Wu, J., Fu, C., Zhang, L., and Tang, J.: Trends of visibility on sunny days in China in the recent 50 years, Atmos. Environ., 55, 339-346, 2012.

Wu, J., Luo, J., Zhang, L., Xia, L., Zhao, D., and Tang, J.: Improvement of aerosol optical depth retrieval using visibility data in China during the past 50 years, J. Geophys. Res., 119, 13,370-313,387, 2014.

Xing, J., Pleim, J., Mathur, R., Pouliot, G., Hogrefe, C., Gan, C. M., and Wei, C.: Historical gaseous and primary aerosol emissions in the United States from 1990 to 2010, Atmos. Chem. Phys., 13, 7531-7549, doi:10.5194/acp-13-7531-2013, 2013.

Xing, J., Mathur, R., Pleim, J., Hogrefe, C., Gan, C. M., Wong, D. C., Wei, C., Gilliam, R., and Pouliot, G.: Observations and modeling of air quality trends over 1990–2010 across the Northern Hemisphere: China, the United States and Europe, Atmos. Chem. Phys., 15, 2723-2747, 2015.

Xu, J. W., Martin, R. V., Morrow, A., Sharma, S., Huang, L., Leaitch, W. R., Burkart, J., Schulz, H., Zanatta, M., Willis, M. D., Henze, D. K., Lee, C. J., Herber, A. B., and Abbatt, J. P. D.: Source attribution of Arctic black carbon constrained by aircraft and surface measurements, Atmos. Chem. Phys., 17, 11971-11989, doi:10.5194/acp-17-11971-2017, 2017.

Xu, L., Guo, H., Boyd, C. M., Klein, M., Bougiatioti, A., Cerully, K. M., Hite, J. R., Isaacman-VanWertz, G., Kreisberg, N. M., Knote, C., Olson, K., Koss, A., Goldstein, A. H., Hering, S. V., de Gouw, J., Baumann, K., Lee, S.-H., Nenes, A., Weber, R. J., and Ng, N. L.: Effects of anthropogenic emissions on aerosol formation from isoprene and monoterpenes in the southeastern United States, Proc. Natl. Acad. Sci. U.S.A., 112, 37-42, doi:10.1073/pnas.1417609112, 2015a.

Xu, L., Suresh, S., Guo, H., Weber, R. J., and Ng, N. L.: Aerosol characterization over the southeastern United States using high-resolution aerosol mass spectrometry: spatial and seasonal variation of aerosol composition and sources with a focus on organic nitrates, Atmos. Chem. Phys., 15, 7307-7336, doi:10.5194/acp-15-7307-2015, 2015b.

Xu, L., Middlebrook, A. M., Liao, J., Gouw, J. A., Guo, H., Weber, R. J., Nenes, A., Lopez-Hilfiker, F. D., Lee, B. H., Thornton, J. A., Brock, C. A., Neuman, J. A., Nowak, J. B., Pollack, I. B., Welti, A., Graus, M., Warneke, C., and Ng, N. L.: Enhanced formation of isoprene-derived organic aerosol in sulfur-rich power plant plumes during Southeast Nexus, J. Geophys. Res., 121, 11,137-111,153, doi:10.1002/2016JD025156, 2016.

Xu, Q.: Abrupt change of the mid-summer climate in central east China by the influence of atmospheric pollution, Atmos. Environ., 35, 5029-5040, 2001.

Xu, X., Wang, J., Henze, D. K., Qu, W., and Kopacz, M.: Constraints on aerosol sources using GEOS-Chem adjoint and MODIS radiances, and evaluation with multisensor (OMI, MISR) data, J. Geophys. Res., 118, 6396-6413, doi:10.1002/jgrd.50515, 2013.

Yang, Y., Liao, H., and Lou, S.: Increase in winter haze over eastern China in recent decades: Roles of variations in meteorological parameters and anthropogenic emissions, J. Geophys. Res., 121, 13,050-013,065, doi:10.1002/2016JD025136, 2016.

Ye, J., Li, W., Li, L., and Zhang, F.: “North drying and south wetting” summer precipitation trend over China and its potential linkage with aerosol loading, Atmospheric Res., 125, 12-19, 2013.

Yin, Z., Wang, H., and Chen, H.: Understanding severe winter haze events in the North China Plain in 2014: roles of climate anomalies, Atmos. Chem. Phys., 17, 1641-1651, 2017.

Yoon, J., von Hoyningen-Huene, W., Kokhanovsky, A. A., Vountas, M., and Burrows, J. P.: Trend analysis of aerosol optical thickness and Ångström exponent derived from the global AERONET spectral observations, Atmos. Meas. Tech., 5, 1271-1299, 2012.

Yoon, J., Burrows, J. P., Vountas, M., von Hoyningen-Huene, W., Chang, D. Y., Richter, A., and Hilboll, A.: Changes in atmospheric aerosol loading retrieved from space-based measurements during the past decade, Atmos. Chem. Phys., 14, 6881-6902, 2014.

Yoon, J., Pozzer, A., Chang, D. Y., Lelieveld, J., Kim, J., Kim, M., Lee, Y. G., Koo, J. H., Lee, J., and Moon, K. J.: Trend estimates of AERONET-observed and model-simulated AOTs between 1993 and 2013, Atmos. Environ., 125, 33-47, 2016.

Young, S. A., Vaughan, M. A., Kuehn, R. E., and Winker, D. M.: The Retrieval of Profiles of Particulate Extinction from Cloud–Aerosol Lidar and Infrared Pathfinder Satellite Observations (CALIPSO) Data: Uncertainty and Error Sensitivity Analyses, J. Atmospheric Ocean. Technol., 30, 395-428, 2013.

Yttri, K. E., Aas, W., Tørseth, K., Kristiansen, N. I., Lund Myhre, C., Tsyro, S., Simpson, D., Bergström, R., Mareckova, K., Wankmuller, R., Klimont, Z., Ammann, M., Kouvarakis, G., Laj, P., Pappalardo, G., and Prévôt, A. S. H.: Transboundary particulate matter in Europe, EMEP Status report, 4/2012, Joint CCC, MSC-W, CEIP and CIAM Report, available at: http://www.nilu.no/projects/ccc/reports/emep4-2012.pdf, last access: 14 October 2015, 2012.

Yu, H., Kaufman, Y. J., Chin, M., Feingold, G., Remer, L. A., Anderson, T. L., Balkanski, Y., Bellouin, N., Boucher, O., Christopher, S., DeCola, P., Kahn, R., Koch, D., Loeb, N., Reddy, M. S., Schulz, M., Takemura, T., and Zhou, M.: A review of measurement-based assessments of the aerosol direct radiative effect and forcing, Atmos. Chem. Phys., 6, 613-666, 2006.

Yue, S., Pilon, P., Phinney, B., and Cavadias, G.: The influence of autocorrelation on the ability to detect trend in hydrological series, Hydrol. Process., 16, 1807-1829, 2002.

Zhang, H., Yee, L. D., Lee, B. H., Curtis, M. P., Worton, D. R., Isaacman-VanWertz, G., Offenberg, J. H., Lewandowski, M., Kleindienst, T. E., Beaver, M. R., Holder, A. L., Lonneman, W. A., Docherty, K. S., Jaoui, M., Pye, H. O. T., Hu, W., Day, D. A., Campuzano-Jost, P., Jimenez, J. L., Guo, H., Weber, R. J., de Gouw, J., Koss, A. R., Edgerton, E. S., Brune, W., Mohr, C., Lopez-Hilfiker, F. D., Lutz, A., Kreisberg, N. M., Spielman, S. R., Hering, S. V., Wilson, K. R., Thornton, J. A., and Goldstein, A. H.: Monoterpenes are the largest source of summertime organic aerosol in the southeastern United States, Proc. Natl. Acad. Sci. U.S.A., 115, 2038-2043, 2018a.

Zhang, J., and Reid, J. S.: A decadal regional and global trend analysis of the aerosol optical depth using a data-assimilation grade over-water MODIS and Level 2 MISR aerosol products, Atmos. Chem. Phys., 10, 10949-10963, doi:10.5194/acp-10-10949-2010, 2010.

Zhang, L., Gong, S., Padro, J., and Barrie, L.: A size-segregated particle dry deposition scheme for an atmospheric aerosol module, Atmos. Environ., 35, 549-560, 2001.

Zhang, L., Jacob, D. J., Knipping, E. M., Kumar, N., Munger, J. W., Carouge, C. C., van Donkelaar, A., Wang, Y. X., and Chen, D.: Nitrogen deposition to the United States: distribution, sources, and processes, Atmos. Chem. Phys., 12, 4539-4554, 2012a.

Zhang, L., Kok, J. F., Henze, D. K., Li, Q., and Zhao, C.: Improving simulations of fine dust surface concentrations over the western United States by optimizing the particle size distribution, Geophys. Res. Lett., 40, 3270-3275, doi:10.1002/grl.50591, 2013.

Zhang, L., Henze, D. K., Grell, G. A., Torres, O., Jethva, H., and Lamsal, L. N.: What factors control the trend of increasing AAOD over the United States in the last decade?, J. Geophys. Res., 122, 1797-1810, doi:10.1002/2016JD025472, 2017.

Zhang, L., Chen, Y., Zhao, Y., Henze, D. K., Zhu, L., Song, Y., Paulot, F., Liu, X., Pan, Y., Lin, Y., and Huang, B.: Agricultural ammonia emissions in China: reconciling bottom-up and top-down estimates, Atmos. Chem. Phys., 18, 339-355, 2018b.

Zhang, Q., Jimenez, J., Canagaratna, M., Allan, J., Coe, H., Ulbrich, I., Alfarra, M., Takami, A., Middlebrook, A., and Sun, Y.: Ubiquity and dominance of oxygenated species in organic aerosols in anthropogenically-influenced Northern Hemisphere midlatitudes, Geophys. Res. Lett., 34, doi:10.1029/2007GL029979, 2007.

Zhang, X. Y., Wang, Y. Q., Zhang, X. C., Guo, W., and Gong, S. L.: Carbonaceous aerosol composition over various regions of China during 2006, J. Geophys. Res., 113, doi:10.1029/2007JD009525, 2008.

Zhang, X. Y., Wang, Y. Q., Niu, T., Zhang, X. C., Gong, S. L., Zhang, Y. M., and Sun, J. Y.: Atmospheric aerosol compositions in China: spatial/temporal variability, chemical signature, regional haze distribution and comparisons with global aerosols, Atmos. Chem. Phys., 12, 779-799, doi:10.5194/acp-12-779-2012, 2012b.

Zhang, Y., Wen, X. Y., and Jang, C. J.: Simulating chemistry–aerosol–cloud–radiation–climate feedbacks over the continental U.S. using the online-coupled Weather Research Forecasting Model with chemistry (WRF/Chem), Atmos. Environ., 44, 3568-3582, 2010.

Zhang, Z., Zhang, X., Gong, D., Quan, W., Zhao, X., Ma, Z., and Kim, S.-J.: Evolution of surface O3 and PM2.5 concentrations and their relationships with meteorological conditions over the last decade in Beijing, Atmos. Environ., 108, 67-75, 2015.

Zhao, C., and Wang, Y.: Assimilated inversion of NOx emissions over east Asia using OMI NO2 column measurements, Geophys. Res. Lett., 36, doi:10.1029/2008GL037123, 2009.

Zhao, Y., Zhang, J., and Nielsen, C. P.: The effects of recent control policies on trends in emissions of anthropogenic atmospheric pollutants and CO_2 in China, Atmos. Chem. Phys., 13, 487-508, 2013.

Zhu, L., Henze, D. K., Cady-Pereira, K. E., Shephard, M. W., Luo, M., Pinder, R. W., Bash, J. O., and Jeong, G. R.: Constraining U.S. ammonia emissions using TES remote sensing observations and the GEOS-Chem adjoint model, J. Geophys. Res., 118, 3355-3368, 2013.

Zhu, L., Henze, D., Bash, J., Jeong, G. R., Cady-Pereira, K., Shephard, M., Luo, M., Paulot, F., and Capps, S.: Global evaluation of ammonia bidirectional exchange and livestock diurnal variation schemes, Atmos. Chem. Phys., 15, 12823-12843, 2015a.

Zhu, L., Henze, D. K., Bash, J. O., Cady-Pereira, K. E., Shephard, M. W., Luo, M., and Capps, S. L.: Sources and Impacts of Atmospheric NH3: Current Understanding and Frontiers for Modeling, Measurements, and Remote Sensing in North America, Current Pollution Reports, 1, 95-116, 2015b.

Zou, Y., Wang, Y., Zhang, Y., and Koo, J.-H.: Arctic sea ice, Eurasia snow, and extreme winter haze in China, Sci. Adv., 3, doi:10.1126/sciadv.1602751, 2017.